ON THE SUPPORT EFFECT OF THE CO_2 METHANATION

Vom Fachbereich Produktionstechnik

der

UNIVERSITÄT BREMEN

zur Erlangung des Grades

Doktor-Ingenieur

genehmigte

Dissertation

von

Jan Ilsemann, M.Sc.

Gutachter: Prof. Dr.-Ing. Jorg Thöming (Universität Bremen)

Prof. Dr. Reinhard Schomäcker (Technische Universität Berlin)

Tag der mündlichen Prüfung: 10.11.2020

Zusammenfassung

Im Zuge der Energiewende wird erwartet, dass der Bedarf an langfristigen Energiespeichertechnologien zur Stabilisierung des Stromnetzes und als Notfallreserve ansteigt. Ein Baustein kann hier die Power-to-Gas Technologie darstellen. Hierbei wird zu Zeiten von überschüssigem Strom aus erneuerbaren Energien, wie Wind- und Sonnenenergie, elektrolytisch Wasserstoff (H_2) hergestellt, welcher in einem zweiten Schritt mit Kohlenstoffdioxid (CO_2) zu Methan (CH_4) und Wasser (H_2O) reagiert (CO_2 Methanisierung). Der Prozess kann in die bestehende Erdgasinfrastruktur eingebettet werden und dabei fossiles Erdgas durch „grünes“, „künstliches“ Erdgas ersetzen und damit einen Beitrag zur Reduktion der CO_2 Emissionen leisten. In der Regel werden für die heterogen-katalysierte CO_2 Methanisierung Al_2O_3 geträgerte Ni- oder Ru-Katalysatoren eingesetzt.

Im Zentrum dieser Arbeit steht der Einfluss des Katalysatorträgers auf die CO_2 Methanisierung. Es wird postuliert, dass insbesondere die Säure-/Baseneigenschaften einen ausgeprägten Einfluss auf die CO_2 Adsorption und Aktivierung haben und dabei andere, aktiviere Reaktionsmechanismen ablaufen können. So können Brønsted basische OH-Gruppen CO_2 in Form von Hydrogencarbonaten binden, wohingegen Lewis basische Sauerstoffleerstellen CO_2 direkt als bidentates Carbonat aktivieren und die elektronische Struktur des Metalldeponats beeinflussen können. In allen Fällen wird angenommen, dass H_2 am Metall dissoziativ adsorbiert. Um diese Effekte genauer zu beleuchten, werden zunächst, einem Baukastenprinzip folgend, Modellkatalysatoren mit uniformen Ruthenium-Nanopartikeln (1 nm im Durchmesser), welche auf Oxiden mit unterschiedlichen Säure-/Baseneigenschaften geträgert werden, betrachtet. Als Träger werden die Seltenerdmetalloxide (REO) Sm_2O_3, Gd_2O_3 und Y_2O_3 (Brønsted und Lewis basisch), ZrO_2 und TiO_2 (nur Lewis basisch), Al_2O_3 und MgO (Brønsted basisch) und SiO_2 (weder Lewis noch Brønsted basisch) vollständig mittels XRD, N_2 Physisorption, TEM und CO_2-TPD in Kombination mit DRIFTS charakterisiert und hinsichtlich ihrer Performance in der CO_2 Methanisierung verglichen. Es zeigt sich, dass die Anwesenheit von Lewis basischen Sauerstoffleerstellen einen ausgeprägten positiven Effekt hat. So ist die katalytische Umsetzung von CO_2 an Katalysatoren mit Lewis basischen Eigenschaften über den gesamten untersuchten Temperaturraum höher als an Katalysatoren ohne Lewis basische Sauerstoffleerstellen. Innerhalb der Lewis basisch geträgerten Katalysatoren tritt allerdings eine Änderung in der aktivsten Katalysatorträgergruppe auf. Im Niedertemperaturbereich (< 300 °C) weisen die ausschließlich Lewis basischen Träger TiO_2 und ZrO_2 die höheren Reaktionsraten auf, wohingegen bei höheren Temperaturen die Katalysatoren mit

Seltenerdmetalloxidträger am aktivsten sind. Mittels komplementären temperatur-abhängigen und isothermen *operando* DRIFTS-Messungen lässt sich dies auf mechanistische Änderungen zurückführen. So wird am Ru-TiO_2 Katalysator lediglich der trägerunabhängige CO-Mechanismus mittels dissoziativer CO_2 Adsorption auf Ru beobachtet, sodass die hohe Aktivität auf die Metall-Träger Wechselwirkung zurückzuführen ist, welche zu einem vorteilhaften CO/H-Verhältnis auf der Ru-Oberfläche führt. Hingegen läuft die Reaktion am ebenfalls Lewis basischen Ru-ZrO_2 Katalysator zusätzlich über bidentate Carbonate auf dem ZrO_2 Träger ab, welche in den nächsten Zwischenschritten zu bidentaten Hydrogencarbonaten und Formiaten hydriert werden. Im Gegensatz dazu verläuft die Reaktion an den REOs zunächst vor allem über den CO-Mechanismus. Bei Temperaturen über 300 °C tritt zusätzlich ein weiterer Mechanismus auf, in dem an Brønsted basischen OH-Gruppen adsorbiertes CO_2 (Hydrogencarbonat) über Formyl-Spezies zu Methan hydriert wird. Hierbei korreliert das Auftreten des zusätzlichen Reaktionswegs gut mit der Temperatur, ab welcher die REO geträgerten Systeme die höchsten Aktivitäten aufweisen.

Auf Grundlage dieser Beobachtungen wird ein neuartiges Ni-Sm_2O_3 Katalysatorsystem mittels eines *one-pot* Sol-Gel-Verfahrens entwickelt, welches im Vergleich zu literaturbekannten und industriellen Systemen wettbewerbsfähig sein soll. Um die bestmögliche Performance zu erzielen, wird hierzu zusätzlich die Ni-Beladung variiert um das richtige Verhältnis aus H_2- (auf dem metallischen Ni) und CO_2-Adsorptionsstellen (auf Sm_2O_3) zu finden. Es zeigt sich, dass eine Ni-Beladung von 30-40 Gew.% die höchsten Umsätze ermöglicht. Die gefundenen Systeme erzielen weiterhin signifikant höhere Umsätze als die Referenzsysteme, insbesondere im Temperaturbereich bis 300 °C, welches auf die höhere CO_2 Adsorptionskapazität der Ni-Sm_2O_3 Systeme zurückzuführen ist.

Allerdings zeigt sich, dass der Ni-Sm_2O_3 Katalysator schnell deaktiviert. Ursächlich hierfür ist, wie mittels einer Kombination von katalytischen Experimenten unter verschiedenen Reaktionsbedingungen, DRIFTS und unterschiedlichen Reaktivierungsprozeduren gezeigt wird, eine Katalysatorvergiftung durch thermisch stabile Carbonate, die an sauerstoffdefizienten Stellen gebunden sind (bidentate und polydentate Carbonate) und dabei aktive Zentren des Katalysators blockieren. Hingegen ist der Katalysator resistent gegenüber Verkokung und Sintern auch unter extremen Bedingungen (85 h bei 490 °C sowie niedrigen H_2/CO_2 Verhältnissen). Dies erlaubt den Katalysator regelmäßig bei hohen Temperaturen zu regenerieren oder die Reaktionsbedingungen (hohe Reaktionstemperaturen bei niedrigen CO_2 Flussraten) anzupassen, sodass die Katalysatorvergiftung minimiert wird.

Die Ergebnisse dieser Arbeit stellen einen Beitrag zur rationalen Katalysatorentwicklung für die CO_2 Methanisierung dar. Es wird deutlich, dass die Basizität ein zweischneidiges Schwert darstellt, welche zu hohen Aktivitäten aber auch neuen Deaktivierungsphänomenen führen kann und entsprechend genau eingestellt werden muss.

Abstract

In a transitioning energy sector, which heavily relies on renewable energies, long-term energy storage with high capacity are required to stabilize power grids and to serve as back-up in prolonged times of energy shortage. Here, the Power-to-Gas (PtG) technology can be part of a solution. In times of surplus power supply, hydrogen (H_2) is produced electrolytically and, in a second step, reacts with carbon dioxide (CO_2) to methane (CH_4) and water (H_2O). The process can be integrated into the existing natural gas infrastructure and as such replace fossil natural gas by "green", synthetic natural gas, thereby contributing to reduce CO_2 emissions. Usually supported Ni or Ru catalysts are used for the heterogeneously catalyzed CO_2 methanation.

The influence of the catalyst support on the CO_2 methanation is at the center of this thesis. It is hypothesized that particularly the acid/base properties have a profound impact on CO_2 adsorption and activation, in dependence of which different, more reactive reaction mechanisms occur. For instance, Brønsted basic OH groups can adsorb CO_2 as hydrogen carbonates, whereas Lewis basic oxygen vacancies can directly activate CO_2 as bidentate carbonate and can further affect the electronic structure of the metal deposit. In all cases, it is assumed that H_2 adsorbs dissociatively on the metal. To gain profound insights into these effects, model catalysts prepared by a building block approach comprising of uniform Ru nanoparticles (1 nm in diameter) and various oxidic supports with different acid/base properties were used. The rare earth metal oxides (REO) Sm_2O_3, Gd_2O_3 and Y_2O_3 (Brønsted and Lewis basic), TiO_2 and ZrO_2 (only Lewis basic), Al_2O_3 and MgO (Brønsted basic), and SiO_2 (non-basic) are chosen, fully characterized by means of XRD, N_2 physisorption, TEM and CO_2-TPD in combination with DRIFTS, and compared regarding their catalytic activity for CO_2 methanation. The results clearly show the beneficial effect of Lewis basic oxygen vacancies. In comparison to the catalysts supported on non-Lewis basic oxides, higher CO_2 consumption rates are found for the REO, TiO_2 and ZrO_2 supported catalysts over the entire investigated temperature range. Yet, among these catalysts a shift in the leading role is observed. In the low-temperature regime (< 300 °C) the catalysts supported on the solely Lewis basic oxides TiO_2 and ZrO_2 exhibit the highest reaction rates, whereas at higher temperatures the REO supported catalysts perform best. Complementary temperature-dependent and isothermal *operando* DRIFTS experiments reveal that this change can be attributed to a shift in the underlying reaction mechanisms. On the Ru-TiO_2 catalyst the support independent CO mechanism via dissociative CO_2 adsorption on the metallic Ru is observed;

yet, the high activity and the clear evidence for the presence of oxygen vacancies point towards a pronounced but indirect metal-support effect, in which the electronic structure of the Ru particle is changed resulting in a more favorable CO/H ratio on the Ru surface. Over the also Lewis basic ZrO_2 supported catalyst, the reaction additionally proceeds by CO_2 activation on oxygen vacancies (bidentate carbonates) on the support, which are subsequently hydrogenated towards methane via bidentate hydrogen carbonates and formates. However, the measured rates are slightly lower than for the Ru-TiO_2 catalyst. In contrast, the reaction proceeds on the REO supported catalysts mainly via the CO mechanism in the low temperature regime. However and coinciding well with the temperature in the catalytic experiments at which the REO supported catalysts take the leading role, an additional reaction pathway sets in. This mechanism involves CO_2 adsorption as hydrogen carbonates on Brønsted basic OH groups that are subsequently hydrogenated via a formyl specie towards CH_4.

Based on these results a novel Ni-Sm_2O_3 catalyst system, prepared by a facile *one-pot* sol-gel method, is developed that is supposed to be competitive with literature-known and industrial reference catalysts. To maximize its performance, the Ni loading is varied to find the right balance between H_2 adsorption sites on metallic Ni and CO_2 adsorption sites on the Ni-Sm_2O_3 perimeter. A Ni loading ranging between 30-40 wt.% is shown to yield the highest activity. In comparison to the reference catalysts, significantly higher conversion levels are achieved over the Ni-Sm_2O_3 xerogel catalysts, particularly at reaction temperatures below 350 °C, which can be attributed to the significantly higher CO_2 adsorption capacity as determined by pulsed CO_2 chemisorption.

However, the developed Ni-Sm_2O_3 catalyst suffers from a rapid, asymptotic deactivation. To unravel the governing deactivation mechanism, catalytic experiments under various reaction conditions, DRIFTS and regeneration experiments are combined and show that the catalyst is poisoned by thermally stable carbonates that are formed on oxygen-deficient sites, and block active sites. In turn, the catalyst is resistant against coking and sintering even under harsh conditions (85 h at 490 °C, as well as severely under-stochiometric feed gas compositions). This allows to periodically regenerate the catalyst at elevated temperatures or to adjust the reaction conditions such that poisoning is suppressed, that is high temperatures and low CO_2 flow rates.

The results of this work contribute to rationalize catalyst development for CO_2 methanation. It is obvious that the support's basicity is a double-edged sword. On the hand it can significantly increase the catalytic turn-over; however on the other hand, it can also lead to catalyst poisoning, and hence requires a careful and precise adjustment.

Acknowledgements

They say it takes a village to raise a child. In my experience, the same can be said for doing a PhD. A shout-out to the following people from "my village":

Marcus Bäumer. Thank you! For giving me, a chemistry rookie, the opportunity and freedom to do my "own" research, your unwavering support and for putting me back on track, when I lost myself in the jungle of data.

I thank *Jorg Thöming* for agreeing to serve as first reviewer of this thesis and his kind support throughout my time at the UFT, whenever it was needed.

I thank *Reinhard Schomäcker* for his interest in my work, his acceptance to be the second reviewer of my thesis and for arousing my interest in catalysis and reaction engineering during my master's degree in the first place.

I thank all members of *MIMENIMA*, and, in particular, *Michaela Wilhelm* and *Kurosch Rezwan* for uncomplicated access to their labs and for providing funding for my research stay in Montreal and all the conferences across the world I could attend. (Though it did not help the CO_2 foot print of this thesis, I cherish the memories and believe it helped me grow a lot as a person.)

I thank *Thorsten Gesing* for his upright interest in my work and all the help with the refinements of the XRD patterns. I always enjoyed our discussions!

I am indebted to *Conny Rybarsch-Steinke* and *Martin Nowak*. Their input, ideas and support with all the practical challenges, i.e. building set-ups, was gold! I hope you are aware of how much I learned from you!

The "*CPEians*" at McGill University. In particular, *Jan "Chief" Kopyscinski, Jose Hernandez* and *Kanchan Dutta*. Thank you for taking me in your group and all the fun times we had!

I thank *Petra Martinovic* and *Oliver Thüringer*, who worked for me as student assistants, for all the hours spent synthesizing samples and at the DRIFTS. I always enjoyed working with you guys, and am grateful that you put up with my spontaneous, but, obviously, super urgent, ideas I came up with five minutes before leaving.

I thank *Sarah Neumann* for being such a helpful and pleasant office mate, who provided me with an occasional chemistry crash course and introduced me to the colloidal methods.

I thank *Vera Suling* for her assistance with all the administrative things and the always enjoyable discussions about Werder.

I am grateful for getting to know so many people at the IAPC and UFT who made most days in and outside of work good fun and I am happy that I found so many friends among them. A special shout-out to *Ingmar* and *Georg* for all the lunch breaks, discussions over a beer and travels. I also thank *Christoph* for his relentless effort to distract me from work.

I thank Annabelle who took on the responsibility to proof-read this thesis. It is great that, despite the distance and the time difference, I can still call you a friend.

I deeply thank *my family*, particularly my parents *Frank* and *Sabrina* and my sister *Anneke*, for their unlimited support, all the fun times, everything they enabled me to do/try in my life, and plenty of "good advice". Here is to you!

Jassi. Thank you! For taking my mind of work on frustrating days, for listening to successful and not so successful stories and simply for being there. Thank you. For everything!

List of Publications (in chronological order)

M. Mirdrikvand, J. Ilsemann, J. Thöming, and W. Dreher, „Spatially Resolved Characterization of the Gas Propagator in Monolithic Structured Catalysts Using NMR Diffusiometry", *Chemical Engineering & Technology*, **2018**, 41, 9, 1871-1880.

M. A. Worsley, J. Ilsemann, T.M. Gesing, V. Zielasek, A.J. Nelson, R.A.S. Ferreira, L.D. Carlos, A.E. Gash, and M. Bäumer, "Chlorine-free, monolithic lanthanide series rare earth oxide aerogels via epoxide-assisted sol-gel method", *Journal of Sol-Gel Science and Technology*, **2019**, 89, 1, 176-188.

J. Ilsemann, A. Sonström, T.M. Gesing, R. Anwander, and M. Bäumer, "Highly Active Sm_2O_3-Ni Xerogel catalysts for CO_2 methanation", *ChemCatChem*, **2019**, 11, 6, 1732-1741.

H.P. Macedo, R.L.B.A. Medeiros, J. Ilsemann, D.M.A. Melo, K. Rezwan, and M. Wilhelm, "Nickel-containing hybrid ceramics derived from polysiloxanes with hierarchical porosity for CO_2 methanation", *Microporous and Mesoporous Materials*, **2019**, 278, 156-166.

J. Ilsemann, A. Straß-Eifert, J. Friedland, L. Kiewidt, J. Thöming, M. Bäumer, and R. Güttel, "Cobalt@Silica Core-Shell Catalysts for Hydrogenation of CO/CO_2 Mixtures to Methane", *ChemCatChem*, **2019**, 11, 19, 4884-4893.

J.A. Hernandez Lalinde, P. Roongruangsree, J. Ilsemann, M. Bäumer, and J. Kopyscinski, "CO_2 methanation and reverse water gas shift reaction. Kinetic study based on in situ spatially-resolved measurements", *Chemical Engineering Journal*, **2020**, 390, 124629.

A. Jones, D. Aziz, J. Ilsemann, M. Bäumer, and H. Hagelin-Weaver, „Effects of low molar concentrations of low-valence dopants on samarium oxide xerogels in the oxidative coupling of methane", accepted at *Catalysis Today*.

A. Jones, D. Aziz, J. Ilsemann, M. Bäumer, and H. Hagelin-Weaver, „Doped samarium oxide xerogels for oxidative coupling of methane – Effects of high-valence dopants at very low concentrations", accepted at *Catalysis Today*.

J. Ilsemann, M.M. Murshed, T.M. Gesing, J. Kopyscinski, and M. Bäumer, „On the support dependency for the CO_2 methanation - Decoupling size and support effects", submitted to *Catalysis, Science & Technology*.

Content

1

INTRODUCTION

1.1 The Need for Energy Storage Systems and the Power-to-Gas Technology

In the wake of climate change and CO_2 emission reduction goals, the German energy sector is transitioning from fossil fuels towards renewable energies.[1, 2] However, the requirements for grid stability and a guaranteed satisfaction of demand at all times are incompatible with the fluctuating, stochastic availability of wind and solar energy, the expected pillars of the future energy system.[3] Yet, despite the possibility to predict future energy demand and supply to a certain extent, fossil fuel power plants cannot provide the dynamic operating behavior required to compensate for the fluctuations in the renewable power supply. Particularly, when large capacities of renewable energies become available, efficient storage technologies are necessary to ensure a stable and reliable energy system.[2, 3]

Energy storage technologies can be grouped according to their form into chemical, electrochemical, electrical, thermal and mechanical storage systems.[4] Inherent to these storage forms are differing capacities and possible storage periods that make them suitable to address different challenges in a future, restructured energy industry. Figure 1-1 shows an overview of

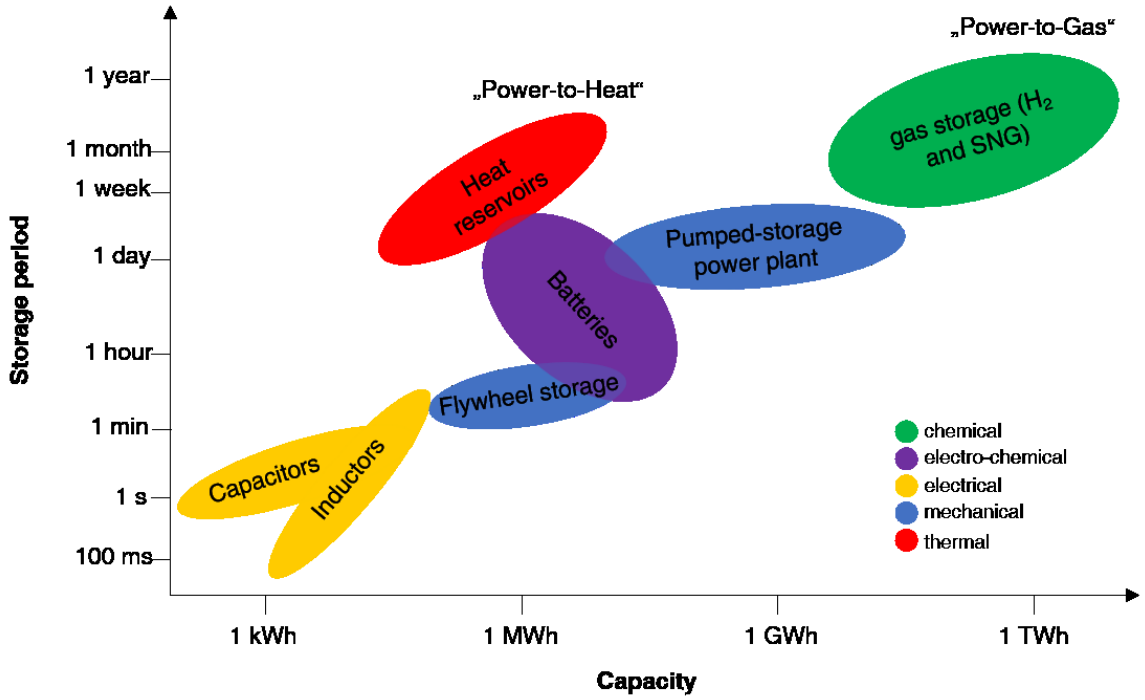

Figure 1-1 **Comparison of different energy storage technologies by their potential capacity and storage period. Adapted from Sterner and Stadler.[4]**

the discussed technologies grouped by the storage type and compares them by the respective storage capacity and period. Short-term storage technologies, such as capacitors and inductors, are destined to ensure grid stability which require dynamic systems to be able to react and supply power in the range of milli seconds to minutes. Long-term storage options, e.g. pumped-storage power plants, in turn, can supply additional energy in times of peak demand, whereas electro-chemical storages are projected to be an important part in the mobility sector. Yet, their low capacity and response time render a significant role for power supply outside the mobility sector unlikely. Chemical storage technologies possess a tremendous potential for applications in the energy sector. Particularly, when high shares of renewables are installed, chemical gas storage is projected to be the only viable option. Synthetic natural gas (SNG) or hydrogen can be generated from surplus energy and be stored in caverns and aquifers. Hydrogen is advantageous in terms of storage efficiency because less process steps are involved compared to the SNG production but suffers from a low volumetric energy density. Synthetic natural gas can be produced by the so-called power-to-gas (PtG) process, is more facile to store, exhibits a higher volumetric energy density and does not require a new energy infrastructure.

At the center of the PtG-process, as schematically depicted in Figure 1-2, are a water electrolysis as well as a methanation unit. In times of surplus energy supply, the power

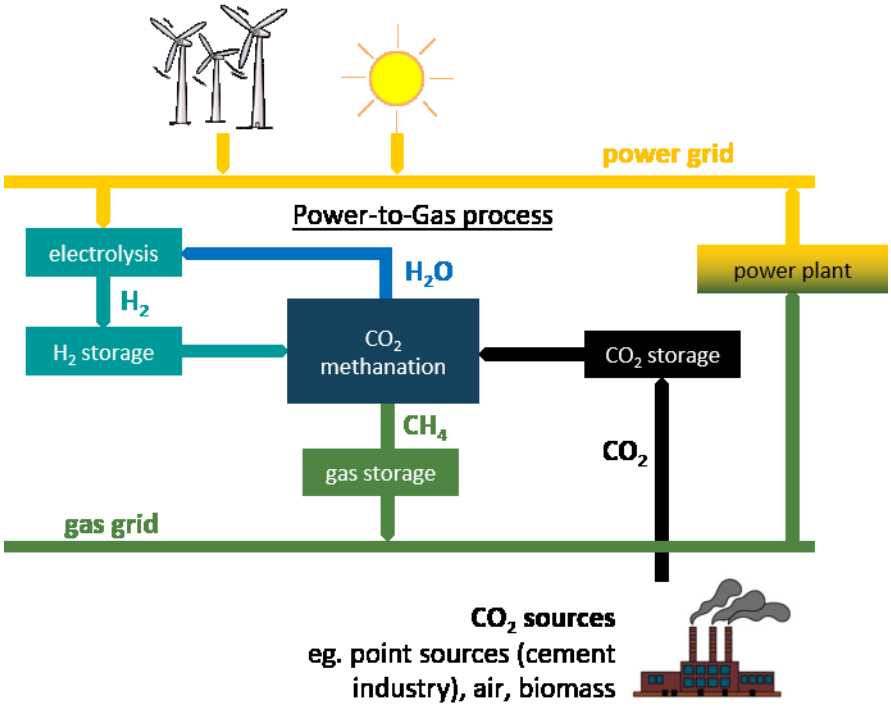

Figure 1-2 **Schematic illustration of the Power-to-Gas process as part of a renewable energy system.**

generated by wind turbines or photovoltaics is used to split water to produce "green" hydrogen (H_2) which in a second step reacts with carbon dioxide (CO_2), harvested at point sources such as cement plants, to form methane (CH_4) and water (H_2O). The product gas can be injected into the existing gas grid for storage and distribution and be used in gas power plants to generate additional power in times of supply shortage.

Although thermodynamically feasible, the reduction of CO_2 to CH_4 is challenging to achieve and requires high temperatures and the presence of a catalyst to yield adequate results. This is the starting point of present thesis.

1.2 About Support Effects in CO_2 Methanation - Objectives of this Thesis

Catalysts for heterogenous gas phase reactions usually comprise nanoparticles ("active phase") deposited on oxidic support materials. The CO_2 methanation constitutes no exception to that rule.[5, 6] When looking at the support, two factors – its surface chemistry and its structural properties - must be considered because they can severely affect the catalytic performance (Figure 1-3).

While the influence of the active component, i.e. nickel or ruthenium, on CO_2 methanation has been studied extensively, the role of the support and its surface chemistry have long been overlooked. Following the traditional view that the CO_x hydrogenation is a (transition)

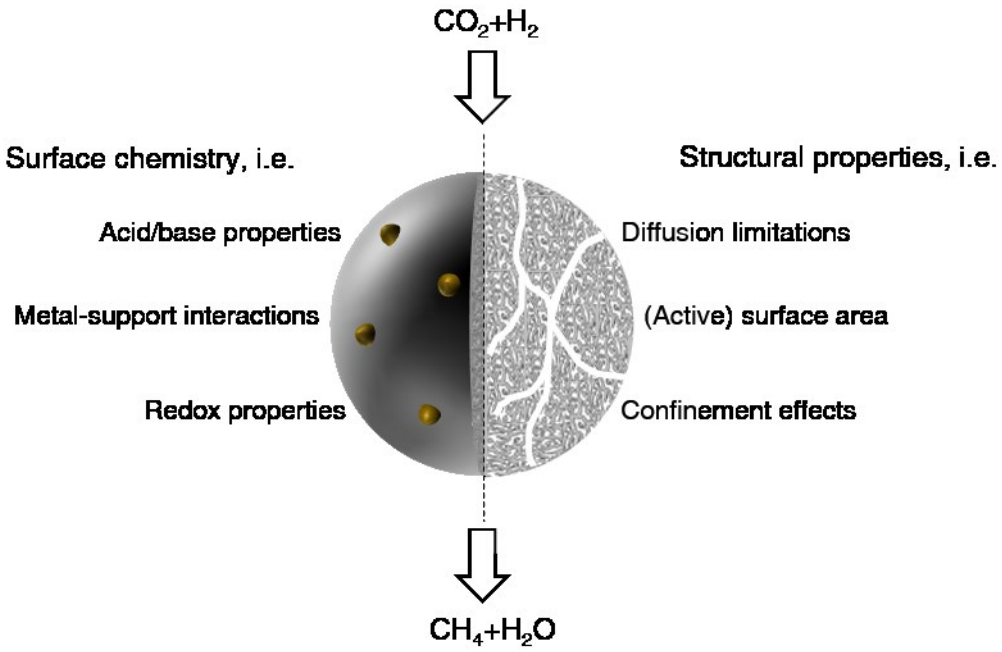

Figure 1-3 **Schematic depiction of support effects on the catalytic performance of a supported catalyst in the CO_2 methanation. The golden hemispheres represent the active component, e.g. metallic nanoparticles.**

metal catalyzed reaction, the support is supposed to provide a large surface area to host small metal nanoparticles, on which the reaction takes place. However, in many cases it is the metal-support interface that was found to be the actual reaction locus during CO_x hydrogenation, and often observed to be the more active site than the (transition) metal alone.[7, 8] Consequently, the common notion that the CO_x hydrogenation is a (transition) metal catalyzed reaction should be reconsidered. By acknowledging this, new possibilities to design more efficient catalysts emerge which consider the support and its material properties as an integral part of the catalyst. By providing additional adsorption sites for the reactants or changing the electronic structure of the metal deposits, the support can directly and indirectly engage in the catalytic cycle and give rise to new/additional reaction pathways leading to higher overall turn overs. With regard to the CO_2 methanation, particularly the acid/base properties are of interest in the adsorption and activation of carbon dioxide. Yet, a fundamental understanding how these affect the reaction mechanism and its efficiency is still limited and require model catalysts for a systematic investigation. To this end, colloidal and sol-gel methods are employed in this thesis as these methods in combination offer full control over the physico-chemical properties of the active component and the support (building block approach). Specifically, the objectives of this thesis are as follows:

1. By using well-defined model catalysts, structure-activity correlations of the support's surface chemistry, i.e. the acid/base properties, can be developed that ultimately

allow to formulate design criteria regarding the support's surface chemistry to partially rationalize future catalyst development.

2. The validity and applicability of these design criteria need to be confirmed. Hence, a novel catalyst system, based on the derived guidelines, is to be developed which is competitive in comparison to industrial and literature standards.
3. Apart from the mere reactivity, the time-on-stream behavior or catalyst stability is affected by the support but is essential for industrial applications. Hence, the deactivation behavior of the most reactive system is to be investigated.

Although this thesis mainly deals with the influence of the support's surface chemistry, the influence of the structural properties is addressed in an extended outlook. It is generally agreed upon that an optimal catalytic efficiency in dependence of the structural properties of the catalyst exists. In order to achieve that, two antagonistic effects on the mesoscale have to be carefully balanced with the pore size being the key parameter. For a given catalyst volume, the smaller the pores, the higher is the active surface area. Additionally, confinement effects might increase the catalytic efficiency, but they are more pronounced in more constricted environments, i.e. smaller pores.[9] If, however, the pore size is too small, diffusion limitations severely restrict the catalytic activity. Similarly to the influence of the surface chemistry, studying these effects systematically requires model catalysts. However, this time the porosity of the support has to be adjusted introducing an additional variable which needs to be controlled. Hence, an effort is made to develop a method that allows to precisely adjust the pore size in xerogels, thereby providing a solid basis for future studies.

1.3 About this Thesis

This thesis is composed of eight chapters of which chapters 3 to 7 provide new insights into different aspects of catalyst synthesis and CO_2 methanation. Specifically,

Chapter 1 puts the present work into an overall context and generally introduces different facets of catalytic support effects to ultimately derive and formulate the objectives of this thesis.

Chapter 2 thoroughly reviews the current state of research on the CO_2 methanation from a catalyst standpoint. Apart from a thermodynamic analysis, this chapter summarizes the applied catalysts and reviews the reported reaction mechanisms as well as occurring deactivation phenomena.

Chapter 3 introduces sol-gel techniques, i.e. the epoxide-addition method, and their potential for the preparation of catalysts. Further, two newly developed expansions to the

epoxide-addition method are introduced that allow the synthesis of lanthanide aero-/xerogels.

Chapter 4 establishes structure-activity correlations by combining extensive characterizations with catalytic experiments and *operando* diffuse reflectance infrared Fourier transform spectroscopy (DRIFTS). A building-block approach is used to isolate support effects from particle size effects of the active component.

Chapter 5 applies and expands the findings from the preceding chapter to design a Ni-Sm_2O_3 xerogel catalyst which is competitive in comparison to literature-known systems as well as an industrial standard. The catalysts are characterized by means of N_2 physisorption, powder X-ray diffraction, transmission electron microscopy and H_2 temperature-programmed reduction. The applicability of xerogel catalysts is demonstrated by a comparison with a catalyst prepared by impregnation.

Chapter 6 presents a detailed study on the time-on-stream behavior of the most promising Ni-Sm_2O_3 catalyst. To this end, stability experiments under different reaction conditions are conducted. Characterization of the spent catalyst and DRIFTS experiments allow to formulate the governing deactivation phenomenon.

Chapter 7 provides an extensive outlook on how the structural properties of the support can affect the catalytic CO_2 hydrogenation and why advanced model catalysts are required for an in-depth study. The synthesis method, developed in Chapter 3, is expanded by the application of structure-directing agents to precisely control the pore size in the xerogels, which can serve as a starting point for future investigations.

Chapter 8 combines and summarizes the findings from the preceding chapters to provide an overall conclusion.

2

CO_2 METHANATION - CURRENT STATE OF RESEARCH

In this chapter the current state of research on the CO_2 methanation is reviewed to put the present work into context. This thesis specifically deals with the kinetics of the CO_2 methanation, however, understanding the thermodynamic constraints is prudent in order to evaluate the kinetic data. After laying the thermodynamic groundwork (chapter 2.1), this chapter addresses the current state of research on the applied catalysts (chapter 2.2). Besides the active component and support materials, promoters and dopants, commonly applied to further enhance the activity and stability of the catalyst, as well as different synthesis methods are discussed. Chapter 2.3 then reviews and classifies the reported reaction mechanisms, while the phenomena leading to catalyst deactivation are introduced in chapter 2.4.

2.1 Thermodynamics of CO_2 Methanation

CO_2 methanation is a highly exothermic and exergonic reaction in which carbon dioxide and hydrogen react to form methane and water (eq. **(2-1)**). The reaction is accompanied by a severe volume contraction of up to 40%, depending on the conversion.

$$CO_2 + 4\ H_2 \leftrightarrow CH_4 + 2\ H_2O \qquad \textbf{(2-1)}$$
$$\Delta_R H_{298K} = -165\ \text{kJ mol}^{-1}$$

$$\Delta_R G_{298K}^{\circ} = -113 \text{ kJ mol}^{-1}$$

Thermodynamically, low reaction temperatures but high pressures are favorable reaction conditions as, following Le Chatelier's principle, the reaction equilibrium is shifted to the product side. Apart from the CO_2 methanation, several other competing side reactions can occur which are listed in Table 2-1.[5, 10, 11] Of the listed reactions, the reverse water-gas-shift reaction (No. 4) is the most commonly encountered side reaction and leads to a lower methane selectivity due to the formation of CO. However, a high methane selectivity must be achieved in order to directly inject the product gas into the natural gas grid.[12] Elemental C, which potentially deactivates the catalyst, can be formed via the Boudouard reaction (No. 5), CO_x reduction reactions (No. 6 and 7) or methane pyrolysis (No. 8). Under typical methanation conditions, the formation of higher hydrocarbons (No. 9 and 10) is generally observed only in small concentrations.

A thermodynamic analysis of the reaction was carried out using the Python program developed and published by Kiewidt.[13] The code uses the Gibbs free energy minimization method and the Peng-Robinson equation of state to determine the thermodynamically achievable CO_2 conversion, CH_4 selectivity, as well as the degree of carbon formation in dependence of the reaction conditions. For the calculations, only hydrogen and carbon dioxide, although in different ratios, were considered to be present in the feed. The results are shown in Figure 2-1. At atmospheric pressure and stoichiometric H_2/CO_2 ratio (4/1),

Table 2-1 Summary of the most relevant reaction, references: [5, 10, 11]

No.	Name	Reaction	Standard heat of reaction / kJ mol^{-1}
1	carbon dioxide methanation	$CO_2 + 4\,H_2 \leftrightarrow CH_4 + 2\,H_2O$	−165
2	carbon monoxide methanation	$CO + 3\,H_2 \leftrightarrow CH_4 + H_2O$	−206
3	reverse dry reforming	$2\,CO + 2\,H_2 \leftrightarrow CH_4 + CO_2$	−247
4	reverse water-gas-shift	$CO_2 + H_2 \leftrightarrow CO + H_2O$	41
5	Boudouard reaction	$2\,CO \leftrightarrow C + CO_2$	−172
6	CO reduction	$CO + H_2 \leftrightarrow C + H_2O$	−131
7	CO_2 reduction	$CO_2 \leftrightarrow C + 2\,H_2O$	−90
8	Methane pyrolysis	$CH_4 \leftrightarrow C + 2H_2$	75
9	Formation of alkanes	$n\,CO + (2n+1)\,H_2 \leftrightarrow C_nH_{2n+2} + n\,H_2O$	
10	Formation of alkenes	$n\,CO + 2n\,H_2 \leftrightarrow C_nH_{2n} + n\,H_2O$	

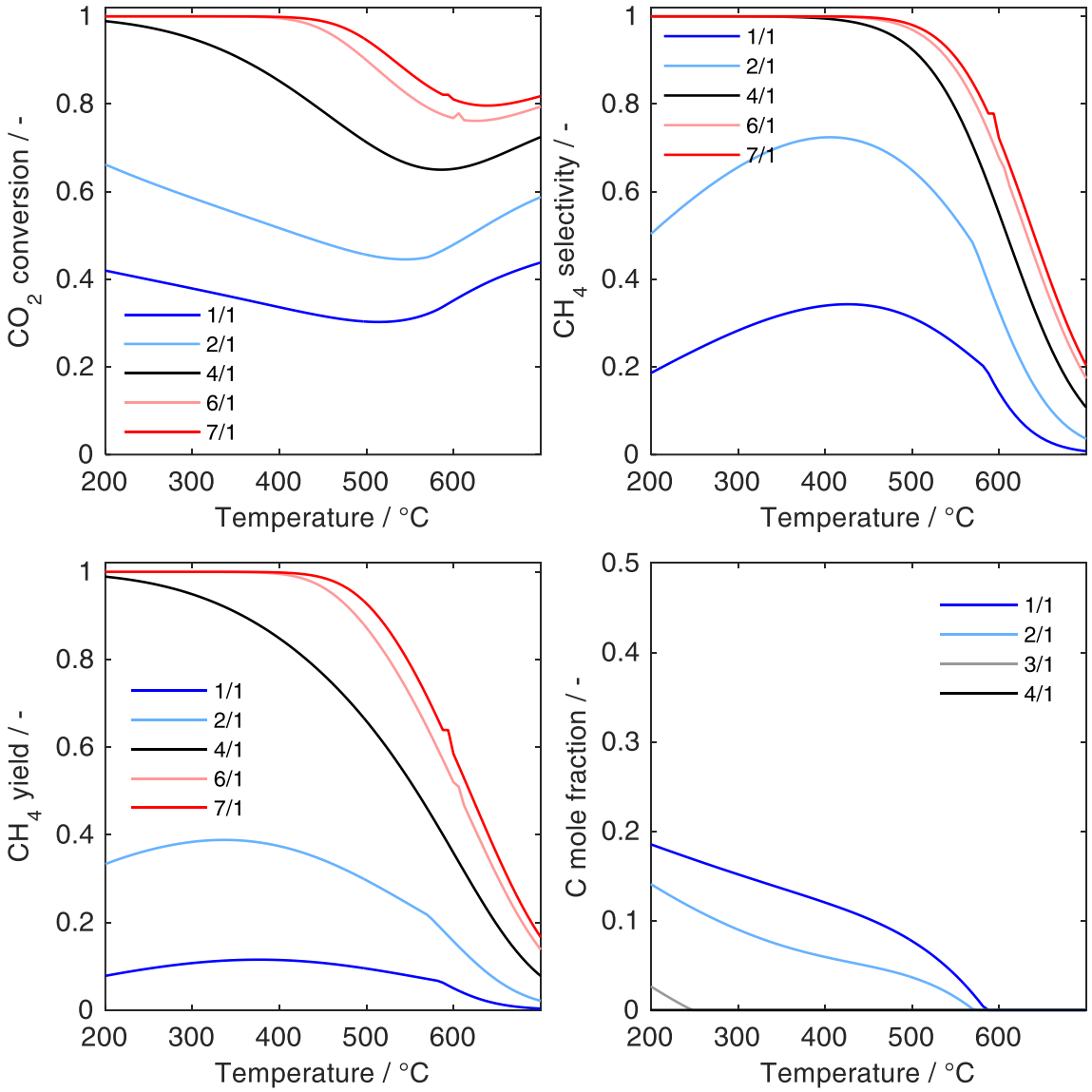

Figure 2-1 **Effect of different H_2/CO_2 ratios and temperatures on the thermodynamic equilibrium, namely CO_2 conversion, CH_4 selectivity, CH_4 yield and elemental carbon fraction at atmospheric pressure.**

complete CO_2 conversion can only be achieved at reaction temperatures as low as 200 °C; with increasing temperature, the equilibrium conversion drops to about 0.85 at 400 °C and to about 0.65 at 600 °C (Figure 2-1a, black curve), before it increases again due to the enhanced formation of CO via the reverse water gas shift reaction. Stoichiometrically, a H_2/CO_2 ratio of 4 is required for the CO_2 methanation. By increasing the ratio to 6, the equilibrium conversion remains at 1 and does not decrease until 400 °C. Additionally, the methane selectivity is higher, as the reverse water-gas shift reaction is suppressed. An under-stochiometric feed, in turn, severely affects the conversion, selectivity and potentially the catalyst stability due to the accumulation of solid carbon on the surface of the catalyst, which is thermodynamically favored at H_2/CO_2 ratios below 3. Although not expected to occur at steady-state reaction conditions, under-stochiometric feed ratios can be encountered

under dynamic reaction conditions and inside the (meso)pores of the catalyst due to the different diffusion coefficients of hydrogen and carbon dioxide. However, the presence of water vapor as a by-product during the methanation can help to prevent accumulation of carbon depositions.[10]

From the thermodynamic restrictions follows, that low reaction temperatures and a stochiometric feed should be targeted as operating conditions. Although the reaction is thermodynamically feasible under these conditions, the eight electron reduction comes with high kinetic barriers that make the use of catalysts inevitable to achieve reaction rates high enough for practical applications. A short review on the applied systems with respect to the most common active components, support materials and preparation methods is the subject of the following subchapter.

2.2 Catalysts for CO_2 Methanation

In an ideal world, a catalyst would exhibit a high activity and methane selectivity at low temperatures and further display long-term stability, which requires the catalyst to be resistant against coking, sintering, attrition and poisoning. To meet these requirements, supported metal catalysts are usually applied, although some studies also investigate unsupported catalysts, such as pure nickel nanoparticles or Raney-nickel catalysts.[7, 14] Most studies focus on Ni as active component (Chapter 2.2.1), which is supported on γ-Al_2O_3 (Chapter 2.2.2). Dopants and promoters are often used to further enhance the catalytic performance and durability of the catalyst (Chapter 2.2.3). Both aspects are also influenced by the preparation method, of which the most relevant ones are described in 2.2.4. Comprehensive reviews dealing specifically with the current state of research from a catalyst point of view have been published by Lv et al.[15], Aziz et al.[16], Gao et al.[6] and Frontera et al.[17].

2.2.1 Active Components

To catalyze the reaction efficiently, elements of the VIIIB group have been found to be the most promising options. Vannice[18] investigated the specific activity of the VIIIB group elements and found the following activity order: Ru >> Fe > Ni > Co > Rh > Pd > Pt > Ir, which is also reflected in parts in the volcano plot suggested by Bligaard et al.[19]. For the derivation of the volcano plot, they calculated the reaction energy for dissociative CO adsorption at 277 °C and set the results in relation to the measured CO methanation activity. Although derived for CO methanation, and specifically for the dissociative CO chemisorption, the plot accurately describes the activity order in CO_2 methanation as well due to the assumed mechanistic similarities of both methanation reactions on metals (see Chapter 2.3). As shown in the volcano plot, cobalt and iron are among the most active metals for the

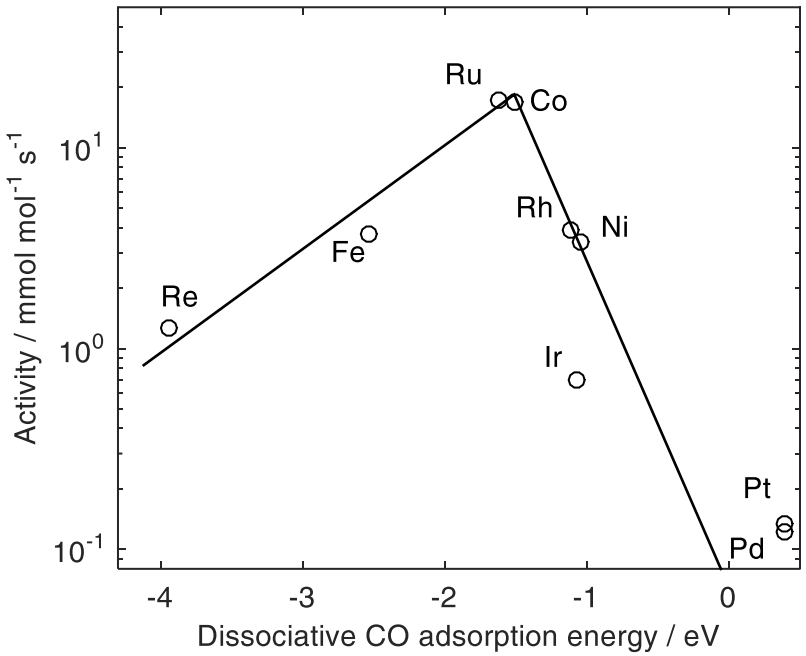

Figure 2-2 CO methanation activity depicted against the dissociative CO adsorption energy at 277 °C for various transition and noble metals. Solid line derived from the Brønsted-Evans-Polanyi relation. Adapted from Bligaard et al.[19] with permission from Elsevier.

methanation. However, while Fe suffers from a poor methane selectivity, Co was long viewed as a Fischer-Tropsch catalyst and tends to form higher hydrocarbons as by-products under methanation conditions.[20, 21] Additionally, Co comes at a significantly higher price than Ni and does not provide substantial advantages in terms of activity, selectivity or the handling of the catalysts. Therefore, most research, as does this thesis, has focused on Ru as the most active, though also most expensive, metal and Ni which offers a high activity and selectivity at a reasonable price.[5, 6, 11] Due to their relevance in this work, the main findings regarding both Ni and Ru as active component are described in more detail below.

Nickel (Ni)

Ni is the most commonly studied material due to its high activity, good methane selectivity and low price in comparison to Co or noble metals.[5, 6, 11, 22] However, its toxicity requires a cautious handling. Furthermore, it tends to form volatile carbonyls ($Ni(CO)_4$) that lead to a loss of active surface area, and eventually, catalyst deactivation.[23] Usually Ni is supported on high surface area supports, but in some cases unsupported nanoparticles and Raney-nickel catalysts were also employed.[7, 14]

It has been shown that the CO_2 methanation is a structure-sensitive reaction on a Ni-SiO_2 catalyst for Ni nanoparticles in the range of 1-7 nm. In terms of the reactivity, Ni particles smaller than 5 nm proved to be significantly more active than larger particles.[24] Also the selectivity is affected by the Ni particle size. Small Ni clusters, even down to single

atoms, have been reported to produce mainly CO, whereas larger particles favored CH_4 formation.[25, 26] Obviously, the Ni particle size is a key parameter for the CO_2 methanation, therefore tuning the particle size was subject to extensive research. Among other factors, such as promoters, impurities, etc., the particle size is severely dependent on the Ni loading and calcination temperature during catalyst synthesis and is, usually, reported to increase with increasing loadings and calcination temperatures.[16, 27–29] Abelló et al.[30] provide an interesting outlier to that rule of thumb. They developed a highly active $Ni(Al)O_x$ catalyst by co-precipitation, which exhibit small Ni crystallites, despite very high Ni loadings of up to 70 wt.%. That system later became the corner stone of the work of the Hinrichsen group (TU Munich) on CO_2 methanation. [31–35] However, these parameters – Ni loading and calcination temperature - also affect the phase composition of the catalyst, which again is crucial for its performance. For supported Ni catalysts, high calcination temperatures tend to form strong NiO-support interactions, ultimately leading to mixed oxides such as $NiAl_2O_4$, whereas low calcination temperatures mostly yield two separated oxides, eg. NiO and Al_2O_3.[36] A similar effect can be observed when varying the loading. An extensive study on the Ni loading was carried out by Zhang et al.[37]. While small loadings formed species with strong metal-support interactions, higher loadings led to Ni containing species with only weak interactions with an Al_2O_3 support. Despite this, the overall degree of Ni reduction decreased with higher loadings. Catalytically, they found that moderate Ni loadings (20 wt.%) are beneficial for CO_2 methanation. Lower loadings led to stronger contributions of the unwanted RWGS, whereas increasing loadings in turn resulted in a higher degree of agglomeration of Ni particles and local destruction of the support. Oftentimes, the phase composition is fairly inhomogeneous in the sample and various Ni species with different metal-support interaction exist.[38, 39] For instance, Hu et al.[38] found three different Ni species after preparing a 10 wt.% Ni-Al_2O_3 catalyst by impregnation. After reduction, each Ni species showed a distinctly different behavior during the catalytic experiments. During the reaction, although difficult to reduce, the species with strong interaction, e.g. stemming from the reduction of $NiAl_2O_4$, possess a higher sinter stability after reduction in comparison to catalysts composed of two separated oxides NiO-Al_2O_3. Instead, the opposite is often reported regarding the activity; separated, easily reducible NiO species produce CH_4 at a higher rate.[27, 38–40]

Ruthenium (Ru)

Ru is often reported to be the most active metal that is also very selective towards methane. However, its low abundance and high price limits its industrial application to catalysts with low Ru loadings. Ruthenium catalysts can be operated over a wide range of reaction conditions without suffering from deactivation phenomena typically observed on Ni catalysts. An activity loss is typically ascribed due to coking or surface restructuring.[6, 16]

Similar to Ni, the CO_x methanation has been shown to be structure-sensitive over Ru catalysts.[41, 42] Ru particles smaller than 1 nm tend to produce more CO, while mainly CH_4 is formed on larger particles.[41] Particularly undercoordinated Ru sites, which are abundant on small Ru particles, were reported to provide highly active sites for CO_2 methanation.[6] Navarro-Jaén et al.[43] investigated the size effect of Ru particles for significantly larger Ru particles. They prepared size-tailored Ru nanoparticles with particle diameters between 16 and 27 nm which were supported on Al_2O_3 and found an increase in activity with increasing particle size which they attributed to an enhanced H_2 availability. Generally, analogous to Ni, the Ru particle size is affected by the Ru loading.[41, 44] For instance, decreasing the Ru loading to 0.1 wt.% on a Al_2O_3 support resulted in a partially atomic dispersion, while increasing the loading led to Ru clusters up to 5 nm for loadings as high as 5 wt.%. Eckle et al.[44] reported a Ru particle size of 0.9 nm when loading 2.2 wt.% Ru on a zeolite and 1.9 nm when the loading was increased to 5.6 wt.% Ru.

Besides from being conventionally supported, Ru-doped catalysts have also attracted attention.[45-47] In contrast to the supported catalysts, Ru is here incorporated into the support matrix to form a solid solution, which has been reported to lower the onset temperature of the reaction in comparison to undoped and supported catalysts. Sharma et al.[46] compared the influence of Ni, Co, Pd and Ru dopants on a ceria catalyst for the CO_2 methanation. They concluded that $Ce_{0.95}Ru_{0.05}O_2$ yields the best performance which they attributed to the significantly enhanced reduction of the $Ce_{0.95}Ru_{0.05}O_2$ catalyst, i.e. the formation of oxygen vacancies. In a follow up work Upham et al.[45] investigated the influence of the degree of surface reduction on the same $Ce_{0.95}Ru_{0.05}O_2$ system. An excess of oxygen vacancies affected the performance negatively, while the absence of any oxygen vacancies also resulted in a poor performance.

2.2.2 Support Materials

Usually, the active component is stabilized as nanoparticles on oxidic support materials. The relevance of the support was clearly evidenced by the work of Riani et al.[7], who found a poor activity for unsupported Ni nanoparticles (8 nm in diameter) in comparison to a highly loaded 125 wt.% Ni-Al_2O_3 (wt. Ni/wt. Al_2O_3) catalyst. In fact, it is widely accepted that the metal-support interface provides the most active reaction locus usually due to enhanced CO_2 adsorption on basic oxidic surfaces. Additionally, surface defects at these interfaces allows to alter the surface morphology as well as electronic structure of the catalyst, that play a decisive role for the adsorption and activation of the involved species.[16, 48, 49]

Among the studied support materials are typically high surface area supports such as Al_2O_3, SiO_2, TiO_2 and ZrO_2, although recently rare earth metal oxides (REOs) emerged as novel, competitive support alternatives due to their basicity and redox properties. Further

support materials such as carbon nanotubes,[50, 51] silicon carbide,[52–54] and composite oxides such as hexaaluminates, and perovskites[55, 56] have been investigated but are not elaborated on at this point.

Alumina (Al_2O_3)

Alumina is the most common support material for CO_x hydrogenation and used in various crystallographic configurations, such as γ, δ, θ and α, of which γ-Al_2O_3 is widely investigated due to its high surface area (typically, in the range of 100-200 m^2/g) and porosity.[6, 57, 58] Further, γ-Al_2O_3 is amphoteric, providing both acid as well as basic surface sites. Upon calcination at temperatures above 1000 °C, α-Al_2O_3 is formed, which serves as a non-porous, low surface area support which is considered to be inert.[58] As one of the drawbacks, γ-Al_2O_3 suffers from deactivation due to coking as well as sintering, especially under hydrothermal conditions. Additionally, control over the phase composition is difficult to achieve and the catalytically inactive and hardly reducible spinel phase $NiAl_2O_4$ easily forms during calcination at higher temperatures when small Ni particles are present.[59–61]

Hu et al.[62] systematically investigated the influence of various γ-Al_2O_3 supports, NiO loadings, calcination temperatures and MgO promotion for the CO methanation. They concluded that the best catalyst has a moderate Ni loading of 20 wt.%, is calcined at relatively low temperatures of around 400 °C and supported on the γ-Al_2O_3 with the highest specific surface area and the smallest mesopores. This promotes the formation of the smallest NiO particles which are, further, significantly easier to reduce. In another study, Gao et al. calcined γ-Al_2O_3 at 600, 800, 1000 and 1200 °C to adjust the structure and surface properties of the alumina support before impregnating the calcined supports with an aqueous Ni-nitrate solution to achieve a NiO loading of 10 wt.%. They found that with an increasing support calcination temperature, the Ni particle size increased due to the decreasing support surface area and acidity caused by the phase transformation from γ to α-Al_2O_3. The interaction of the NiO particles with the support becomes weaker with increasing support calcination temperature. Catalytically, the low-surface area, inert and non-porous Al_2O_3 supported catalyst exhibited the highest activity as well as stability. While the authors attribute the high stability to the absence of acidic surface sites, which are generally linked to promote coking, they explain the high activity with the easily reducible Ni species.

Silica (SiO_2)

As a catalyst support, silica is usually in its amorphous form providing a precisely tuneable specific surface area, pore volume as well as a pore size.[6] Its interaction with transition metals is relatively weak which allows for an easier reduction of the deposited transition metal in comparison to γ-Al_2O_3 supported catalysts.[21] Due to its acidic surface properties,

SiO_2 is prone to coking, does not allow CO_2 adsorption on the support and, similar to γ-Al_2O_3, lacks a high stability under hydrothermal conditions.[6] The unfavorable surface chemistry is also the reason why SiO_2 is not deemed to be a relevant support for industrial applications; however, it is frequently used as a model catalyst support to understand e.g. particle size effects of the active component.[24, 63–65] In a series of publications, Aziz et al.[66–68] looked at mesostructured silica nanoparticles as a support material for the Ni catalyzed CO_2 methanation. Their support material offered a tremendously high surface area (around 1000 m^2/g) as well as a high defect site density, contributing to a small Ni particle size as well as CO_2 activation on the support, respectively. Catalytically, the mesostructured silica supported Ni catalyst produced CH_4 at a higher rate and with a better selectivity than e.g. a Ni-γ-Al_2O_3 catalyst.

Titanium dioxide (TiO_2)

TiO_2 is a reducible metal oxide which strongly interacts with metals. As a polymorph, stochiometric TiO_2 exists in eleven different modifications, six of them are stable under ambient conditions.[69] Rutile is the thermodynamically most stable configuration followed by anatase and brookite. Anatase has gained the most attention as a catalyst support due to its high specific surface area and its strong interaction with metallic nanoparticles. However, it is rather unstable as the pore structure collapses easily when it is exposed to high temperatures.[69, 70] Upon calcination at 465 °C, anatase transforms into the more stable modification rutile,[70] though, the phase stability was shown to depend on the crystallite size.[71] Rutile is less commonly used as support material, but it is often applied as a model support in surface science studies because of the high stability of the crystal phases. In contrast to anatase, rutile does not show a significantly strong metal-support interaction.[69, 72] Rutile as well as anatase have been applied for the CO_2 methanation. Kim et al.[73] and Lin et al.[74] concluded that rutile is superior to support Ru nanoparticles, as, compared to anatase, rutile can stabilize the highly dispersed nanoparticles, whereas the particles tend to migrate on the anatase surface to form larger less-active clusters.

TiO_2 easily forms oxygen deficient structures either by thermal reduction in an inert atmosphere at temperatures above 400 °C or under reducing conditions starting at around 200 °C.[75–77] The formed oxygen vacancies are shown to be highly reactive for the activation of CO_2. Huygh et al.[78] performed DFT calculations on TiO_2 (001) surfaces and concluded that CO_2 adsorption and dissociation is unfeasible on a stochiometric surface, whereas an oxygen-deficient surface can efficiently activate the C-O bond. Similar results were obtained by, e.g., Varilla et al.[79]. Kattel et al.[8] compared unsupported with TiO_2 supported Pt nanoparticles and pointed out the relevance of oxygen vacancies at the metal-support interface

as a stable adsorption site for CO_2, which is not sufficiently bound to Pt to be converted efficiently.

Panagiotopolou and coworkers devoted much of their research to noble metals supported on TiO_2 for various methanation reactions,[80-84] after they had found the highest activity for a Ru-TiO_2 catalyst in comparison to Al_2O_3, SiO_2 and CeO_2 supported systems, though they do not elaborate on the reasons for the superior activity.[84] In a later work, they showed that the CO_2 methanation on Ru-TiO_2 proceeds through a CO intermediate which is formed through a preceding reverse water-gas shift reaction involving formates as an intermediary species.[82]

Zirconia (ZrO_2)

Zirconia is a thermally stable oxide, which occurs in three different crystallographic modifications – the monoclinic phase which is stable up to 1200 °C, the tetragonal phase which is stable up to 1900 °C and the cubic phase which is stable above 1900 °C. Additionally, a metastable tetragonal phase has been reported.[85] For catalytic purposes, usually the monoclinic and tetragonal phases are of most interest, particularly the former is of interest as it exhibits a 5 to 10-fold higher CO_x adsorption capacity in comparison to the tetragonal phase.[86] In comparison to γ-Al_2O_3 and SiO_2, zirconia provides a rather low surface area, ranging between 40-100 m^2/g (when calcined at 600 °C), depending on the calcination temperature and crystallographic phase.[85] It possesses acidic as well as basic properties of weak strength, and further, easily forms solid solutions upon the addition of a second component.[85] Even though ZrO_2 is an irreducible oxide under conditions typically relevant for catalysis, zirconia still can act as a redox catalyst, similarly to TiO_2.[87] For instance, it has been shown that the surface lattice oxygen is involved in redox cycles during partial oxidation of methane.[87] The oxygen mobility can be further increased by stabilizing cubic ZrO_2 with a second component such as CeO_2 or Y_2O_3 to yield $Ce_{1-x}Zr_xO_2$ and $Y_{2-x}Zr_xO_3$ which introduces additional oxygen vacancies in the mixed oxides.[88]

ZrO_2 has been shown to be a promising support alternative for the CO_x methanation due to its acidic/basic characteristics as well as its interaction with CO/CO_2.[17, 89-91] Similar to TiO_2, CO_2 can be activated efficiently on oxygen vacancies on the ZrO_2 support. These vacancies not only exhibit a beneficial effect on the reactivity, but also increase the stability by suppressing coke formation,[91, 92] possibly by facilitating the reverse Boudouard reaction. For instance, Li et al.[91] compared a Co-Al_2O_3 with a Co-ZrO_2 catalyst and found a significantly increased reactivity for the ZrO_2 supported catalyst, which they attributed to the successful CO_2 activation on the support as well as a significantly enhanced stability during long-term experiments. In comparison, the Al_2O_3 supported catalyst deactivated quickly due to coking and the formation of cobalt aluminate. Similar results were obtained by da Silva

et al.[93] who compared a Ni-ZrO_2 catalyst with a Ni-SiO_2 catalyst, pure Ni, as well as with a physical mixture of Ni and ZrO_2. They found a significantly improved activity for the Ni-ZrO_2 catalyst for the CO_x methanation in comparison to the other systems, which they attributed to adsorption of CO_x on the ZrO_2 support in proximity to the metal particle as well as to an enhanced hydrogen spillover from the metal to the support.

Rare earth metal oxides (REOs)

Generally, the lanthanides and scandium as well as yttrium are commonly grouped as *rare earth elements*, despite not being particularly rare in terms of abundance. The corresponding oxides can be distinguished into light rare earth metal oxides (REOs), such as La_2O_3, Pr_6O_{11} and Sm_2O_3, and heavy REOs like Y_2O_3, Gd_2O_3 and Tb_4O_7. REOs offer intriguing properties due to their acid/base and redox properties. They possess basic surface sites that decrease in number and strength with higher atomic number because of the decreasing ionic radius of the cation (which can, therefore, be viewed as an extension to the "lanthanide contraction").[94] Furthermore, rare earth metal oxides generally exist in the trivalent state as sesquioxides (Re_2O_3), although, Ce, Pr and Tb can also be tetravalent, thus forming dioxides and mixed-valent oxides. For example, ceria can be present either as Ce_2O_3 or CeO_2, whereas praseodymium oxides can commonly be encountered as Pr_2O_3, Pr_6O_{11} and PrO_2, though various other intermediate oxides exist. In turn, Sm_2O_3 and Eu_2O_3 can form SmO and EuO under strongly reducing conditions.[95] Due to the existence of several oxidation states of the rare earth elements, they are often considered as reducible materials. Oxygen mobility is also higher for rare earth elements which can occur in the tetravalent state.[96]

For CO_2 methanation, REOs, in particular ceria, have only recently started to attract attention as suitable catalyst supports and are mostly applied due to their favorable basicity.[97–103] In fact, it was the highly regarded work by Pan and coworkers[104] who introduced the beneficial effect of basic sites for the CO_2 methanation, that brought attention to ceria-based supports. They compared a Ni-Al_2O_3 with a Ni-$Ce_{0.5}Zr_{0.5}O_2$ catalyst and found a significantly superior performance for the latter. They classified the strength of the respective basic sites into three categories based on the CO_2 desorption temperature during CO_2-temperature programmed desorption measurements (CO_2-TPD): (1) weak basic sites, of which CO_2 desorbs at temperatures below 250 °C; (2) medium basic sites of which CO_2 desorbs in a temperature range between 250 °C and 700 °C and (3) strong basic sites which release CO_2 at temperatures above 700 °C only. While the Al_2O_3 supported catalyst possessed both weak and strong basic sites on which CO_2 was bound either too weak or too strong to participate in the reaction, the Ni-$Ce_{0.5}Zr_{0.5}O_2$ exhibited only medium basic properties.[104] Several works later confirmed their results.[32, 35, 105, 106] For instance, Tada et al.[105] investigated 10 wt.% Ni supported on CeO_2, α-Al_2O_3, TiO_2 and MgO for the CO_2 methanation prepared by incipient

wetness impregnation and found the highest activity in CO_2 methanation and CH_4 selectivity for the CeO_2 supported catalyst. While they explained the high activity of the Ni-CeO_2 catalyst with the high CO_2 adsorption capacity as shown by CO_2-TPD measurements and the partial reduction of the CeO_2 surface, they linked the high CH_4 activity with the superior CO methanation activity of the CeO_2 supported catalyst which converts the by-product CO of the CO_2 methanation in a subsequent step to CH_4. To date, ceria or ceria-zirconia composite supports certainly received the most attention, while other REOs have long been overlooked as catalyst supports for the CO_2 methanation, although they offer tremendous potential. For instance, Muroyama et al.[90] prepared several Ni catalysts by impregnating conventional supports such as Al_2O_3 and ZrO_2 as well as several rare earth metal oxides, specifically Sm_2O_3, La_2O_3, Y_2O_3 and CeO_2. They ranked the catalysts based on the CH_4 yield in the following order: Ni-Y_2O_3 > Ni-Sm_2O_3 > Ni-ZrO_2 > Ni-CeO_2 > Ni-Al_2O_3 > Ni-La_2O_3. While they observed a weak dependence on the basic properties, other factors such as the vastly differing Ni particle size on the different supports, ranging between 4 and 210 nm, and the different reduction behaviors of the catalysts must be considered as influential factors. Similarly, Yamasaki et al.[107] found that samarium containing nickel catalysts, either as part of an alloy or as catalyst support, enhance CO_2 methanation activity in comparison to monoclinic zirconia supported catalysts that they attributed to a higher Ni dispersion and surface area.

2.2.3 Promoters

Oftentimes, promoters, generally referring to a third component, are added to the supported catalysts to enhance the activity and/or stability of the catalyst. Usually, promotors are distinguished into structural and electronic promoters.[108] Structural promoters influence the formation and stability of the active phase, while electronic promoters directly affect the reaction mechanism and the associated elementary steps. In reality, oftentimes it is not possible to clearly distinguish if the added component acts as a structural or electronic promotor, or both.

With regards to CO_2 methanation, there is a vast amount of literature on the influence of promoters. Most studies either report on an increased CO_2 adsorption capacity due to a basic additive, a higher dispersion or smaller particle size of the active component or higher number of defect sites. All of which can contribute positively to the reactivity as well as stability. For instance, MgO has been reported to increase the sinter stability (structural promoter) while also increasing the CO_2 adsorption capacity.[109, 110] Similarly, Mn has been shown to increase the Ni dispersion as well as significantly enhances CO_2 adsorption which led to a drastic increase in activity compared to unpromoted Ni catalysts.[32, 33, 106, 111] Lanthanum is another frequently used promoter known to increase Ni dispersion as well as CO_2 and

H_2 uptake.[112–114] Incorporated into a MCM-41 support, it decreases the Ni particle size and enhances NiO-MCM-41 interaction, ultimately preventing both coking and sintering.[115] As an another rare earth metal oxide promoter, CeO_2 facilitates the reduction by altering the interaction between Ni and Al_2O_3.[116] A positive effect on the reducibility is also achieved when using Pt as a promoter, which additionally contributes to a higher reactivity and stability by an enhanced H_2 spillover to remove chemisorbed oxygen/oxide species under catalytic conditions.[117, 118] Zr, in turn, can reduce carbon deposition as well as sintering.[119–122]

Recently alkali additives, such as Li, Na, K and Cs, have attracted much attention.[83, 123, 124] Petala and Panagiotopoulou[83] found that promoting a 0.5 wt.% Ru-TiO_2 catalyst with small amounts of Na (0.2 wt.%) leads to higher turnover frequencies than 5 wt.% Ru catalyst. However, when promoting the 5 wt.% Ru-TiO_2 catalyst, no promotional effect of the alkali additives was observed. As the higher Ru loading also resulted in significantly larger Ru particles, it is likely that the promotional effects of the alkali additive were superimposed by the structure sensitivity of the reaction. Based on DRIFTS-MS experiments, Panagiotopoulou[124] found that the nature of Ru bonded CO species as well as their coverage was dependent on the type of alkali promotion and enabled a different, highly efficient reaction mechanism in comparison to the unpromoted Ru-TiO_2 catalyst. Kowalzyk et al.[123] added K as a promoter to a Ru-C catalyst and found an increased methanation reactivity; in turn, adding Ba to the catalyst inhibited the catalytic turnover, which agrees with findings by Barrientos et al.[125]. They specifically investigated the influence of Zr, Mg, Ba and Ca oxides on the catalyst stability during CO methanation. Only ZrO_2 could increase the reactivity as well as significantly slow down the carbon formation rate, whereas adding CaO had an adverse effect on both the CH_4 as well as coke formation rate.

2.2.4 Catalyst Preparation Methods

The catalytic performance is also impacted by the catalyst preparation method, which affects the dispersion of the active phase as well as reducibility due to differing the metal-support interactions.[16, 126, 127] The most commonly applied techniques are impregnation and (co-)-precipitation, but also sol-gel and core-shell techniques have attracted significant attention and are reviewed below. Less common methods include, but are not limited to, flame-spray pyrolysis,[117, 128] microemulsion,[129] ion exchange,[130] as well as solution combustion[131] techniques.

Impregnation

Impregnation certainly is the most frequently used synthesis technique. A dry powder support is impregnated with an aqueous solution of a dissolved metal salt. Depending on the amount of liquid, the impregnation technique can be subdivided into “incipient wetness

impregnation" and "wet impregnation". When the former approach is applied, the volume of the impregnating liquid corresponds to the pore volume of the support, whereas for the latter approach an excess volume of impregnating liquid is used. The synthesis technique is often perceived as simple, although the underlying principles of impregnation and drying are rather complex. According to Khodakov et al.[21], important synthesis parameters are temperature and time of support drying prior to impregnation, the rate of addition of the impregnating solution and the conditions during drying (temperature, time, atmosphere). If more than one component is to be impregnated, the impregnation order also becomes relevant.[50, 132, 133] For instance, co-impregnating Ni and Mg on a SiO_2 support led to an improved stability and reactivity during CO_2 methanation compared to a sequentially impregnated catalyst.[132] Similarly, Fratalocchi et al.[134] investigated the catalytic consequences of the order of Pt depositions on a Co-Al_2O_3 catalyst. If Pt was deposited first, small Co particles could be more easily reduced, which the authors ascribed to the resulting stronger interaction of Pt and Co, giving rise to a higher reactivity.

(Co-)precipitation

Other commonly investigated approaches are (co-) precipitation techniques. Here, either the active component is precipitated directly onto the support or the support and active component are co-precipitated to form catalysts that have often been reported to exhibit highly defective structures. These surface defects expected to be beneficial for the CO_2 methanation.[30, 32, 33, 135] Despite high loadings, co-precipitated Ni-Al_2O_3 catalysts can provide a higher Ni dispersion as well as more favorable metal-support interaction than catalysts synthesized by impregnation techniques.[30, 136, 137] During co-precipitation, the choice of precipitant (e.g. Na_2CO_3, NH_4OH, NaOH and $(NH_4)_2CO_3$) severely affects the catalyst structure and its catalytic performance.[138, 139] For instance, using NaOH as precipitation agent resulted in significantly larger Ni particles in comparison to catalysts that were precipitated with Na_2CO_3 or $(NH_4)_2CO_3$. The influence was also reflected in the catalytic performance during CO_2 methanation which followed the same trend as the metal particle size.[138]

Sol-Gel techniques

Other frequently investigated catalysts are synthesized by sol-gel techniques. A detailed description of the process can be found in Chapter 3. Sol-gel derived catalysts usually exhibit a very uniform structure due to the homogenous mixing of the precursors of both the active component and the support as well as strong interaction between the active phase and the support because of the partial encapsulation of the active phase.[140, 141] On one hand, the sinter stability can be improved due to partial encapsulation, but on the other hand, this might also lead to a loss of active surface area, if the active component is no longer accessible.[126]

Further advantages of sol-gel techniques include the ability to adjust the physical properties of the catalyst such as the surface area, porosity and particle size.[99, 142–144] However, sol-gel derived catalysts are often more difficult to reduce as the homogenous approach favors the formation of mixed oxides and strong metal-support interactions.[145] Consequently, a lower activity during e.g. Fischer-Tropsch synthesis and CO_2 methanation was observed.[126, 127] Ocampo et al.[140], in turn, compared Ni-CeO_2-ZrO_2 catalysts prepared by sol-gel and impregnation methods and found a higher reactivity and stability for the former. This is due to the partial incorporation of Ni^{2+} cations into the support matrix, which was facilitated by the homogenous sol approach. The solution based approach allowed the investigation of the effect of the ceria-zirconia composition on the structural properties and catalytic reactivity in a follow up work and yielded homogenous solid solutions over a wide range of Ce/Zr ratios, of which a composition of 60/40 was found be optimal.[141] Atzori et al. prepared Ni-CeO_2 catalysts with various Ni/Ce molar ratios by a sol-gel route.[99, 142] They found their systems to be very active in comparison to an impregnated γ-Al_2O_3 supported catalyst and linked the high activity to the nickel-ceria interaction which facilitated NiO reduction as well as preventing agglomeration of Ni particles. However, the authors further speculate that CO_2 activation would occur on the nickel-ceria interface and thus contribute to a higher activity as well.

One of the drawbacks of the previously discussed techniques is the rather random particle size distribution of the active phase due to the poor control over the particle formation process. This, however, can be overcome when using colloidal approaches or approaches that incorporate the colloidal synthesis of the active component, such as core-shell catalysts. While purely colloidal approaches are more suited for scientific purposes, e.g. to determine particle size effects,[43] core-shell catalysts are also interesting from a industrial perspective.

Core-shell

Core-shell or 'egg-yolk' catalysts consist of an active core that is encapsulated by an inert but porous shell. There are a multitude of expected advantages. An increased sinter stability as well as a confinement effect is expected due to the encapsulation of the active core.[146–148] Additionally, the combination of physical and chemical functionalities can be systematically investigated due to the individual control over the particle size of the active component as well as the porosity of the surrounding shell.[148, 149] Based on a simulation study, core-shell particles are predicted to be the optimal particle type for the CO_2 methanation as they reduce the thermal sensitivity of the reactor while ensuring a high methane yield.[150] In fact, the superior reactivity of the core-shell architecture for the CO_x methanation has been experimentally proven by several studies.[63, 92, 151] For instance, Han et al.[151] compared a Ni@SiO_2

with an impregnated catalyst for the methanation of CO. They found a higher activity for the core-shell catalyst, however, as is often the case in such comparative studies, the particle sizes differed significantly, making it impossible to attribute the high activity to the core-shell structure alone. We used a more rigorous approach to investigate the influence of the core-shell architecture in an isolated manner.[63] In this research, instead of encapsulating a colloidal Co core, we synthesized the core and shell separately and, subsequently, deposited the Co nanoparticle on the outside of the SiO_2 shell. Penetration of the shell material could be prevented as the size of the Co core (40 nm) exceeded the pore size of the SiO_2 shell (~ 3 nm). During CO_2 methanation, the core-shell catalysts were about twice as active as the supported Co-SiO_2 catalyst. Even more drastic, the supported catalyst produced hardly any methane but was mostly active for the RWGS reaction, whereas the Co@SiO_2 catalyst produced mainly CH_4. We attributed these observations to the confinement effect and the associated higher chance of re-adsorption and hydrogenation of the CO intermediate.

2.3 Reaction Mechanisms

The reaction mechanism of CO_2 methanation is still a highly debated topic and a consensus difficult to achieve as the mechanism depends on:

- the active component and its particle size (structure-sensitivity),
- the surface chemistry of the support, and
- the reaction conditions, particularly if a stochiometric or over-stochiometric H_2/CO_2 feed ratio is used.[152]

Additionally, differences in the interpretation of the data cannot be neglected. Spectroscopic data (i.e. DRIFTS) alone does not allow one to unambiguously separate spectator and intermediary species, and mathematical models disregard the physical presence of reaction intermediates all together. Even combined efforts sometimes lead to conflicting results as is shown in our work on a Ni-Al_2O_3 catalyst, which combines DRIFTS experiments with extensive spatially-resolved kinetic measurements, and thus, underlines the importance of isotopic labelled, transient experiments.[153]

Alike in all studies, H_2 is shown to adsorb dissociatively on the metallic particle. The main discrepancy in the reported mechanisms addresses the formation of adsorbed CO as a reaction intermediate, and if so, how it is formed and how it is further hydrogenated ("*CO pathways*"). The other mechanism strand considers carbonates on the support as the main intermediate ("*carbonate pathways*"). Figure 2-3 shows a schematic summary of the reaction pathways found in the literature.

For the "*CO pathways*" (as shown in the upper part of the figure), CO bound on the metal is either formed through dissociative CO_2 adsorption on the metal or via a preceding

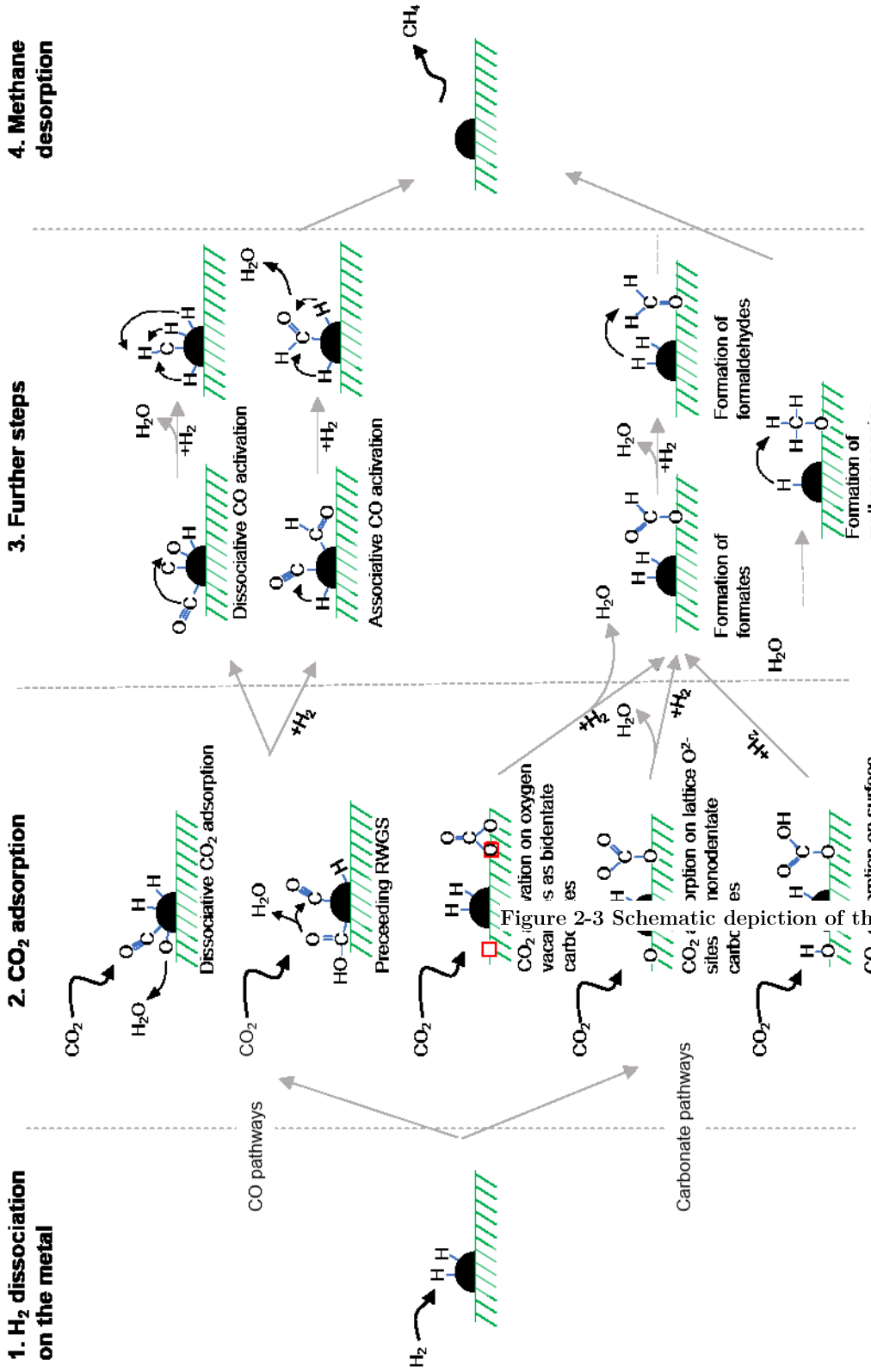

Figure 2-3 Schematic depiction of the reported CO_2 methanation

reverse water gas shift reaction (associative CO_2 adsorption).[44, 81, 154] For the latter, the reaction proceeds via formates which originate from CO_2 adsorption and subsequent hydrogenation at the metal-support interface. The species then undergoes another dehydration step to yield CO. The next step requires the C-O bond to cleave either by an unassisted dissociation to C and O or through a H-assisted mechanism to a formyl (HCO) or carbon hydroxyl specie (COH).[44, 64] Evidence for the associative CO_2 adsorption mechanism has been published by Panagiotopoulou et al.[81] over a Ru-TiO_2 catalyst. Their DRIFTS experiments revealed the formation of formates on the Ru-TiO_2 interface which were subsequently dehydrated to CO at the perimeter. In turn, Eckle et al.[44] performed combined steady-state isotopic transient kinetic analysis (SSTIKA) and DRIFTS measurements and found that CO_2 adsorbs dissociatively on a Ru-Al_2O_3 as well as a Ru-zeolite catalyst. Regarding the further reaction progress, they clearly identified HCO as a reaction intermediate (associative CO activation), however, they could not draw conclusions on the additional hydrogenation steps. In contrast, Chen et al.[64] combined SSITKA and transient chemical analysis with microkinetic modelling over a Co-SiO_2 catalyst and concluded that CO adsorbed on the metal dissociates to elemental C and O (dissociative CO activation). Further, the reaction seems to be rate-controlled by the hydrogenation of a CH_x intermediate, as opposed to most studies which assume the C-O bond cleavage to be rate-determining.

While the "*CO pathway*" can potentially occur on all catalysts, as it can proceed on the metallic particle alone, the "*carbonate pathways*" require an active support to adsorb or directly activate CO_2, therefore, rendering the catalyst bifunctional. Consequently, the mechanism depends on the type of support and its surface chemistry.

On supports with the ability to form oxygen vacancies, such as CeO_2, ZrO_2 and TiO_2, CO_2 hydrogenation can follow a redox pathway, similar to a Mars-van-Krevelen type of mechanism.[155, 156] Wang et al.[155] performed SSITKA-DRIFTS experiments over a Ru-CeO_2 catalyst to propose the following mechanism: H_2 removes a lattice oxygen from the oxidic support to generate a vacant site. Next to the vacancy, CO_2 adsorbs on a lattice O^{2-} ion and donates one oxygen atom to heal the vacant site, forming a bidentate carbonate (b-CO_3^{2-}), which can also be understood as an "active CO species" on the support. H atoms from the metal spills over to hydrogenate b-CO_3^{2-} on the support to form formates ($HCOO^-$), formaldehyds (CH_2O) and methoxy (CH_3O) intermediates to eventually yield methane, while a new vacancy is created at a different location on the support. Similarly, Cardenás-Arenas et al.[156] coupled isotopic labelled experiments with DRIFTS on a Ni-CeO_2 catalyst on the basis of which they suggest a slightly different reaction mechanism. As usual, H_2 reduces NiO particles to metallic Ni, while generating oxygen vacancies on the CeO_2 support. However, H_2 only partially reduces the NiO-CeO_2 interface which serves as the adsorption site for CO_2.

Here, CO_2 dissociates and donates its oxygen atoms to the oxygen-deficient ceria support to restore the oxygen balance. These oxygen atoms can now be transferred throughout the support lattice using the previously generated oxygen vacancies. This restores the active site at the NiO-CeO_2 interface without requiring another H_2 reduction step specifically at the interface. Additionally, their isotopic experiments reveal desorption of H_2O as the slowest step in their proposed mechanism, however, it is not formed on the same active sites required for CO_2 activation.

In contrast to supports exposing oxygen vacancies, supports with basic lattice O^{2-} sites and/or OH groups, such as MgO and Al_2O_3, adsorb CO_2 to form monodentate carbonates (m-CO_3^{2-}) and hydrogen carbonates (HCO_3^-), respectively. [104, 157, 158] In either of the two cases, it is often assumed that the formed carbonates are, subsequently, dehydrated to formates before being hydrogenated as outlined above.[104, 154, 159] For instance, Aldana et al.[154] considered a Ni-$Ce_{0.5}Zr_{0.5}O_2$ to act as both a reducible and basic support. Their extensive DRIFTS-MS experiments revealed that CO_2 adsorbs as monodentate, bidentate and hydrogen carbonates on the metal-support interface, which further react to form formates, formaldehydes and methoxy species before eventually yielding methane. Similar results on a Ni-$Ce_{0.5}Zr_{0.5}O_2$ catalyst, were obtained by Pan et al.[104, 159] who further specified that monodentate carbonates would react to a more active monodentate formate, whereas hydrogen carbonates would lead to rather unreactive bidentate formates. Cardenás-Arenas et al.[156] also performed isotopic labelled and DRIFTS experiments on a Ni-Al_2O_3 catalyst. They propose that hydroxyl groups are formed upon H_2 reduction of the NiO-Al_2O_3 interface. CO_2 adsorbs on the generated hydroxyl groups at Ni-Al_2O_3 perimeter sites to form hydrogen carbonates, part of which further react to formates. These either decompose to CO and H_2O or they are hydrogenated to CH_4 and H_2O.

Usually in most publications, only one reaction mechanism towards methane is reported per catalyst, although in fact, multiple reaction pathways often occur simultaneously.[154, 160] Vesselli et al.[160], for instance, suggested two parallel reaction pathways on an unsupported Ni catalyst, which were dependent on the surface coverage with H atoms and various carbonaecous species. Initially, on a mostly H-covered surface, CO_2 was quickly hydrogenated towards methane via a hydrocarboxyl intermediate. Reactive formates were hydrogenated to methane as well, however, at a significantly slower rate and thus, accumulated on the surface. With increasing time, the fast reaction pathway was suppressed due to the gradual poisoning of the Ni surface with the slower intermediate leading to a lower activity level. This example nicely illustrates not only that multiple reaction pathways can be present at the same, but also how the primary mechanism depends on the "history" of the catalyst, i.e. how the

mechanism can be affected from catalyst deactivation, which will be the topic of the following subchapter.

2.4 Catalyst Deactivation

Catalyst deactivation generally refers to a loss of activity with time-on-stream and can be of reversible or irreversible nature. Deactivation can have mechanical, chemical as well as physical origins, but always occurs concomitantly with the main reaction.[161, 162] Usually, the responsible phenomena are distinguished into six categories: sintering, poisoning, coking, phase transformation, loss of loss of active components (due to attrition and volatilization) and masking. Pertaining to lab-scale CO_2 methanation, the first three phenomena are of most relevance and are described below.

Sintering

For supported catalysts, sintering refers to a loss of active surface area that occurs due to the surface migration and coalescence of the supported metal nanoparticles and is a thermally activated process.[161] Mechanistically, it can proceed by the migration of either metal atoms or entire crystallites or by vapour transport between crystallites and particles.[162] The latter two mechanisms are commonly referred to as Ostwald ripening.[163] Hüttig and Tamman proposed semi-empirical correlations at which sintering due to atom mobility ($T_{\text{Tamman}} = 0.5\ T_{\text{melt}}$, where T_{melt} is the melting temperature) or defect annealing ($T_{\text{Hüttig}} = 0.3\ T_{\text{melt}}$) occurs.[164] According to the melting temperatures of Ni ($T_{\text{melt, Ni}} = 1455$ °C) and Ru ($T_{\text{melt, Ru}} = 2334$ °C) sintering would be expected at temperatures above 436 °C and 700 °C ($T_{\text{Hüttig}}$), respectively, which are well below the commonly investigated temperature regime for the CO_2 methanation. However, in reality, sintering is often observed below these temperatures as sintering is also a function of the interparticle distance, the metal-support interaction, the embedment of metal particles into the support as well as the reaction atmosphere.[23, 163, 165, 166] For instance, higher temperatures and the presence of steam significantly accelerate Ni sintering.[163] Also, particle size effects of the active component have to be considered. Munnik et al.[23] comprehensively showed that larger Ni particles (~ 8 nm) provide a higher long-term sinter stability, whereas smaller Ni particles (~3-4 nm) form $Ni(CO)_4$ more easily, leading to a significant particle growth by Ostwald ripening and local destruction of the support.

Fouling – coking

Coking is a form of fouling and refers to the physical blocking of adsorption sites and pores due to the deposition of elemental carbon. Usually, the type of carbon is subdivided into at least four different forms: adsorbed atomic carbon, metal carbides, amorphous carbon,

and crystalline graphitic carbon. They are formed at different temperatures, in an increasing order, ranging between 150 – 1000 °C and exhibit a decreasing reactivity towards hydrogen which can make their removal difficult.[162, 167] Additionally, carbon filaments and whiskers are commonly encountered over a wide range of reaction conditions.[162, 167]

Under CO_x methanation, coking can occur as a product of the CO disproportionation ("Boudouard reaction"), CO_x reduction as well as CH_4 pyrolysis (see No. 5-8, in Table 2-1). Although it is thermodynamically predicted at understoichiometric H_2/CO_2 ratios, coking has seldomly reported to be an issue during CO_2 methanation, but it is one of the major problems in CO methanation.[167, 168] The carbon formation rate is not only a function of the reaction conditions, but also depends significantly on the applied catalyst, more specifically the type of metal, crystallite size, promoter and catalyst support.[162] Consequently, there are ways to render the catalyst coking resistant. For instance, while C formation is favored on acidic surface sites, it can be suppressed on catalysts with basic surface characteristics.[91] Li et al.[91] found that oxygen vacancies on a Co-ZrO_2 render the catalyst more stable towards coking, possibly by promoting the reverse Boudouard reaction. In turn, adding noble metals to the catalysts can significantly slow down carbon formation, due to the low mobility of carbon atoms on/in noble metals, which retards the nucleation process.[167, 168] Depending on the type of carbon and its associated reactivity towards hydrogen or oxygen, the catalyst can be reactivated by hydrogenating or oxidizing the deposited carbon.[162]

Poisoning

Poisoning refers to the activity loss due to the strong chemisorption of a molecule to an active site, therefore blocking it from additional reactants or affecting the adsorption mode of other species due to an electronic effect.[161, 162] Depending on the strength of interaction, a distinction is made between catalyst poisons and inhibitors.[161] The former refers to the strong, at times irreversible, chemisorption of the poisoning substance, whereas the latter adsorbs only weakly and reversibly on the active sites. Generally, the poisoning substances can be either impurities in the feed as well as educts or products.

In respect of the CO_x methanation, most catalysts react sensitively to feed impurities such as chlorine, ammonia, and sulfur compounds.[5] Particularly, the influence of sulfur compounds has been investigated and concluded to be harmful for catalysts even in concentrations as low as 1 ppb.[5, 161, 162] Wolf et al.[169] investigated the effect of H_2S and SO_2 on a Ni based catalyst and concluded that the catalyst deactivates due to a site-blocking effect and not an electronic effect.

The role of water on the CO_x methanation is still under debate. While it is well-established that H_2O acts as an inhibitor by blocking adsorption sites, it is still unclear if H_2O also oxidizes the catalyst.[67, 170] Mutz el al., indeed, observed the oxidation of Ni during periods of

H_2 dropout, however, they ascribe the oxidation rather to CO_2 or oxygen impurities in the feed stream than H_2O.[171–173]

Though so far not discussed for CO_x methanation, bifunctional catalysts with basic supports can be deactivated by the formation of thermally stable carbonates as observed during the related water-gas shift reaction.[174] In turn, noble metal catalysts such as Ru are easily poisoned by CO, which can be present either as an educt or a by-product.[175]

3

Synthesis Strategies for Catalysts Derived by Sol-Gel Techniques

Although not all catalysts in this thesis are prepared by sol-gel techniques, xerogel catalysts/supports play a pivotal role and therefore need to be introduced. However, at this point it is important to note what this chapter is not about. This chapter does not introduce or review sol-gel techniques per-se, nor does it review catalytic active materials prepared by sol-gel methods in general; instead, the focus is limited to a few fundamentals, explaining why sol-gel derived materials offer tremendous potential for catalytic studies and how the sol-gel process works (Chapter 3.1). The epoxide-addition method developed by Gash et al.[176] is a very popular synthetic route which allows the fabrication of metal oxide xerogels from simple metal salts and is in the center of this thesis (Chapter 3.2), however, the procedure fails when applied to lanthanides. Therefore, we developed two modified synthetic methods by expanding the classical epoxide-addition method, which are introduced in Chapter 3.2.1 and 3.2.2. A short excursus on the preparation and performance of doped and undoped Sm_2O_3 xerogel catalysts for the oxidative coupling of methane is given in Chapter 3.3 to demonstrate the stability and versatility of the developed syntheses to round out this chapter.

Parts of Chapters 3.2.1, 3.2.2 and 3.3 have been published in peer-reviewed journals and are adapted from the publications.

3.1 Fundamentals

Sol-gel chemistry is a versatile process to prepare metal oxides with high specific surface area and porosity and can thus be used for a vast amount of different applications such as drug delivery, coatings, insulating materials and catalysis.[177, 178] To understand its potential for the development of catalytic materials, it is helpful to first introduce the synthesis procedure that consists of three basic steps: (1) formation of a colloidal dispersion (the so-called sol), (2) gelation to form a wet gel, and (3) drying of the wet gel, as schematically illustrated in Figure 3-1.

First, sols are formed through hydrolysis and polycondensation of a homogenous precursor solution (usually alkoxides are used) which leads to the formation of colloidal particles. Controlled conditions are required to ensure the stability of the sol towards agglomeration and precipitation. Here, several factors need to be considered, such as temperature or the polarity

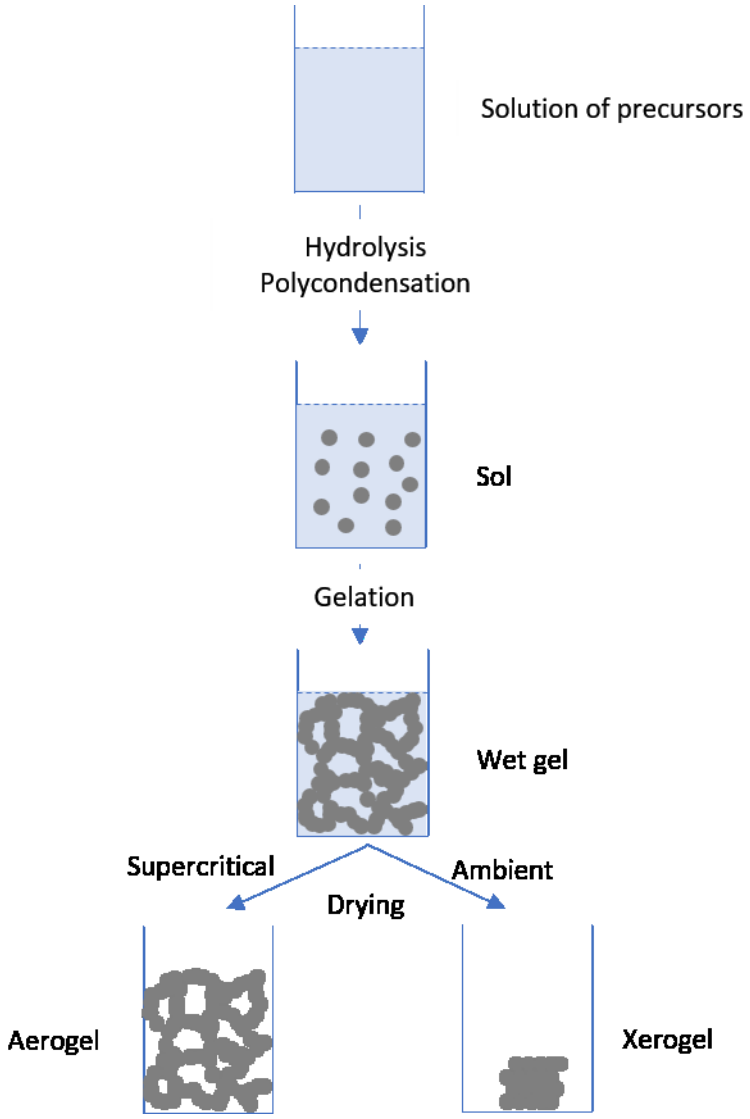

Figure 3-1 Schematic depiction of the sol-gel process. Own depiction, adapted from ref.[178].

of the solvent. To initiate gelation, which transforms the sol into a rigid network, usually the pH of the reaction solution is changed. Such change reduces the electrostatic barrier to agglomeration, thereby promoting the cross-linking of several clusters and ultimately forming a three-dimensional solid network which encloses the solvent. After gelation, the gel is usually left undisturbed for a certain period of time to ensure full gelation of the sol (aging) and/or further functionalization. To remove the solvent from the wet gel, two different methods can be applied – supercritical or ambient drying. During the ambient drying process, the solvent evaporates from the pores, therefore, inducing capillary forces due to the interaction of the fluid with the surrounding pore walls which lead to a collapse of the pore structure accompanied by the shrinkage and destruction of the initially monolithic structure (*xerogel*). If, instead, the solvent is removed under supercritical conditions, no capillary forces are present and the initial structure remains intact (*aerogel*).

At given reaction conditions, the performance of a catalyst is a function of its composition, surface chemistry, structure and texture. In this regard, the advantages of the sol-gel technique for the catalyst synthesis become easily apparent. In contrast to impregnation or precipitation techniques, the control over each step of the synthesis process allows to adjust the physico-chemical properties of the catalyst owing to the number of adjustable process variables, including the type and concentration of precursor, reaction temperature, amount of water, solvent, as well as aging and drying conditions.[179] Single component catalysts can be prepared with high purity and with precise control over the micro structure. For instance, depending on the type of precursor, a fibrous Al_2O_3 structure can be derived from $AlCl_3 \cdot 6\ H_2O$ as precursor, whereas simply using $Al(NO_3)_3 \cdot 9\ H_2O$ instead leads to a "cloud-like" structure.[180] Also, complex multi-component catalysts can be synthesized with a highly homogenous structure as a result of the sol formation and the associated mixing at the molecular scale.[59, 181] The simultaneous and homogenous mixing has also been reported to result in an intimate contact between the active and supporting phase, potentially improving the sinter stability of the catalyst, therefore making sol-gel derived catalysts an interesting option for heterogeneously catalyzed high-temperature reactions.[182] By controlling the drying conditions, the choice of solvent, synthesis temperature, pH of the solution or the addition of templates during the synthesis, the synthesis can be tuned to fabricate denser or lighter materials with varying specific surface area, pore volume and pore size.[183] Apart from powders and monoliths, thin coatings on e.g. monolithic catalyst carriers such as honeycombs or sponges can also be prepared, proving further the versatility and potential of sol-gel techniques for catalytic applications. Yet, the versatility and precise control comes at a price. Disadvantages of the sol-gel approaches are e.g. the large shrinkage during ambient drying,

high costs of the precursors, particularly when alkoxides are used, and long processing times. Further due to the number of involved parameters, a scale-up of the synthesis is difficult.[183]

In the literature a vast amount of different synthesis methods exists, most of them rely on metal alkoxides as precursors, however, their sensitivity towards heat, light, moisture, as well as their high costs and toxicity render their handling difficult. To overcome these drawbacks, Gash and coworkers[176] introduced the "epoxide-addition method" which enables the synthesis of metal oxide aerogels from simple metal salts.

3.2 The Epoxide-Addition Method

In 2001, Gash and coworkers developed a new method commonly referred to as "epoxide-initiated gelation" or "epoxide-addition method" that allows the synthesis of metal oxide materials from simple metal nitrates and halides. Crucial for the technique is the addition of an epoxide (e.g. propylene oxide or trimethylene oxide) that acts as an acid scavenger to drive the hydrolysis and condensation of the hydrated metal ions. A detailed description of the mechanism can be found in the publications by Gash et al.[176, 178, 184] as well as Clapsaddle et al.[185, 186], while a brief summary of their method is given below.

In comparison to metal alkoxides, the sol-gel chemistry of metal nitrates is rather complex as depending on the oxidation state of the metal, the pH value of the reaction media and the concentration of the reactants different species are formed. Before condensation reactions and gel formation can take place, hydrolysis of the metal precursor is required. Under aqueous conditions, three different hydrated metal ions can occur, governed by the oxidation state of the metal, with either aquo (OH_2), hydroxo (OH) or oxo (=O) ligands (eq. (3-1)).

$$[M(OH_2)]^{z+} \leftrightarrow [M(OH)]^{(z-1)+} + H^+ \leftrightarrow [M=O]^{(z-2)+} + 2H^+ \qquad (3\text{-}1)$$

Low-valent cations (z<4) form aquo, hydroxo and aquo-hydroxo complexes, higher valent cations, in turn, yield only oxo as well as oxo-hydroxo complexes. The formation of these species initiates the condensation process that occurs either through olation or oxolation. During the former mechanism hydroxy bridges are formed between two metal centers, whereas during the latter process an oxo bridge is formed. Condensation is usually restricted to the formation of dimers and tetramers, which is not sufficient to yield a solid network or gel. To enable further polymerisation to achieve the transition to a gel, a change of the reaction conditions must occur. This, for instance, can be a change of the pH value of the solution. In the epoxide-addition method, this is achieved by the addition of an epoxide.

As depicted in Figure 3-2, the epoxide acts as a proton scavenger where the epoxide oxygen is first protonated by an acid, before the conjugate base irreversibly opens the epoxide

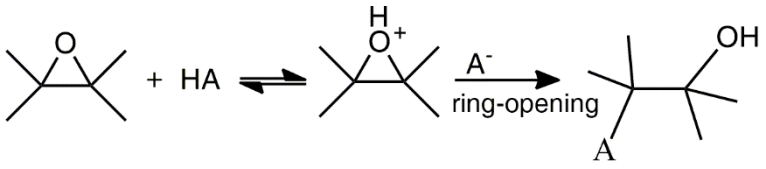

Figure 3-2 Schematic depiction of the protonation and subsequent ring-opening reaction as proposed by Gash et al.[176].

ring by a nucleophilic attack that gradually and uniformly increases the pH value of the reaction solution.[185] Generally, various epoxides are feasible, but gelation times have been reported to be significantly shorter for 1,2-epoxides (e.g. propylene oxide or cyclohexene oxide) than those for 1,3-epoxides due to their higher reactivity and the associated faster rise in the pH value. Apart from the type of epoxide, the anion of the metal salt can also significantly affect the gelation. For instance, the rate at which the epoxide is protonated depends on the relative nucleophilicity of the present species, while the anion can also have a weak-complexing ability (e.g. nitrates as opposed to chlorides).[178]

While this synthesis is applicable to many elements, such as Al, Fe and Cr, it is not suitable to produce pure lanthanide gels from either chlorides or nitrates, but for different reasons. Mechanistically, aqua complexes of the corresponding lanthanide cations (here shown for samarium) are formed by dissolving the chloride or nitrate precursors in ethanol. To enable a slow deprotonation of the cation acid, propylene oxide is used as a proton scavenger (eq. (3-2)). This leads to a shift of the equilibrium of reaction (3-2) to the product side.

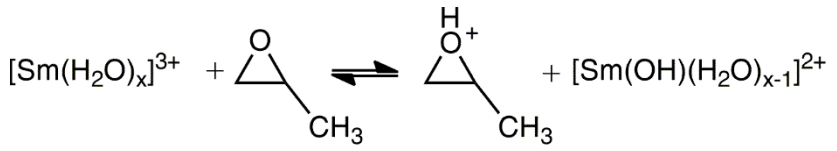

(3-2)

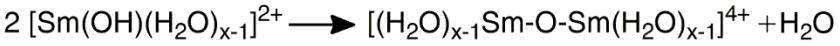

(3-3)

As mentioned before, to initiate gelation the conjugate base needs to perform a nucleophilic attack on the protonated epoxide. However, nitrate anions are poor nucleophiles and in case of rare earth elements, they are unable to induce the ring opening of the epoxide to initiate the polycondensation (eq. (3-3)). Consequently, the pH-value of the remains constant as has been observed by Clapsaddle et al.[186], thus preventing gelation. The chloride anions in solution, in turn, can easily perform a nucleophilic attack on the protonated propylene oxide and, therefore, irreversibly remove one product out of the equilibrium reaction to gradually increase the pH of the solution. But while gelation occurs, Clapsaddle et al.[186] also showed that the use of chloride precursors leads to the formation of chloro-aqua complexes, which upon calcination resulted in considerable amounts of oxychlorides, rather than pure

oxides when applied to rare earth elements. To solve this issue, we developed two methods to produce chlorine-free monolithic REO gels which shall be briefly introduced below.

3.2.1 Expanding the Epoxide-Addition Method I – The Ammonium Carbonate Method

The first proposed solution to prepare pure lanthanide gels from nitrate precursors is only briefly summarized here, as the synthesis is not applied in the course of this thesis. For more details, the interested reader is referred to the corresponding publication (Worsley, Ilsemann, Gesing, Zielasek, Nelson, Ferreira, Carlos, Gash and Bäumer, *Journal of Soi-Gel Science and Technology*, 2019, 89, 1, 176-188).

To realize the sol-gel transition with nitrate precursors, we addressed the pH control of the solution. As stated previously, the pH remains constant when using the nitrates, while gelation, in fact, requires an alkaline and slowly rising pH. However, with the addition of ammonium carbonate and moderate heat, the conditions for gelation were satisfied. Following the synthesis procedure described below, stable gels could be produced for all lanthanide nitrate hydrates, except for cerium. When performing the synthesis at room temperature, no gelation occurred. This is presumed to be due to the need to sufficiently decompose ammonium carbonate to generate the pH increase needed for gel formation. Ammonium carbonate is known to decompose and release ammonia in hot water, thus the moderate heating to 60 °C facilitates this process. Other methods to increase the pH value at room temperature were also experimented, e.g. adding a strong base, e.g. ammonia vapor or ammonium hydroxide, but either led to precipitates or inhomogeneous gels. The prepared gels were dried supercritically and subsequently calcined at 650 °C to yield crystalline aerogels. Additional details on the synthesis as well as extensive structural characterizations by electron microscopy, X-ray photoelectron spectroscopy (XPS), N_2 physisorption, X-ray diffraction (XRD), thermal gravimetric analysis (TGA) and photoluminescence spectroscopy can be found in the aforementioned publication.[187]

Synthesis procedure

Prior to the synthesis, an oversaturated ethanolic ammonium carbonate solution was prepared by mixing 30 mL ethanol (200 proof) with 3 mL deionized water, and 1.5 g $(NH_4)_2CO_3$ under vigorous stirring. This dispersion was then heated to 50 °C and decanted to yield the oversaturated solution.

To prepare the sol-gel solution, lanthanide nitrate hydrate (3 mmol) was dissolved in 3 mL ethanol. Next, 1.6 g of an epoxide (e.g., propylene oxide) and 5.2 mL of the oversaturated ethanolic ammonium carbonate solution were added. The sol-gel solution was sealed in a vial and heated to 60 °C until a gel is formed (minutes to hours). The alcogel was then washed (in acetone or dry alcohol) to remove any by-products (e.g., water). Supercritical

drying (e.g., methanol or liquid carbon dioxide) was used to produce the aerogel. Ambient drying can be used to produce a higher density monolith (xerogel), whereas the crystalline structure can be modified by calcination.

3.2.2 Expanding the Epoxide-Addition Method II – The Citric Acid Method

In comparison, our modified "PO-CA-method" also uses nitrates as precursors but draws from the well-known "Pecchini method"[188], which uses citric acid (CA) as a chelating ligand to enhance the control over the hydrolysis and condensation reaction sequences. The applicability of the synthesis procedure has been successfully demonstrated for almost the entire lanthanide series, specifically La, Ce, Pr, Nd, Sm, Gd, Tb and Y. An image of the formed sols and gels is presented in Figure 3-3. The remaining elements have not been tested. Gelation occurred within a few seconds, while in the absence of citric acid, a white precipitate occurred after several days, revealing the imperative of the co-presence of citric acid and propylene oxide for the gel formation.

The developed synthesis is one of the central parts of this thesis; almost all catalysts in this thesis have been prepared by this procedure or by adaptions from it demonstrating the versatility and robustness of the synthesis procedure. The detailed procedure is descripted below, while extensive characterizations are given over the course of this thesis.

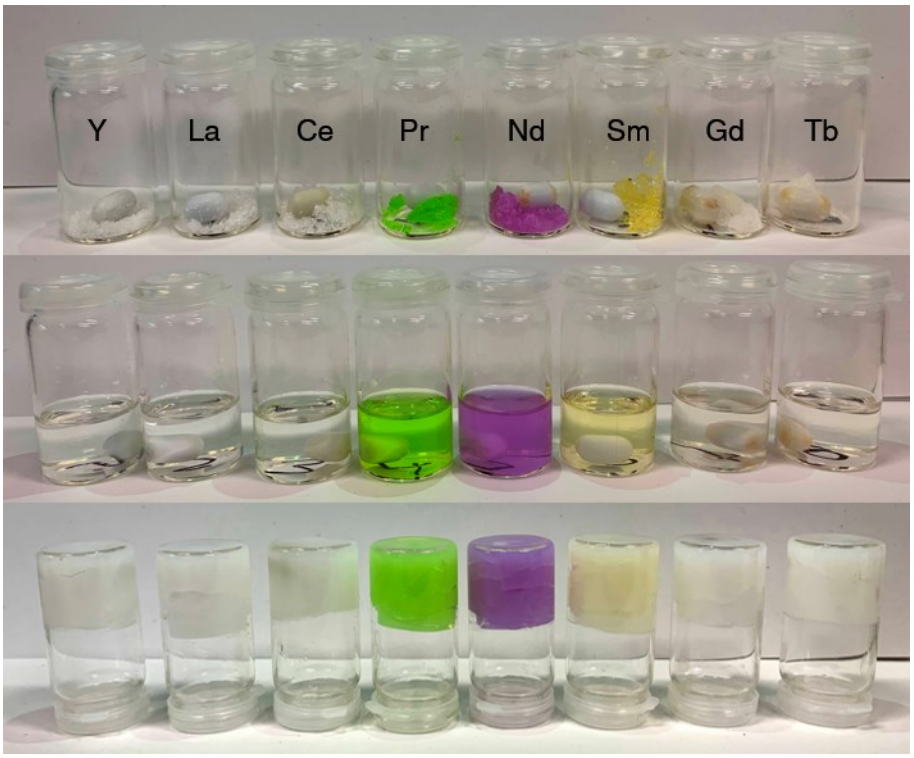

Figure 3-3 **Photos of different stages of the sol-gel process for the tested rare earth elements. (top) image of the nitrates; (middle) image after dissolution prior to PO addition; (bottom) image of the formed, rigid and opaque gels.**

Synthesis procedure

To prepare the sol-gel solution, first lanthanide nitrate hydrate was dissolved in absolute ethanol (1.7 g ethanol/1 mmol metal salt) while stirring in a polyethylene vial. Next, citric acid (CA, Roth, 99.5%, anhydrous) was added (1 mmol CA per 1 mmol metal salt). Once dissolution was complete, propylene oxide (Aldrich, 99.5%) was quickly added to the mixture as the gelation initiator (11 mmol of PO per 1 mmol of metal salt). The resulting solution was stirred, while gelation occurred rapidly within a few seconds. The formed gel was allowed to age undisturbed for at least 24 hours. To remove any residues of the synthesis, a solvent exchange with pure ethanol was conducted three times by decanting the old solvent. Ambient drying for at least five days yielded xerogels, which were subsequently calcined in air at 600 °C (heating ramp 1 °C min^{-1}) for at least 2 hours.

3.3 Excursus – Doped Sm_2O_3 Xerogels for the Oxidative Coupling of Methane

Materials synthesized by the PO-CA method were also used in a cooperative study with the working group of Helena Hagelin-Weaver (University of Florida – Gainesville) for the oxidative coupling of methane (OCM) to produce ethylene from methane.

Ethylene is a valuable industrial feedstock for many plastics, such as polyethylene, which are traditionally produced by steam cracking of ethane or naphtha.[189, 190] Since the 1980s, a lot of research has been devoted to an alternative way of ethylene production – the oxidative coupling of methane. In comparison to the traditional steam cracking, the OCM is operated at lower temperatures (500-750 °C as opposed to temperatures above 800 °C during steam cracking) and able to convert methane, usually from natural gas, to ethylene.[189, 190] If instead of natural gas, synthetic natural gas is used, the OCM can potentially be a complementary technique to the CO_x methanation. However, so far, no industrial relevant process could be established. This is mostly due to the thermodynamic obstacles which favor the combustion products CO and CO_2 over the formation of valuable C_{2+} species.[190, 191] The reaction is typically catalyzed by mixed metal oxides which contain combinations of rare earth metal oxides, alkali or alkaline earth metals.[189] Additional dopants are commonly used to further improve the catalytic performance, such that complex multi-component catalysts are formed. So far, the most promising catalysts to achieve industrially relevant C_{2+} yields have been reported to be Mn-Na-WO_4/SiO_2, $La_{0.6}Sr_{0.4}Co_{0.2}Fe_{0.8}O_{3-x}$, and $Bi_{1.5}Y_{0.3}Sm_{0.2}O_{3-x}$.[192–194] While these complex catalyst mixtures achieve good catalytic performances, they are not suitable for systematic catalyst studies as the influence of single components are difficult to separate, and thus not be fully understood. Consequently, the complexity of the catalyst must be reduced to a single metal oxide catalyst as a host, if dopant effects are to be unravelled. Sm_2O_3 is widely

considered to be one of the most active and selective single metal oxides for the OCM, and therefore, a prime candidate as a host material to study dopant effects in an isolated manner.[195–197] The preparation of such materials by classical impregnation techniques requires solid state diffusion of the dopant ion from the catalyst surface into the bulk of the host oxide, which can result in inhomogeneous samples and surface enrichment. In contrast, our developed sol-gel method allows to synthesize pure and multi component systems from a highly homogenous sol, which increases the likelihood of a successful and uniform distribution of dopants inside the Sm_2O_3 matrix. Therefore, an in-depth analysis of the dopant-oxide interaction is possible.

In two separated studies, we investigated the effect of low-valence (oxidation state ≤ 2, thus lower than the oxidation state of Sm^{3+} in Sm_2O_3) and high-valence (oxidation state >2) dopants on the structural properties and catalytic performance of Sm_2O_3 xerogels at very low concentrations (0.1 and 1.0 mol%) for the OCM. Our main findings are briefly summarized in the following two subchapters. For more information, the reader is referred to the corresponding full papers:

- Chapter 3.3.1 – The Effect of Low-Valence Dopants

  A. Jones, D. Aziz, J. Ilsemann, M. Bäumer, and H. Hagelin-Weaver, „Effects of Low Molar Concentrations of Low-Valence Dopants on Samarium Oxide Xerogels in the Oxidative Coupling of Methane", *accepted at Catalysis Today*, 2020
- Chapter 3.3.2 – The Effect of High-Valence Dopants

  A. Jones, D. Aziz, J. Ilsemann, M. Bäumer, and H. Hagelin-Weaver, „Effects of Low Molar Concentrations of High-Valence Dopants on Samarium Oxide Xerogels in the Oxidative Coupling of Methane", *accepted at Catalysis Today*, 2020.

3.3.1 The Effect of Low-Valence Dopants

In a first study, we doped Sm_2O_3 with 0.1 and 1.0 mol% of low-valence transition (Ag, Ni and Cu) and alkali metals (Li and K). If incorporated successfully, low-valent dopant (LVD), defined as metal ions with an oxidation state below Sm^{3+}, are expected to increase the number of oxygen vacancies and thus the number of basic sites in the Sm_2O_3 host lattice,[198] which is widely accepted to be beneficial for the OCM.[192, 199] Apart from catalytic experiments, all catalysts were characterized by N_2 physisorption, CO_2-TPD and XRD before and after the reaction to gain insight into the oxide-dopant interaction.

The successful synthesis of the doped samples confirms the robustness and versatility of the developed PO-CA synthesis method and demonstrates its broad applicability. XRD measurements of the prepared samples reveal that all dopants could be successfully incorporated interstitially in the Sm_2O_3 lattice. Alkali metal and even transition metal dopants significantly improve the catalytic performance as compared to the undoped Sm_2O_3 catalyst.

For the higher dopant level (1.0 mol%) and at temperatures below 700 °C, the highest C_{2+} yield is obtained over the alkali doped samples, particularly over the K-doped catalyst. At higher temperatures the Ag-doped catalyst performed best in terms of activity and selectivity. At this concentration level, Ni and Cu appear undesirable as dopants due to their low activity and selectivity, and are even inferior to the undoped Sm_2O_3. Doping the catalysts with only 0.1 mol% yields a similar pattern. The Li and K containing samples obtained in the highest CH_4 yield, while the Ag and now also the Ni doped samples exhibit a superior performance compared to the undoped catalyst, too. Even at these low dopant concentrations CO_2-TPD measurements revealed a significant increase of basic sites on all catalysts, contributing to the improved catalytic performance. However, the basicity is not the only decisive factor to consider for an enhanced reactivity as it was evident that Cu doping was not effective. Despite the markedly higher CO_2 uptake for the Cu-doped sample as compared to the undoped sample, the reactivity was inferior, suggesting the influence of a second parameter – the crystallographic phase. For most catalysts, before the reaction, the lattice consists mainly of the more active cubic phase, except for the 1.0 mol% Ni and Cu doped catalysts that exhibit major contributions of the less reactive monoclinic phase. While all catalysts suffered from a loss of basic sites during the time-on-stream experiments, the K-doped samples were able to stabilize the cubic phase successfully during these experiments, whereas a transformation to significant amounts of the unfavorable monoclinic phase was detected on the other catalysts by post-reaction XRD measurements. Accordingly, the highest stability was observed on the 0.1 mol% K-doped catalyst.

3.3.2 The Effect of High-Valence Dopants

In a follow-up work, the effect of high- and equal-valence dopants (HVD/EVD), specifically Y, Gd, Zr and V, incorporated in Sm_2O_3 was investigated at the same concentration levels (0.1 and 1.0 mol%) for the catalytic effects in the oxidative coupling of methane. In contrast to LVDs, the impact of HVDs and EVDs is more difficult to predict. Theoretical studies suggest that HVDs increase the energy of oxygen vacancy formation and thus render the surface more Lewis acidic, which has been shown to be detrimental for the catalytic activity in the OCM.[198, 200, 201] Yet, a higher energy of oxygen vacancy formation can also limit over-oxidation of CH_4 and thus improve the C_{2+} selectivity. Additionally, HVDs can be activated by oxygen from the gas phase to form MeO^{x+} (Me = dopant metal) that now act as LVDs.[198] All sample were characterized by means of N_2 physisorption, CO_2-TPD and XRD before and after the reaction to complement the catalytic data.

When used in very low concentrations (0.1 mol%) and at temperatures below 700 °C, all HVDs improve the activity and C_{2+} selectivity. Surprisingly, this includes transition metal dopants with multiple possible oxidation states like V (possible oxidation states +5, +4, +3

and +2), that are usually reported to over-oxidize methane, but only when used in very low concentrations. The best performance was achieved over the catalyst containing 0.1 mol% Gd and the most drastic improvements occurred in the low-temperature regime between 500-600 °C. These catalysts also perceived a higher stability during time-on-stream experiments at 700 °C in comparison to the catalysts with the higher dopant level and the undoped Sm_2O_3. The inferior performance of the catalysts with the higher dopant level is probably caused by dopant segregation during the reaction. Neither the stability nor the activity correlates with the number of basic sites as determined by CO_2-TPD, instead the ability to stabilize the cubic Sm_2O_3 phase against transforming into the monoclinic phase and sintering appears to be the decisive factor.

4

Establishing Support-Activity Correlations by Decoupling Size and Support Effects

This chapter lays the groundwork for the Chapters 5 and 6 and aims to understand the influence of the support's surface chemistry, i.e. the acid-base properties on the ruthenium catalyzed CO_2 methanation. Parts of this chapter have been submitted to *Catalysis, Science & Technology* and are adopted here verbatim.

4.1 What to Expect from this Chapter.

While the influence of the active component (e.g. Ni or Ru) is well understood, the catalytic performance is strongly influenced by the applied support material and its surface chemistry, but a fundamental understanding is still missing. Most studies trying to shed light on such effects have focused on standard support materials so far, such as Al_2O_3, SiO_2, MgO and TiO_2. Only in recent years also less often used support materials, such as Sm_2O_3 and CeO_2, have gained attention in the literature based on their favourable and rich surface chemistry.[5, 6, 22] In this way, new options for improved catalysts became apparent, but only a few studies systematically investigated the mechanistic influence of the support so far – a prerequisite for a targeted catalyst design for this reaction. One obstacle that complicates systematic studies in this direction results from the mentioned structure-sensitivity of the

CO_2 methanation. Due to the difficulty to prepare identical or at least similar particle sizes of the active component (in this case Ru) on different support materials by conventional methods (such as wet impregnation), support effects often cannot be clearly differentiated from particle size effects.[202] As these methods are normally based on the in-situ formation of the metallic nanoparticles on the support, their size generally strongly depends on the surface chemistry of the support and factors, such as its crystallinity, porosity and potential impurities, to name just a few. Accordingly, most studies conducted so far in order to compare different support materials could not systematically account for varying particle sizes of the active component; consequently, such approaches fell short in identifying clear trends. Instead, building block approaches which employ colloidal particles with uniform size should be utilized.

In terms of the active component, we focus on Ru nanoparticles due to their reported high specific activity, thus allowing to prepare catalysts with low loadings – we target 1.0 wt.% - to prevent agglomeration of the nanoparticles on the support surface while still providing a significant activity. The Ru nanoparticles are prepared following a well-established synthesis route in basic ethylene glycol developed by Wang et al.[203]. In contrast to most colloidal routes, this synthesis does not require organic ligands, e.g. polyvinylpyrrolidone (PVP), to protect the nanoparticles from agglomerating during the synthesis and thus eliminates the necessity for their removal before the catalytic experiments, which otherwise is a prerequisite in order not to affect the catalytic results. Further, the prepared nanoparticles need to be small enough to enter the pore network of the support materials which usually exhibit mesopores, i.e. pores with a diameter between 2 and 50 nm. In our case, the anticipated diameter of the Ru nanoparticles is 1 nm, thus fulfilling the criterium.[203]

With respect to the question which support materials are favourable or unfavourable to achieve high activities and selectivities for the hydrogenation of CO_2, the acid-base properties of the support are expected to play a particularly important role. In case of an inert support, all necessary elementary steps involving the competitive dissociative adsorption of H_2 *and* CO_2 must take place on the surface of the metallic Ru nanoparticles alone ("CO pathway", Figure 4-1). Since CO formed as an intermediate of the dissociative CO_2 adsorption is more strongly bound on Ru than H_2, it can poison the surface depending on the temperature, thus limiting the activity.[44, 102, 204] However, in case of basic supports, three possible scenarios can lead to additional possibilities for CO_2 adsorption and activation on the support surface so that a beneficial influence on the activity can be expected:

1) CO_2 adsorption on the support

As a mild acid, CO_2 can adsorb on basic sites of a corresponding support. Brønsted basic OH groups, for instance, can react with CO_2 to form hydrogen carbonates (pathway 1, Figure

4-1), whereas Lewis basic sites in the form of lattice oxygen, for instance, can bind CO_2 as monodentate carbonates. In either case, CO_2 does not need to adsorb on Ru alone, thus increasing the CO_2 surface concentration, which can lead to an increased activity when assuming a Langmuir-Hougen-Hinshelwood-Watson mechanism.[46, 105, 142, 154, 205, 206] Yet, aiming at improving the activity in this way, the stability of the resulting carbonates must be considered. Neither carbonates that are bound too weakly so that they easily decompose again nor highly stable carbonates, which are unreactive in the temperature range where the methanation reaction is carried out, are expected to increase the activity in the explained way.[104] If basic sites of "intermediate" strength are available, it is likely that CO_2 adsorption on these sites leads to carbonate species that can subsequently be hydrogenated to methane on the surface. This occurs either at the perimeter of the supported metal particles or within the range of surface diffusion of adsorbed H, which is a function of the support's surface characteristics.[207]

2a) CO_2 activation on oxygen vacancies

Also oxygen vacancies can act as Lewis bases that not only provide sites for CO_2 adsorption but can also lead to an additional activation.[78, 208–212] Exceeding the beneficial effect of a basic support according to option 1), the option of CO_2 to form bidentate carbonates upon adsorption on such vacancies, represents a first reduction of the molecule if the oxygen atom filling the vacancy is left there in the further course of the reaction to CH_4 (pathway 2a, Figure 4-1).[91, 213] In a separate step, a new vacancy can be created if two H atoms, spilling over from the Ru particle, react with lattice O to form H_2O which then desorbs. Overall,

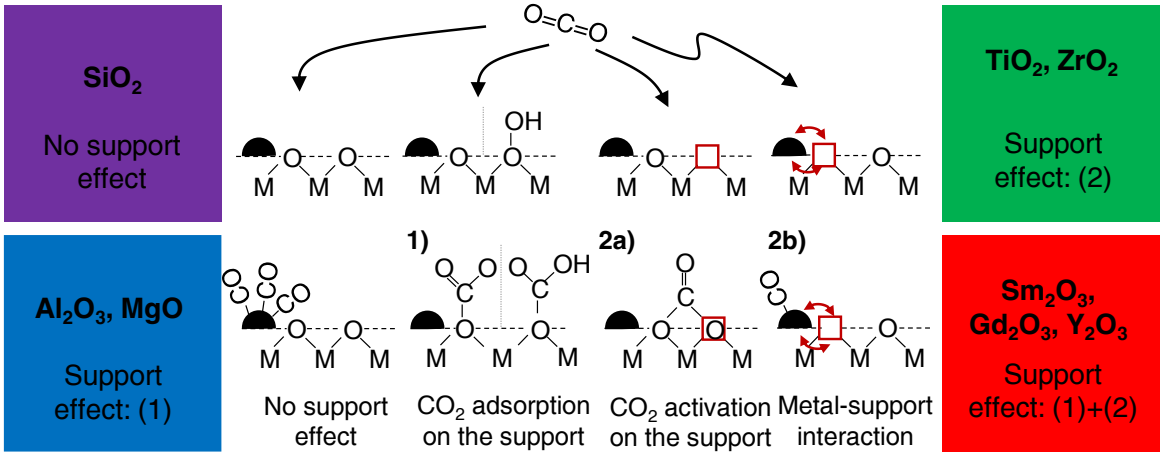

Figure 4-1 **Conceptual depiction of the possible support effects and classification of the used support materials. No support effect ("CO pathway"), (1) CO_2 adsorption as monodentate or hydrogen carbonate, (2a) CO_2 activation as bidentate carbonate and (2b) metal-support interaction; red squares indicate an oxygen vacancy, red arrows indicate electronic interactions. In all cases H_2 is expected to adsorb dissociatively on the metal (not shown here due to simplicity reasons).**

such a scenario corresponds to a Mars-van-Krevelen mechanism, contributing in this way to the catalytic turn over on the surface of the catalyst. TiO_2 and ZrO_2 for example, are well-known for their ability to form sub-stoichiometric oxides, therefore exhibiting oxygen vacancies.[78, 88, 214] The ability to form oxygen-deficient structures is also inherent to the rare earth metal oxides Sm_2O_3, Gd_2O_3 and Y_2O_3.[214, 215]

2b) CO_2 activation on the metal due to oxygen vacancy induced metal-support interactions

Lewis basic oxygen vacancies can also contribute indirectly to a higher activity of the Ru nanoparticles by a metal-support interaction. If not contributing according to option 2a) (e.g. because the interaction with CO_2 is too weak), the presence of oxygen vacancies on the support can still have a promotional effect for the reaction by modifying the electronic structure of the metal deposits.[216–218] Specifically, it was found that such an interaction can reduce the CO surface coverage as the most strongly bound reaction intermediate on the Ru surface, thus resulting in more free sites for H_2 adsorption and dissociation.[128] In other words, the support can also contribute to a higher activity by preventing a gradual self-poisoning due to accumulation of CO on the surface of the Ru nanoparticles (pathway 2b, Figure 4-1).[128]

Aiming at a clarification to which extend the described possibilities of a support effect can be exploited to increase the methane yield for the Ruthenium-catalyzed CO_2 methanation, we investigated a variety of support materials exhibiting different acid-base properties. To rule out superimposed particle size effects on the catalytic performance, which – as detailed above – are expected due to the structure sensitivity of the reaction, we used a novel building block approach by synthesizing colloidal Ru nanoparticles independently from the support in a first step. In this way, a narrow size distribution could be obtained and, in a subsequent step, these particles were deposited on various support materials, enabling us to systematically study the effect of different support characteristics while keeping the Ru particle size constant. In sum, eight different support materials were chosen which can be grouped in four categories along their acid/base properties: (1) Gd_2O_3, Sm_2O_3 and Y_2O_3 exhibiting both Lewis as well as Brønsted basic properties;[215, 219] (2) TiO_2 and ZrO_2 exhibiting Lewis basic but no Brønsted basic sites;[215] (3) Al_2O_3 and MgO which expose Brønsted basic but no Lewis basic sites;[102, 220] and (4) SiO_2 as a support material without Brønsted and Lewis basic properties.

All Ru loaded oxides were fully characterized by means of atomic absorption spectroscopy (AAS, to determine the Ru loading), N_2 physisorption, powder X-ray diffraction (XRD) and transmission electron microscopy (TEM). CO_2-temperature programmed desorption (CO_2-TPD) in combination with diffuse reflectance infrared Fourier-transformed spectroscopy (DRIFTS) measurements were used to identify the type of potential carbonates formed on

the various supports and to characterize and quantify the basicity of the catalysts. Then, all catalysts were tested with respect to their activity and selectivity for CO_2 methanation under identical conditions. In parallel, *operando* DRIFTS was employed to gain further insight into the surface species formed under reaction conditions enabling us to correlate the trends observed in the catalytic experiments with the support's basicity in the Brønsted and Lewis sense. Details on the experimental procedures can be found in the appendix A and B.1.

4.2 Catalysts

Eight different catalyst systems were prepared by depositing colloidal Ru nanoparticles on various oxidic supports. A Ru loading of 1 wt.% was targeted in all cases.

Support materials

Al_2O_3 (Sasol, Puralox SBa 200, 98%), MgO (Acros, 98%), SiO_2 (Sigma, Davisil 646, 99%), TiO_2 (Evonik, Aeroxide P25, 99.5%), ZrO_2 (Chempur, 99%) were purchased, whereas Sm_2O_3, Gd_2O_3 and Y_2O_3 were synthesized in-house by the sol-gel route introduced in Chapter 3.2.2.

Ru nanoparticles

Ru nanoparticles with an average size of 1 nm were prepared by a colloidal synthesis route previously reported by Wang et al.[203]. In short, 0.223 g $RuCl_3 \cdot xH_2O$ (Chempur, 41 wt.% Ru content) was dissolved in 25 mL ethylene glycol (Merck) and further diluted with 25 mL 0.5 M NaOH (VWR, 99%) in ethylene glycol. The resulting solution was placed in an oil bath pre-heated to 150 °C for 90 min under stirring to ensure full reduction of Ru and nanoparticle formation. The particles were finally precipitated by adding eight equivalents (vol./vol.) 1 M HCl to the solution. After centrifugation at 40 Hz, the Ru nanoparticles could be collected as solid particles by decanting the HCl. To deposit the nanoparticles on the support, the nanoparticles were redispersed in four equivalents (vol./vol.) of acetone (p.a., Merck) and the required amount of the support material (particle size 75-150 µm) was added, before the solvent was removed by rotary evaporation under vacuum so that a dried powder was obtained.

The following compositions were determined by AAS and used for calculating the reaction rates: 0.8 wt.% Ru-Sm_2O_3, 0.8 wt.% Ru-Y_2O_3, 0.8 wt.% Ru-Gd_2O_3, 1.0 wt.% Ru-TiO_2, 0.8 wt.% Ru-ZrO_2, 1.0 wt.% Ru-Al_2O_3, 1.2 wt.% Ru-MgO and 1.0 wt.% Ru-SiO_2. The differences in the loading resulted from different losses during precipitation and the subsequent decanting of the residual HCl.

4.3 Structural Characterization by XRD

As the catalytic performance of supported catalysts can also depend on the crystal structure of the support,[28, 221] X-ray diffraction measurements were performed to identify the present phases. Representative X-ray diffraction patterns of all samples are presented in Figure 4-2 and reveal that all supports were crystalline, except for SiO_2 being X-ray amorphous.

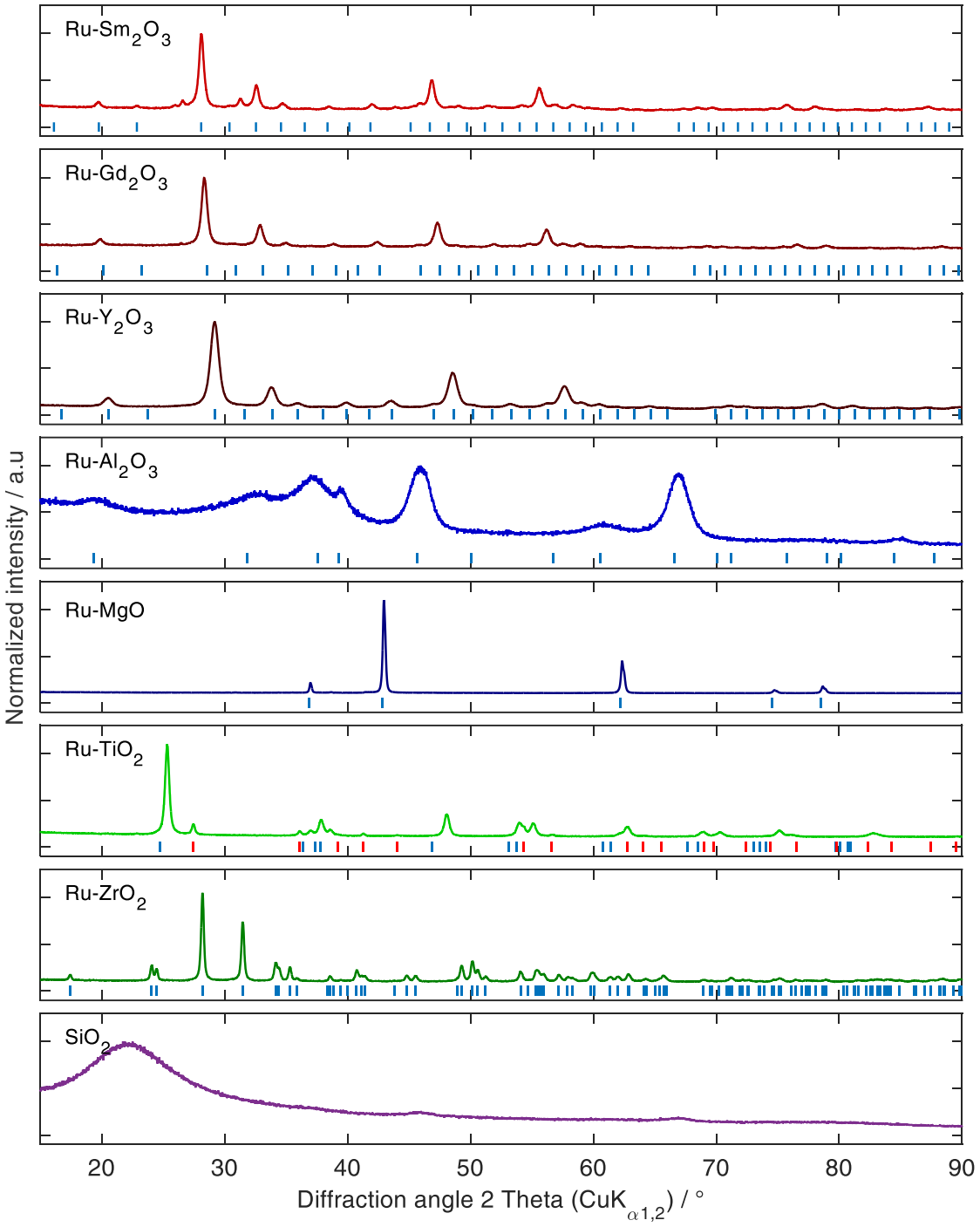

Figure 4-2 X-ray powder diffraction patterns of the investigated catalysts. The tick marks indicate the possible Bragg reflections of the respective oxide phases. Sm_2O_3, Gd_2O_3 and Y_2O_3 - $Ia\bar{3}$;[187] γ-Al_2O_3 - $Fm\bar{3}m$;[222] MgO - $Fm\bar{3}m$;[223] TiO_2 – P $4_2/mnm$ (red) and I $4_1/amd$ (blue);[224, 225] ZrO_2 - $P12_1/c1$.[226]

The rare earth metal oxides exhibit the expected crystal structures of cubic Sm_2O_3, Gd_2O_3 and Y_2O_3 ($Ia\bar{3}$). The TiO_2 employed in this study was comprised of a mixture of 8 wt.% rutile and 92 wt.% anatase, whereas, all other purchased support materials consisted of only one phase, namely, monoclinic ZrO_2 (space group: $P12_1/c1$), γ-Al_2O_3 ($Fm\bar{3}m$) and cubic MgO ($Fm\bar{3}m$). Diffraction peaks of Ru^0 or RuO_x are not detected in any of the diffractograms as expected because of the low loading and the small particle size (see also Chapter 4.5).

4.4 Structural Characterization by N_2 Physisorption

The specific surface areas, pore volumes as well as pore size distributions were analyzed for all catalysts using N_2 physisorption (Table 4-1); the corresponding isotherms and pore size distributions are shown in Figure 4-3 and Figure 4-4. Apart from the typical porosity descriptors – the specific surface area, pore volume and average pore size - the maximum of the pore size distribution is stated as an additional measure to reflect, which is the most common pore size as the average pore size can be an inaccurate descriptor as it is easily inflated by outliers. The data is evaluated following the recommended IUPAC classification. Accordingly, the REO as well as Al_2O_3 and SiO_2 supported catalysts clearly are mesoporous oxides as indicated by the hysteresis loop in the N_2 isotherms (type IV) and the derived pore size distributions. The shape of the isotherms measured on Ru-TiO_2 and Ru-ZrO_2 hint to the presence of mainly macropores (pore diameter > 50 nm), whereas no reliable pore size distribution could be derived for the MgO supported catalyst.

Table 4-1 **Specific surface area, pore volume as well as the average pore size and the maximum in the pore size distribution, determined by N_2 physisorption measurements. For a rough estimation of the statistical error, the Ru-Sm_2O_3 sample was measured three times. The reported value is the averaged value and the error corresponds to the standard deviation which is considered to be representative also for the other samples.**

Sample	Specific surface area / $m^2 g^{-1}$	Pore volume / $cm^3 g^{-1}$	Average pore radius / nm	Max. of pore radius distribution / nm
Ru-Gd_2O_3	35	0.08	4.5	3.0
Ru-Sm_2O_3	36±1	0.14±0.01	7.5±0.2	6.4±0.1
Ru-Y_2O_3	61	0.13	4.4	3.0
Ru-Al_2O_3	195	0.46	4.7	3.2
Ru-MgO	12	0.03	-	-
Ru-TiO_2	60	0.54	17.0	26.3
Ru-ZrO_2	16	0.13	15	13
Ru-SiO_2	224	0.84	7.5	5.0

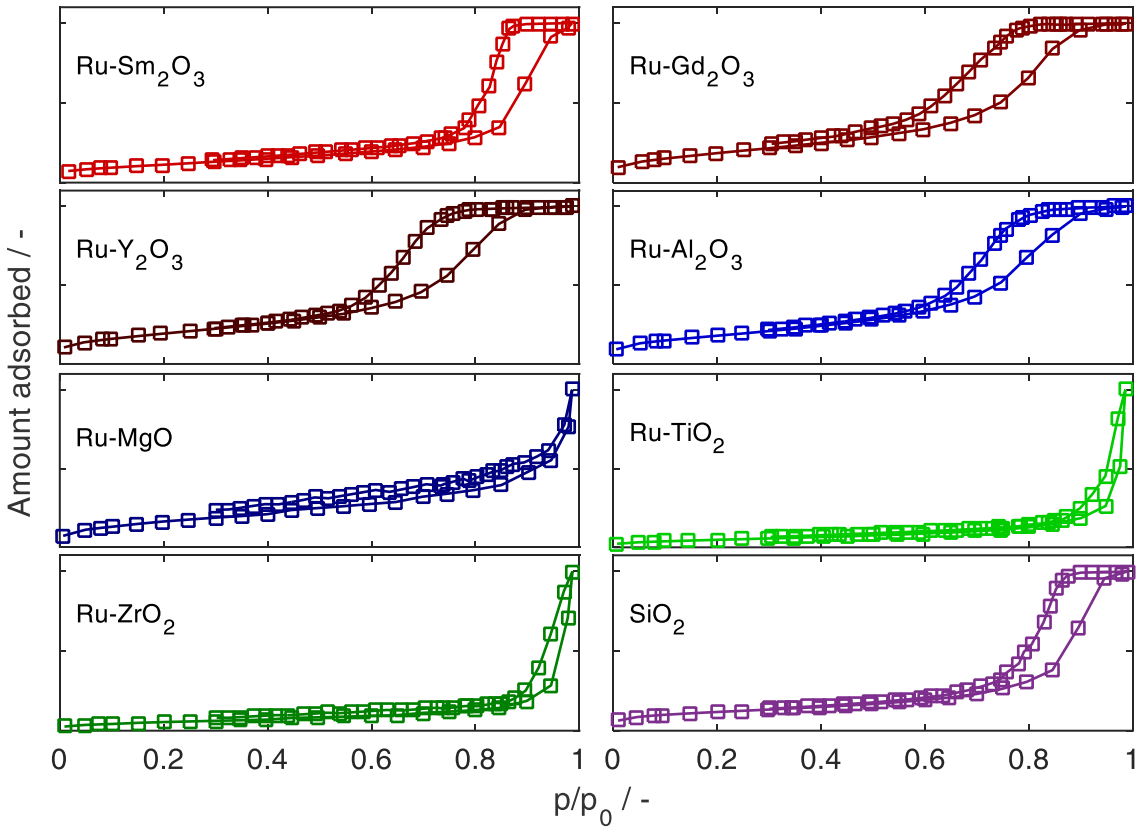

Figure 4-3 N_2 physisorption isotherms of the investigated catalysts.

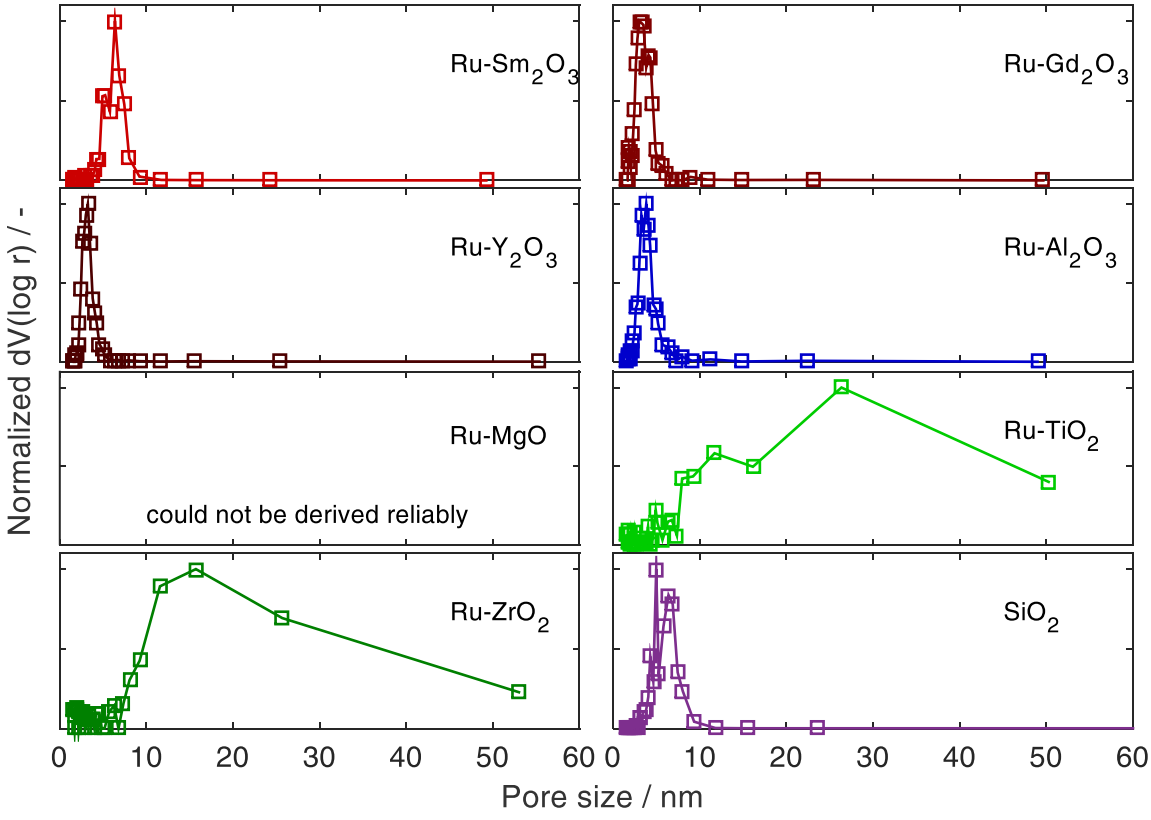

Figure 4-4 Derived pore size distributions using the BJH model (applied to the desorption branch of the isotherm) of the investigated catalysts.

4.5 Structural Characterization by TEM

Transmission electron micrographs of the colloidal Ru dispersion were acquired in order to determine and verify the particle size. For the synthesis used, a diameter of 1.0 nm is expected.[203] In addition, the catalysts were investigated by TEM to ensure that, after supporting the Ru nanoparticles on the various oxides, their size did not change. Selected spots on the samples were measured by EDX to confirm the correct identification as Ru or support material. To determine the particle size distribution and the mean particle size in all other cases, at least 150 Ru particles were evaluated for each sample. Representative images and the corresponding Ru size distributions are shown in Figure 4-5. According to these results, the as-prepared Ru nanoparticles exhibited the expected diameter of 1.0 ± 0.2 nm and a narrow size distribution. After deposition onto the various supports, they preserved their size

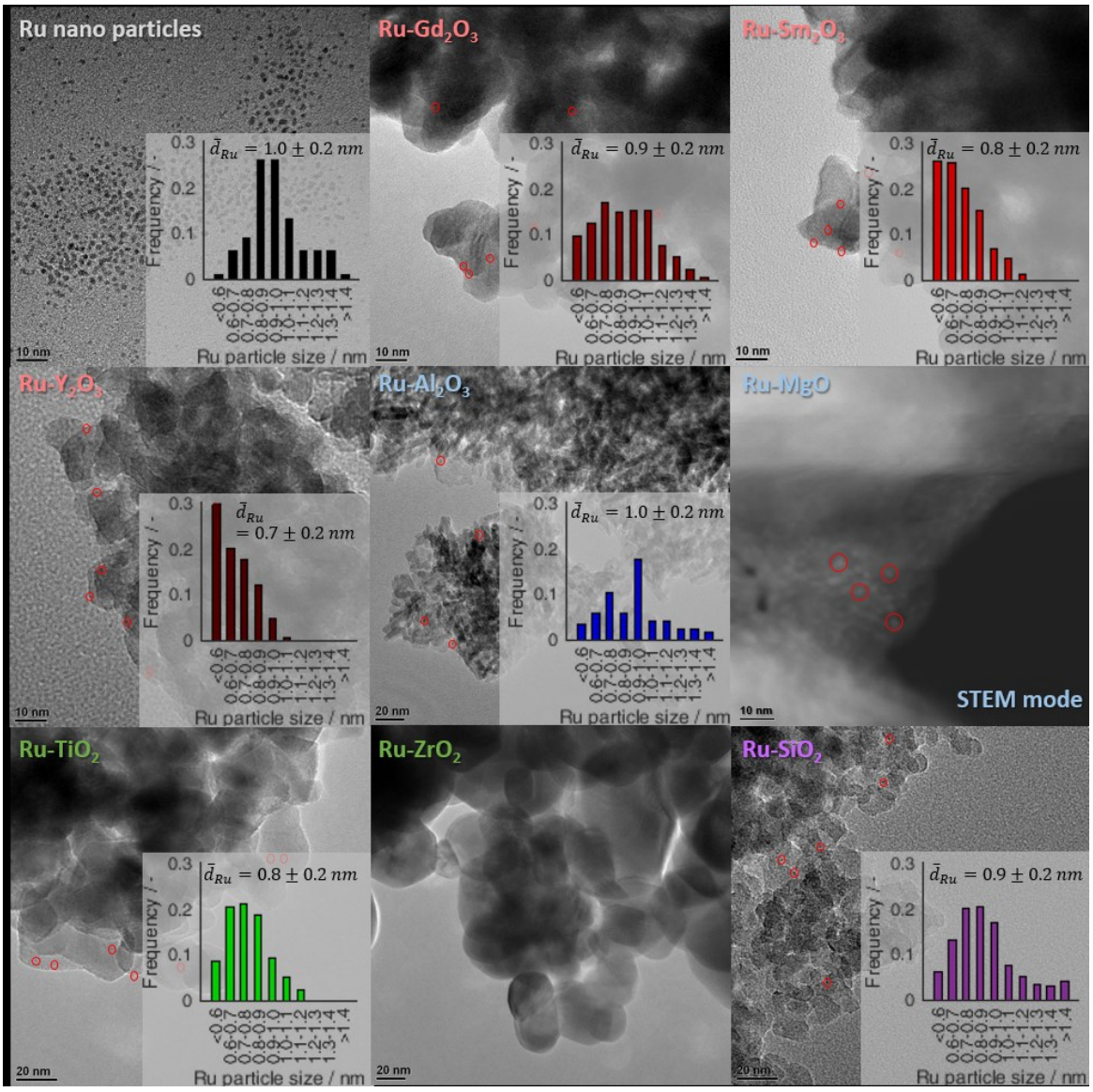

Figure 4-5: **TEM images of the synthesized Ru nanoparticles (red circles) and the supported catalysts, as well as the respective Ru particle size distribution.**

within the respective standard deviations, so that in line with the experimental approach of this study, an influence of different Ru particle sizes on the catalytic performance of the different catalysts can be ruled out. In no case, agglomerates of Ru particles were observed, proving that a fine dispersion of the active component could be achieved. As the Ru particle diameter was smaller than the average pore size of the supports, we assume that the Ru nanoparticles were able to penetrate the pores during evaporation of the solvent so that a homogeneous deposition inside the pore network of the support materials could be achieved. Unfortunately, in case of Ru-ZrO_2 the contrast between Ru and ZrO_2 was too low due to the similar atomic mass, rendering it impossible to clearly detect the Ru particles (in both TEM and STEM mode). For Ru-MgO, no Ru particles could be distinguished in TEM mode, but were clearly evidenced by STEM.

4.6 Determination of the Basicity

As described in the introduction, it can be expected that the acid/base properties of the different support materials or, more precisely, the presence of basic Brønsted and Lewis centers play an important role for the activity of the prepared catalysts for the methanation of CO_2. In order to characterize such sites, CO_2-TPD measurements were conducted for all catalysts investigated in this study. In addition to the information about their strength, their density on the surface can also be assessed by integrating the corresponding TPD signals which correlate to the amount of adsorbed CO_2.

Prior to CO_2 saturation, the samples were subjected to the same pre-treatment applied for the catalytic experiments. Figure 4-6 shows the desorption profiles acquired for the various catalysts. In addition, Table 4-2 summarizes the amounts of adsorbed CO_2 as well as the derived surface densities of basic site in all cases. For the calculations, the specific surface areas determined by N_2 physisorption were considered. To further characterize the nature of the adsorbed CO_2 species, i.e. the carbonates formed on the oxide supports, complementary DRIFTS measurements were conducted. To assure comparability, the same pre-treatment as carried out for the catalytic tests and the TPD measurements were applied (Figure 4-7). In the following section, the results are discussed per defined oxide class.

Ru-Gd_2O_3, Ru-Sm_2O_3 and Ru-Y_2O_3

As detailed in the introduction, the rare earth metal oxides are expected to exhibit Brønsted as well as Lewis basic sites on the surface. CO_2 desorption is observed for these catalysts mainly between 200-400 °C – a temperature range, that reveals medium basicity

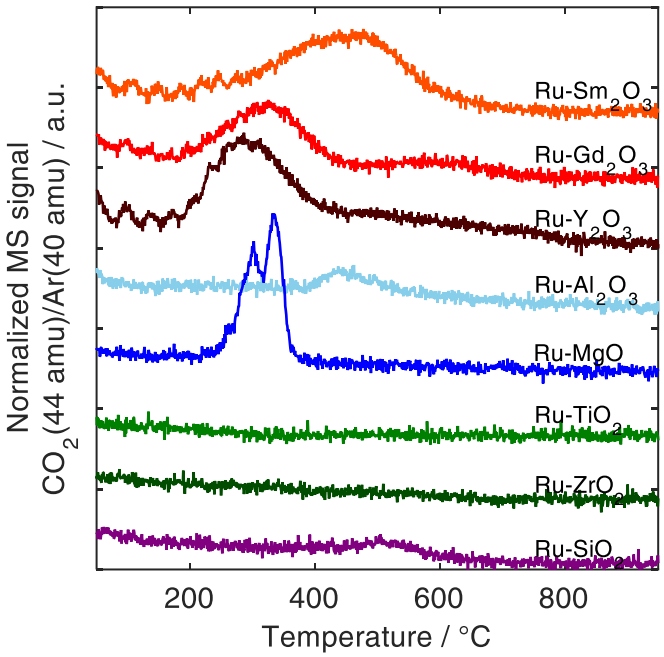

Figure 4-6 **CO_2-TPD measurements of the investigated catalysts. Conditions: ~100 mg catalyst, saturated at 50 °C, temperature ramp 5 °C min^{-1}. All samples were activated in H_2 prior to the measurements at 400 °C for 1 h.**

of these sites in good agreement with the literature.[94] Such sites are favourable as the range of desorption temperatures coincides with the potential reaction temperatures for the CO_2 methanation, meaning that the fixation of CO_2 is neither too weak nor too strong. The strength of the basicity among the investigated rare earth oxides follows the trend expected based on the lanthanide contraction, which predicts a decrease in basicity with a decreasing radius of the rare earth cation. Accordingly, the desorption peaks for these catalysts shift to lower temperatures with increasing atomic number. As far as the amount of adsorbed CO_2 is concerned, the rare earth metal oxide supported catalysts show the highest CO_2 adsorption capacity of all investigated samples and the determined densities of basic sites correspond

Table 4-2 **Amount of CO_2 desorbed from the various catalysts and calculated surface density of basic sites.**

Sample	Amount desorbed / µmol CO_2 g_{cat}^{-1}	Density of basic sites / µmol CO_2 m_{cat}^{-2}
Ru-Gd_2O_3	333	9.5
Ru-Sm_2O_3	644	17.9
Ru-Y_2O_3	759	12.4
Ru-Al_2O_3	198	1.0
Ru-MgO	319	26.6
Ru-TiO_2	0	-
Ru-ZrO_2	0	-
Ru-SiO_2	77	0.3

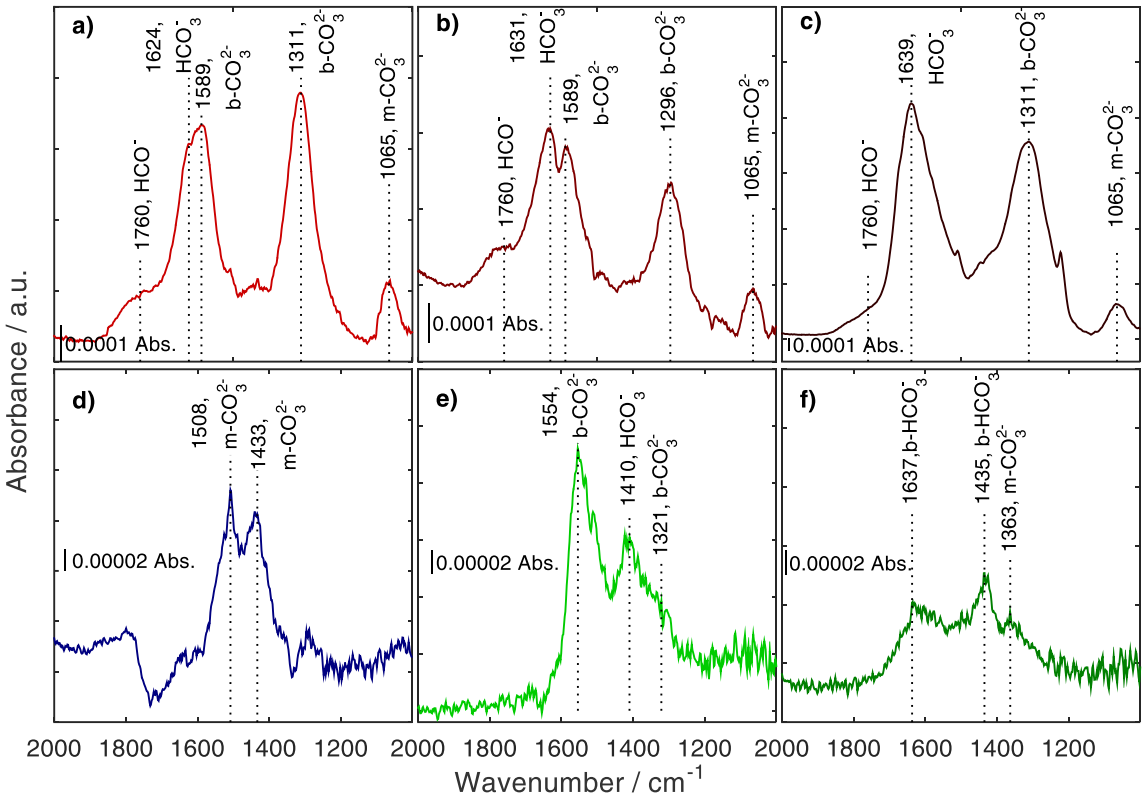

Figure 4-7 CO_2 adsorption mode after saturation with CO_2 for 30 min at 50 °C by DRIFTS; a) Ru-Sm_2O_3, b) Ru-Gd_2O_3, c) Ru-Y_2O_3, d) Ru-MgO, e) Ru-TiO_2 and f) Ru-ZrO_2.

well with values reported in the literature.[94, 102] DRIFTS experiments carried out for these catalysts yielded similar spectra revealing the presence of monodentate (m-CO_3^{2-}, 1065 cm^{-1}), bidentate (b-CO_3^{2-}, 1589 cm^{-1} and 1296 - 1311 cm^{-1}) and hydrogen carbonates (HCO_3^-, 1624 - 1639 cm^{-1}) on the surface (Figure 4-7 a-c).[154, 227] Monodentate carbonates correspond to CO_2 adsorbed on lattice oxygen of the REO support, whereas hydrogen carbonates are formed upon CO_2 adsorption on Brønsted basic OH surface groups, which are apparently present in abundance on these supports. In addition, the spectra also prove the formation of bidentate carbonates indicating the presence of the Lewis basic oxygen vacancies on the surfaces of the REO supports as expected.[227, 228] Such bidentate carbonates form when CO_2 adsorbs by donating one oxygen atom to such a vacancy. When the oxygen atom remains in the vacancy, i.e. in the lattice of the oxide, the formation of such bidentate carbonates can be understood as a first reduction step of CO_2 along its full reduction to CH_4. By comparing the relative peak intensities for HCO_3^-, b-CO_3^{2-} and m-CO_3^{2-}, we can draw qualitative conclusions regarding their relative abundance on the surface. According to this analysis, for Sm_2O_3, bidentate carbonates (b-CO_3^{2-}) dominantly form upon CO_2 adsorption, indicating a prevalence of oxygen vacancies as basic sites on this catalyst, whereas for the Ru-Gd_2O_3 and the Ru-Y_2O_3 catalyst OH groups leading to HCO_3^- species are apparently more abundant and dominate the adsorption behaviour of CO_2 here. On the contrary, monodentate carbonates (m-CO_3^{2-}) are minority species in all three cases.

Ru-Al_2O_3 and Ru-MgO

Al_2O_3 chosen as an example of an oxide support exhibiting Brønsted basicity but lacking Lewis basic oxygen vacancies, shows only a weakly pronounced CO_2 desorption peak which is centered around 500 °C, in accordance with what has also has been observed by other authors.[229] The comparatively low adsorption capacity agrees well with published values.[102] In agreement with the low adsorption capacity, the acquired DRIFT spectra do not reveal noticeable absorption bands due to carbonate formation, and are, therefore, not shown here. On the contrary, for Ru supported on MgO, chosen as another representative of this class of oxide supports, a distinct CO_2 desorption feature in form of a narrow double peak between 300-400 °C was detected. Even though the corresponding temperatures are at the lower end of desorption temperatures expected for MgO, similar values have also been reported in the literature previously.[230] As inferred from the DRIFT spectra, CO_2 is bound to the MgO surface in form of m-CO_3^{2-} species as indicated by the two pronounced features at 1508 cm^{-1} and 1433 cm^{-1} (Figure 4-7d), while exhibiting no indications for bidentate species.[231, 232]

Ru-TiO_2 and Ru-ZrO_2

In contrast to the Brønsted basic supports, hardly any CO_2 desorption is observed for the catalysts supported on Lewis basic oxides, i.e. on TiO_2 and ZrO_2. The DRIFT spectra (Figure 4-7e and f) for the two catalysts, however, reveal the formation of at least some carbonate species upon CO_2 adsorption. In case of Ru-TiO_2, a sharp peak at 1554 cm^{-1} and a weakly pronounced shoulder at around 1321 cm^{-1} point to b-CO_3^{2-} on the surface, in agreement with the expected presence of Lewis basic oxygen vacancies on TiO_2.[227, 233, 234] Furthermore, a peak at 1410 cm^{-1} can be assigned to HCO_3^- species, which proves the additional existence of some Brønsted basic OH groups probably formed during the reductive pre-treatment of the sample with H_2. The ZrO_2 supported catalyst (Figure 4-7f) on the other hand, shows a different CO_2 adsorption behaviour. Here, monodentate carbonates (1363 cm^{-1}) and bidentate hydrogen carbonates (b-HCO_3^-, 1435 and 1637 cm^{-1}) prevail, whereas bidentate carbonates do not seem to form on this support.[221, 235–237] Yet, the detection of bidentate hydrogen carbonates reveals the relevance of oxygen vacancies as Lewis basic adsorption sites on this support as well, but suggests that either hydroxyl groups located in the vicinity are involved or that bidentate carbonates at the metal-support perimeter are quickly hydrogenated by H atoms spilling over from the metal. In any event, the absence of any notable peaks in the CO_2-TPD spectra indicates that the surface concentration of all kinds of basic sites is low in the case of both oxides. Even though low CO_2 adsorption capacities have been observed for titania and zirconia before,[90,238] the finding appears puzzling and conflicting at first sight with their choice as good representatives of Lewis basic supports which expose high concentrations of oxygen vacancies at the surface. In case of the TiO_2 supported catalyst, a probable explanation is

that carbonates are not bound sufficiently strong to the catalyst surface, i.e. bidentate carbonates have been shown to desorb from TiO_2 at around 25 °C,[239] which is below the saturation temperature in our TPD experiments. In contrast, the chosen saturation temperature is probably not high enough to chemisorb CO_2 on the ZrO_2 surface. This is backed by the temperature-dependent DRIFTS study on Ru-ZrO_2 (see Chapter 4.8.2), where the formation of carbonates is clearly evident at 100 °C. In either case, a saturation temperature of 50 °C does not appear to be best suited for the TiO_2 and ZrO_2 supported catalysts. It must be noted though, that, due to the temperature-dependence of CO_2 chemisorption and the stability of the formed adsorbates on different oxides, a universally applicable CO_2 saturation temperature does not exist. Additionally, it must be kept in mind that the formation of Lewis basic oxygen vacancies is a function of temperature and also dependent on the surrounding gas atmosphere. To verify this and to prove the formation of oxygen vacancies during activation, we additionally carried out in-situ Raman measurements between 200-400 °C in H_2 atmosphere for the Ru-TiO_2 and Ru-ZrO_2 catalyst. A detailed description of the experiments and the obtained spectra can be found in the appendix (Figure B-1). In short, this experiment corresponds to a H_2 temperature-programmed reduction (H_2-TPR) experiment but allows us to specifically follow structural changes in the support, whereas a H_2-TPR experiment would yield the overall reduction behaviour of the catalyst, including the reduction of the RuO_x nanoparticle, only. Increasing the temperature, no significant changes of the TiO_2 support are detectable in the spectra until 300 °C, indicating a low and constant oxygen vacancy density. At higher temperatures, however, a significant blue shift of the E_g vibrational mode occurs (Figure 4-8), which can be attributed to their increasing formation. It has been reported in the literature that the reduction of pure TiO_2 to an oxygen-deficient phase can be expected above 300 °C,[75–77] in agreement with the data presented here. Using a correlation between the Raman shift and the O/Ti ratio proposed by Parker and Siegel,[240] the Raman shift observed at 400 °C (153 cm^{-1}) corresponds to an O/Ti ratio of around 1.9. Under the assumption that the oxygen vacancy concentration is homogenously distributed and also representative for the surface, this result corresponds to an oxygen vacancy density of 20.8 µmol m^{-2} at the surface, which is of similar magnitude as observed for the REO and MgO supported catalysts. As shown in the next chapter describing the catalytic observations, the catalyst is cooled down in inert gas atmosphere after the activation step. Hence, the determined state of reduction should represent the state of the catalyst after reductive pre-treatment before exposing the catalyst to the reaction atmosphere. During the subsequent reactivity experiment, that is conducted in the temperature range between 200 and 400 °C, the poor stability of carbonates on the TiO_2 supported catalysts thus renders a contribution of the support effect (2a) unlikely. Instead, a positive effect due to the indirect support mechanism (2b) as explained in the introduction can be expected.

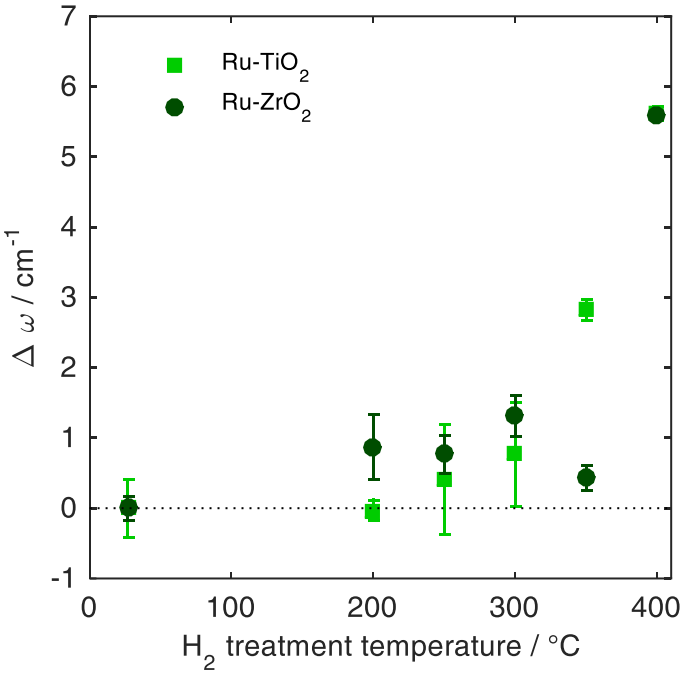

Figure 4-8 Temperature-dependent changes of Raman frequencies (Δω) of Ru-TiO_2 (147 cm^{-1}) and Ru-ZrO_2 (174 cm^{-1}) under H_2 atmosphere.

Unfortunately, for ZrO_2 no such quantitative correlation between the Raman shift and the stoichiometry is available. However, a blue shift of the Raman signal was detected for ZrO_2 as well when applying the same conditions, is indicative of an increased concentration of oxygen vacancies formed after the reductive pre-treatment also in this case.

Ru-SiO_2

Unexpectedly in the first place, SiO_2 which should expose neither Lewis nor Brønsted basic sites shows a small but detectable broad desorption peak between 500-600 °C in the CO_2-TPD spectrum. The corresponding DRIFT measurements (not presented here), however, provided clear evidence that this feature does not belong to any specific basic adsorption centers for CO_2 on the surface, since no absorption bands occurred in the corresponding spectra. Although the origin of the TPD peak is unclear, possibly caused by residual, "trapped" CO_2 inside the pore network, the DRIFTS results confirm the classification of SiO_2 as a non-basic support in agreement with the literature.[241]

4.7 Catalytic Experiments

The CO_2 conversion rates and CH_4 selectivity achieved between 200 °C and 400 °C in the CO_2 methanation experiments are shown in Figure 4-9 for the various catalysts. The presented graphs are colour-coded to allow easy differentiation between the four different support categories used in this study - green for the solely Lewis basic supports (TiO_2 and ZrO_2),

red for the ones exhibiting both Lewis as well as Brønsted basic sites (REOs), blue for the Brønsted basic supports (Al_2O_3 and MgO) and purple for the non-basic SiO_2. Since the reaction rates are referred to the actual Ru loading determined by AAS, the observed differences in the catalytic performance of the catalysts can be – because the Ru particle size is the same in all cases - directly attributed to support effects, i.e. to its surface chemistry. The Weisz-Prater criterion was calculated for all data points, taking Knudsen diffusion (when in agreement with the determined average pore sizes) into account, to verify the absence of internal mass transport limitations in the investigated temperature range (see Table B-1). Only at 400 °C, an influence of diffusion limitation on the observed rates cannot be fully excluded as indicated by the corresponding Arrhenius plots (Figure B-2). Moreover, the stability of the catalysts was checked by extended catalytic runs at 400 °C over 10 h showing stable conversions (see Figure B-3). The reproducibility of the catalytic results was ensured by conducting several consecutive runs as well as tests with different synthesis batches (see Figure B-4).

Considering the temperature-dependent progression of both, the CO_2 conversion rates and CH_4 selectivities, the results can be distinguished into two temperature regions – one below and one above 310 °C. Below 310 °C, the activity follows the order: Ru-TiO_2> Ru-ZrO_2 ≈ Ru-Gd_2O_3>Ru-Sm_2O_3 > Ru-Y_2O_3 > Ru-Al_2O_3 > Ru-SiO_2 > Ru-MgO. This trend suggests that Lewis basic oxygen vacancies which are characteristic for TiO_2 and ZrO_2 as well as for the REOs have a promotional effect and increase the activity in this temperature regime. Above 310 °C, the activity follows another order: Ru-Gd_2O_3> Ru-Sm_2O_3 > Ru-Y_2O_3 >

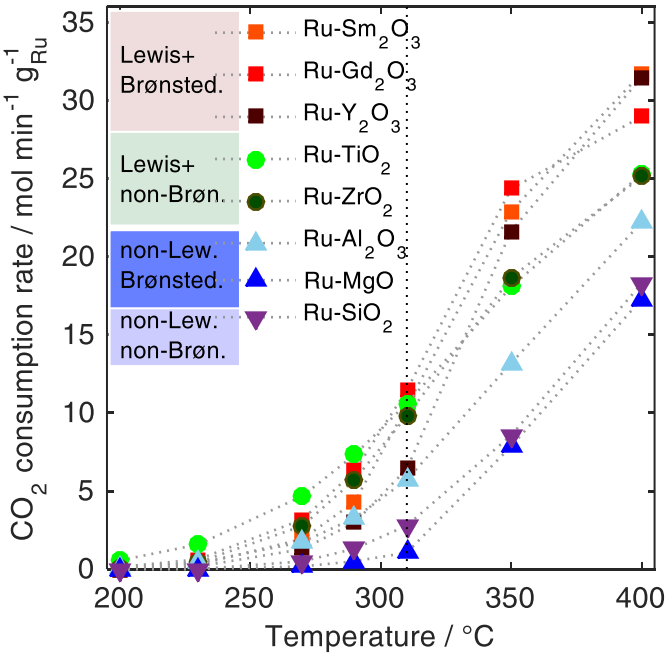

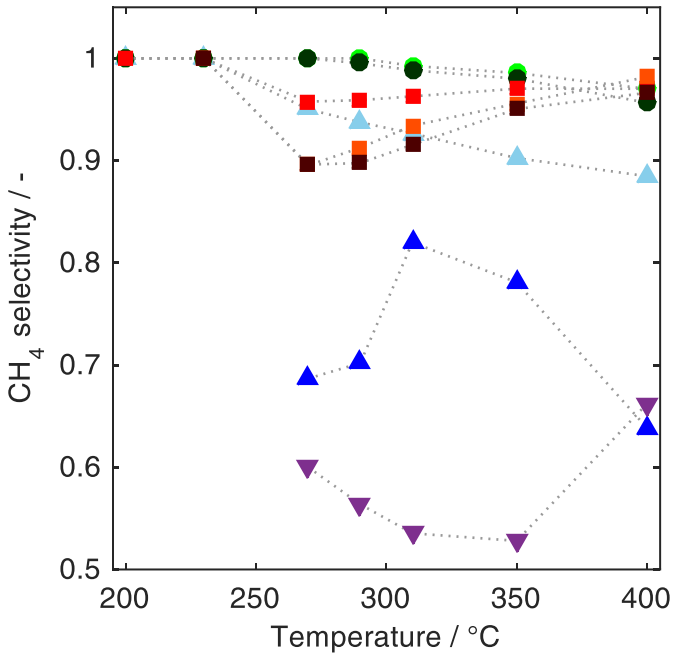

Figure 4-9 **(top) CO_2 conversion rates and (bottom) CH_4 selectivities for all cataysts in the investigated temperature range. Reaction conditions: pressure 1 bar, flow rate 50 mL min^{-1}, 4/1/5 H_2/CO_2/Ar, 50 mg catalyst. The vertical line at 310°C indicates a change regarding the best performing catalysts.**

Ru-ZrO_2 > Ru-TiO_2 > Ru-Al_2O_3 > Ru-MgO > Ru-SiO_2. At these temperatures, the REO supported catalysts yield higher activities and thus outperform the titania and zirconia supported catalysts. This finding suggests an additional promotional effect of Brønsted basic OH groups present on the REO surfaces but not on TiO_2 and ZrO_2. In both temperature regimes, the catalysts supported on oxides without Lewis basic properties (MgO, Al_2O_3 and SiO_2) show lower CO_2 conversions, the highest of which is observed for the Al_2O_3 supported catalyst, which also exhibits the highest methane selectivity.

4.8 *Operando* DRIFTS

To allow a more detailed mechanistic interpretation of the catalytic results and to identify the surface species involved, we carried out temperature-dependent DRIFTS experiments mimicking the reaction conditions. As in some cases species involved in the catalytic reaction and spectator species were difficult to distinguish based on these experiments, we tried to further clarify the situation by additional isothermal experiments at 350 °C.

4.8.1 Over Lewis and Brønsted Basic Supported Catalysts

Representative for the REO supported catalysts, the results of the temperature-dependent measurements for Ru-G_2O_3 are presented in Figure 4-10 (top). Performing the same experiments on the Ru-Sm_2O_3 catalyst essentially yield the identical results as is to be expected

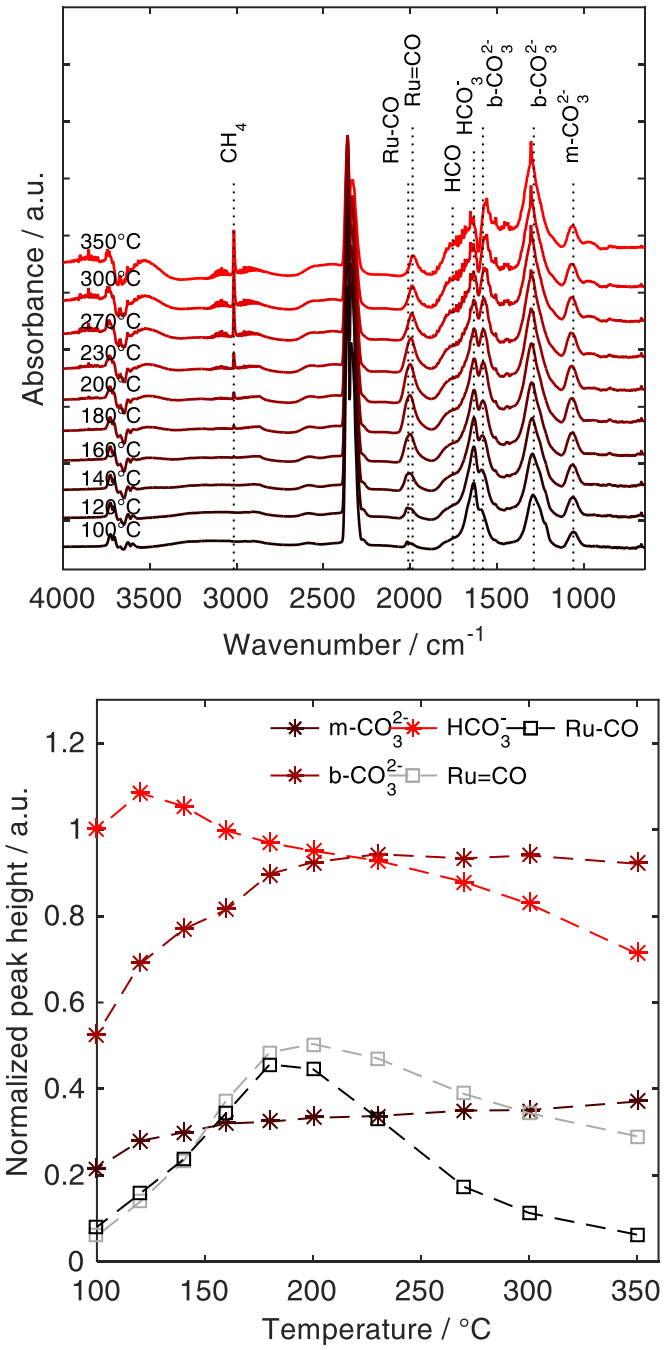

Figure 4-10 (top) Temperature-dependent DRIFTS reaction study on Ru-Gd_2O_3; (bottom) normalized peak height for m-CO_3^{2-}(1061 cm^{-1}), b-CO_3^{2-} (1576 cm^{-1}), HCO_3^- (1633 cm^{-1}), bridge-bonded CO on Ru (Ru=CO, 1990 cm^{-1}) and linearly bound CO on Ru (Ru-CO, 2019 cm^{-1}) as a function of reaction temperature; conditions: 5 vol.% CO_2, 20 vol.% H_2 in He, $\dot{V}_{tot}$=100 mL min^{-1}.

due to the similarities of Gd_2O_3 and Sm_2O_3. The results are therefore not discussed here separately, but can be found in the appendix (Figure B-5 and Figure B-6). After reductive pre-treatment, we exposed the Ru-Gd_2O_3 catalyst to the reaction gases at 100 °C and then stepwise increased the temperature to ultimately 350 °C. By starting well below the expected onset temperature for the reaction, we aimed at capturing adsorbed surface species possibly

involved in the reaction but not detectable at higher temperatures where they undergo fast turnover. Already at 100 °C, CO_2 is dissociatively adsorbed on Ru as indicated by the formation of bridge-bonded CO (Ru=CO, 1990 cm^{-1}) and linearly bound CO on the Ru nanoparticles (Ru-CO, 2019 cm^{-1}).[44, 102, 242] In addition, a variety of bands is observed, which can be assigned to monodentate carbonates (m-CO_3^{2-}, 1060 cm^{-1} and 1508 cm^{-1}),[154, 227, 243] bidentate carbonates (b-CO_3^{2-}, 1288 cm^{-1} and 1583 cm^{-1}), [227] and hydrogen carbonates (HCO_3^-, 1633 cm^{-1}, 1437 cm^{-1} and 3626 cm^{-1}).[227] An additional shoulder at around 1755 cm^{-1} can furthermore be related to a formyl species (HCO).[44, 244] First indications of gaseous CH_4 can be detected already at 140 °C in form of the C-H stretch vibration (3016 cm^{-1}). With increasing temperature also the bending vibrations of gaseous CH_4 at 1304 cm^{-1} evolve.[245, 246]

To gain information about the trends regarding the relative abundance of the various species as a function of temperature, we performed a background correction and normalized the peak heights[1] of all occurring species to the most intense peak at 100 °C originating from HCO_3^- at 1633 cm^{-1} (Figure 4-10 (bottom)). While the intensity of monodentate and bidentate carbonates steadily increases with increasing temperature, HCO_3^- species (1633 cm^{-1}) apparently first accumulate on the surface, before their coverage slowly drops at temperatures above 120 °C. In contrast, linearly and bridge-bonded CO on Ru (2019 cm^{-1}) increasingly form up to 200 °C but then start vanishing at higher temperatures, the stronger bound bridge-bonded CO surviving longer than linearly bound CO. This behaviour confirms that CO is formed as an intermediate on Ru already at low temperatures and is further reduced to CH_4 only at temperatures beyond 200 °C.

The results of the additionally performed isothermal DRIFTS experiments are shown in Figure 4-11. After activation at 400 °C and subsequent flushing with He to remove residual H_2 in the DRIFTS cell, the sample was exposed to 5 vol.% CO_2 in He for 15 min at 350 °C and several spectra were recorded over time (red spectra). Overall, very similar bands as compared to the temperature-dependent measurements were obtained. The characteristic signals for absorbed CO on Ru again indicate dissociative adsorption of CO_2 on the nanoparticles in the absence of H_2. While the peak at 2011 cm^{-1} corresponds to linearly bound CO on Ru, its shoulder at lower wavenumbers can be assigned to bridge-bonded CO.[44, 102, 242] Absorption bands for monodentate carbonates (848, 1060 and 1508 cm^{-1}), bidentate carbonates (848, 1288 and 1581 cm^{-1}) and hydrogen carbonates (848, 1606 and 3626 cm^{-1}) are observed again and prove adsorption of CO_2 on lattice oxygen and oxygen vacancies as well as on OH groups present on the Gd_2O_3 surface.[154, 227, 243] As H_2 was not present in the feed,

[1] Note that, although the peak area would provide a superior measure, the peak height was used to derive information on the relative surface coverage as the spectra proved to be too complex to perform an accurate deconvolution on. Using the peak height instead has been deemed appropriate by several other studies.[44, 199, 316, 317]

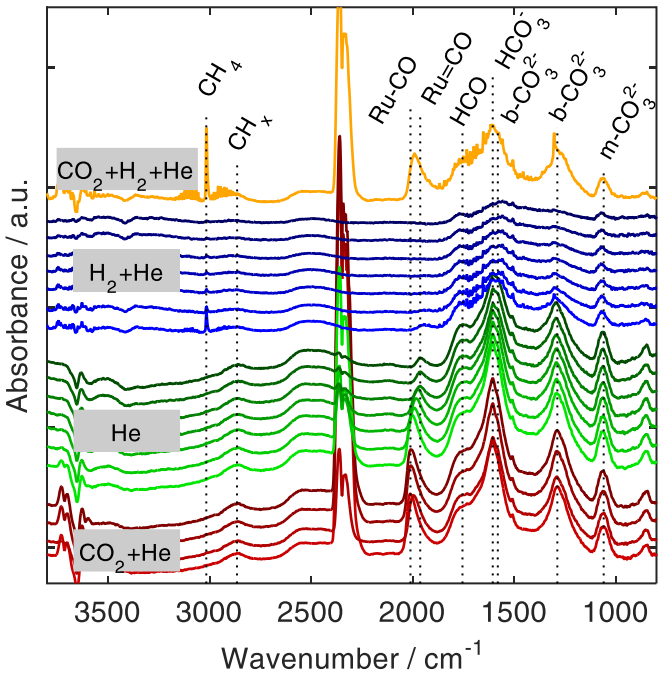

Figure 4-11 Isothermal DRIFTS experiments carried out for Ru-Gd_2O_3 at 350 °C under different gas atmospheres. Red spectra: exposure to 5 vol.% CO_2 in He for 15 min; green spectra: pure He for 20 min; blue spectra: subsequent exposure to 20 vol.% H_2 in He; yellow spectra: exposure to 5 vol.% CO_2 and 20 vol.% H_2 in He, $\dot{V}_{tot}$=100 mL min^{-1}. Temporal evolution of the spectra from lighter to darker colors (bottom to top).

we believe that the formyl species indicated by the band at 1755 cm^{-1} originate from CO that spills over from Ru to the support and reacts with H remaining on Ru nanoparticles after the activation at perimeter sites.[44, 244] When stopping the CO_2 exposure and purging the cell with He for 20 min (green traces), the intensities of the bands of CO adsorbed on Ru decrease rapidly. While the one for linearly bound CO disappears completely after 11 min, a small peak for bridge-bonded CO stays. On the contrary, the band belonging to monodentate carbonates (1060 cm^{-1}) on the support remains constant after stopping the CO_2 exposure, revealing that this species is thermally stable at 350 °C and a spectator species. The features assigned to hydrogen carbonates, bidentate carbonates as well as to formyl species, however, slowly lose intensity over time. If then 20 vol.% H_2 are added to the feed (blue traces), two sharp peaks, representative for gaseous methane, immediately appear at 3016 cm^{-1} and 1304 cm^{-1}, before declining slowly over the next few minutes.[245, 246] Concomitantly, the absorption bands assigned to HCO_3^- and b-CO_3^{2-} drastically decrease, suggesting that they are consumed by reacting further to methane. Upon exposure to the reactant mixture (yellow trace), qualitatively the same spectrum as observed during the temperature-dependent measurements, including significant bands for gaseous CH_4, is observed.

As an explanation for these results, we tentatively propose the occurrence of three reaction mechanisms on the REO supported catalysts having different weight as a function of temperature. All three involve the dissociative adsorption of H_2 on Ru, following the common

notion,[44, 102] but differ with respect to CO_2 adsorption and activation. A support-independent pathway is the dissociative adsorption of CO_2 on Ru leading to CO as an intermediate which is then further reduced. Our temperature-dependent DRIFTS results suggest that this pathway is predominant at temperatures below 300 °C. Due to the presence of the Brønsted basic OH groups and Lewis basic sites on the surface of the REOs, adsorption of CO_2 is additionally possible on the support in form of carbonates. In particular, OH groups leading to hydrogen carbonates and oxygen vacancies giving rise to the formation of bidentate carbonates enable two additional reaction pathways, denoted (1) and (2a) in the introduction, whereas monodentate carbonates formed by CO_2 adsorption on Lewis basic lattice oxygen sites appear to be just spectator species. Both support-related reaction pathways most likely involve formyl species (HCO) formed either by H-assisted abstraction of oxygen from hydrogen carbonates, or by hydrogenation of bidentate carbonates with H. HCO is expected to further transform to CH_4 via intermediates not detected by DRIFTS. The involvement of these carbonates according to mechanisms (1) and (2a), however, is limited to higher temperatures, when considering the CO_2-TPD results. The desorption peak centered at ~300 °C suggests that the carbonates might be too stable in the low temperature region to contribute to the catalytic conversion. Yet, at higher temperatures (above 310 °C), it is likely that the superior performance of the REOs results from the participation of hydrogen carbonates and bidentate carbonates in the reaction, i.e. from the higher overall concentration of adsorbed CO_2 on the surface. These carbonates can be hydrogenated by dissociated hydrogen formed on Ru at perimeter sites or within the range of H surface diffusion.[154, 202] In this context, the rather low specific surface area of the REO supported catalysts is beneficial as it increases the density of basic sites per m^2, and therefore, the amount of adsorbed CO_2 in proximity of the Ru particles as opposed to supports with a higher specific surface area.

4.8.2 Over Lewis but Non-Brønsted Basic Supported Catalysts

At reaction temperatures below 310 °C, the TiO_2 and, to a lesser extent, the ZrO_2 supported catalysts outperform the REO supported ones. An obvious assumption are the Lewis basic oxygen vacancies present on these supports which, in analogy to the REOs, offer additional adsorption sites for CO_2. In contrast to the REOs, however, these carbonates apparently can take part in the catalytic turnover already at lower temperatures according to mechanism (2a). Indeed, it has been reported in the literature that oxygen vacancies on TiO_2 and ZrO_2 are highly reactive with respect to the adsorption and activation of CO_2.[208–211] Although a similar catalytic behaviour is observed for the ZrO_2 and TiO_2 supported catalysts, our DRIFTS data indicate different surface species formed on both supports. Notably, in case of titania, the data do not support the assumption of CO_2 activation on the support at all on first sight.

Ru-ZrO_2

For Ru-ZrO_2, the formation of carbonates can indeed be inferred from the temperature-dependent DRIFTS measurements, presented in Figure 4-12 (top). The spectra reveal that, at 100 °C, CO_2 can adsorb on the ZrO_2 support in the form of monodentate carbonates (1518 and 1488 cm^{-1})[235, 247], formates ($HCOO^-$, 1360, 1377 and 1383 cm^{-1})[235, 248] and bidentate hydrogen carbonates (b-HCO_3^-, 1469 and 1628 cm^{-1}).[221, 236] The feature at 1979 cm^{-1} corresponding to bridge bonded CO on Ru confirms that, in addition and expectedly, the possibility of dissociative CO_2 adsorption on the metal nanoparticles exists. Also the peak at 2063 cm^{-1} (not seen for the REO supports, but also for Al_2O_3 and SiO_2) which is growing with increasing temperature in analogy to the band at 1979 cm^{-1}, can be ascribed to CO adsorbed on Ru.[44, 249] The blue shift, however, points to partially oxidized Ru (Ru^+-CO) that may be present at the particle perimeter due to metal-support interactions.[44] First bands of gaseous CH_4 (3016 cm^{-1}) appear at 230 °C in agreement with the onset of the reaction.[81]

In analogy to the evaluation of the DRIFT spectra in case of the REO supported catalysts, we used the peak intensities to get insight into the abundance of the various surface species as a function of temperature. An increasing background in the carbonate region of the spectra (1700 - 1400 cm^{-1}), hampering the quantitative analysis in case of m-CO_3^{2-} and b-HCO_3^-, rendered a careful background correction necessary. In this way, the data shown in Figure 4-12 (bottom) have been obtained which evidence a clear trend. (Here, all peak heights were normalized to the band of b-HCO_3^- at 1469 cm^{-1} representing the maximum peak at 100 °C in this case.) With increasing temperature, the coverages of all adsorbed species increase first, pass a maximum – yet at different temperatures - and then decrease again. For b-HCO_3^- the maximum occurs at 180 °C, i.e. at the lowest temperature. For $HCOO^-$ the maximum is rather plateau-like and the coverage of this species starts decreasing at around 230 °C. Notably, this temperature corresponds well to the temperature where first indications of CH_4 evolution are visible in the IR spectra. On the contrary, the CO coverage on the Ru nanoparticles starts declining at ~ 300 °C. Thus, unlike to the REO supported system, the DRIFTS results suggest that the reaction on Ru-Zr_2O proceeds via $HCOO^-$ as a reaction intermediate in the low temperature regime. Although the data do not clarify how it is formed two options appear plausible. The species could either originate from b-HCO_3^- (through an unassisted C-O bond cleavage, i.e. elimination of an O atom) or from m-CO_3^{2-} (via a H-assisted C-O cleavage). The latter option, however, is unlikely, since the coverages of m-CO_3^{2-} and $HCOO^-$ on the surface evolve differently as a function of temperature (see Figure 4-12); in particular, the surface coverage of the monodentate carbonates only slightly

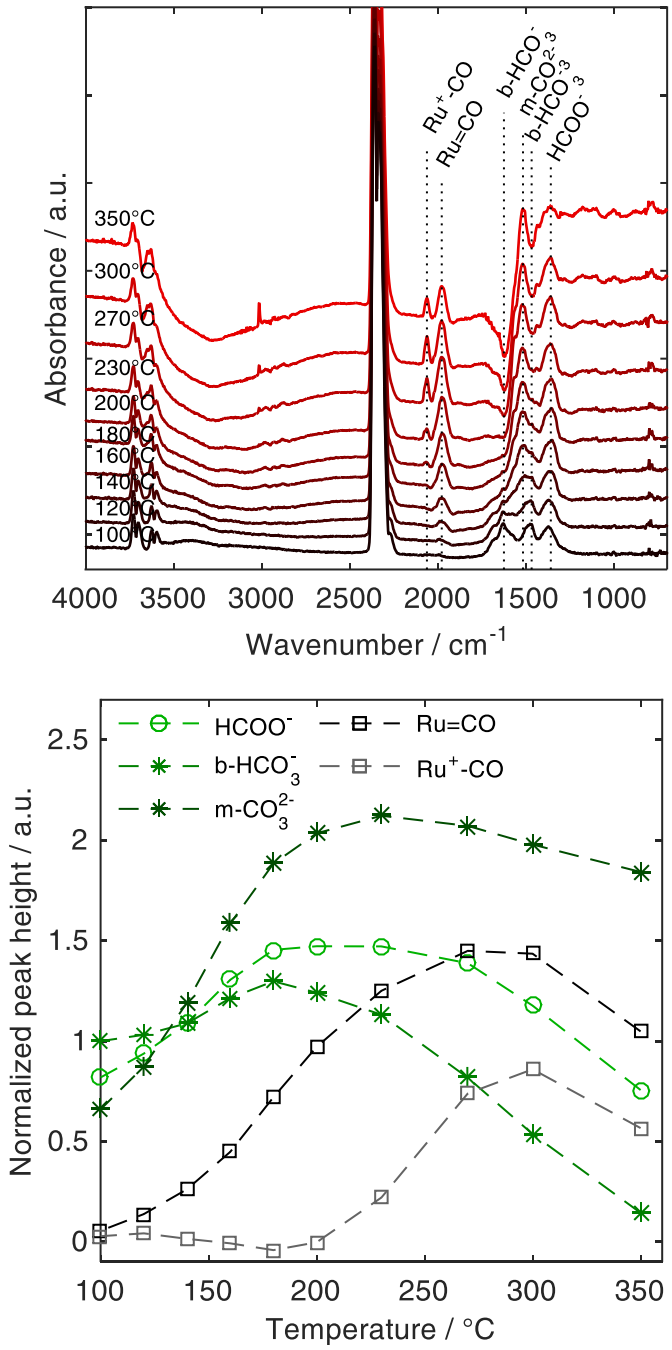

Figure 4-12 (top) Temperature-dependent DRIFTS – reaction study on Ru-ZrO_2, (bottom) normalized peak height for $HCOO^-$(1360 cm^{-1}), b-HCO_3^- (1469 cm^{-1}), m-CO_3^{2-} (1518 cm^{-1}), Ru=CO (1979 cm^{-1}) and Ru^+-CO (2063 cm^{-1}) vs. reaction temperature, conditions: 5 vol.% CO_2, 20 vol.% H_2 in He, $\dot{V}_{tot}$=100 mL min^{-1}.

decreases at temperatures above 230 °C, whereas b-HCO_3^- and $HCOO^-$ more rapidly vanish from the surface. Consequently, b-HCO_3^- species are more probably involved in a reaction pathway taking place on the support in addition to the Ru-based mechanism (mechanism (2a)), though further clarification is needed how b-HCO_3^- is formed on the support.

The isothermal experiments (Figure 4-13), again, allow further mechanistic insight. When, after reductive pre-treatment, the catalyst was exposed to CO_2 and He at 350 °C (red traces), mostly bidentate carbonate, indicated by a pronounced peak at 1560 cm^{-1},[86, 236] formed, confirming the presence and reactivity of oxygen vacancies towards CO_2 on the ZrO_2 support. Bands associated with monodentate carbonates (1506 cm^{-1}) and bidentate hydrogen carbonates (shoulder at 1606 and 1446 cm^{-1}) are present as well, though with only minor intensities.[86, 235, 236, 247] Signals between 1950 and 2100 cm^{-1} confirm the presence of various CO species on Ru (Ru-CO: 2011 cm^{-1} and Ru^{+}-CO: 2079 cm^{-1}).[44, 249] Upon purging with He (green traces), bands associated with monodentate and bidentate carbonates remain fairly stable, whereas b-HCO_3^- fully desorbs until the end of the purging step as can be derived from the vanishing associated signal. However, after exposing the sample to H_2 in He (blue traces), the immediate reappearance of the b-HCO_3^- signal and concurrent disappearance of the band associated with b-CO_3^{2-} strongly indicate that both species are closely intertwined. It can be reasonably assumed that b-CO_3^{2-} species in proximity of a Ru particle are quickly hydrogenated to form b-HCO_3^-. It has to be noted, that the negative peaks between 1900 and 2100 cm^{-1} hint to the presence of minor amounts of adsorbed CO prior to the background collection, probably stemming from the synthesis as protective ligand.[250] Upon the subsequent exposure to the reaction gases (yellow trace), CH_4 evolves with a peak at 3016 cm^{-1}, while now also

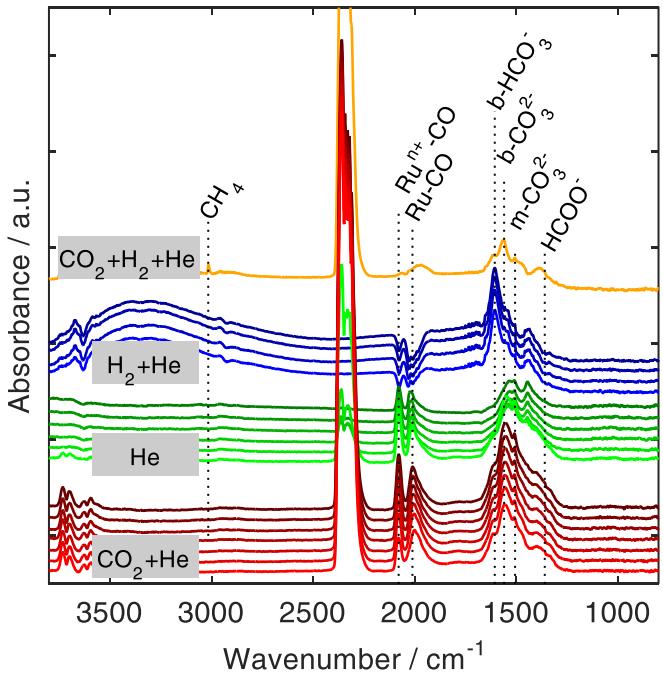

Figure 4-13 Isothermal DRIFTS experiments carried out for Ru-ZrO_2 at 350 °C under different gas atmospheres. Red spectra: exposure to 5 vol.% CO_2 in He for 15 min; green spectra: pure He for 20 min; blue spectra: subsequent exposure to 20 vol.% H_2 in He; yellow spectra: exposure to 5 vol.% CO_2 and 20 vol.% H_2 in He, $\dot{V}_{tot}$=100 mL min^{-1}.Temporal evolution of the spectra from lighter to darker colors (bottom to top).

the previously absent band for $HCOO^-$ appears at 1360 cm^{-1}. In contrast to the temperature-dependent measurements, bands associated with b-CO_3^{2-} (1560 cm^{-1}), which previously could not be detected reliably due to background instabilities in that specific region, are clearly visible now. Hence, mechanistically the reaction appears to proceed through CO_2 activation on Lewis basic oxygen vacancies as bidentate carbonates. Species located in proximity of a Ru particle undergo further hydrogenation to bidentate hydrogen carbonates and, then, formate species. This pathway seems to govern at low temperatures, until around 270 °C the Ru-based mechanism sets in as indicated by the decreasing CO coverage on Ru. Interestingly, this temperature is higher as observed for the REO supported catalysts, where the DRIFT spectra indicate a contribution of this pathway already at 180 °C. Notably, it seems a general trend that the onset temperature of the Ru-based mechanism is support dependent, as revealed when comparing the temperatures at which Ru-CO species are first detected (see Figures showing the temperature-dependent DRIFTS results 4-10, 4-12, 4-14, 4-16, 4-18 and 4-19). As the Ru particles are identical in all cases (same size), the different behavior points to support-specific metal-support interactions (in analogy to (2b)), changing the electronic structure of the Ru deposits and in turn the CO binding strength.

Ru-TiO_2

Although TiO_2 is also an oxide exhibiting Lewis basic oxygen vacancies, Ru supported on this support shows a distinctly different adsorption behavior than Ru-ZrO_2 indicating a different mechanistic scenario. The temperature-dependent DRIFT spectra acquired for this catalyst (Figure 4-14) show only a few and very weakly pronounced features. In analogy to the REO supported catalysts, CO_2 adsorbs dissociatively on Ru already at 100 °C as indicated by the absorbance band at 1995 cm^{-1} attributable to a CO species on Ru. In analogy to ZrO_2, also a Ru^+-CO species (due to partially oxidized Ru) is present on the surface as can be concluded from the band at 2083 cm^{-1}.[81] In contrast to zirconia and the REOs, no pronounced bands corresponding to carbonate species are observed. Moreover, the spectra provide no evidence that any species accumulates on the catalyst surface with increasing temperature. Instead, also the weak features of CO adsorbed on Ru completely disappear at around 230 °C, whereas the bands of gaseous CH_4 appear already at 160 °C.

As in the case of the other catalysts, we carried out isothermal experiments (Figure 4-15) to gain further information, but conducted them in a slightly different way (as the same approach did not lead to clear conclusions (see Figure B-7 in the appendix). In a first step, CO_2 (in He) was admitted to the DRIFTS cell while keeping the sample at 350 °C. As a consequence, the two peaks assignable to linearly bound CO on Ru and CO on Ru^+ emerged in the spectrum, in agreement with the results discussed above. In addition, a new, yet only weakly pronounced peak at 1060 cm^{-1} appears, pointing to m-CO_3^{2-} formed on the TiO_2 sup-

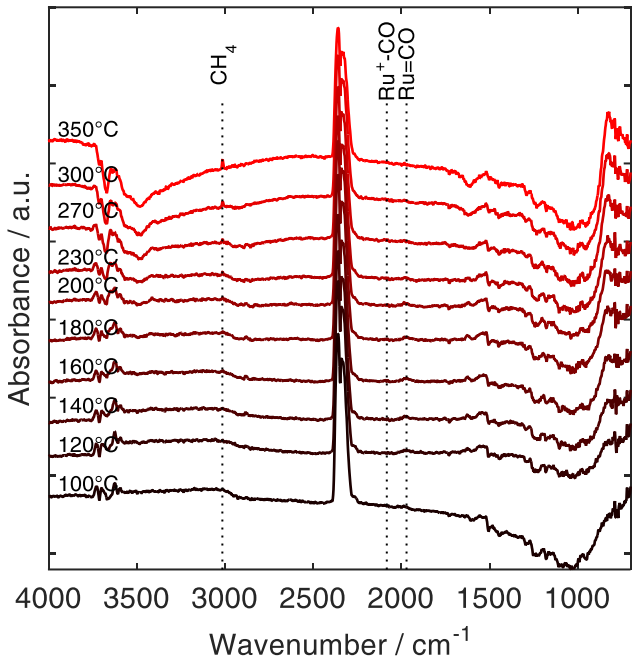

Figure 4-14 **Temperature-dependent DRIFTS – reaction study on Ru-TiO_2; conditions: 5 vol.% CO_2, 20 vol.% H_2 in He, $\dot{V}_{tot}$=100 mL min^{-1}.**

port in small amounts under these conditions. Upon additional admission of H_2, formation of gaseous CH_4 is immediately observed, as discernible from the band at 3016 cm^{-1}, whereas the peaks associated with adsorbed CO on Ru disappear. Even though CO_2 was constantly

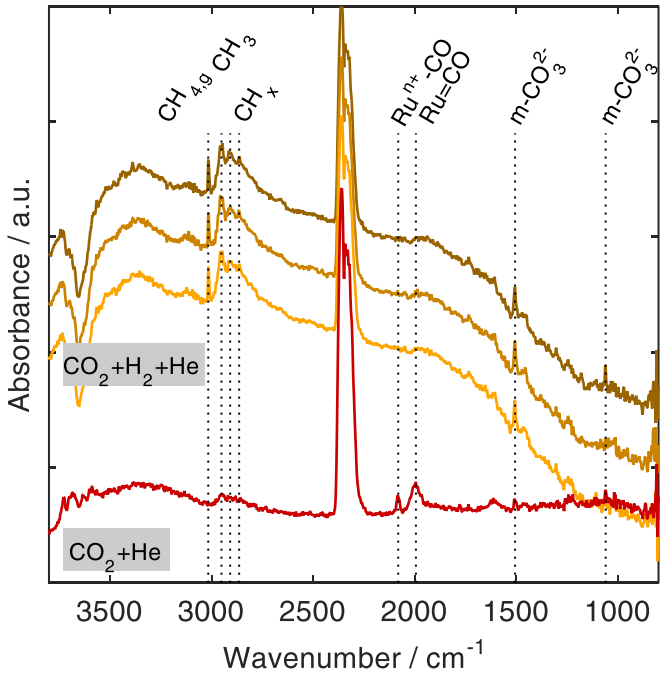

Figure 4-15 **Isothermal DRIFTS - reaction study on Ru-TiO_2 at 350 °C, red spectra: after exposing the catalyst to 5% CO_2 in He for 15 min; yellow spectra: in 5 vol.% CO_2, 20 vol.% H_2 and 75 vol.% He, $\dot{V}_{tot}$=100 mL min^{-1}.**

fed to the DRIFTS cell and an ongoing CH_4 evolution was observed, no peaks due to adsorbed CO on Ru came up anymore, indicating a rapid conversion of these species. On the contrary, m-CO_3^{2-} accumulates on the surface now as can be concluded from the increase of the corresponding peaks (1060 and 1506 cm^{-1}).[44] Furthermore, a peak triplet at 2951, 2908 and 2864 cm^{-1} is observed in the spectra that points to the formation of adsorbed CH_x species.

In summary, our results for Ru-TiO_2 suggest that the reaction proceeds basically only on Ru via CO formed upon dissociative adsorption of CO_2 on the Ru nanoparticles. Even though monodentate carbonates can obviously form on the titania support, their stability in the presence of H_2 renders an active role in the reaction unlikely. Although this conclusion is in agreement with Marwood et al.[251], who also reported that CO on Ru is the main intermediate on this catalyst, it raises the question how the high activity of this system can be explained. The detection of CO on Ru already at low temperatures is a hint that the reaction on metal nanoparticles runs more efficiently for TiO_2 than for the other supports so that activities similar to ZrO_2 (and the REOs) can be achieved even in the absence of subsidiary support-related reaction pathways. As detailed in the introductory remarks of this chapter, such a promotional effect can result from an indirect participation of oxygen vacancies that are clearly observed in the Raman spectra of this catalyst (see Chapter 4.6). In the literature, such an promotion has been attributed to an electronic effect (mechanism 2b) repressing CO poisoning and thus leading to a more favourable ratio of H/CO on the surface of the Ru nanoparticles.[128, 217]

4.8.3 Over Non-Lewis but Brønsted Basic Supported Catalysts

In contrast to the Lewis basic supported catalyst, the non-Lewis but Brønsted basic Ru-Al_2O_3 and Ru-MgO catalysts yield a significantly lower reactivity and selectivity, which, assumedly, can be attributed to the absence of Lewis basic oxygen vacancies on these catalysts. Our DRIFTS data on the Al_2O_3 and MgO supported catalyst support the notion that the Brønsted basic centers on the support provide additional CO_2 adsorption capacities; yet, conversion of the adsorbed species appears to be slow.

Ru-Al_2O_3

The results of temperature-dependent measurements on the Ru-Al_2O_3 catalyst are shown in Figure 4-16. After activation and upon exposition to the reaction gases at 100 °C, only two features of hydrogen carbonates (1657 and 1440 cm^{-1}) are formed.[249, 252] As these species are formed by CO_2 adsorption on hydroxyl groups, this, hence, justifies the classification of Al_2O_3 as an oxide with Brønsted basic properties. As for the Lewis basic supported catalysts, the possibility for dissociative CO_2 adsorption on Ru is given as is indicated by the evolving

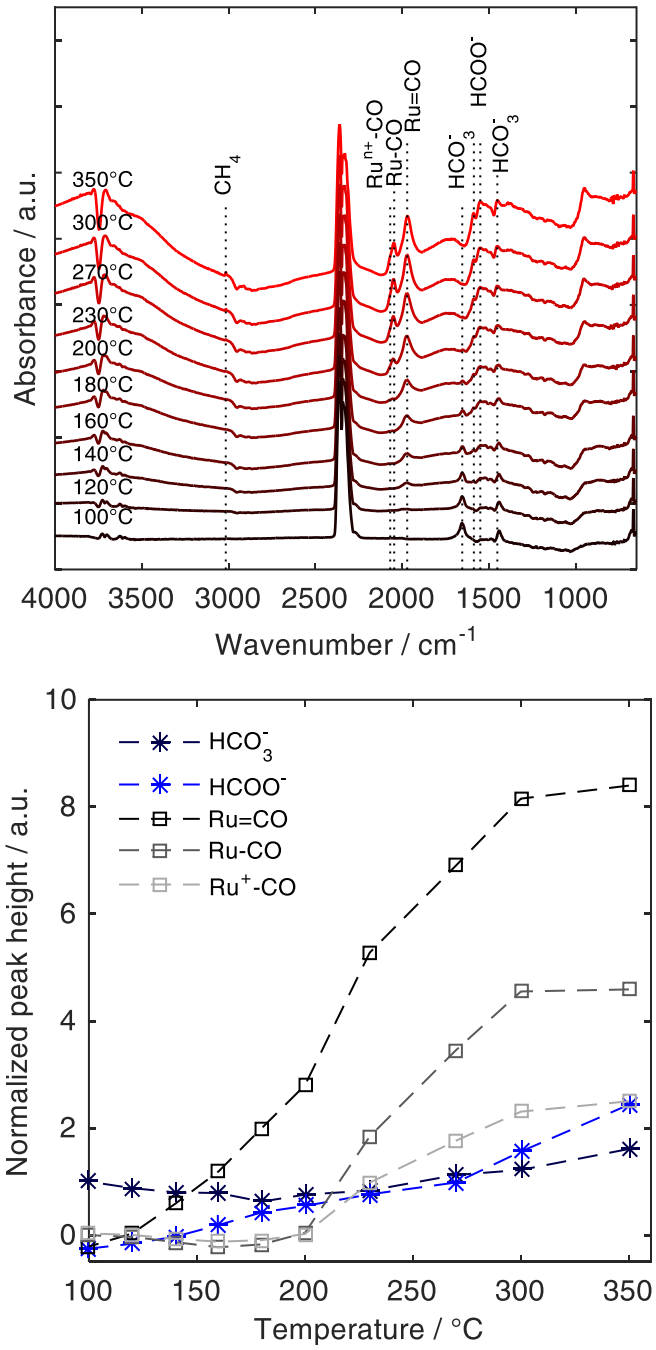

Figure 4-16 (top) Temperature-dependent DRIFTS – reaction study on **Ru-Al_2O_3**, (bottom) normalized peak height for HCO_3^- (1441 cm^{-1}), $HCOO^-$ (1587 cm^{-1}), Ru=CO (1971 cm^{-1}), Ru-CO (2046 cm^{-1}) and Ru^+-CO (2069 cm^{-1}); conditions: 5 vol.% CO_2, 20 vol.% H_2 in He, $\dot{V}_{tot}$=100 mL min^{-1}.

band for multiply bound CO on Ru at 1971 cm^{-1}; however, in contrast to the supports with Lewis basic oxygen vacancies, this seems to require a higher activation energy as the features appear at elevated temperatures only.[44, 249] Further increasing the temperature also linearly adsorbed CO on Ru and CO adsorbed on interfacial Ru^+ sites form as can be derived by the appearance of the associated feature at 2046 cm^{-1} and a shoulder at 2069 cm^{-1}, respectively.[44,

[249] Additionally, formates reveal themselves by a double peak at 1587 and 1550 cm^{-1},[44, 253] whereas, first indications for gaseous CH_4 (3016 cm^{-1}) are detected at 270 °C. After a careful background correction, the peak heights were normalized to the initial intensity of the feature assigned to HCO_3^- at 1441 cm^{-1}. Hydrogen carbonates are present in abundance at 100 °C, but decline steadily with rising temperatures, whereas concurrently, the surface coverage with formates increases. Interestingly, CO species on Ru steadily accumulate before reaching a plateau at temperatures above 300 °C.

Based on the temperature-dependent DRIFTS data, the origin of formates as well as the formation mechanism of the adsorbed CO species remains unclear and require additional isothermal experiments (Figure 4-17). Upon admission of CO_2 and He (red traces), features for Ru=CO and Ru^+-CO are detected at 1998 cm^{-1} and 2069 cm^{-1}, respectively,[44, 249] therefore, confirming dissociative CO_2 adsorption on Ru as observed on the other catalyst. The peak at 2046 cm^{-1}, particularly under consideration of the additional shoulder at 1957 cm^{-1}, is difficult to assign unambiguously and has been reported to contain contributions of linearly adsorbed CO on Ru as well as geminal di-carbonyls ($Ru(CO)_2$) on low coordinated Ru sites.[249] According to the literature, geminal di-carbonyls are thermally stable and not reactive towards methane.[249] On the support, no peaks associated with formate species form, but two bands at 1643 and 1444 cm^{-1} indicate the presence of HCO_3^-. Additionally, a small peak at

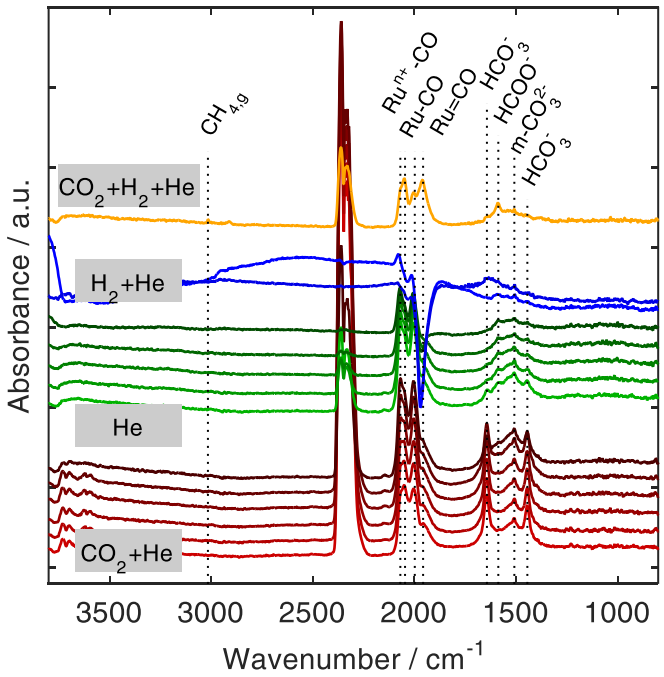

Figure 4-17 **Isothermal DRIFTS experiments carried out for Ru-Al_2O_3 at 350 °C under different gas atmospheres. Red spectra: exposure to 5 vol.% CO_2 in He for 15 min; green spectra: pure He for 20 min; blue spectra: subsequent exposure to 20 vol.% H_2 in He; yellow spectra: exposure to 5 vol.% CO_2 and 20 vol.% H_2 in He, $\dot{V}_{tot}$=100 mL min^{-1}. Temporal evolution of the spectra from lighter to darker colors (bottom to top).**

1508 cm^{-1} is attributed to the presence of small amounts of m-CO_3^{2-}.[252] During the subsequent purging step in He, the support is depleted as the bands for carbonate species quickly disappear, whereas the slow decline of the features in the CO region point towards a high thermal stability of the adsorbed CO species. However, in the presence of H_2 (blue traces) and except for the feature attributed to Ru^+-CO, the peaks immediately disappear and instead a pronounced negative peak arises, that hints to some residual CO prior to the background collection, possibly stemming from the synthesis. Upon the subsequent simultaneous exposure of the catalyst to the reaction gases (yellow traces), CH_4 forms immediately with a small peak at 3016 cm^{-1}. Also, the so-far absent band for $HCOO^-$ (1587 cm^{-1}) occurs, whereas no pronounced features attributable to HCO_3^- are observed. As the formation of HCO_3^- is clearly evidenced in the preceding steps, the absence of the corresponding features indicates a rapid conversion to $HCOO^-$. In the CO region of the DRIFTS spectra, the peaks attributed to Ru^+-CO and Ru=CO as well as Ru-CO and $Ru(CO)_2$ reappear.

Unfortunately, based on the data itself no clear distinction between spectator and intermediary species can be made. In accordance with the literature, it is confirmed that CO_2 adsorbs in a dissociative manner on Ru as well on OH groups on the support to form hydrogen carbonates, but their reactivity towards CH_4 remains unclear (mechanism 1).[44, 249] Drawing on the relative temperature-dependent evolution and the isothermal experiments, it is likely that HCO_3^- species in proximity of Ru particles react with adsorbed H from the metal to formates. Marwood et al.[251] and Solymosi et al.[254] concluded that due to the concentration gradient most formates migrate from the metal-support perimeter to the support, where they cannot undergo further reduction, but slowly accumulate. Consequently, only part of the formate species can be considered as active intermediates. However, such a distinction cannot be made by our means and requires more sophisticated approaches involving labelled isotopic experiments. We confirmed the presence of the support independent CO mechanism; however, consumption of the adsorbed CO species appears to be slow and leads to a progressive accumulation of CO species on Ru with increasing temperature – a trend we did not observe on the Lewis basic catalysts (REOs, TiO_2 and ZrO_2) – underlining the effect of the support on the Ru particle itself (mechanism 2b) that seems to be absent here. This is also reflected in the required higher activation energy for CO_2 dissociation on Ru which can reasonably only be explained by less favorable metal-support interactions.

Ru-MgO

In this study also classified as an oxide with Brønsted basic properties but without the ability to form Lewis basic oxygen vacancies, the temperature-dependent DRIFTS results on Ru-MgO point to a similar mechanistic scenario as observed over the Ru-Al_2O_3 catalyst (Figure 4-18). Upon exposure of the activated catalyst to the reactive atmosphere at 100 °C,

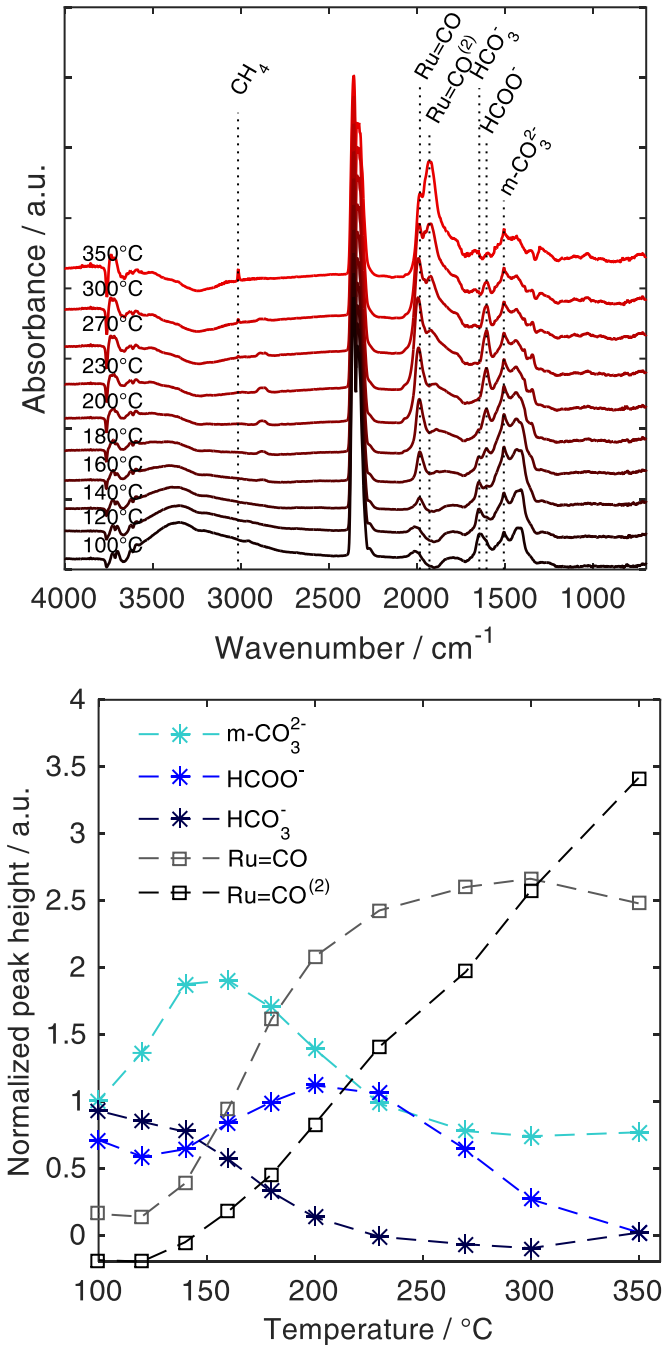

Figure 4-18 (top) Temperature-dependent DRIFTS – reaction study on **Ru-MgO**, (bottom) normalized peak height for m-CO_3^{2-} (1508 cm^{-1}), $HCOO^-$ (1606 cm^{-1}), HCO_3^- (1647 cm^{-1}), Ru=$CO^{(2)}$ (1930 cm^{-1}) and Ru=CO (1984 cm^{-1}); conditions: 5 vol.% CO_2, 20 vol.% H_2 in He, $\dot{V}_{tot}$=100 mL min^{-1}.

bands for HCO_3^- (1647 and 1410 cm^{-1}) appear, confirming the expected Brønsted basicity of MgO and the adsorption of CO_2 on such sites.[157, 255] A rather sharp peak at 1508 cm^{-1} indicates CO_2 adsorption on lattice O^{2-} as monodentate carbonate, which also contributes to the peak at 1410 cm^{-1}.[255, 256] Additionally, a small shoulder at 1606 cm^{-1} can be related to the presence of small amounts of formates.[257] In the CO region of the spectra, a broad but clearly visible

peak for bridge-bonded CO on Ru evolves at 2009 cm^{-1} shifting to lower wavenumbers (1984 cm^{-1}) while also becoming more pronounced. An additional band at 1930 cm^{-1}, which can also be assigned to a CO species on Ru, probably in a bridged or multiply bound configuration (Ru=$CO^{(2)}$), occurs at 180 °C and grows rapidly in height with increasing temperatures, while indications for methane can be detected at 270 °C. Further, secondary formate bands (1339 and 1389 cm^{-1}) start appearing.[257]

The analysis of the relative peak intensities (normalized in respect to the intensity of m-CO_3^{2-} at 1508 cm^{-1} representing the maximum peak height at 100 °C), reveals that with increasing temperature the surface coverage with HCO_3^- steadily declines, whereas it passes through a maximum at around 160 and 200 °C for m-CO_3^{2-} and $HCOO^-$, respectively. Notably, at temperatures above 230 °C the surface is depleted quickly of $HCOO^-$ which corresponds well to the onset temperature of the reaction and consequently points towards an active involvement of $HCOO^-$ towards methane. As discussed for the previous catalysts, monodentate carbonates and hydrogen carbonates are both plausible precursors for formate formation. However, the presence of significant amounts of formates at 100 °C already and its initial development of the surface coverage in relation to the coverage with HCO_3^- and m-CO_3^{2-}, rather indicates that HCO_3^- is the more reactive specie. Yet, this does not rule out that monodentate carbonates also react to formates, though this seems to occur at higher temperatures. On the contrary, CO species on Ru accumulate rapidly. Their consumption appears to set in only at temperatures above 300 °C, in agreement with the observations on the Ru-Al_2O_3 catalyst. The required temperature is in both cases significantly higher than for the catalysts exposing Lewis basic oxygen vacancies. As the results appear conclusive and due to the poor performance of the Ru-MgO catalyst, no isothermal DRIFTS experiments were carried out.

Consequently, we tentatively propose that the reaction proceeds mainly via a support-assisted pathway, in which CO_2, adsorbed as hydrogen carbonate and monodentate carbonates in vicinity of a Ru particle, is subsequently hydrogenated through formate to ultimately yield methane (mechanism 1). This mechanism appears to set in at significantly lower temperatures than the support independent pathway that seems to be suppressed due to the accumulation of adsorbed CO on Ru.

4.8.4 Over Non-Lewis and Non-Brønsted Basic Supported Catalysts (Ru-SiO_2)

In terms of the methane formation rate, the SiO_2 supported catalyst performed the worst in our study. The obvious explanation would be the absence of Lewis and Brønsted basic sites, such that no promoting support effect would occur. This assumption seems to be confirmed by the temperature-dependent DRIFTS reaction study (Figure 4-19). No absorption

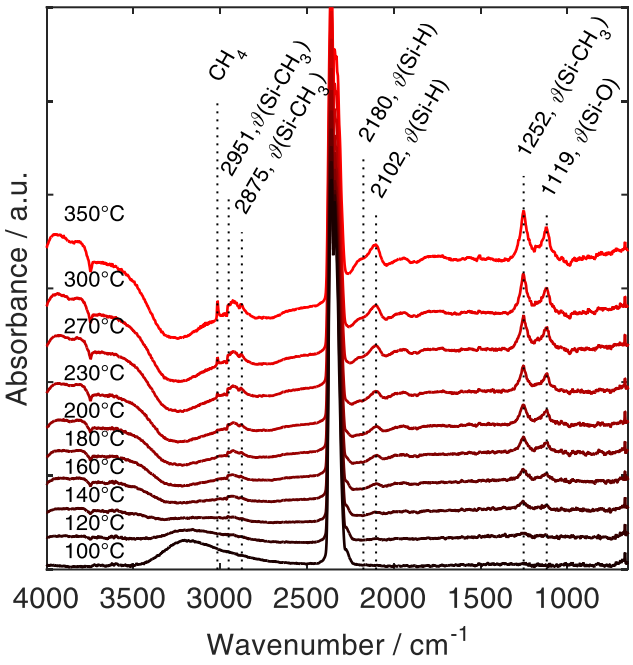

Figure 4-19 Temperature-dependent DRIFTS – reaction study on Ru-SiO_2; conditions: 5 vol.% CO_2, 20 vol.% H_2 in He, $\dot{V}_{tot}$=100 mL min^{-1}.

bands, except for gaseous CO_2, are detected until 140 °C, where features at 1119, 1252, 2102 cm^{-1} evolve that grow with increasing temperature and cannot be attributed to any CO_2 adsorption products. The absorbance bands at 1119 cm^{-1}, 2102 cm^{-1} and the evolving shoulder at ~2180 cm^{-1} can be attributed to the vibrational modes of ν(Si-O), ν(Si-H) and ν(Si-H), respectively, of a silica hydride species.[258, 259] Unfortunately, the latter two bands potentially superimpose adsorption features for CO on Ru, which would be expected in the same range. The peak at 1252 cm^{-1} in combination with broad feature between 2875 and 2951 cm^{-1} can be attributed to the formation of CH_3 groups on Si centers.[259, 260] Despite the absence of any unambiguous indications for CO_2 adsorption/activation on the Ru-SiO_2 catalyst, its activity is clearly evidenced at temperatures above 200 °C by the absorbance band for gaseous methane at 3016 cm^{-1}. The isothermal reaction study expectedly does not show any absorbance bands either and is therefore not discussed here, but attached in the appendix (Figure B-8).

Mechanistically, none of the observed bands are related to the adsorption of CO_2 on the support, therefore ruling out any of the proposed support-assisted pathways (1), (2a) and (2b). Consequently, the reaction most likely proceeds via the support independent pathway through dissociative CO_2 adsorption on Ru, though definite evidence is scarce.

4.9 Interim Conclusions

In this chapter, we investigated the support effect, more specifically the influence of the support's Lewis and Brønsted basicity, on the Ru catalyzed CO_2 methanation. By using a

building block approach, colloidal Ru nanoparticles with a narrow size distribution were prepared (1 nm) and deposited on eight different supports. In this way, an influence of the Ru particle size on the catalytic performance could be excluded and differences in activity and CH_4 yield observed for the investigated catalysts directly linked to differences in the basicity of the chosen supports. To cover different types of basic surface sites, four categories of oxides were considered in the study: REOs exhibiting Brønsted and Lewis basic sites, Al_2O_3 and MgO as representatives of Brønsted but non-Lewis basic supports, TiO_2 and ZrO_2 being non-Brønsted but Lewis basic and SiO_2 as an example of a support which shows neither Brønsted nor Lewis basic properties. The strength and density of Lewis and Brønsted basic sites was investigated by combining CO_2-TPD with DRIFTS experiments.

Our results for the REO supports as well as for ZrO_2 and TiO_2 clearly prove a beneficial effect of oxygen vacancies. Acting as Lewis basic adsorption sites for CO_2, they open new support-related mechanistic pathways for the methanation reaction in addition to the pathway via dissociative adsorption of CO_2 on the Ru nanoparticles available on all supports. However, they also increase the reactivity indirectly by an electronic effect that affects the surface coverage of the Ru nanoparticle with adsorbed CO species leading to more favorable CO/H ratios. These catalysts thus outperform those supported on Al_2O_3, MgO and SiO_2 in the whole investigated temperature range from 200 °C to 400 °C. The leading role with respect to CO_2 conversion and CH_4 formation rate, however, changes around 310 °C. Below 310 °C, Ru supported on TiO_2 and ZrO_2 perform best, whereas at higher temperatures the REO supported catalysts show higher activities.

Temperature-dependent and isothermal DRIFTS under reactive atmosphere in combination with CO_2-TPD measurements indicate that in case of Ru-ZrO_2 oxygen vacancies enable adsorption and activation of CO_2 in the form of bidentate carbonates that are quickly hydrogenated to bidentate hydrogen carbonates and formate species. For the REO supports, the data revealed that not only Lewis basic oxygen vacancies but also Brønsted basic OH groups serve as adsorption sites for CO_2. The resulting bidentate and hydrogen carbonates start contributing to the catalytic turn-over at temperatures above 300 °C, in agreement with the temperature range where the REO supported catalysts start to perform better than titania or zirconia supported ones. At lower reaction temperatures, however, these carbonates are too stable rendering their involvement in the reaction unlikely. Here, adsorption and activation of CO_2 and all following catalytic steps appear to take place on the Ru nanoparticles alone following the common pathway via dissociative CO_2 adsorption just on the metal. Interestingly, in case of Ru-TiO_2 the DRIFT studies under reaction atmosphere provided no indications for CO_2 adsorbed on the TiO_2 support (in the form of bidentate carbonates) and its involvement in the reaction even though Raman spectroscopy clearly revealed the abundant presence of oxygen vacancies. In view of the high activity of this catalyst in particular

at lower temperatures, it is likely that the oxygen vacancies promote the activity indirectly via an electronic metal-support interaction which leads to a more favourable CO/H ratio on the Ru nanoparticle as a result of a weaker bonding of CO.

According to this study, an improvement of the activity and selectivity of metal supported CO_2 methanation catalysts supports exhibiting surface basicity should be chosen. Depending on the intended reaction temperature, Lewis basic oxygen vacancies and Brønsted basic OH groups on the surface can contribute differently according to the strength of these sites. At higher temperatures, REO supports turned out to be particularly interesting supports outperforming other supports with basic surface sites.

5

An Unconventional Catalyst System – Highly Active Ni-Sm_2O_3 Catalysts

Parts of this chapter have been published in J. Ilsemann, A. Sonström, T. Gesing, R. Anwander and M. Bäumer, "Highly Active Sm_2O_3-Ni Xerogel catalysts for CO_2 methanation", *ChemCatChem*, 2019, 11, 6, 1732-1741 and are adopted here verbatim (with permission by Wiley).

5.1 What to Expect from this Chapter

In the previous chapter, the imperative nature of Lewis and Brønsted basic sites on the catalyst support was demonstrated. Yet, the approach via colloidal Ru nanoparticles is more suited for scientific model studies and not necessarily applicable for industrial applications. However, it is believed that the preceding study offers guidelines for the future preparation of highly active catalyst systems, which shall be demonstrated here. Rare earth metal oxides, such as Sm_2O_3, were shown to be particularly promising catalyst supports for CO_2 methanation and are therefore chosen for further studies. Instead of Ru, Ni was applied as active component due to its similar reactivity and CH_4 selectivity while coming at a significantly lower price and of high importance owing to the often reported metal loadings of 20 wt.%

and higher.[30–33, 37, 261] The synthesis method reported in Chapter 3.2.2 allows the incorporation of additional components during the synthesis, and thus, the simple fabrication of Sm_2O_3-Ni catalysts by a one-pot approach was achieved. Materials synthesized by this method are used to test if the design criteria developed in the preceding chapter can be applied to synthesize competitive systems. Specifically, the scope of this chapter is threefold:

1. It is likely that the mechanistic findings from the previous chapter, i.e. CO_2 adsorption and activation on the REO support, apply to Ni based catalysts as well, and consequently a bifunctionality of system can be assumed. If the catalyst is indeed bifunctional, an optimal Ni loading should exist which balances CO_2 adsorption sites on the Ni-Sm_2O_3 perimeter and H_2 dissociation sites on metallic Ni particles, leading to a maximized catalytic performance. This Ni-to-Sm_2O_3 ratio must be found.
2. Often one-pot methods can lead to the encapsulation of the active component by the support material making it inaccessible for the reactants and thus less reactive than impregnated samples. By comparing the one-pot xerogel catalysts with a catalyst prepared by impregnating pristine Sm_2O_3 with the identical Ni loading, insights into the effect of the preparation method can be gained.
3. The potential of this catalyst can only be evaluated if the performance is put into context with reference catalysts. To this end, the catalytic performance is compared with an industrial methanation catalyst (Ni-Al_2O_3) and published reference kinetics of a well-known Ni-Al_2O_3 system.[31]

Note that this chapter does not address questions of catalyst stability and only focuses on the characterization of the as-prepared catalysts as well as the reactivity data. The time-on-stream behavior of the catalyst is topic of the subsequent Chapter 6.

5.2 Catalysts

Pure samaria and Samaria/nickel xerogels with 4, 11, 33, 39, 64 and 89 wt.% Ni were synthesized according to the PO-CA method described in Chapter 3.2.2. The specific amounts used are summarized in Table C-1 (appendix).

For the reference catalyst prepared by incipient wetness impregnation (denoted IWI), the pristine Sm_2O_3 support was synthesized according to the procedure described above. After calcination, the powders were, due to the small pore volume, impregnated three times with an oversaturated aqueous Ni solution. Therefore, $Ni(NO_3)_2 \cdot 6\ H_2O$ was dissolved in deionized water while continuously stirring the solution at 60 °C overnight. After each impregnation step, the powder was dried at 120 °C for 2 hours in air. Then the powder was calcined again at 600 °C for 1 hour after the last impregnation step.

To benchmark the catalytic performance, an industrial methanation catalyst (9 wt.% Ni-Al_2O_3) is used. However, the manufacturer does not want to be disclosed. An overview on the provided characterizations as well as some additional characterizations performed in-house are attached in Chapter C.6.

5.3 Characterizations

All catalysts have been fully characterized by means of XRD, TEM, N_2 physisorption and H_2-TPR. The details on the procedures are given in A.2 and B.1 in the appendix.

5.3.1 Structural Characterizations by XRD

The samples were analyzed by powder XRD to quantitatively evaluate their phases and to determine their crystallite sizes. The acquired X-ray diffraction pattern are shown in Figure 5-1. The patterns were analyzed by Rietveld refinement using the structural models for Ni (space group $Fm\bar{3}m$), NiO (space group $Fm\bar{3}m$) and Sm_2O_3 (space groups $I2_13$ and $Ia\bar{3}$). Representative results for the refinement of 39 wt.% Ni-Sm_2O_3 are depicted in Figure 5-2.

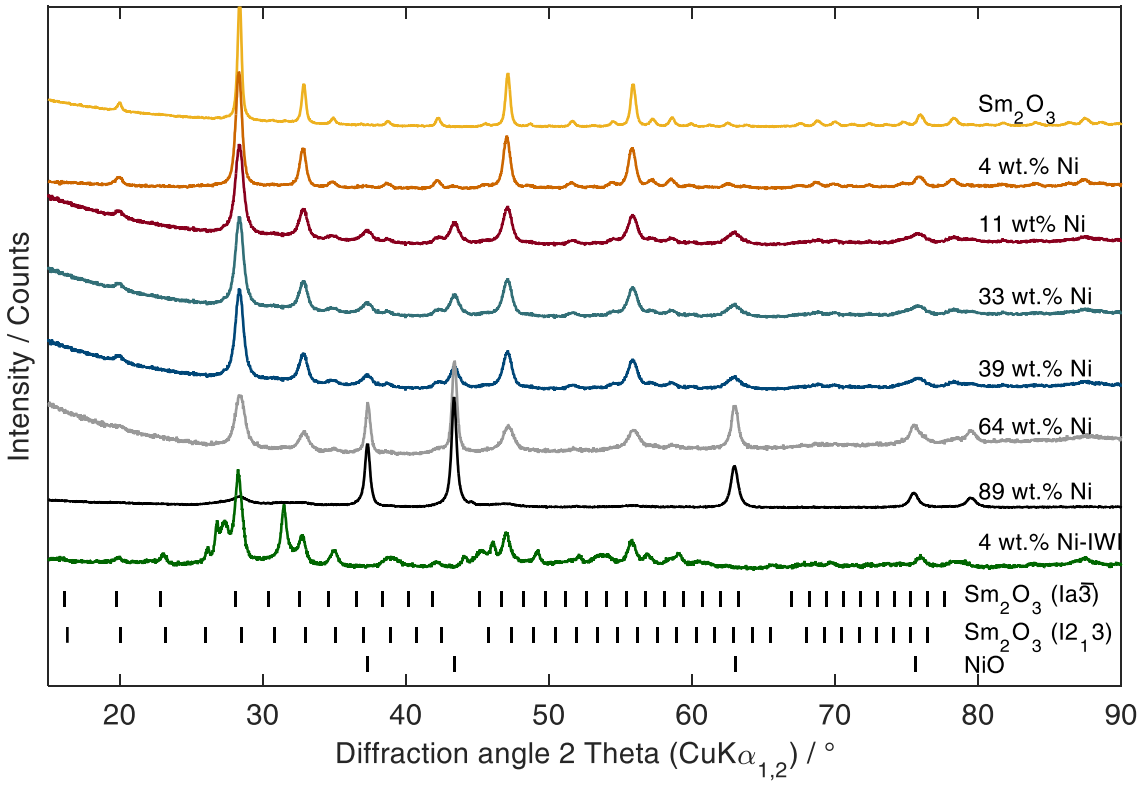

Figure 5-1 XRD pattern of the prepared xerogels. The tick marks below the X-ray diffraction pattern indicate the possible reflection positions for cubic Sm_2O_3 with the space groups **$Ia\bar{3}$** and **$I2_13$** and cubic NiO.

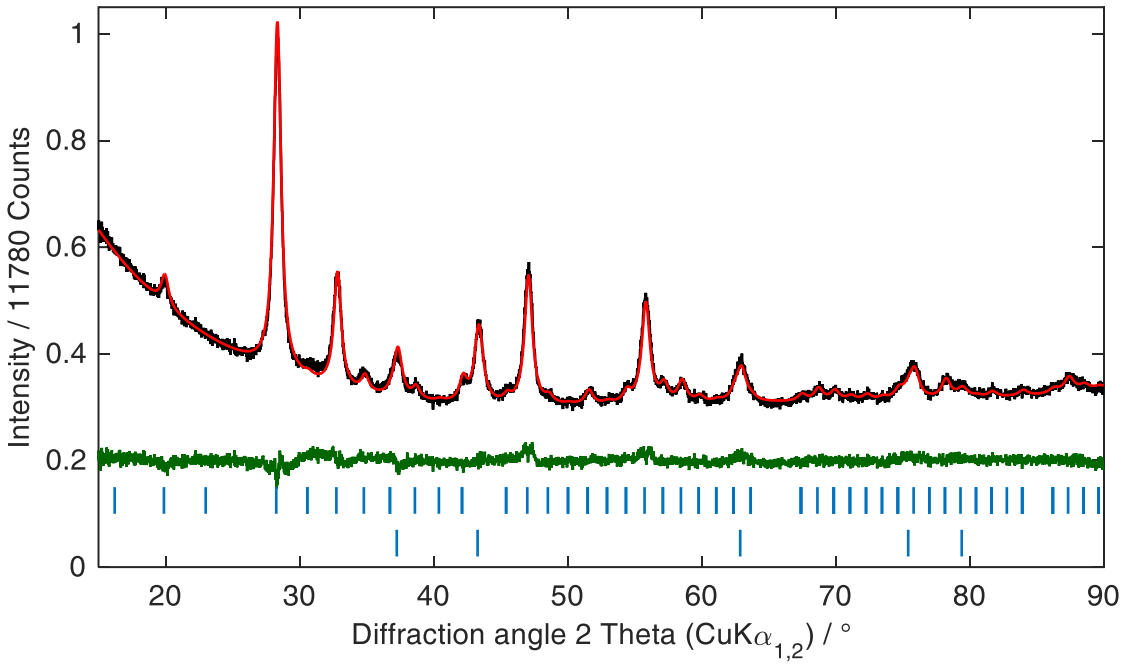

Figure 5-2 **Rietveld plot of 39 wt.% Ni-Sm_2O_3; observed pattern in black, calculated pattern in red, difference curve in green. The possible reflection positions of Sm_2O_3 and NiO are given as tick marks, top row: Sm_2O_3 ($Ia\bar{3}$), bottom row: NiO**

All diffraction patterns exhibit the typical reflections for cubic C-type Sm_2O_3 (space group $Ia\bar{3}$) at 28.45°, 32.87°, 47.09° and 55.88° 2 Theta (Cu-radiation). Upon an increasing Ni content, the characteristic diffraction peaks for NiO ($Fm\bar{3}m$) become predominant. The quasi-binary samples can be explained by a combination of the two pure materials, showing no additional peaks, that could be attributed to the unwanted perovskite. The sample 11 wt.% Ni-Sm_2O_3 also contains diffraction peaks for A-type Sm_2O_3 ($I2_13$) at 28.26°, 32.75° and 46.99° 2 Theta, indicating that the phase transformation from the A-type to the C-type phase has not been fully accomplished, yet.[187] This would suggest that the calcination duration is at the lower limit to achieve full phase transformation. However, since a second thermal treatment step (reduction of the catalyst) follows, during which residual A-type Sm_2O_3 is transformed into C-type, which could be evidenced by post-reduction XRD measurements (Figure C-1 in the appendix), this finding most likely does not affect the catalytical results. Remarkably, the sample with 89 wt.% Ni shows three further peaks, though small, at 44.5°, 51.9° and 76.5 2°Theta. Zhang[262] synthesized pure NiO films by a sol-gel route based on nickel acetate tetrahydrate and assigns the same peaks to Ni^0 or Ni^{3+}, assuming a disproportionation reaction during the annealing step at 500 °C.

$$3\,NiO \rightarrow Ni + Ni_2O_3 \tag{5-1}$$

Based on our Rietveld refinements, we attribute these reflections to metallic Ni ($Fm\bar{3}m$). Since calcination takes place in air, we believe that the addition of citric acid leads to a reducing atmosphere by decomposing to elemental carbon at 600 °C and as a results reducing

Table 5-1 Lattice parameters a, crystallite size L_{Vol}(IB)and NiO loading as calculated by Rietveld refinement.

wt.% Ni in Sm_2O_3	NiO a / pm	Sm_2O_3 ($Ia\bar{3}$) a / pm	Average crystallite size L_{Vol} (IB) / nm		NiO /wt.%
			NiO	Sm_2O_3 ($Ia\bar{3}$)	
Sm_2O_3	-	1092 ±1	-	20 ±1	-
4 wt.% Ni	419 ±1	1093 ±1	14 ±1	13 ±1	5 ±1
11 wt.% Ni	418 ±1	1093 ±1	15 ±1	10 ±1	14 ±1
33 wt.% Ni	418 ±1	1094 ±1	11 ±1	6 ±1	38 ±1
39 wt.% Ni	418 ±1	1093 ±1	8 ±1	9 ±1	43 ±1
64 wt.% Ni	418 ±1	1091 ±1	18 ±1	8 ±1	69 ±1
89 wt.% Ni	417 ±1	1094 ±1	19 ±1	6 ±1	91 ±1 (0.7 ±0.1 Ni)
4 wt.% Ni-IWI	418 ±1	1094 ±1	7 ±1	26 ±1	5 ±1

the NiO. Furthermore, it is noteworthy that the diffraction peaks of the samples containing both NiO and Sm_2O_3 are slightly broadened, indicating a smaller average crystallite size as compared to pure samaria. Table 5-1 summarizes the calculated lattice parameters, the average crystallite sizes L_{Vol}(IB) as well as the NiO loading of the catalyst. All lattice parameters are in good agreement with the literature.[263, 264] The average crystallite size of NiO is in the range of 8 to 19 nm, whereas Sm_2O_3 crystallites ($Ia\bar{3}$) are considerably smaller, ranging between 6 and 10 nm. Except for the sample with intermediate Ni loadings the crystallites sizes behave as expected. An increased loading of the respective element also causes an increase in their average crystallite size and vice versa.

While the XRD measurements are fully conclusive for the xerogel catalysts, the impregnated catalyst exhibits some deviations that need to be discussed in more detail. First of all, we found considerable amounts of A-type Sm_2O_3 (~38±1 wt.% determined by Rietveld analysis) as well as, secondly, $Sm_2O_2CO_3$ (28±1 wt.%) with main reflections at 23.06°, 26.79°, 31.49° and 46.11° 2 Theta. Taking into account that the pure Sm_2O_3 did not contain any A-type Sm_2O_3 but only the ordered C-type and assuming that upon calcination first the A-type is formed which over time transforms into the C-type,[187] the question arises how, seemingly, the opposite occurred during impregnation. As stated in Chapter 5.2, we used an aqueous Ni-nitrate solution to impregnate the Sm_2O_3 support multiple times, consequently, it appears likely that during the drying step small amounts of HNO_3 are produced. However, samaria can be easily dissolved by an acid, and thus might be attacked and partially dissolved by the formed HNO_3.[264] Upon the subsequent calcination step, the Sm_2O_3 lattice is reformed but as the second calcination step is shorter, the duration is not sufficient to complete the reformation of the cubic C-type Sm_2O_3 lattice. This is also related to the presence of $Sm_2O_2CO_3$.

It has been reported that $Sm_2O_2CO_3$ is an intermediary compound in the formation of Sm_2O_3 by releasing CO_2 during calcination, indicating again that the calcination time was not sufficient to achieve the full transformtion.[265, 266] In contrast to the 11 wt.% Ni-Sm_2O_3 catalyst, the high temperature reduction step prior to the reaction is sufficient to reduce NiO to metallic Ni, yet considerable amounts of A-type Sm_2O_3 as well as $Sm_2O_2CO_3$ are still present (see Figure C-2 in the appendix). Consequently, an influence on the catalytic performance cannot be excluded.

5.3.2 Structural Characterizations by TEM

Transmission electron micrographs of the various samples after calcination were acquired to understand if the particles are single crystals or multi crystalline. As visible in the TEM images (Figure 5-3), all samples exhibit a particulate structure as expected for xerogels derived from nitrates.[180] Unfortunately, no clear contrast is visible in the micrographs allowing to distinguish between NiO and Sm_2O_3 particles. Even EDX measurements did not reveal significant variations in the composition which would allow to correlate a certain shape or area with either NiO or Sm_2O_3. For the sample with 4 wt.% Ni, the particle size ranges mainly between 11 and 15 nm; however, some significantly larger particles, > 20 nm in diameter, are also present. Since NiO and Sm_2O_3 crystallites are similar in size as determined by XRD, no clear distinction by size is possible either. Upon an increasing Ni loading the primary particle sizes range between 14-19 nm, 16-20 nm, 20-24 nm and 17-22 nm for the

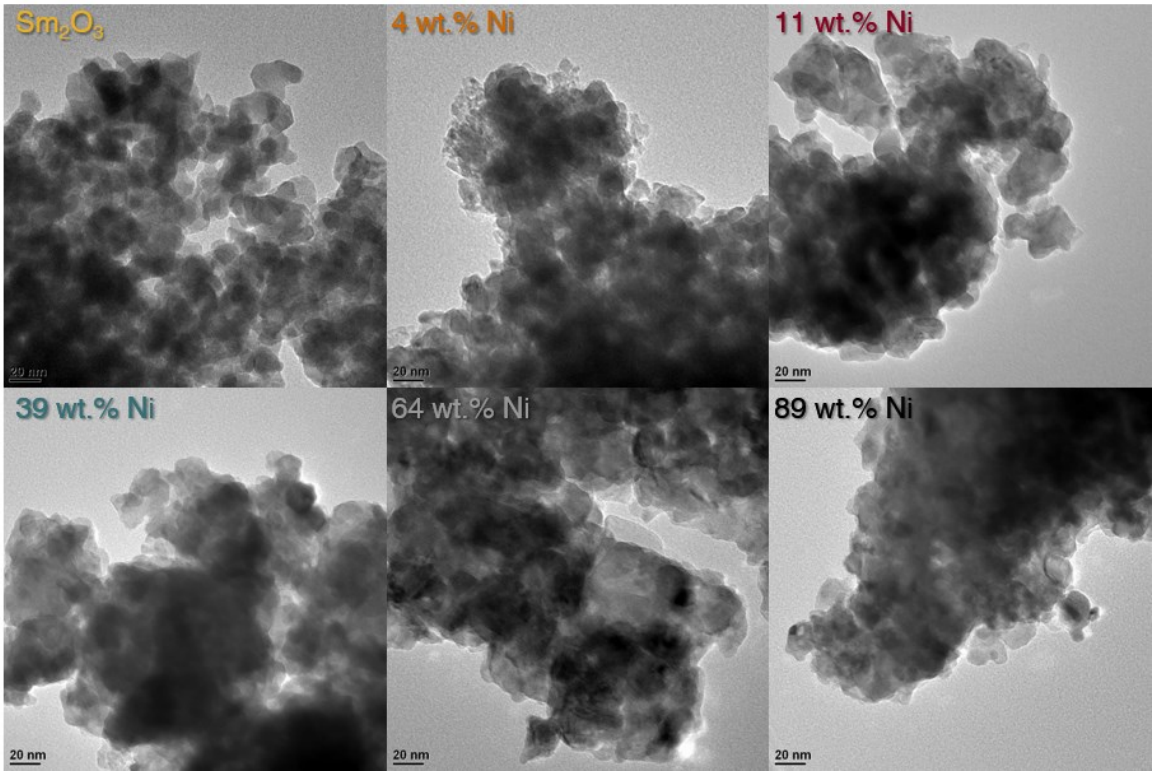

Figure 5-3 TEM images of selected Sm_2O_3 xerogels.

samples with 11 wt.%, 39 wt.%, 64 wt.% and 89 wt.% Ni, respectively. The difference of the TEM particle size to the crystallite size determined by XRD indicates the formation of polycrystalline particles. All samples exhibit crystal fringes, as can exemplarily be seen for the sample 64 wt.% Ni-Sm_2O_3, proving further the crystallinity of the samples.

5.3.3 Structural Characterizations by N_2 physisorption

N_2 physisorption measurements were conducted to obtain information about the catalysts' structures in dependence of the Ni loading. The results are shown in Table 5-2 as well as Figure 5-4. Except for the sample with the highest Ni loading, the obtained specific surface areas (SSA) follow a trend in that a decreasing SSA is observed with increasing Ni amount. Impregnating and recalcining the sample does not affect the porosity as the SSA, pore volume and pore radius remain almost unchanged in comparison to the pure Sm_2O_3, hinting to a high thermal stability of the Sm_2O_3 xerogel. The specific surface areas are rather small; e.g. Neumann et al.[182] synthesized Sm_2O_3-Al_2O_3 xerogels by a similar route and achieved specific surface areas as high as 117 $m^2\ g^{-1}$. The smaller surface areas can be explained by the high molar mass of the samaria. When comparing the results to other Sm_2O_3 supported systems, the values are, however, in good agreement with the literature. Zhang et al.[267] found a SSA for a Ni-Sm_2O_3 xerogel prepared by a different route after calcination at 550 °C of 8 $m^2\ g^{-1}$, whereas Gomez-Sainero et al.[268] synthesized Sm_2O_3-CeO_2 powders, which they calcined at 800 °C, with 9.7 $m^2\ g^{-1}$ SSA. Using the IUPAC classification, all samples exhibit, as shown in Figure 5-4, type IV isotherms indicating mesopores and are, therefore, considered suitable for catalytic applications. Micropores appear to be absent as no steep increase in N_2 uptake is measured at low p/p_0 values. With increasing Ni content, the hysteresis loop changes from H2-type, indicative for porous materials with spherical pores, to H3-type, which is characteristic for slit-shaped pores and plate-like particles. The derived pore size distributions are

Table 5-2 BET/BJH results for the synthesized xerogel powders.

Sample	Specific surface area / $m^2\ g^{-1}$	Pore volume[1] / $cm^3\ g^{-1}$	Average pore radius[2] / nm	Max. in pore radius distribution[2] / nm
Sm_2O_3	31	0.12	7.5	5.1
4 wt.% Ni	28	0.08	6.2	4.2
11 wt.% Ni	22	0.06	5.5	3.8
33 wt.% Ni	21	0.06	6.1	4.2
39 wt.% Ni	19	0.06	6.1	5.1
64 wt.% Ni	9	0.02	4.7	1.9
89 wt.% Ni	13	0.05	8.0	1.9
4 wt.% Ni-IWI	27	0.11	7.9	5.1

[1] calculated by the Barret-Joyner-Halenda (BJH) method at $p/p_0 = 0.99$

[2] calculated of the desorption branch using the BJH method

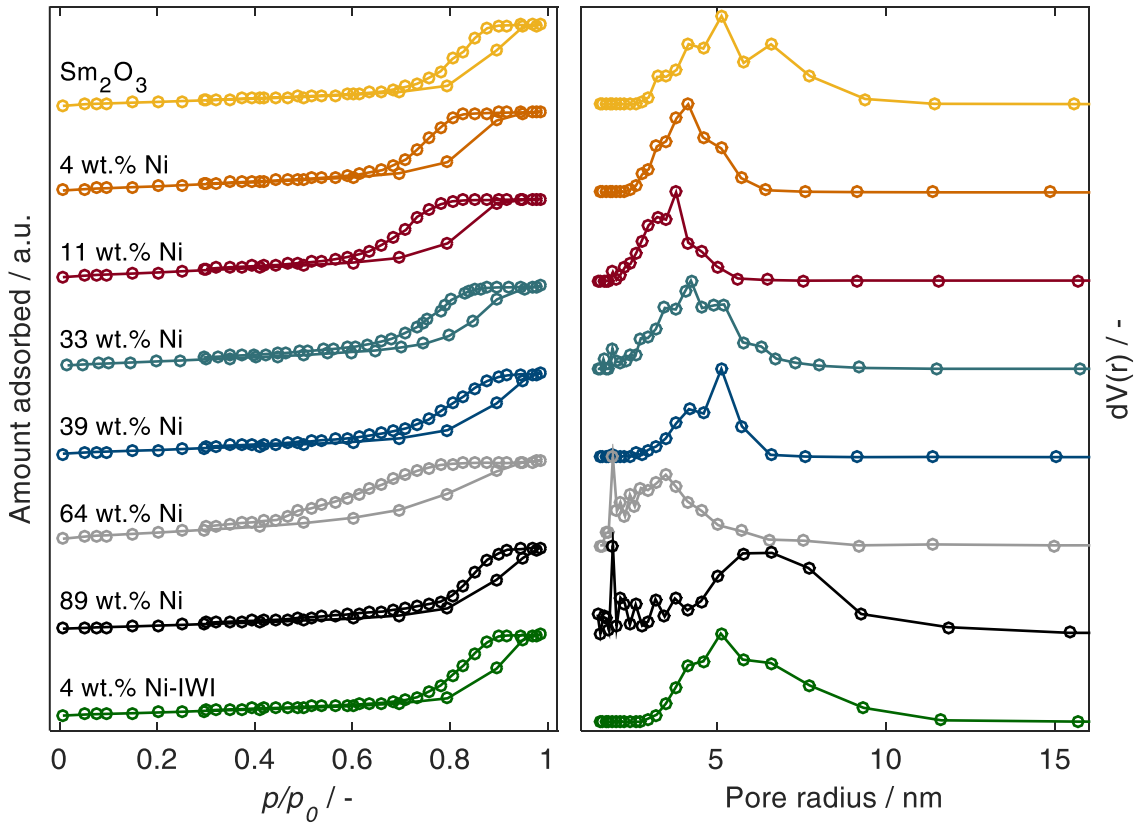

Figure 5-4 **(left) N_2 adsorption/desorption isotherms and (right) pore size distribution as determined by the BJH method of the synthesized xerogels.**

rather broad. Additional Hg intrusion porosimetry measurements confirmed the absence of the macropores, possibly undetected by N_2 physisorption as shown in Figure C-3 (appendix). Further, adding Ni to the synthesis reduces the pore volume of the mixed systems with a rough trend towards smaller pore volumes with increasing Ni loading. Under consideration of the pore size distribution and the decreasing surface area, this suggests that the addition of Ni leads to denser and less porous xerogels.

5.3.4 Characterization of the Reducibility by H_2-TPR

H_2-TPR profiles were recorded to study and compare the reducibility as well as the interaction between NiO and Sm_2O_3 (Figure 5-5) Prior to the data collection, pre-experiments revealed the necessity to pre-treat the samples at 400 °C for 10 h in order to ensure full dryness and the absence of any adsorbed impurities. Since the XRD results revealed the absence of any mixed phases, only one reduction peak is expected in the scanned temperature regime accounting for the reduction of NiO to metallic Ni. As references, a pure Sm_2O_3, synthesized by the same sol-gel method, and a NiO sample, prepared by decomposing $Ni(NO_3)_2 \cdot 6\ H_2O$ at 600 °C for 2 hours, were used. Although all profiles were recorded with around 75 mg of the respective powder, the profiles are scaled by the respective sample mass

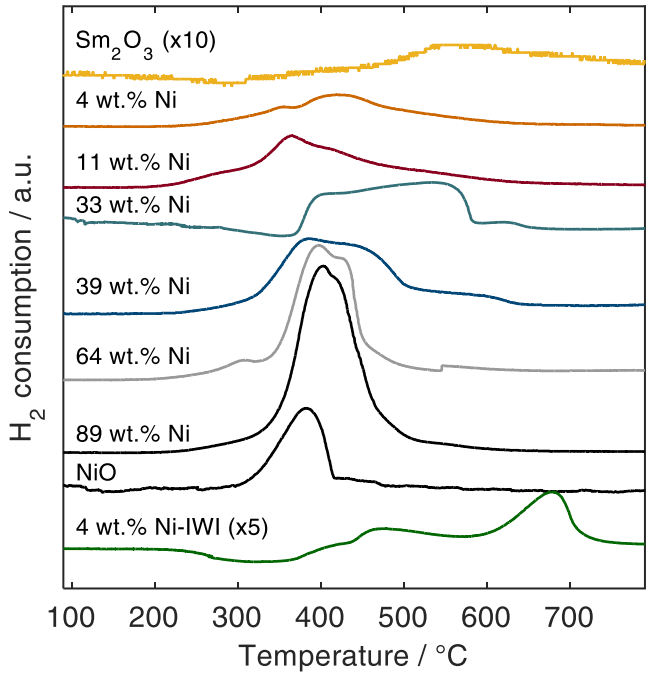

Figure 5-5 TPR profiles of the synthesized xerogels. Heating ramp 5 °C min^{-1}. The samples were pre-treated at 400 °C in He for 10 h prior to the reaction.

to allow a better comparison. As the TCD signal of the pure Sm_2O_3 sample was too weak to be properly displayed, we magnified the intensity by the factor 10. Similarly, the signal intensity for the impregnated reference was enlarged by a factor of 5 to facilitate the detection of the high temperature reduction peak. The pure NiO sample shows a clear, distinct peak centered around 380 °C, which is close to reported values by e.g. Jankovic et al.[269]. The highly loaded samples with 64 wt.% and 89 wt.% Ni show a remarkably similar reduction profile and resemble the profile of pure NiO, although slightly shifted to higher temperatures which might result from the embedment in Sm_2O_3. Similar findings have been reported by Augusto et al.[270] for Ni-CeGd catalysts who argue that, with increasing calcination temperature and metal loading, the reduction profiles become similar to the bulk behavior.[270] At lower loadings, the profiles are less clearly pronounced, exhibiting multiple peaks and shoulders, which are though in the same temperature region. This contrasts to the results on the impregnated catalyst, which show a main reduction peak at significantly higher temperatures (680 °C), preceded by a shoulder at temperatures above 400 °C. As the XRD results revealed the presence of only one NiO species and no mixed oxides for all catalysts, the diffuse profiles indicate the presence of NiO in different chemical environments characterized by a varying interaction with Sm_2O_3.[36, 37] Further, the xerogel catalysts show a pronounced tailing, which occurs in the same temperature region as the reduction of the pure Sm_2O_3. Samaria is considered a thermally stable oxide which does not undergo complete reduction, however, it possesses the ability to form oxygen vacancies in a reducing atmosphere at elevated

temperatures.[95] We, thus, attribute at least part of the tailing to the formation of oxygen vacancies within the Sm_2O_3 structure.

5.3.5 Determination of Adsorption Capacities by Pulsed H_2 and CO_2 Chemisorption

H_2 followed by CO_2 pulse titration experiments were carried out to determine the H_2 and CO_2 uptake of the catalysts in dependence of the Ni loading. Under consideration of the XRD and N_2 physisorption data and the assumption that hydrogen is adsorbed on metallic Ni whereas CO_2 is chemisorbed on the Sm_2O_3 support, the Ni surface area and Ni dispersion can be calculated. Additionally, the specific Sm_2O_3 surface area is estimated by deducting the specific Ni surface area from the overall specific surface area as determined by N_2 physisorption. The results are compiled in Table 5-3.

In terms of the H_2 uptake, no clear trend becomes obvious and the derived Ni surface areas vary between 1.3 and 6.7 $m^2\ g^{-1}_{cat}$ with a rough tendency towards larger Ni surface areas with increasing Ni content. The absence of a clear trend can be reasoned with the decreasing overall specific surface area determined by N_2 physisorption. For the samples with 64 and 89 wt.% Ni loading, the higher Ni content, at least in part, is annulled by the lower specific surface area as a result of the synthesis. The Ni dispersion, in turn, follows the expected trend, except for the 4 wt.% Ni-Sm_2O_3 catalyst. Higher Ni loadings lead to a less efficient exposition of Ni surface atoms. Interestingly, the H_2 uptake and the corresponding Ni surface area as well as Ni dispersion is significantly higher for the impregnated catalyst compared to the xerogel catalyst with the corresponding loading. In fact, the H_2 chemisorption capacity of the impregnated catalyst is comparable to the xerogel catalysts with higher Ni loadings, which is also reflected in the superior Ni dispersion. This indicates a poorer accessibility of Ni atoms for the xerogel catalyst, which can at least partially be explained

Table 5-3 **H_2 and CO_2 adsorption capacities of the Ni-Sm_2O_3 catalysts determined by pulsed chemisorption at 30 °C. Additionally, the Ni surface area, Ni dispersion and Sm_2O_3 surface area are stated.**

	H_2 uptake / µmol g^{-1}	Ni surface area / $m^2\ g^{-1}$	Ni dispersion / %	CO_2 uptake / µmol g^{-1}	Sm_2O_3 surface area[a] / $m^2\ g^{-1}$
4 wt.% Ni	17	1.3	4.9	154	26.7
11 wt.% Ni	75	5.9	8	114	16.1
39 wt.% Ni	68	5.4	2.4	121	15.6
64 wt.% Ni	85	6.7	1.6	60	2.3
89 wt.% Ni	56	4.4	0.7	39	8.6
4 wt.% Ni-IWI	70	5.5	16.5	100	21.5

[a] approximated by deducting the Ni surface area from the overall BET surface area

with the larger Ni crystallites as determined by XRD and the larger volume-to- surface ratio.

Following the H_2 titration measurements, the CO_2 uptake was determined by pulsed titration. Here, the adsorption capacity of the systems decreases for higher Ni loadings as is to be expected due to the higher proportion of Ni on the specific surface area and the decreasing overall specific surface area, adding up to a low specific Sm_2O_3 surface area available for CO_2 adsorption.

5.4 Catalytic Performance

All catalysts were tested for CO_2 methanation in a temperature interval between 200-400 °C at a total flow rate of 50 mL min^{-1} with the feed gas being composed of 4/1/5 $H_2/CO_2/Ar$ and at a weight hourly space velocity (WHSV) of 60 L_N g_{cat}^{-1} h^{-1}. Prior to the reaction, the samples were reduced in-situ at 500 °C for 10 h under flowing hydrogen. The catalyst stability is addressed in detail in Chapter 6. Additional results on the simultaneous CO/CO_2 methanation are presented and discussed in the appendix C.5.

5.4.1 Influence of Ni loading

The CO_2 conversion as well as CH_4 selectivity at the investigated temperatures are depicted in Figure 5-6 for all synthesized catalysts. Generally, the catalysts exhibit an exceptional conversion level, particularly at low and medium temperatures. The samples reported here have a low onset temperature, being already active at 250 °C, while the methane selectivity is for all samples and temperatures tremendously high. Interestingly, the sample with 39 wt.% Ni shows the highest conversion level, whereas the catalysts with 64 and 89 wt.% Ni perform worse as compared to the 39 wt.% Ni loaded catalyst but are among each other very similar, despite the differing Ni loading. Smaller Ni loadings, in turn, lead to the lowest conversion levels. At high temperatures exceeding 300 °C, kinetic limitations lead to only small increases in conversion, despite drastically higher temperatures. The methane selectivity is close to 100%, independently of the Ni loading. However, with increasing temperature the selectivity is slightly decreasing due to CO formation via the endothermic reverse water-gas shift reaction.

To explain the results, mechanistic as well as morphological reasons appear likely. On Ni catalysts, it is known that CO_2 adsorption takes primarily place at the metal-support interface rendering a pure Ni catalyst inactive for low temperature CO_2 methanation.[7, 154] This is also in accordance with pre-experiments over unsupported Ni. In case of the catalysts with 64 and 89 wt.% Ni loading, the Ni portion of the surface is already very high (in particular when considering the large difference in molar mass of the two components) so that the area for CO_2 adsorption on Sm_2O_3 is rather low (Table 5-3). Apparently, the 39 wt.% Ni-Sm_2O_3

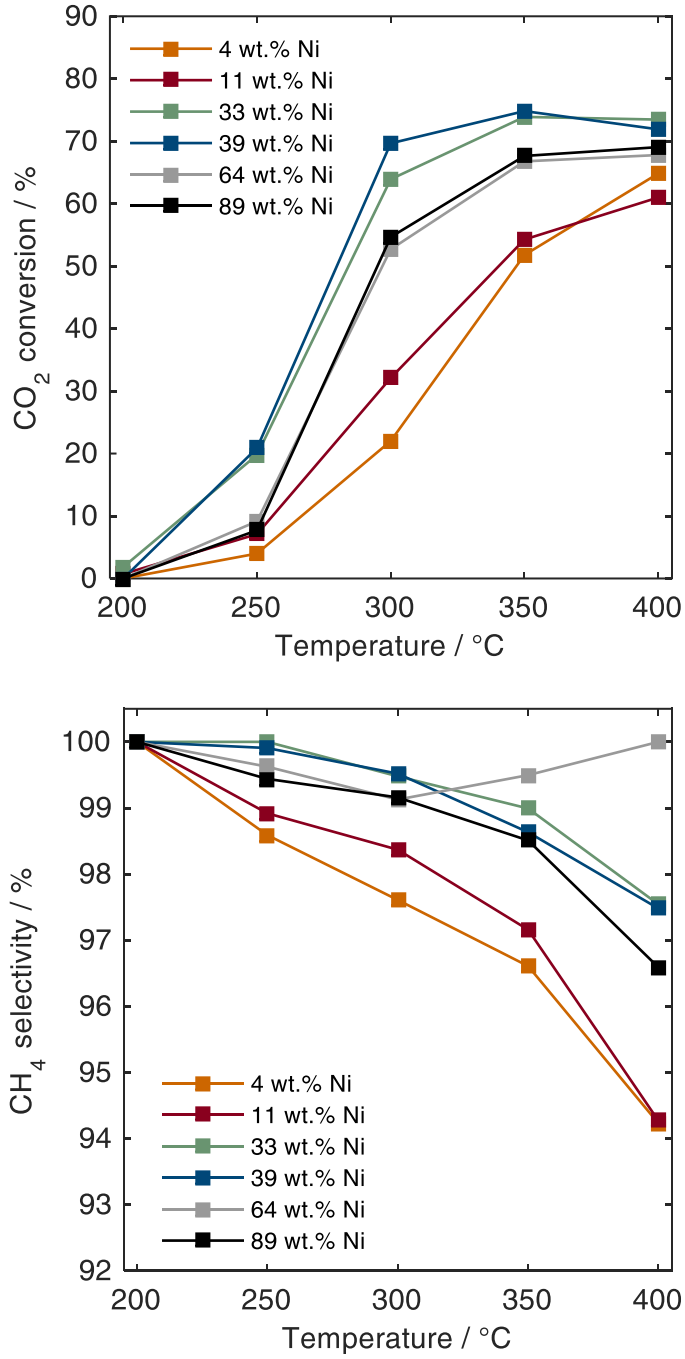

Figure 5-6 **CO_2 conversion (top) and corresponding CH_4 selectivity (bottom) for various temperatures and Ni loadings. Reaction conditions: pressure 1 bar, flow rate 50 mL min^{-1}, feed composition 4/1/5 H_2/CO_2/Ar, 50 mg catalyst.**

catalyst offers the best ratio of Sm_2O_3 (CO_2 adsorption) and Ni sites (H_2 adsorption and dissociation) including a high number of perimeter sites. In addition, the samples with 64 and 89 wt.% Ni loading, have a significantly smaller specific surface area, as discussed before. Another factor, playing a role, could be the smaller pore radii or larger crystallite sizes in the latter two cases. However, calculating the Weisz-Prater criterion according eq. (5-2)

$$\mathrm{WP}=\frac{r\,\rho_{\mathrm{cat}}\,d_{\mathrm{cat}}^{2}}{4c_{\mathrm{CO_2}}D_{\mathrm{CO_2}}^{\mathrm{eff}}}<1, \tag{5-2}$$

in which r denotes the measured reaction rate, ρ_{cat} the catalyst density, d_{cat} the catalyst particle diameter, c_{CO2} the CO_2 concentration in the fluid and $D_{\mathrm{CO_2}}^{\mathrm{eff}}$ the effective diffusion coefficient of CO_2 in H_2 under consideration of Knudsen diffusion, shows no intra particle diffusion limitations for reaction temperatures below 350 °C, thus eliminating the pore size as an influential factor.[273] In contrast, the significantly smaller average crystallite size of 39 wt.% Ni-Sm_2O_3 is a likely factor, as small crystallite sizes are considered to be favorable for the activity in structure-sensitive reactions like the CO_2 methanation.[16, 202] Yet, it has to be kept in mind that the structure-sensitivity was determined over an inert supported Ni catalyst (Ni-SiO_2).[24] The active sites are hence different from the bifunctional Ni-Sm_2O_3 catalyst, such that the Ni particle size observations of the Ni-SiO_2 cannot be readily transferred to the Sm_2O_3 supported catalyst.

In addition, we determined the activation energy for the catalysts with 11 wt.%, 39 wt.% and 64 wt.% Ni for the interval 230-300 °C. The corresponding graph is attached in the appendix (Figure C-4). The activation energies were derived to be 82.4±3.8 kJ mol^{-1}, 81.6±2.7 kJ mol^{-1} and 83.5±3.9 kJ mol^{-1} for the catalysts with 11 wt.%, 39 wt.% and 64 wt.% Ni, respectively. The determined activation energies are at the lower end of previously reported values for Ni based systems and do not differ significantly from the activation energy of the reference kinetics (77.5±6.9 kJ mol^{-1}). Yang et al.[274] found an activation energy of 95 kJ mol^{-1}, whereas others reported values between 80-106 kJ mol^{-1} on various Ni based systems.[275, 276]

5.4.2 Comparison with Reference Catalysts

The catalytic performance is compared against three different references.

- By comparing the 4 wt.% Sm_2O_3 xerogel catalyst against the equally loaded catalyst prepared by impregnation, insights into the effect of the preparation method can be gained.

To evaluate the overall potential of Sm_2O_3 supported Ni catalysts for the CO_2 methanation, the best performing catalyst (39 wt.% Ni-Sm_2O_3) is further compared against two types of Ni-Al_2O_3 catalysts.

- For one, an industrial methanation catalyst is run under the identical conditions to benchmark the Ni-Sm_2O_3 catalyst against an industrial standard (Ni-γ-$Al_2O_3^{ind.}$). Table 5-4 summarizes some key characteristics of the catalyst in parts provided by the supplier as well as determined in-house. Additional and more detailed data on the characterization of the system are attached in the appendix C.6. Unfortunately, no reliable information regarding the Ni crystallite size could be derived by XRD.

Table 5-4 **Summary of the main physico-chemical properties of the reference catalysts. H_2 and CO_2 adsorption capacity of the industrial reference catalyst (Ni-$Al_2O_3^{ind.}$) determined by H_2 and CO_2 titration at 30 °C. Additionally, the Ni surface area and Ni dispersion are stated. For details, see Chapter C.6 (appendix). Values for the literature reference catalyst (Ni-$Al_2O_3^{lit.}$) are taken from Koschany et al.[31], if provided.**

	Ni loading / wt.%	Ni crystallite size / nm	H_2 uptake / µmol g^{-1}	Ni surface area / m^2 g^{-1}	Ni dispersion / %	CO_2 uptake / µmol g^{-1}
Ni-$Al_2O_3^{ind.}$	9	-	73	5.7	9.6	42
Ni-$Al_2O_3^{lit.}$	19	16.6	-	21.3	6.1	-

- Secondly, the comparison with a highly active literature system (19 wt.% Ni-$Al_2O_3^{lit.}$) is made by implementing their micro-kinetic model in an isothermal 1D pseudo-homogenous reactor model, assuming ideal conditions, e. g. no inter- or intra-particle diffusion limitations, such that only the mass balance had to be solved numerically. The reaction conditions have been chosen to reflect our conditions, such that a direct comparison of the catalytic performance under identical conditions is possible. To this end, the rate equation by Koschany et al.[31] was employed without any alterations The rate equation and kinetic parameters are given in the appendix (Table C-2). Note that the authors do not consider the RWGS in their rate equation and assume a CH_4 selectivity of 100%, which is therefore not included in the figure. Details on the catalyst specifications taken from their publication are stated in Table 5-4, as well.

For the comparison, the supported catalysts are defined as one unit and thus the CO_2 conversion and CH_4 selectivity are used as a direct measure for the performance of the catalysts. Admittingly, this represents rather an engineering approach, since the space-time-yield as an engineering key indicator is readily derivable from the data, whereas from a catalysis perspective a comparison per active site would be more appropriate. Yet, we refrained from calculating reaction rates per surface area or turnover frequencies (TOFs) as there is no consensus on the active site, let alone the number of active sites. To give an impression nevertheless, the Ni surface area as stated in Table 5-3 and Table 5-4 are considered in the discussion of the results.

An often-stated disadvantage of sol-gel derived catalysts is the non-accessibility of the active component due to its encapsulation by a non- or microporous support shell,[277] and the characterization data presented over the course of this chapter does not allow to reject this notion. While no significant amounts of micropores are present (as determined by the N_2 physisorption measurements), pulsed H_2 chemisorption revealed a significantly lower Ni

dispersion for the xerogel catalyst, indicating accessibility issues caused by the larger Ni crystallite size and thus higher volume-to-surface ratio but potentially also by encapsulated Ni particles. Yet, despite this, an equally good to superior catalytic performance in both CO_2 conversion and CH_4 selectivity of the xerogel catalyst to the impregnated reference was found (Figure 5-7). The present characterization data do not allow to unambiguously elaborate on

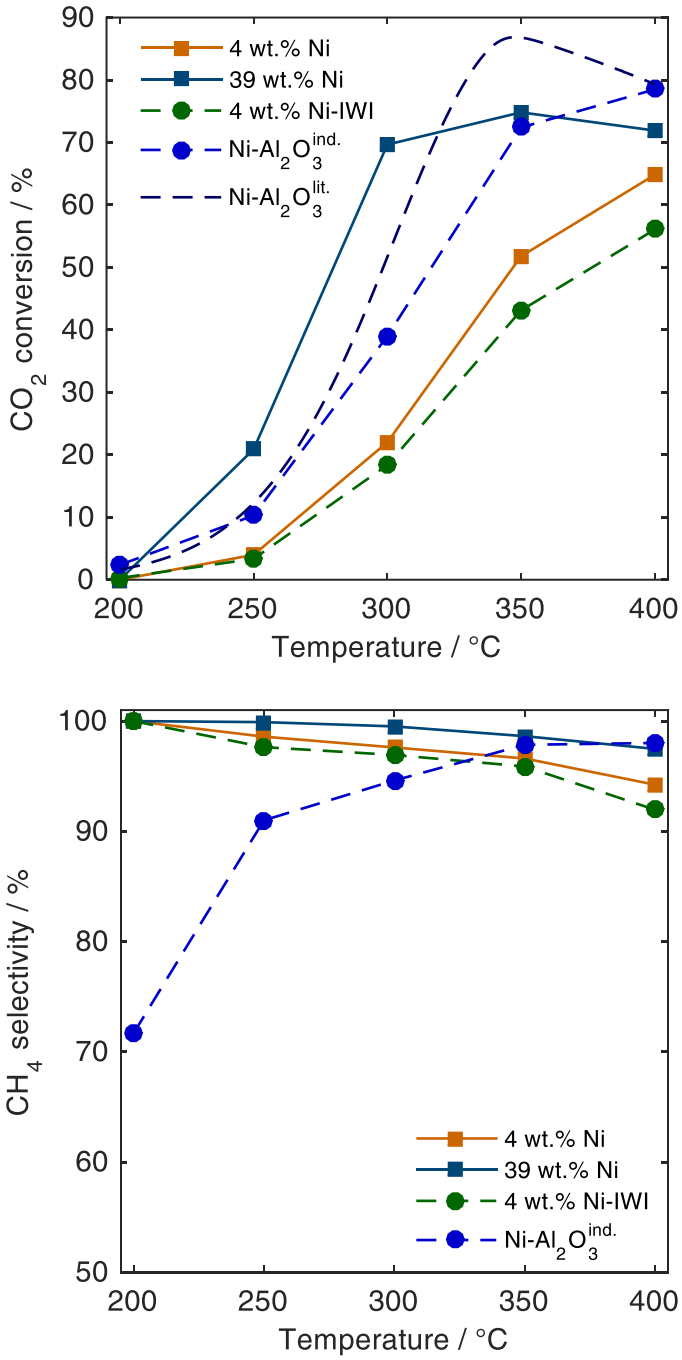

Figure 5-7 CO_2 conversion (top) and corresponding CH_4 selectivity (bottom) for the Ni-Sm_2O_3 xerogel catalyst in comparison to three reference catalysts. Reaction conditions: pressure 1 bar, flow rate 50 mL min^{-1}, 4/1/5 $H_2/CO_2/Ar$, 50 mg catalyst, reduced at 500 °C for 10 h in H_2 prior to the reaction; reference kinetics adopted from Koschany et al.[31].

the origins of the higher reactivity for the xerogel catalyst. Differences in the Ni loading as well as in the porosity (pore size and surface area) can be excluded as these parameters do not differ significantly for the two catalysts. A different reduction behavior is possible but post-reduction XRD measurements confirm the full reduction for both catalysts, in spite of the significantly higher reduction temperature as derived by H_2-TPR. Probably, the reduction time was long enough to make up for the slowed down reduction kinetics to ultimately achieve full reduction of NiO to metallic Ni, nonetheless. Taking into account that for the impregnated catalyst the Ni crystallite size after reduction is smaller (6±1 nm, whereas it is 9±1 nm for the xerogel catalyst, see Table D-1) and considerably closer to the reported optimal Ni particle size (2-3 nm) compared to the xerogel catalyst,[24] a Ni crystallite effect as origin for the superior performance of the xerogel catalyst seems unlikely. Consequently, the difference in the CO_2 conversion can probably be reasoned with the presence of the additional structural phases in the impregnated 4 wt.% Ni-Sm_2O_3 catalyst, specifically the cubic Sm_2O_3 phase ($I2_13$) and $Sm_2O_2CO_3$. Both phases are present after reduction, as evidenced by additional XRD measurements (Figure C-2), thereby potentially affecting the catalytic reactivity in a negative way. Yet, so far, no investigations regarding the influence of different samarium oxide phases in CO_2 methanation have been reported.

The potential of the Sm_2O_3 supported catalysts become immediately obvious upon comparison with the reference kinetics (Ni-$Al_2O_3^{lit}$) and the industrial methanation catalyst (Ni-$Al_2O_3^{ind.}$), particularly in the low to intermediate temperature regime. For instance, the reactivity of the 39 wt.% Ni-Sm_2O_3 at 300 °C is about 40% higher (rel.) than the reference kinetics under identical conditions despite the significantly lower Ni surface area for the Ni-Sm_2O_3 catalyst.

Even more striking is the comparison with the industrial standard. While the CO_2 conversion at 300 °C is already almost double as high, the superior performance becomes even more pronounced upon consideration of the higher CH_4 selectivity for the samaria supported catalyst. Considering the comparatively low Ni loading (9 wt.%) of the industrial catalyst, one might argue that the higher reactivity is not surprising due to the higher Ni loading of the Ni-Sm_2O_3 catalyst, however, it has to be kept in mind, that a higher loading does not necessarily equal a higher reactivity as is also demonstrated in Chapter 5.4.1 and in line with observations by Zhang et al.[37]. In fact, comparing the Ni surface area of the industrial reference catalyst with the 39 wt.% Ni-Sm_2O_3 catalyst shows very similar values, hence an almost identical number of potential H_2 adsorption sites are present on both catalysts. The superior performance can consequently be attributed to the higher CO_2 adsorption capacity of the 39 wt.% Ni-Sm_2O_3 catalyst, which exceeds the capacity of the Ni-$Al_2O_3^{ind}$ reference catalyst by a factor of ~ 3. It is further hypothesized that this effect is strengthened by the lower overall BET surface area of the Ni-Sm_2O_3 catalyst (19 m^2 g^{-1}, in comparison to SSA_{Ni-}

$_{Al2O3}$ = 145 m^2 g^{-1}, see Chapter C.6 for more details) resulting in a higher density of CO_2 adsorption sites and thus potentially a larger number of active, adsorbed CO_2 species in proximity of the Ni particle.

5.5 Interim Conclusions

Drawing on the findings of Chapter 4, this chapter applied those findings as well as successfully expanded the synthesis method introduced in Chapter 3.2.2 to prepare Ni-Sm_2O_3 xerogel catalysts. The Ni loading was varied over a wide range between 4 and 89 wt.% to find the optimal Ni content for a maximized methane yield. The catalysts are characterized by means of XRD, N_2 physisorption, TEM, H_2-TPR as well as pulsed H_2 and CO_2 chemisorption to describe the physico-chemical properties in dependence of the Ni loading.

All xerogels are mesoporous and consist of separated but crystalline oxides. From a catalytic perspective, an intermediate Ni loading (30-40 wt.%) should be targeted which we attribute to Ni particle size effects as well as a favorable ratio of H_2 dissociation sites on the metallic Ni and CO_2 adsorption sites on the Sm_2O_3 support, particularly on the metal-support perimeter. In comparison to an impregnated reference catalyst with identical loading, the xerogel catalyst exhibits a comparable but slightly superior reactivity. The optimized Ni-Sm_2O_3 catalysts are highly competitive and outperform an industrial Ni-Al_2O_3 methanation catalyst as well as a literature known system, of which the published kinetics were used to calculate its catalytic performance under our reaction conditions. The superior performance of the Ni-Sm_2O_3 catalyst can be attributed to the higher CO_2 chemisorption capacity and, under consideration of the specific surface area, to a significantly higher density of basic sites in proximity of the Ni particles.

Although not discussed at this point, the catalyst stability proved to be an issue, and is therefore the topic of the following chapter.

6

The Ambivalence of Basic Sites - Deactivation Mechanism of Ni-Sm_2O_3 Xerogel Catalysts

In the previous chapter, highly active Ni-Sm_2O_3 xerogel catalysts were synthesized, characterized and applied for the CO_2 methanation. However, their time-on-stream behavior has not been addressed yet, despite providing essential insights into the catalyst stability and deactivation behavior. It is therefore subject of extensive efforts in this chapter.

6.1 What to Expect from this Chapter.

Apart from a high activity and selectivity towards the desired product, the catalyst lifetime is of utmost importance, particularly from an industry perspective. Yet, little is known about the occurring deactivation behavior, which obviously depends on the applied catalyst and the reaction conditions. As outlined in Chapter 2.4, sintering of the active component and coking are often considered to be most prominent deactivation phenomena, while, in fact, the deactivation mechanism is unknown due to the lack of characterizations of the spent catalyst and careful time-on-stream experiments.[31] Extensive time-on-stream experiments under varying process conditions and careful characterization of the spent catalyst are inevitable to gain in-depth insight into catalyst deactivation. Ewald et al.[35] provide one of the few studies which addresses the deactivation of a Ni-Al_2O_3 catalyst in such a detailed manner.

They explained the observed activity loss of up to 65 % within 160 h with Ni particles sintering and a loss of the specific surface area which, as a result, decreases the CO_2 adsorption capacity of the catalyst. However, if catalysts with basic surface properties are applied, their findings are not sufficient to describe the occurring deactivation phenomena. For instance, Muroyama et al.[90] observed a severe loss of activity over 10 h on stream at 300 °C for their Ni-Sm_2O_3 catalyst which they could not explain with neither sintering nor coking. Consequently, the occurring deactivation phenomena is still a matter of debate.

This chapter contributes here by addressing the time-on-stream behavior and deactivation mechanism of the 33 wt.% Ni-Sm_2O_3 catalyst. By a careful variation of the process conditions during extended time-on-stream experiments combined with the characterization of the spent catalysts, *operando* DRIFTS measurements and catalyst regeneration experiments ultimately a sound deactivation mechanism is formulated.

Despite the focus on the 33 wt.% Ni-Sm_2O_3 system, time-on-stream experiments were conducted also for the catalysts with different Ni loadings, the impregnated Ni-Sm_2O_3 reference catalyst and the industrial Ni-Al_2O_3 system, of which the results are attached in the appendix and briefly summarized here. These experiments reveal that the Ni-Sm_2O_3 catalysts deactivate independent of the Ni loading and initial conversion level (see Figure D-1), hence, justify the restriction to focus on the 33 wt.% Ni-Sm_2O_3 catalyst for an in-depth study of the governing deactivation mechanism. The activity loss is further found to be completely reversible upon a regeneration step in H_2 at 490 °C for 4 h. In comparison, the industrial Ni-Al_2O_3 catalyst exhibits a stable conversion over the entire time-on-stream experiment. Yet, even at the end of the stability experiment, the catalyst is still considerably outperformed by Ni-Sm_2O_3 catalysts with high and intermediate Ni loadings. In turn, a more pronounced deactivation is found over the impregnated catalyst. The corresponding catalytic results and post characterization data by XRD and N_2 physisorption are presented in the appendix D.3 and reveal the absence of sintering.

6.2 Catalysts, Characterizations and Standard Reaction Conditions

All measurements were conducted using the 33 wt.% Ni-Sm_2O_3 catalysts. The findings are assumed to be representative for all xerogel catalysts. The experimental procedures were identical as reported in the preceding chapter and can be found in the corresponding parts in the Appendix A and C. To unravel the deactivation mechanism, the main influential reaction parameters T, p_{CO2}, as well as the H_2/CO_2 ratio were systematically varied. The following reactions conditions were defined as the base case ("standard reaction conditions"):

- $T = 300$ °C,
- $\dot{V}_{\text{total}} = 50$ mL min^{-1} with a composition of 4/1/5 H_2/CO_2/Ar,

- $p = 1$ bar,
- time-on-stream = 600 min,
- $m_{cat} = 40$ mg, and
- catalyst reduction at 500 °C for 10 h, (temperature ramp: 1 °C min^{-1})

If the reaction conditions deviate from the standard reaction conditions, they are explicitly stated at the beginning of the respective subchapter and are further summarized in Table 6-1. For all measurements, it was made sure that the reaction equilibrium is not constraining, therefore the amount of catalyst had to be adjusted for the high temperature experiments. After each experiment, the catalyst was regenerated at 490 °C in H_2 for 4 h and subsequently subjected to the identical reaction conditions as during the preceding experiment to check for irreversible effects.

To enable a simple and direct comparison of the activity loss in the different experiments, the relative activity a_{rel} defined in eq. (6-1) as

$$a_{rel}(t) = \frac{X_{CO_2,t}}{X_{CO_2,t=0}}, \tag{6-1}$$

in which $X_{CO2,t}$ denotes the CO_2 conversion at a specific time t and $X_{CO2,\ t=0}$ the initial conversion, is displayed against the time.

6.3 Catalytic Results

6.3.1 Catalytic Results I - Activation Energies Before and After an Aging Period

Prior to the parameter variation study, the activation energy was determined before and after an aging period to clarify if over the course of the experiment a change in the reaction mechanism took place. A change in the activation energy hints to change in the reaction mechanism associated with the nature of active sites, whereas a constant activation energy is indicative for a loss of active sites.[166] After reduction, the activation energy was determined in the temperature interval between 230 °C and 310 °C before aging the catalyst for 1000 min at 300 °C under the standard reaction conditions (Figure 6-1). Subsequently, the measurements to derive the activation energy were conducted again under identical conditions. The calculated activation energies are:

- Prior to catalyst aging: $E_{A,\ fresh} = 81.8 \pm 7.6$ kJ mol^{-1}
- After catalyst aging: $E_{A,\ aged} = 82.2 \pm 6.6$ kJ mol^{-1}

and therefore, strongly indicate no change in the occurring reaction mechanism. The activity loss, most likely, can be ascribed to a loss of active sites. Further, the derived activation energies are well within previously reported values[274–276] and confirm the findings from Chapter 5.4.1.

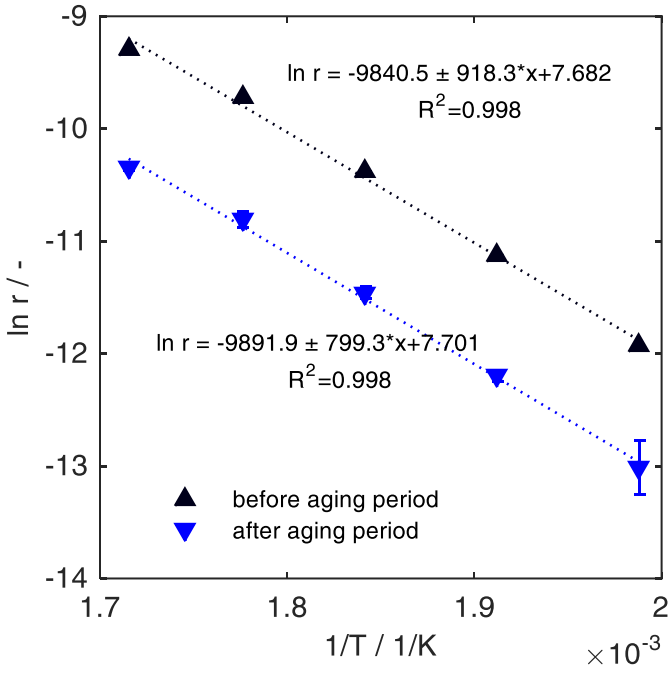

Figure 6-1 **Arrhenius plot for the determination of the activation energy of the 33 wt.% Ni-Al_2O_3 catalyst before and after an aging procedure. Conditions: T = 230-310 °C, p = 1 bar, $\dot{V}_{total}$ = 50 mL min^{-1} composed of 4/1/5 H_2/CO_2/Ar, m_{cat} = 14 mg.**

6.3.2 Catalytic Results II - Influence of the Reaction Conditions

H_2/CO_2 ratio

Thermodynamically, the H_2/CO_2 ratio has the most profound impact on the equilibrium conversion and the selectivity. From that follows that coking occurs at H_2/CO_2 ratios below 3, and if at the same time high conversion levels are achieved even catalyst oxidation has been reported to become an issue due to the high H_2O/H_2 ratio.[278] Consequently, by varying the H_2/CO_2 ratio we aimed at elucidating if either phenomena deactivates the catalyst. All experiments were conducted under the same conditions as specified above, however, instead of varying the CO_2 partial pressure, H_2 was modulated such that H_2/CO_2 ratios of 1.3/1, 4/1 and 6.7/1 were achieved, while using Ar as balance gas such that a total flow rate of 50 mL min^{-1} was ensured. Table 6-1 summarizes the initial CO_2 conversion and CH_4 selectivity. Notably, the CH_4 selectivity is hardly affected by an under-stochiometric H_2/CO_2 ratio. This can probably be reasoned with the bifunctionality of the Ni-Sm_2O_3 catalyst that relies on CO_2 adsorption on the support (see Chapter 4.8.1 and 6.3.3), whereas H_2 is expected to adsorb dissociatively on the metallic Ni particle. As there are no indications for adsorbed CO species on Ni, non-competitive adsorption of H_2 and CO_2 can be assumed. Consequently, the selectivity is less prone to react sensibly to the feed composition if the adsorbed CO_2 on

Table 6-1 Initial CO_2 conversion and CH_4 selectivity for the time-on-stream experiments.

T / °C	H_2/CO_2 / -	$\dot{V}_{CO2}$ / mL min^{-1}	$\dot{V}_{tot}$ / mL min^{-1}	m_{cat} / mg	$X_{CO2,0}$ / %	$S_{CH4,0}$ / %
300	1.3/1	5	50	40	21.8	95.6
300	4/1	5	50	40	48.6	99.0
300	6.7/1	5	50	40	58.4	99.5
400	4/1	5	50	33	72.0	97.1
490	4/1	5	50	5	55.5	76.6
300	4/1	2	50	40	54.6	99.4
300	4/1	5	50	40	48.1	98.9
300	4/1	8	50	40	47.2	98.8

the support is thermally stable, preventing its dissociation to CO. Hence, mainly the CO_2 conversion is affected by the availability of H_2 or the lack thereof, as is reflected in the data. Generally, the relative time-on-stream performance, as shown in Figure 6-2, follows the same asymptotic behavior as during the base case under the standard reaction conditions. Based on these results, any kind of coke formation or catalyst oxidation should be excluded for being responsible for the deactivation as the results contradict the thermodynamics of coke formation as well as catalyst oxidation which would be favored at lower H_2/CO_2 ratios. Instead, an improved catalyst stability was found with lower H_2/CO_2 ratios.

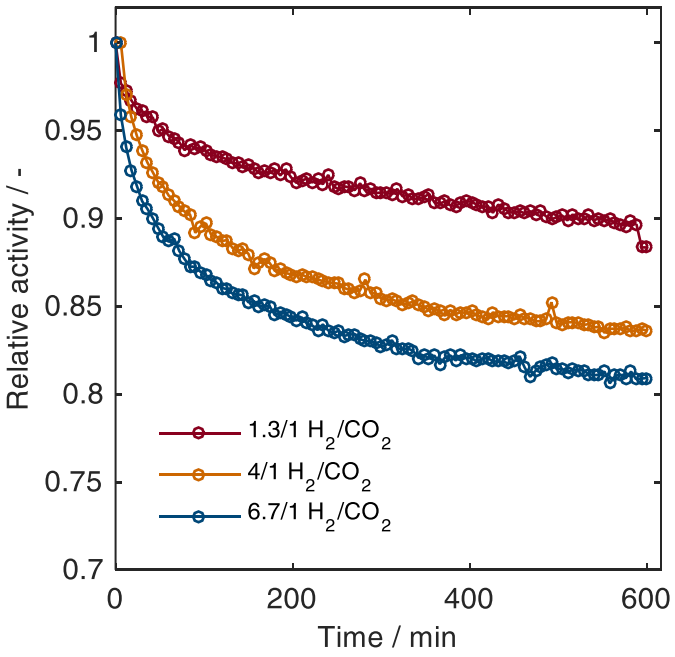

Figure 6-2 Influence of the H_2/CO_2 ratio on the catalyst stability. Conditions: $T = 300$ °C, $p = 1$ bar, $\dot{V}_{tot} = 50$ mL min^{-1} with 5 mL min^{-1} CO_2, Ar as balance, $m_{cat} = 40$ mg.

Influence of the reaction temperature

We further investigated the influence of the temperature on the catalyst stability. The temperature was set to 300, 400 and 490 °C. In order to avoid any limitations due to the equilibrium, the amount of catalysts used was lowered to 5 mg and 33 mg for experiments at 490 °C and 400 °C, respectively. The corresponding initial CO_2 conversion and CH_4 selectivity are given in Table 6-1 as well. As thermodynamically predicted, reaction temperatures exceeding 400 °C leads to a drastic decrease in the CH_4 selectivity due to significant contributions of the unwanted RWGS as side reaction. Unexpectedly in the first place, higher reaction temperatures markedly improve the catalyst stability. This points towards catalyst poisoning as the governing deactivation mechanism, probably due to the formation of excessively stable carbonates. Although beneficial in the short term, elevated temperatures raise questions about the sinter stability of the catalyst in the long run. Therefore, we performed with the catalyst three runs for 600 min at 490 °C, re-reducing the catalyst after each run at 490 °C for 10 h (in total: ~75 h on-stream). Even after the final run, the initial activity is fully restored indicating that the catalyst did not sinter significantly (see Figure D-4 in the appendix). This is confirmed by characterization of the spent catalyst. To this end, powder X-ray diffraction as well as N_2 physisorption measurements were carried out on the Ni-Sm_2O_3 catalyst after the reductive pre-treatment as well as after ~75 h time-on-stream at 490 °C as this marked the harshest conditions. As summarized in Table 6-2, characterizations of the spent catalyst reveal an impressively high thermal stability. Merely, the Sm_2O_3 crystallite

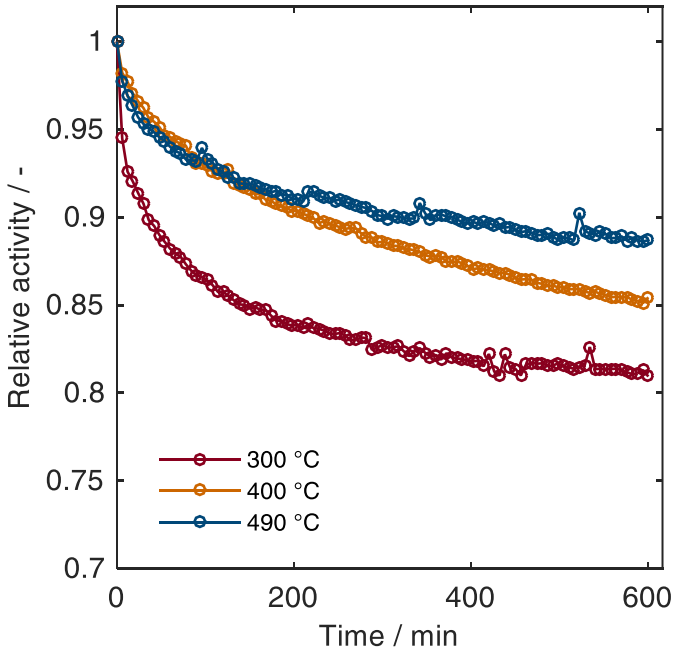

Figure 6-3 **Influence of the reaction temperature on the catalyst stability. Conditions: T = var., p = 1 bar, $\dot{V}_{tot}$ = 50 mL min^{-1} composed of 4/1/5 H_2/CO_2/Ar, m_{cat} = 40 mg.**

Table 6-2 **Specific surface area as well as Ni and Sm_2O_3 crystallite sizes of the 33 wt.% Ni-Sm_2O_3 catalyst as-synthesized, after reduction and after an ~75 h time-on-stream experiment at 490 °C.**

	As-synthesized	After reduction	After reaction
Specific surface area / $m^2\ g^{-1}$	21	21	22
Ni crystallite size / nm	10.3 ± 0.2[1]	8.3 ± 0.1	8.8 ± 0.2
Sm_2O_3 crystallite size ($Ia\bar{3}$) / nm	6.4 ± 0.4	12.7 ± 0.1	14.4 ± 0.1

[1] NiO crystallite size

size increased considerably during the reaction, however, this appears not to impact the catalyst's reactivity. The Ni crystallite size remained constant during the experiment, whereas the specific surface area decreased only marginally.

Influence of the CO_2 flow rate

Based on the temperature-dependence of the catalyst stability, poisoning appears to be the predominant issue. Here, the formation of thermally stable carbonates is likely due to the propensity of Sm_2O_3 to form such species (as is shown in Figure B-5 and Chapter 6.3.3). Consequently, increasing the flow rate of CO_2 should lead to a faster deactivation rate and was, therefore, set to 2 mL min^{-1}, 5 mL min^{-1} and 8 mL min^{-1}. As can be easily seen by the normalized activities in Figure 6-4, the conducted experiments support the notion that car-

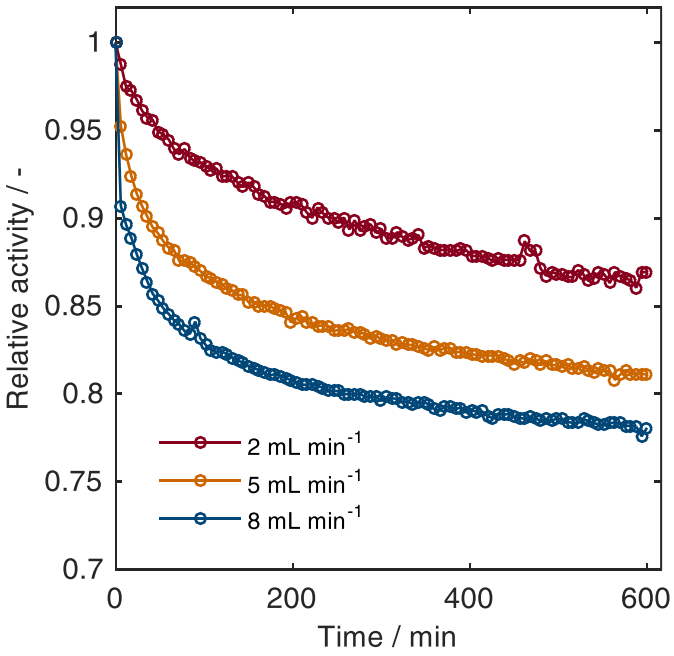

Figure 6-4 **Influence of the CO_2 flow rate on the catalyst stability. Conditions: T = 300 °C, p = 1 bar, $\dot{V}_{tot}$ = 50 mL min^{-1} composed of 4/1/X H_2/CO_2/Ar (as balance), m_{cat} = 40 mg.**

bonaceous species likely cause the deactivation as the relative activity drop increases the higher the CO_2 flowrate, i.e. the number of CO_2 molecules in contact with the catalyst. After 600 min, the relative activity drop is 13%, 19% and 22%.

6.3.3 Identification and Stability of Surface Adsorbates by DRIFTS

So far, the results strongly indicate that the catalyst suffers from poisoning due to excessively stable carbonates which block active sites. To confirm these observations and to understand if there is a specific type of carbonate that causes the activity loss, DRIFTS measurements were conducted.

After reductive pre-treatment and background acquisition (see appendix C.1 for the detailed description), the catalyst was exposed to the reaction gases (5 vol.% CO_2, 20 vol.% H_2 in He, total flow rate 100 mL min^{-1}) at 300 °C for 20 min. In the corresponding DRIFT spectra (Figure 6-5, red trace) evidence for monodentate (1060, 1342 and 1508 cm^{-1}), bidentate (856 and 1560 cm^{-1}) and polydentate carbonate (856, 1060 and 1459 cm^{-1}) species can be observed, whereas two sharp peaks at 1304 and 3016 cm^{-1} can be assigned to gaseous CH_4, thus confirming the reactivity of the catalyst.[227, 279, 280] Interestingly and in contrast to the observations on the Ru-Sm_2O_3 catalyst in Figure B-5 and Figure B-6, no indications for hydrogen carbonates (expected around 1654 cm^{-1}), formyl (expected around 1760 cm^{-1}) or adsorbed CO species (expected between 1900-2200 cm^{-1}) are found, pointing to a different mechanistic scenario for the Ni-Sm_2O_3 catalyst which apparently heavily relies on carbona-

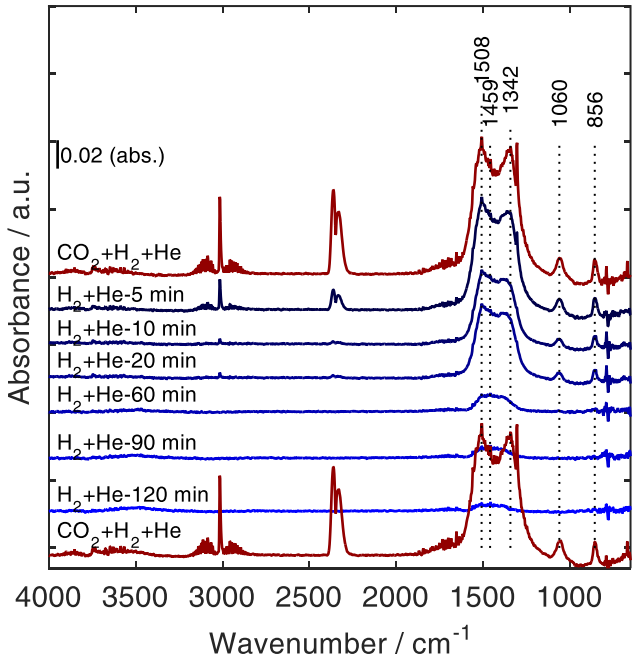

Figure 6-5 *Operando* DRIFTS experiments at 300 °C in different gas atmospheres. Red traces: exposure to 5 vol.% CO_2, 20 vol.% H_2 in He at a total flow rate of 100 mL min^{-1}. Blue traces: exposure to 20 vol.% H_2 in He at a total flow rate of 100 mL min^{-1}.

ceous species in line with the observations of Aldana et al.[154] on a Ni-CeO_2-ZrO_2 catalyst. Upon removal of CO_2 from the feed, surface coverage with carbonates decreases only slowly. Even after 120 min in H_2 and He, a broad absorption band between 1300 and 1600 cm^{-1} still indicates the presence of residual carbonates on the Sm_2O_3 support, however, the features are too undefined to reliably assign them to a specific species. Daturi et al.[227] attribute a higher thermal stability to bi- and polydentate carbonates than to monodentate carbonates on a CeO_2 support. Exposing the catalyst to the reactive conditions again, qualitatively restores the initial surface coverage and activity.

6.3.4 Reactivating the Catalyst

While the DRIFTS data confirms the presence of thermally stable carbonates, the data is, unfortunately, not fully conclusive which type of carbonate – monodentate or bi-/polydentate – poisons the catalyst. However, reactivation experiments are helpful to further elucidate the deactivation mechanism. After a standard time-on-stream experiment as defined in 6.2 the catalysts were regenerated at different temperatures, gas atmospheres and durations. After the regeneration step, another catalytic run under identical conditions followed to evaluate the efficiency of the applied regeneration procedure. The results are depicted in Figure 6-6. While decreasing the regeneration temperature to 400 °C simply increases the time required until the initial activity is achieved again from 4 to 8 h, strongly reducing conditions are imperative to yield a significant regeneration effect. When the catalyst was regenerated in Ar at 490 °C, the initial activity level could only be restored to ~88 % (at the end of the preceding time-on-stream experiment the activity level was at 84%), whereas the

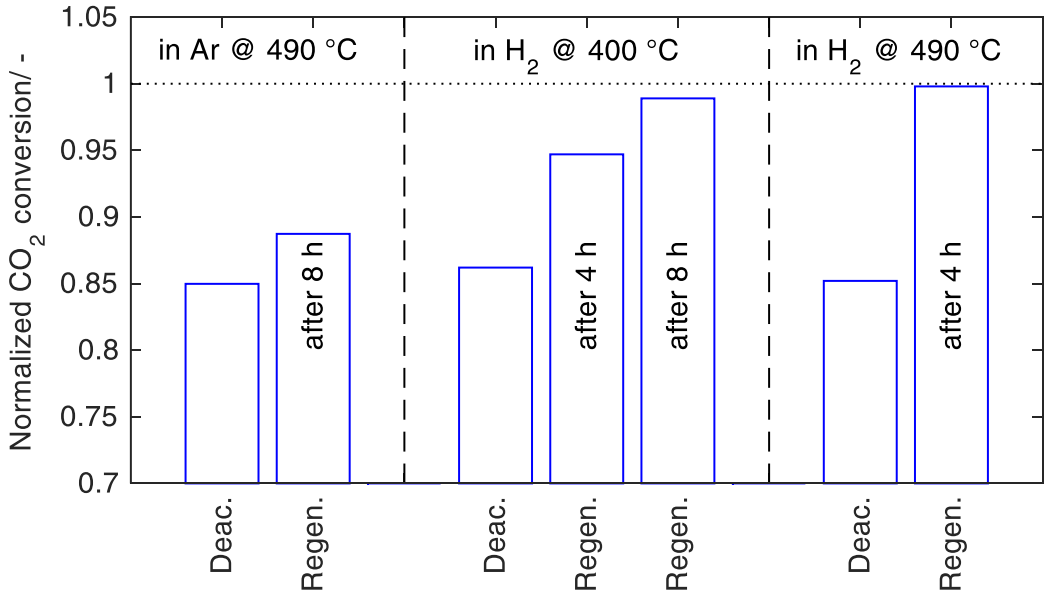

Figure 6-6 Influence of different atmospheres and temperatures to regenerate the spent catalyst.

full activity level could be achieved when H_2 was used instead of Ar. Consequently, desorption of carbonates, as also occurs in Ar atmosphere, is not sufficient to regenerate the catalyst but the catalyst needs to be re-reduced.

6.4 Putting the Pieces Together – A Sound Deactivation Mechanism

The results from the preceding subchapters can be used to propose a sound deactivation mechanism on Ni-Sm_2O_3 catalyst during CO_2 methanation as well as to formulate strategies how to limit its implications. Neither coking nor sintering occur during the time-on-stream experiments even under harsh conditions that would actually favor the occurrence of either phenomenon and are, therefore, not expected to pose problems under reasonable conditions within the investigated range. In fact, catalyst poisoning due to thermally stable carbonates appears to be the predominant deactivation mechanism as is shown by the accelerated deactivation for higher CO_2 partial pressures. *Operando* DRIFTS measurements confirm the formation of mono-, bi- and polydentate carbonates and show their slow desorption from the surface. Yet, regeneration experiments prove that desorption of carbonates from the surface is not sufficient to restore the catalytic activity, but that the catalyst support requires re-reduction, therefore ruling out monodentate carbonates (CO_2 adsorbed on lattice O^{2-}) as the predominant deactivation cause. Instead, stable carbonates formed on oxygen deficient sites poison the catalyst, which apparently desorb as CO, donating one oxygen atom to heal the oxygen vacant site in the samaria lattice. Restoring such site requires reducing conditions and high temperatures (as is shown by the H_2-TPR results on pristine Sm_2O_3 in Chapter 5.3.4). Consequently, the proposed mechanism also explains the observed improved stability with higher temperatures at which carbonates are increasingly destabilized and oxygen vacant sites are regenerated more easily. A schematic summary of the proposed deactivation mechanism is given in Figure 6-7. The proposed deactivation mechanism is in line with findings of Kim and Thompson[174], who assume that carbonates and formates formed at oxygen deficient sites deactivate an Au-CeO_2 water-gas shift catalyst and suggest that surfaces should be modified to minimize oxygen deficiency for a stable operation.

A remark – Why do we not observe catalyst deactivation over the Ru-Sm_2O_3 catalyst?

At this point, the seemingly contradictory time-on-stream behavior of the Ru-Sm_2O_3 catalyst, despite the identical support, shall not be omitted. As shown in Figure B-3 (appendix), the catalyst does not deactivate during the conducted time-on-stream experiment at 400 °C. Hence, the formation of thermally stable bi- or polydentate carbonates appears to be less of

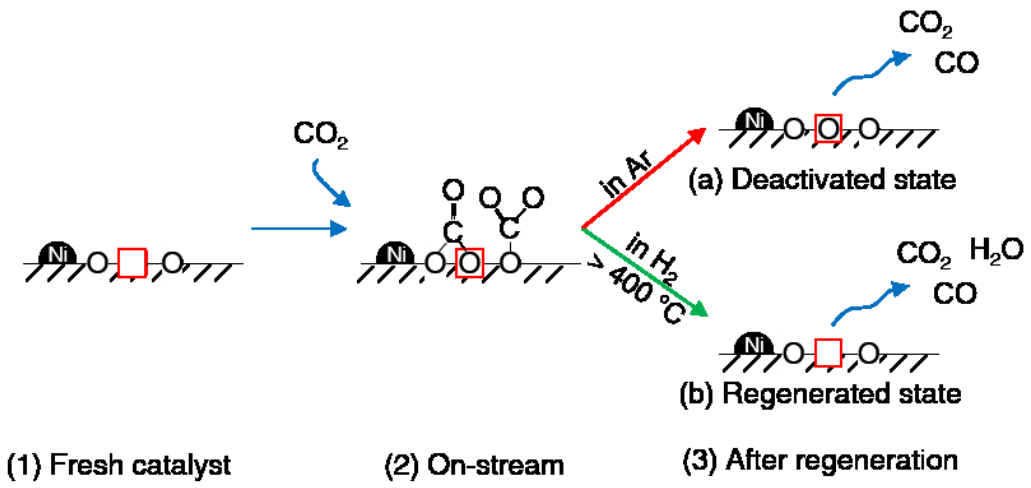

Figure 6-7 **Schematic depiction of the proposed deactivation mechanism and associated surface state of the catalyst during different stages of the lifetime experiment.**

an issue for the Ru catalyst. This is confirmed by the isothermal DRFITS experiments (Figure B-6) that, first of all, show no absorbance bands for polydentate carbonates. Furthermore, bidentate carbonates are formed in abundance but appear to be removed from the Sm_2O_3 surface in H_2 atmosphere in a significantly shorter time than from the Ni-based catalyst. Yet, additional research is required to understand the effect of the active component on the catalyst stability.

6.5 Interim Conclusions

This chapter elaborates on the time-on-stream behavior of the Ni-Sm_2O_3 catalyst, exemplarily studied at the catalyst with 33 wt.% Ni loading, under different atmospheres to understand the governing deactivation mechanism. It could be demonstrated that the catalyst stability is dependent on the process conditions; yet easily reversible by a regeneration step in H_2 and at elevated temperatures. Particularly higher reaction temperatures and lower CO_2 flow rates improve the time-on-stream behavior. In combination with *operando* DRIFTS and regeneration experiments, the results show a propensity of the catalyst to form stable carbonates at oxygen deficient sites (bi- and polydentate carbonates) which block active sites and, thus, poison the catalyst. Characterization of the spent catalyst by XRD and N_2 physisorption reveal a high thermal stability of the xerogel catalyst, which should allow to adjust the process conditions, i.e. higher reaction temperatures or periodic regeneration steps, such that the high activity can be maintained or restored. The results reveal the ambivalent effect of the basicity of the catalyst support, on the one hand improving the reactivity while at the same time giving rise to additional deactivation mechanisms.

A remark – Influence of transient reaction conditions on the time-on-stream behavior

The Power-to-Gas technology is often expected to be implemented in decentralized, small scale applications. However, for these small-scale applications large storage systems are unfeasible due to the associated costs. Instead, dynamic reaction conditions that minimize temporary storage capacities are often discussed as a novel approach, implying a departure from the usually applied steady-state conditions. In these small-scale systems, transients in the reaction conditions are to be expected that imply an additional uncertainty.[174, 281] Yet, efforts regarding the time-on-stream behavior under transient feeds are scarce, so far.[282] Mutz et al.[172, 173] investigated the stability of supported Ni particles during H_2 dropouts and found a fast bulk like oxidation of Ni if oxygen impurities are present in a H_2-free feed.

Obviously, dynamic process conditions can have multiple facets, but from a catalyst point of view and with respect to the CO_2 methanation, particularly changing H_2/CO_2 ratios and, as a consequence of that in combination with the exothermicity of the methanation reaction, reaction temperatures are of concern. To this end, additional experiments designed to understand the impact of transient reaction temperatures and H_2/CO_2 ratios were performed and are presented in the appendix E.

7

Extended Outlook – Towards the Influence of the Structural Properties

The previous chapters elaborated on the effect of the support's surface chemistry on the CO_2 methanation. However, apart from that, also the internal mass transport (pore diffusion) is a function of the support, although of its structural properties, and is usually assumed to be either reaction rate limiting or not. This chapter shows that this notion is actually inaccurate and oversimplified (Chapter 7.1). In fact, different diffusions velocities of the reactants within the pore network as well as confinement effects can drastically affect the catalytic performance; however, their systematic investigation is difficult to achieve and requires advanced model catalysts for a conclusive and in-depth investigation of the structural properties on the catalytic performance. Chapter 7.2 contributes here by expanding the current "toolbox" by methods to precisely tailor the structural properties of Sm_2O_3 xerogels. Combining the new methods with the already established synthesis of Ru nanoparticles opens the path for systematic investigations of the catalytic performance in dependence of the structural properties in the future.

Parts of Chapter 7.1 have been published as a collaborative work in J. Ilsemann, S. Straß-Eifert, J. Friedland, L. Kiewidt, J. Thöming, M. Bäumer and R. Güttel, "Cobalt@Silica

Core-Shell Catalysts for Hydrogenation of CO/CO_2 Mixtures to Methane", ChemCatChem, 2019, 11, 19, 4884-4893, of which only a brief summary is given in the following subchapter.

7.1 The Beneficial Effect of a Porous Network

When the effect of the pore size on the catalytic efficiency is discussed, this is usually boiled down to the question if diffusion inside the catalyst particle is limiting the reaction rate or to balance the "active surface area vs. pore size conflict". Consequently, efforts have been made to increase the pore size or to synthesize catalyst particles with hierarchical porosity to facilitate mass transfer inside the catalyst to enhance the reactivity without sacrificing too much active surface area and to shift diffusion limitations to higher temperatures and larger catalyst particles.[283] However apart from that, a porous network inherently generates a confinement effect, with a locally increased residence time and a higher chance of readsorption of products and intermediary species affecting the catalytic activity and selectivity.[9, 284–287]

In a recent collaborative work with the group of Prof. Güttel (Ulm University), we demonstrated that there can be a beneficial effect of a porous network beyond the typical "active surface area vs. pore size" notion.[63] In that study, we compared a cobalt@silica core-shell catalyst ($Co@mSiO_2$), where an active Co core is fully encapsulated by an inert, mesoporous SiO_2 ($mSiO_2$) shell, with a supported $Co\text{-}mSiO_2$ catalyst comprised of the identical Co particles and $mSiO_2$ support regarding their catalytic performance in the CO_2 methanation. As, for the supported catalyst, the size of the Co core (~40 nm) exceeded the $mSiO_2$ pore size (~3 nm), the Co cores could not penetrate the pore network of the silica support and the particles were thus deposited on the outer surface, only. This approach enabled us to investigate the effect of the porous shell in an isolated manner. A schematic depiction of the systems is given in Figure 7-1. Two findings stood out:

1. The CO_2 conversion for the core-shell catalyst was significantly higher than for the supported $Co\text{-}mSiO_2$ catalyst. For instance, even though the reactants had to diffuse through the porous shell to get to the active Co core, the $Co@mSiO_2$ catalyst was about 3x as active as the supported catalyst at 350 °C.
2. Even more drastic differences could be observed regarding the CH_4 selectivity, which was about 4-5x higher for the $Co@mSiO_2$ catalyst.

For the interpretation of these findings, two underlying phenomena are plausible – mass transfer as well as confinement effects. For the catalytic turnover, the concentration of the reactive species in proximity of the active nanoparticle is decisive. For the core-shell catalyst, the composition at the reaction locus obviously depends on the diffusive transport of reac-

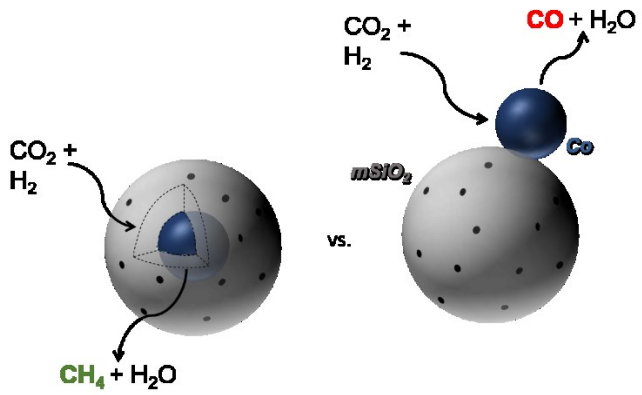

Figure 7-1 **Schematic depiction of the Co@mSiO$_2$ core-shell catalyst and the supported reference catalyst. Reprinted with permission.**[63]

tants and products through the porous shell. Consequently, the diffusion rates governed by the molecular diffusion coefficients and the pore size, as well as the effective diffusion length given by the spatial arrangement of the active nanoparticles inside the supporting shell is important. We believe that the pore size plays a major role for the core-shell architecture, rather than the diffusion length. This hypothesis becomes evident, if the effect of the pore size on the diffusion mechanism, in particular for meso- and microporous materials, is considered. While Knudsen diffusion occurs in mesoporous structures, configurational diffusion dominates in microporous catalysts.[288] The latter mechanism depends strongly on the size ratio of the pore and the diffusing molecule, as well as on the interaction between the wall and molecule, among other factors.[288] Thus, a tremendously different composition in close proximity of the shell encapsulated cobalt core compared to the gas bulk and to the surface exposed Co particles in the supported Co-mSiO$_2$ is very likely, owing to the size difference between the pores and the involved molecules. Similar findings have been observed for related reactions where the selectivity is highly sensitive to the reactant concentration ratios at the active sites like such as the Fischer-Tropsch synthesis.[289, 290] Rytter et al. found a higher CH_4 selectivity with increasing catalyst particle size that they attributed to the faster diffusion of H_2 than CO, and thus to an increasingly over-stoichiometric H_2/CO ratio at the active sites with increasing pore length.[289] In other words, the reactant mixture segregated along the pore length.

Another possible explanation for the reported observations on the Co@mSiO$_2$ catalyst is based on an extension to the confinement effect, specifically on the restricted exit of product molecules through the silica shell, encapsulating the Co nanoparticles. Considering that CO_2 does not adsorb on SiO_2 surfaces, as shown in Chapter 4.8.4, the reaction proceeds solely over the cobalt surface, where CO_2 adsorbs dissociatively,[291, 292] leading to the desorption of CO as a byproduct. The restricted exit effect in the confined environment might increase the probability for readsorption of CO on cobalt as compared to the supported reference

catalyst. Thus, the methanation of the CO intermediate is favored for the core-shell structure, which explains the higher CH_4 selectivity observed. Similar findings have been reported recently by Le et al.[293], who showed that the confinement effect present in silica nanopores enhances the CH_4 formation rate during CO_2 methanation.

Admittingly, these findings describe two extreme cases – fully encapsulated vs. non-encapsulated active Co core; however, it is fair to assume that these findings are also applicable to catalysts with uniform properties as the investigated cases de facto represent active sites at the inlet and the end of a pore within a catalyst with a uniform distribution of active sites along the pore length. If, now, effects of the structural properties on the catalytic performance for supported catalysts are to be studied systematically, factors affecting the surface reaction (e.g. particle size effects of the active component or differences in support's surface chemistry) must be excluded, while a uniform distribution of the active component has to be ensured. This eliminates impregnation, *one-pot* sol-gel and (co-) precipitation techniques for catalyst preparation, evident for instance in Takahashi et al.[144]. They prepared Ni-SiO_2 xerogels and controlled the pore size by templating methods to investigate pore size effects during CH_4 reforming. However, the addition of the template also affected the Ni particle size, such that no clear trends in the catalytic reactivity were found. Consequently, future research strategies must rely on more complex building block approaches if supported catalysts are to be studied. This thesis tries to contribute here by establishing a method to precisely tailor the pore size of Sm_2O_3 xerogels, which can then either be used to support uniform Ru nanoparticles or as a single-component catalyst.

7.2 Controlling the Porosity of Sm_2O_3 Xerogels

The development of synthesis strategies for materials with controlled porosity or even hierarchically ordered structures has been of great interest in the recent past due to their high importance for a wide range of applications. Among the frequently used techniques are sol-gel methods. As described in Chapter 3 already, during the sol-gel process a network consisting of aggregated particles is formed, in which the number, size and density of the particles in a specific volume can be adjusted by the synthesis conditions. After formation of a rigid gel, the space occupied by the solvent between the solid network equals the potential pore volume/pore size after drying.[294] Basically, the efforts made to control this space can be grouped into two categories – controlling the effects of solvent removal and templating techniques – which are described in the following subchapter.

7.2.1 Feasible Strategies

The final pore structure is determined by the shrinkage of the network during the solvent removal from the wet gel due to capillary forces induced by the retracting solvent meniscus.

As the extent of shrinkage is determined by the balance between the collapsing resistance of the gel (stiffness) and the present force of contraction (capillary pressure), either the stiffness can be increased or the capillary forces can be decreased to adjust the pore size.[295, 296] The stiffness, for instance, can be controlled by the rate of polycondensation during the sol-gel transition or by the appropriate conditions during the subsequent aging step.[295, 297] The capillary forces, in turn, are a function of the liquid-vapor interfacial energy (surface tension), the wetting angle and the pore radius. For instance, replacing the solvent inside the pore structure with a solvent possessing a lower surface tension would reduce the capillary forces, and thus, lead to larger pores. In the extreme case, the wet gel is dried with supercritical fluids, thus eliminating the capillary forces as an influential factor inside the structure and an aerogel is obtained. The wetting angle, in turn, can be adjusted by rendering the gel surface hydrophobic, however, that approach is usually limited to SiO_2 containing xerogels as the hydrophic groups are mostly silanols.[294] Ren et al.[298] introduced an elegant way of adjusting the pore size of an Al_2O_3 aerogel prepared by the epoxide-addition method by simply decreasing the molar ratio of propylene oxide to metal salt during the synthesis from the usually reported 11:1, which results in a slower polycondensation reaction and significantly less porous gels. It is believed that the different porosities would also be reflected in xerogels, due to the dependence of the capillary forces of the pore radius. Unfortunately, this method however only allows to decrease the pore size, as increasing the amount of propylene oxide quickly led to precipitation, instead of gelation.

If, however, the pore size of a gel is to be increased beyond the "inherent" level, templating techniques have to be used to generate additional or larger pore spaces during the synthesis. These techniques are appealing due to their simplicity and are, usually, distinguished into hard and soft templating techniques. While for the former the pore structure resembles the added solid template, this relationship holds not true for the soft templating techniques. These synthetic approaches rely on phase separation effects, therefore, the term "structure-directing agent (SDA)" is deemed more appropriate and used from here on.[294] Polymeric additives as structure-directing agents induce a phase separation process usually by spinodal decomposition of the system that separates the mixture into a SDA rich and a SDA poor phase.[299] Concomitantly to the phase separation, the sol-gel transition occurs until the gelation point, described by the formation of a solid network and the associated sharp rise of the viscosity, is reached. Nakanishi et al.[299] could show that the structure is basically frozen in in that specific shape, due to the irreversibility of the polycondensation reaction of the sol. That "snapshot" of the gel structure depends on the relative time of occurrence of phase separation and gelation. Consequently, all parameters affecting the sol-gel transition can have a pronounced effect on the final structure of the gel as different "snapshots" of the phase separation process are taken.

Extensive studies on various types of structure-directing agents have been conducted, usually comparing the effect of different polymeric additives on their ability to induce phase separation. In particular, Nakanishi and coworkers[144, 299–303] have contributed here to understand the underlying principles of phase separation and how this can be applied to produce porous Al_2O_3, SiO_2 and Fe_2O_3 gels. According to their findings, particularly hydrogen-bonding additives such as polyethylene glycol/oxide or poly acrylamide are best suited to induce phase separation. However, no such efforts have been reported for rare earth metal oxides, neither could mathematic correlations be established describing the structural parameters in dependence of the type or amount of additive for any metal oxide, so far. If, though, highly defined model catalysts are to be studied, such relationships need to be established first to truly tailor the structural properties. As the propensity to induce phase separation depends on the additive and its interaction with the sol, we first screened different structure-directing agents for their applicability and captured two "snapshots" of the phase separation process by conducting the synthesis at two different temperatures. Based on these results, we chose the most promising additive for a concentration variation study to, ultimately, establish an empirical correlation between the used additive amount and the resulting structural properties.

7.2.2 Comparing the Effect of Different Structure-Directing Agents

In the following, the effect of additives with different molecular weight on the structural properties of Sm_2O_3 xerogels, prepared by the PO-CA method (see Chapter 3.2.2), is investigated. Specifically, we examine the influence of block polymers with different molecular weight (polyethylene oxides: molecular weight 8,000, 100,000, 600,000 and 1,000,000 g mol^{-1}, denoted as PEG8000, PEO100K, PEO600K and PEO1M, respectively) and a block copolymer (Pluronic P123, molecular weight: 5800 mol g^{-1}) on their ability to introduce large meso- or even macropores into a Sm_2O_3 xerogel as these additives have been successfully applied to adjust the porosity in SiO_2 and Al_2O_3 gels.[299–301, 304, 305] Identical amounts of the additives (0.01 g) were dissolved in the ethanolic solutions before the addition of citric acid. Small amounts of deion. H_2O (1 mL) had to be added as well to increase the solubility of the solid polymers. All other amounts were kept the same as stated in Chapter 3.2.2, but solvent exchange was performed in hexane as in pre-experiments sharper pore size distributions could be obtained. Further, the calcination time was increased to 4 h as some samples were not fully crystalline. For reference purposes, a pure Sm_2O_3 xerogel was prepared following the same adapted synthesis procedure but without any polymeric additives. Since the scale-up of the process might be difficult due to the number and complexity of involved steps, i.e. phase separation and gelation, the target yield was fixed at 0.5 g of Sm_2O_3 at all times. As our method leads to the formation of a rigid gel within a few seconds, we additionally

performed the synthesis in an ice bath (-18 °C) to slow down the gelation kinetics to allow more time for the phase separation to take place. This adjustment successfully delayed gelation of the sol by several hours. The detailed descriptions of the synthesis procedures are stated in the appendix F.1. After calcination, all samples were analyzed by N_2 physisorption regarding their structural properties. Additional SEM images were acquired from selected samples. The procedural descriptions can be found in the appendix F.2.

Table 7-1 summarizes the specific surface area, pore volume and average pore size, whereas Figure 7-2 shows the measured isotherms and derived pore size distributions for the samples prepared at ambient conditions. For a better visibility, the isotherms are normalized to their overall N_2 uptake. Note that for the presentation of the pore size distribution, the logarithmic differential distribution dV(log r) was chosen as that representation shows small and large pores equally well and is plotted against the pore radius on a log-scale. However, this representation only indicates which pores sizes are present, whereas their abundance cannot be derived directly. Therefore, we included an additional measure (maximum in the pore size distribution), which states the most abundant pore size. The data is also normalized to the maximum value for a simplified comparison. All additives drastically alter the structural properties of the Sm_2O_3 xerogel, albeit in different ways. The small hysteresis loops in the measured isotherms indicate mainly macroporous samples with some contribution of

Table 7-1 **Specific surface area, pore volume as well as the average pore size and the maximum in the pore size distribution, as determined by N_2 physisorption measurements for Sm_2O_3 xerogels without and with different types of additives prepared at two temperatures.**

Additive	Specific surface area / $m^2\ g^{-1}$	Pore volume / $cm^3\ g^{-1}$	Average pore radius / nm	Max. in pore radius distribution / nm
No additive	23	0.06	5.3	3.5
PEG8000	28	0.32	22.6	15.1
PEO100K	40	0.35	17.4	12.6
PEO600K	6	0.02	8.7	1.9
PEO1M	7	0.03	8.1	1.9
P123	9	0.09	19.6	25.7
At -18 °C				
PEG8000	42	0.29	14.3	9.4
PEO100K	29	0.23	15.9	12.4
PEO600K	23	0.15	13.1	10.6
PEO1M	20	0.14	14.3	9.3
P123	42	0.3	14.4	9.5

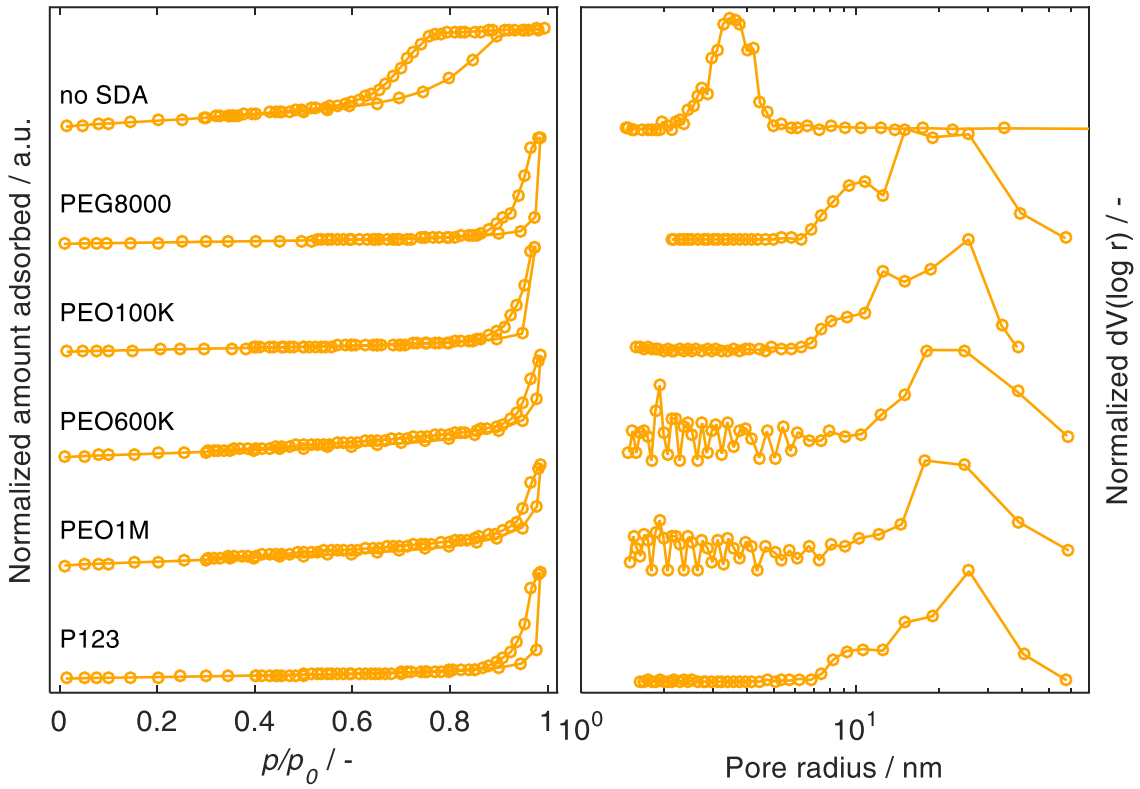

Figure 7-2 **(left) N_2 physisorption isotherm of the Sm_2O_3 xerogels with 0.01 g of various SDA; (right) derived pore radius distributions. The pore radius is plotted on a logarithmic scale. The synthesis was performed at ambient conditions (22 °C)**

mesopores. The absence of a sharp increase in the N_2 uptake at low relative pressures confirms that no micropores are present in any sample. Additives with the lowest molecular weight (PEG8000, PEO100K and P123) significantly enlarged the average pore radius to medium-to-large mesopores. Interestingly, only the addition of PEG8000 and PEO100K also increased the pore volume, whereas the addition of P123 led to a considerably denser Sm_2O_3 xerogel. Instead of increasing the porosity, using PEO600K and PEO1M as structure-directing agents compressed the Sm_2O_3 structure as the pore volume and specific surface area are significantly smaller than for the reference sample. Further, these xerogels exhibit a poorly defined, rather inhomogeneous pore size distribution.

When the synthesis is performed at -18 °C, the hysteresis loops in the isotherms become more pronounced, clearly indicating mesoporosity (Figure 7-3). The derived pore size distributions are considerably sharper for all additives, and shifted to smaller radii. No drastic compacting of the Sm_2O_3 xerogel due to the addition of PEO600K, PEO1M and P123 was observed. In fact, decreasing the synthesis temperature led to less distinct differences between the used structure-directing agents as indicated by the similar porosity parameters, albeit still smaller than for the additives with a lower molecular weight. In other words, a lower

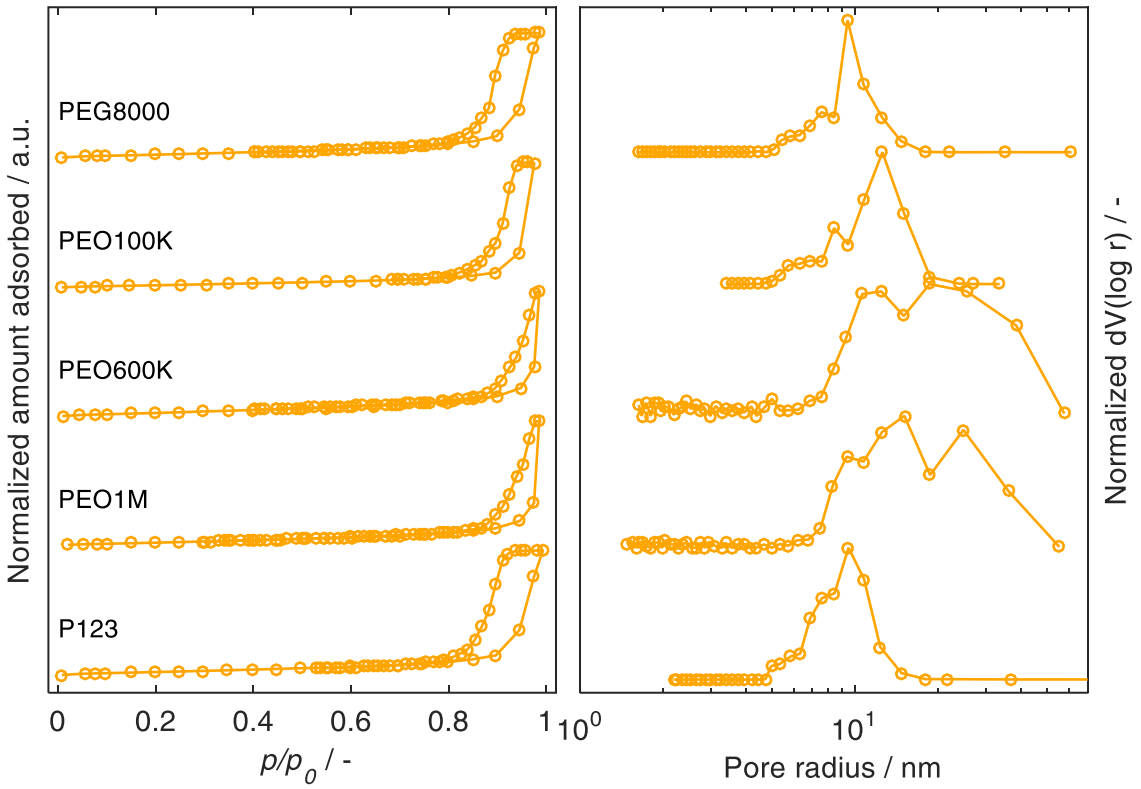

Figure 7-3 **(left) N_2 physisorption isotherm of the Sm_2O_3 xerogels with 0.01 g of various additives; (right) derived pore radius distributions. The pore radius is plotted on a logarithmic scale. The synthesis was performed in an ice bath at -18 °C**

synthesis temperature resulted in more homogenous and finer structures. A more pronounced effect of the structure-directing agent addition, however, is achieved at ambient synthesis temperatures. Distinct differences in the micro structure in dependence of the applied additive are also observed in the SEM images (Figure 7-4). While, in comparison to the additive-free Sm_2O_3, an increased pore size is visible for all SDAs (as was to be expected from the N_2 physisorption experiments), an interconnected network formed upon addition of PEG8000 and PEO100K, whereas a coarser, rather fragmented structure of almost spherical particulates formed in the presence of PEO600K and PEO1M. Given that PEG8000 and PEO100K-PEO1M only differ in the chain length of the (-CH_2-CH_2-O-) block, the observed differences in the microstructure can be explained with the relative time of occurrence of phase separation and gelation. Coarser, even fragmented structures are formed, the longer the time difference between phase separation and gelation is.[294, 299] It is likely that due to the higher molecular mass and the larger amount of possible hydrogen binding sites of PEO600K and PEO1M, phase separation proceeds significantly faster as for the lighter additives, whereas the gelation time is not significantly affected by the type of additive. Consequently, the time difference between phase separation and gelation is larger for the additives with a higher molecular weight, giving rise to the rather fragmented structures. According to Feinle et

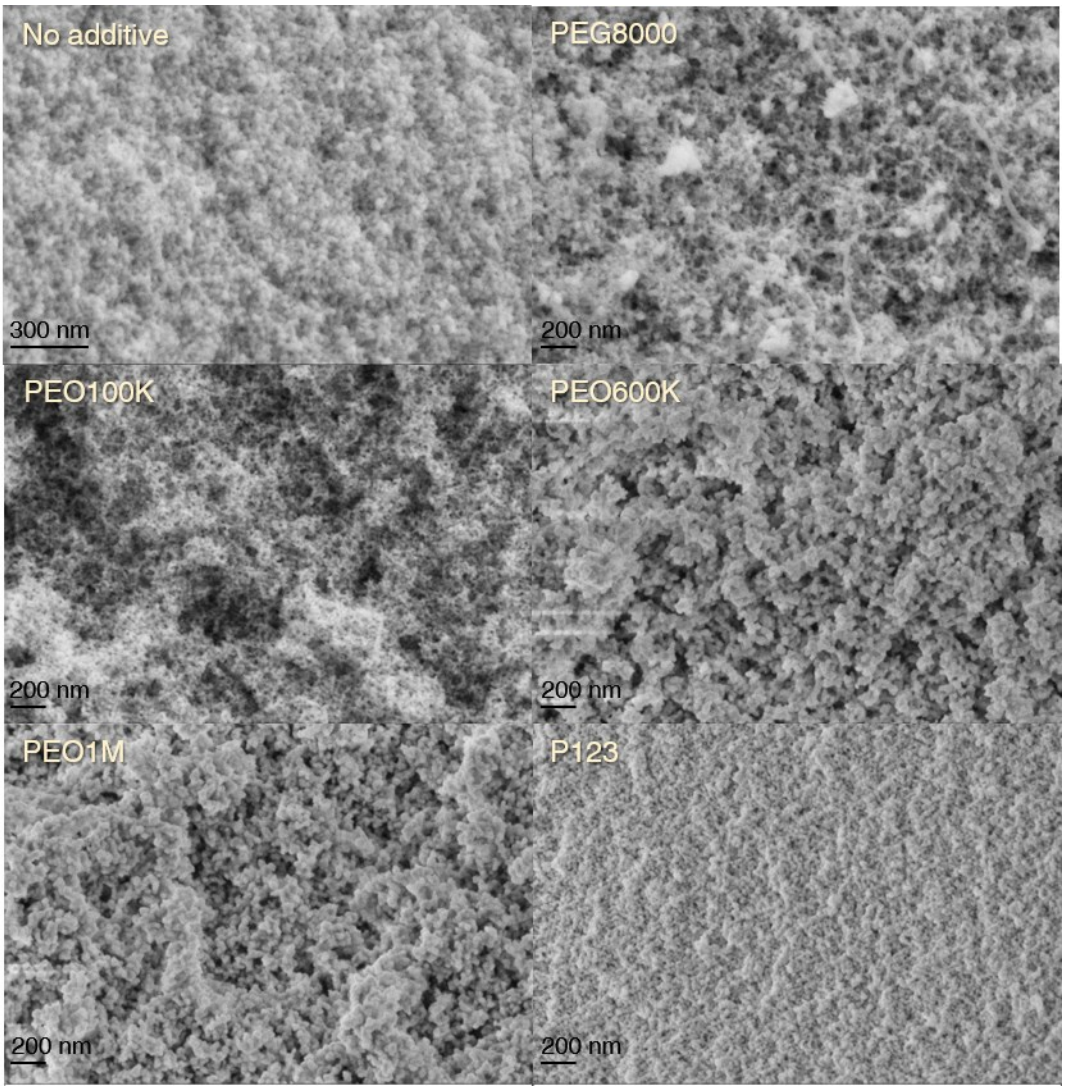

Figure 7-4 SEM images of Sm_2O_3 xerogels prepared with and without structure-directing agents. All samples, except the sample without additive, were synthesized at -18 °C.

al.[294], this can, in extreme cases, even lead to non-monolithic structures. This, however, was not observed during our experiments.

7.2.3 Tailoring the Structural Properties – The Influence of the Amount of PEG8000

Based on these results, we chose to narrow the focus on the effect of PEG8000 as a structure-directing agent, as the sharpest pore size distribution comprised of mainly large mesopores and a clearly interconnected network was achieved upon its addition. To investigate if we can, actually, tailor the porosity by the addition of PEG8000, we varied the added amount of PEG8000 by several order of magnitudes (0.001 g up to 0.1 g, target yield Sm_2O_3: 0.5 g) and, again, performed the synthesis at ambient temperature as well as at -18 °C.

For the samples produced at ambient conditions, Figure 7-5 shows the N_2 physisorption isotherms and the derived pore size distributions, while Table 7-2 summarizes the porosity

parameters. Again, following the IUPAC classification, the measured N_2 isotherms indicate the formation of mostly large mesopores as well as a few small macropores. Only the sample containing 0.001 g PEG8000 shows a pronounced hysteresis loop and pore size distribution in the mesoporous regime. Additionally, the pore size distribution is significantly sharper as for the samples with higher amounts of additives. Generally, no clear trends on the amount of PEG8000 added to the synthesis can be observed and the pore size distributions appear rather broad and undefined, indicating an abrupt, uncontrolled process. However, when the gelation is slowed down, a clear picture evolves showing distinct trends in dependence of the amount of PEG8000. The hysteresis loop in the N_2 isotherms (Figure 7-6) decreases in size with increasing amount of additive and the derived pore size distributions are shifted to larger pore sizes as is also reflected in the average pore size (Table 7-2). In fact, plotting the pore volume, average pore size and maximum in the pore size distribution against the amount of PEG8000 reveals a logarithmic relationship between the structural parameters and the PEG8000 addition with remarkable accuracy over a wide range of added PEG8000 amounts (Figure 7-7). Apparently, the structural properties are highly sensitive to the addition of small amounts of PEG8000, while larger amounts have only an incremental, additional effect

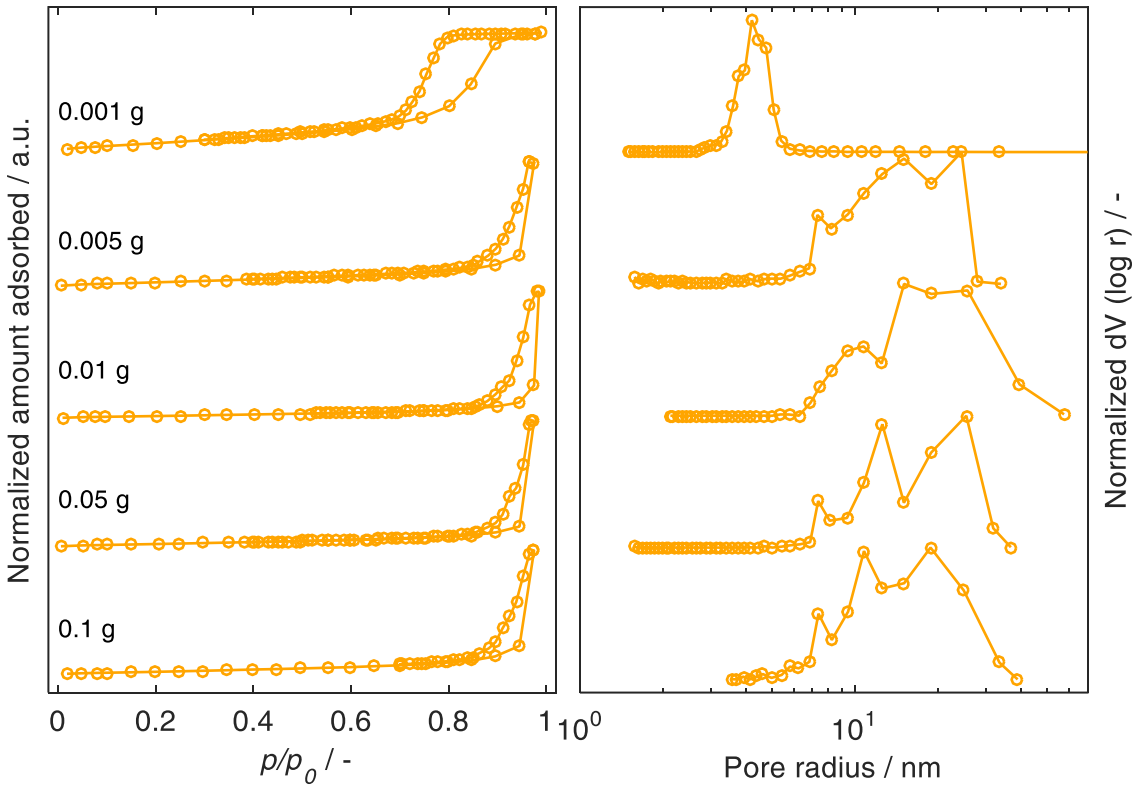

Figure 7-5 (left) N_2 physisorption isotherm of the Sm_2O_3 xerogels with various amounts of PEG8000; (right) derived pore radius distributions. The pore radius is plotted on a logarithmic scale. The synthesis was performed at ambient conditions (22 °C).

Table 7-2 **Specific surface area, pore volume as well as the average pore size and the maximum in the pore size distribution, as determined by N_2 physisorption measurements for Sm_2O_3 xerogels prepared with different amounts of PEG8000 and at two different synthesis temperatures.**

PEG8000 concentration	Specific surface area / $m^2 g^{-1}$	Pore volume / $cm^3 g^{-1}$	Average pore radius / nm	Max. in pore radius distribution / nm
0.001	32	0.09	5.8	4.2
0.005	30	0.18	11.9	7.2
0.01	28	0.32	22.6	15.1
0.05	29	0.26	17.8	12.7
0.1	29	0.22	14.7	10.7
At -18 °C				
0.001	19	0.04	4	1.9
0.005	41	0.19	9.3	6.3
0.01	42	0.29	14.3	9.4
0.05	40	0.35	17.2	9.4
0.1	37	0.38	20.2	15.1

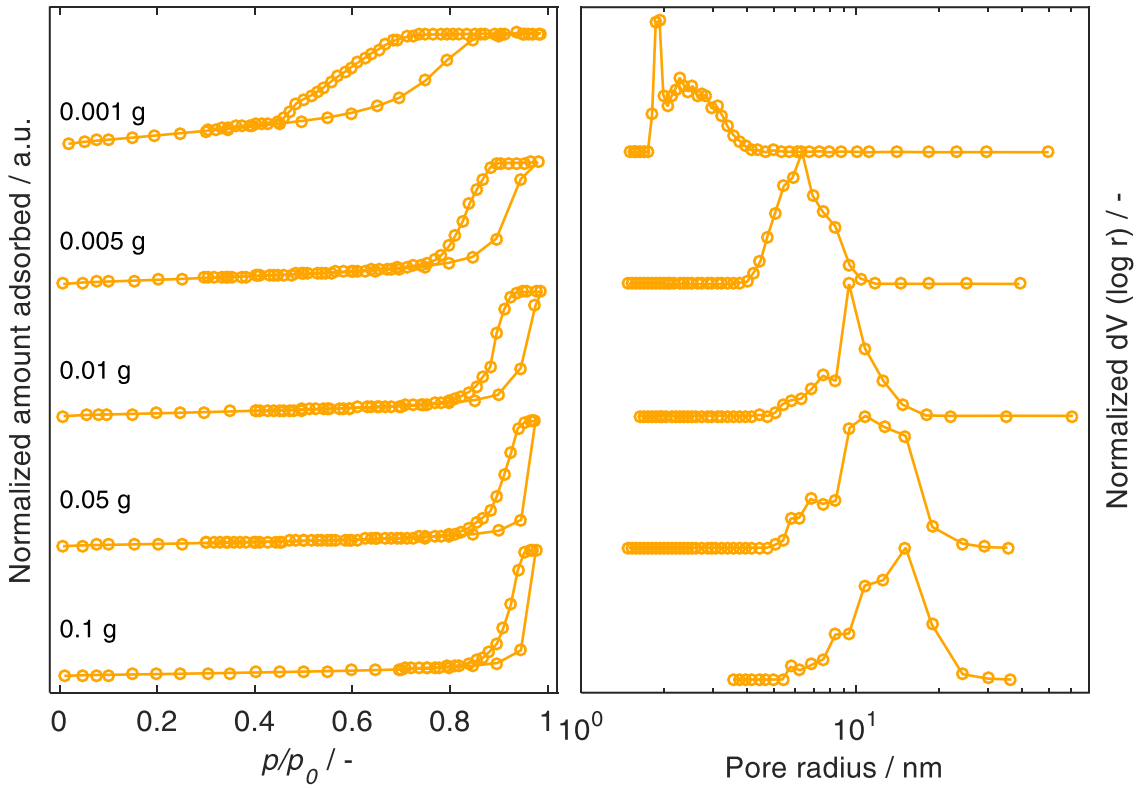

Figure 7-6 **(left) N_2 physisorption isotherm of the Sm_2O_3 xerogels with various amounts of PEG8000; (right) derived pore radius distributions. The pore radius is plotted on a logarithmic scale. The synthesis was performed in an ice bath (-18 °C).**

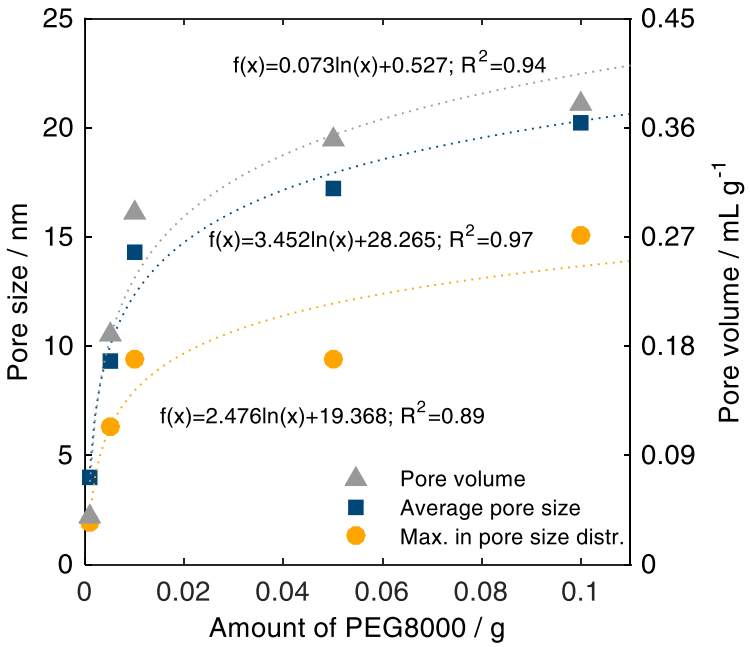

Figure 7-7 Dependency of the pore size and pore volume of Sm_2O_3 xerogels on the amount of PEG8000. The synthesis was performed at -18 °C.

on the structure, possibly due to micelle formation. Additional SEM images were recorded for the samples with large amounts of PEG8000 (Figure 7-8) and confirm the formation of an interconnected network, rather than the formation of a fragmented structure.

7.3 Interim Conclusion

This chapter illustrated the importance of the structural properties as a decisive factor for the catalytic performance using a Co@mSiO_2 core-shell catalyst, and thereby motivates the necessity for systematic studies on the influence of the structural properties. A pre-requisite for such studies is the ability to prepare support materials with precisely tunable pore sizes.

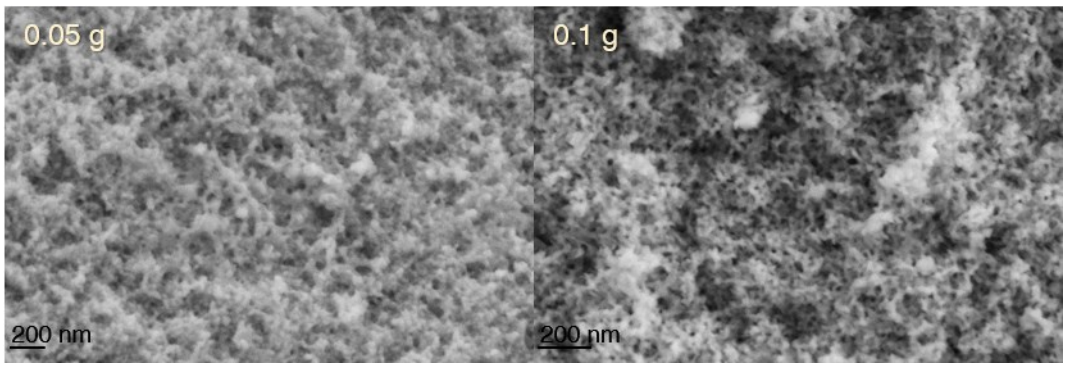

Figure 7-8 SEM images of Sm_2O_3 xerogels prepared with 0.05 and 0.1 g PEG8000 synthesized at -18 °C.

In this chapter, this could be achieved by expanding the sol-gel method established in Chapter 3 by the addition of structure-directing agents to induce phase separation in the sol prior to gelation, ultimately leading to larger pores. To this end, polyethylene oxides (block polymer) with different molecular weights ranging between 8,000 and 1,000,000 g mol^{-1} as well as a block co-polymer (Pluronic P123) were tested and compared regarding their ability to affect the porosity during the synthesis of Sm_2O_3 xerogels. The presented method clearly shows the potential of PEG8000 as a structure-directing agent and allows to precisely tailor the structural properties of Sm_2O_3 xerogels if the gelation process is sufficiently slowed down, which was achieved here by performing the synthesis at -18 °C. Yet, additional experiments are required to elucidate the pore forming mechanism, i.e. the time scale of phase separation. Understanding and manipulating the underlying time scales is expected to contribute to a broader applicability to tailor the porosity of other REOs and transition metal oxides as well as in the scale-up of the synthesis. Yet, the highly defined Sm_2O_3 xerogels can potentially be applied as tailored single-component catalysts or as model catalyst support for studies regarding the structural parameters, already.

8

Conclusion

In recent years, the CO_2 methanation has developed into an often-investigated reaction due to its potential to reduce CO_2 emissions in the atmosphere and its applicability in the power-to-gas process as a long-term energy storage with high capacity. To date, the viability of the process is hampered by the lack of catalysts which are able to activate and reduce the stable CO_2 at low reaction temperatures. Usually, supported catalysts are applied that are comprised of an active component (i.e. Ni and Ru) and an oxidic, high-surface area support. While the role of the active component is well understood, this thesis puts the support at the center and considers it at as an integral part to design more efficient catalysts. It was hypothesized that the support's surface chemistry, i.e. the acid/base properties play an integral role in the adsorption and activation of carbon dioxide to enhance the reactivity. Specifically, this thesis aimed at:

- isolating and understanding the influence of the acid/base properties of the support by studies on supported Ru model catalysts to develop support-activity correlations,
- applying these correlations in order to produce a highly active catalysts which is competitive with industrial standards and literature systems,

- and understanding the time-on-stream and deactivation behavior of the developed systems.

To this end, model catalysts with uniform Ru particles were deposited on four different oxide classes grouped according to their type of basicity: rare earth metal oxides (Sm_2O_3, Gd_2O_3 and Y_2O_3) with Brønsted and Lewis basic sites, TiO_2 and ZrO_2 as Lewis but non-Brønsted basic supports, as well as MgO and Al_2O_3 as Brønsted but non-Lewis basic oxides, and SiO_2 which exhibits neither Brønsted nor Lewis basic sites. This approach allowed to investigate the influence of the surface properties of the various supports in an isolated manner. Extensive characterization by means of N_2 physisorption, XRD, TEM and CO_2-TPD complemented by DRIFTS (to study the CO_2 adsorption mode) were carried out and confirmed the aforementioned classification.

The catalytic results indicate the imperative presence of Lewis basic oxygen vacancies for a high catalytic reactivity as the catalysts exposing such vacant sites – the REO, ZrO_2 and TiO_2 supported ones - yield the highest methane formation rate over the investigated temperature range. Temperature-dependent and isothermal DRIFTS experiments under reactive atmosphere reveal a progressive accumulation of CO species on Ru, formed upon dissociative CO_2 adsorption, for catalysts supported on oxides without Lewis basic oxygen vacancies (Al_2O_3, MgO and SiO_2) - a trend which is not observed on catalysts exposing such Lewis basic sites. This points towards a poisoning of the Ru surface and indicates the importance of effects induced by the support (electronic effect due to metal-support interaction) on the Ru particle to avoid such poisoning to provide sufficient sites for H_2 adsorption and dissociation. However, among the catalysts with Lewis basic properties, a change in the most active support class occurs at around 310 °C. At lower temperatures, the catalysts supported on oxides with only Lewis basic sites (TiO_2 and ZrO_2) exhibit the highest activity, whereas at higher temperatures the REO supported catalysts perform best. This can be reasoned with a shift in the mechanistic regime. In case of the Ru-TiO_2, DRIFTS experiments and CO_2-TPD measurements show that the high activity is caused by an indirect effect of the support on the Ru particle, facilitating the support-independent CO pathway. In turn, CO_2 is additionally activated on oxygen vacancies to form bidentate carbonates that react via bidentate hydrogen carbonates and formates to methane over the ZrO_2 supported catalyst. On the REO supported catalysts, DRIFTS data showed that not only Lewis basic oxygen vacancies but also Brønsted basic OH groups adsorb CO_2 to form bidentate and hydrogen carbonates, respectively. However, their hydrogenation starts at temperatures above 300 °C, which coincides well with the temperature at which the REO supported catalysts perform best.

Based on these results, catalysts with surface basicity should be applied for CO_2 methanation; yet, the choice of a specific basic support has to be made considering the indented reaction temperatures. For reaction temperatures between 300-400 °C, which are to be

expected particularly in polytropic reactors, REOs appear to be a promising choice of support material. Consequently, Sm_2O_3 was chosen as support for the preparation of a highly active Ni-Sm_2O_3 catalyst to test the applicability of the derived guidelines. To optimize the Ni-Sm_2O_3 catalyst, the right balance between H_2 dissociation sites (on metallic Ni) and CO_2 adsorption sites (on Sm_2O_3) had to be found and required a study on the influence of the Ni loading. To this end, a sol-gel approach was applied because of its simplicity and possibility to produce highly homogenous catalysts with various Ni loadings and high thermal stability. An intermediate Ni loading of 30-40 wt.% Ni is found to yield the highest CO_2 conversion which is attributed to the small Ni crystallite size (6 nm) and the Ni-to-Sm_2O_3 ratio for an adequate balance of H_2 dissociation and CO_2 adsorption sites. The developed catalyst produces significantly higher CH_4 yields as an industrial Ni-Al_2O_3 catalyst as well as a well-known literature system (19 wt.% Ni-Al_2O_3). In comparison to a reference catalyst prepared by impregnating pristine Sm_2O_3 with an aqueous Ni solution, the xerogel catalyst exhibits a higher reactivity and thus, underlines the applicability of sol-gel derived materials for catalytic purposes.

However, the high reactivity is only partly sustainable as the Ni-Sm_2O_3 catalysts suffer from a rapid, but reversible deactivation in dependence of the reaction conditions but independent of the Ni loading. Yet, despite the rapid deactivation the activity after 600 min is still higher than found on the industrial reference catalyst. By variation of the reaction conditions, characterization of the spent catalysts, DRIFTS experiments and regeneration experiments, it could be established that the catalyst is poisoned by thermally stable carbonates that are formed on oxygen-deficient sites and block active sites. In other words, the support's basicity is of ambivalent character and needs to be carefully tuned to increase CO_2 adsorption for higher reaction rates without binding it excessively strong to avoid a self-poisoning. Other common phenomena like sintering and coking can be excluded even under harsh and prolonged experiments, i.e. for 85 h at 490 °C and for severely under-stoichiometric H_2/CO_2 ratios, respectively. The variation of the process conditions show that the stability can be increased by adjusting the process conditions to higher temperatures and lower CO_2 partial pressures. In this respect, particularly the high thermal stability of the xerogel catalyst is of importance as it allows to run the reaction at elevated temperatures and to periodically remove the poisoning species by a high temperature treatment in reducing conditions.

The present thesis aims at contributing to rationalize catalyst development for CO_2 methanation; yet it also reveals that, to date, none of the common support materials is a clear frontrunner which produces the highest methane yield over the entire relevant temperature range between 200 and 400 °C. Such a universal catalyst support will probably need to combine the advantages of REOs and TiO_2 or ZrO_2. In this light, doping the REOs with

low-valent dopants to increase the oxygen vacancy density could provide an interesting starting point. Furthermore, mixed oxides, i.e. perovskites (ABO_3), appear as a promising support class due to their inherent basicity and oxygen mobility. In pre-experiments (not shown here) the applicability of the developed synthesis route could be expanded to produce $SmTiO_3$ and $SmZrO_3$ perovskites. As addressed in the extended outlook already, an understanding of the structural parameters and hence an optimization of such is still scarce. A methodology to precisely adjust the structural properties of Sm_2O_3 xerogels by the simple addition of structure-directing agents has been developed and expands the "tool box" for preparing well-defined model catalysts that can serve as a starting point for future studies.

- Na, Jan. Was macht die Forschung?
Sie ist fertig, Opa. Sie ist endlich fertig

.

APPENDICES

A. Catalytic Set-Up and Standard Techniques

A.1 Catalytic Set-Up

All catalytic experiments were conducted in the set-up schematically depicted in Figure A-1. The gas flow rates of Ar, H_2, CO_2 and CO or CH_4 were controlled by mass-flow controllers (Bronkhorst Mättig). Additionally, Ar could be flowed through a saturator to co-feed water. To preheat the gases and to prevent water from condensing inside the set-up, all tubing was heated to at least 120 °C.

The catalysts were loaded in a fixed-bed reactor (quartz glass tube reactor, inner diameter 6 mm), operated at atmospheric pressure, and fixated with quartz wool. Reactor heating was achieved by a self-designed metal block oven, which was controlled by a thermocouple placed at the end of the catalyst bed.

The effluent gases passed through a cold trap (operated at -1 °C) to remove water formed as a reaction product before they were analyzed with an on-line compact gas chromatograph (Global Analyser Solution) equipped with a thermal-conductivity sensor. A RT-Molsieve 5 Å column (15 m) was used to separate CO and CH_4, whereas CO_2 was separated on a RT-Porabond column (30 m).

For some experiments, a non-dispersive IR sensor (NDIR, Sick AG) equipped with a Multor module for the simultaneous detection of CO, CO_2 and CH_4 was used, instead of the µGC. By running standard samples on the NDIR and µGC it was ensured that the catalytic results do not differ between both analysis tools. If the NDIR is used, it is explicitly stated below the figures.

The residence time distribution of the set-up was determined for the typical flow rate of the catalytic experiments (50 mL min^{-1}). To this end, a new set point was sent to the MFC at t = 0 s and the evolution of the signal was tracked by the NDIR. The cumulative distribution function $F(t)$ is shown in Figure A-2. After 160 s no changes in the concentration are detected anymore. The measured profile can by described fairly well by a cascade model of ideally mixed continuously stirred tank reactors with a number of tanks N = 75 and a residence time τ = 98 s.

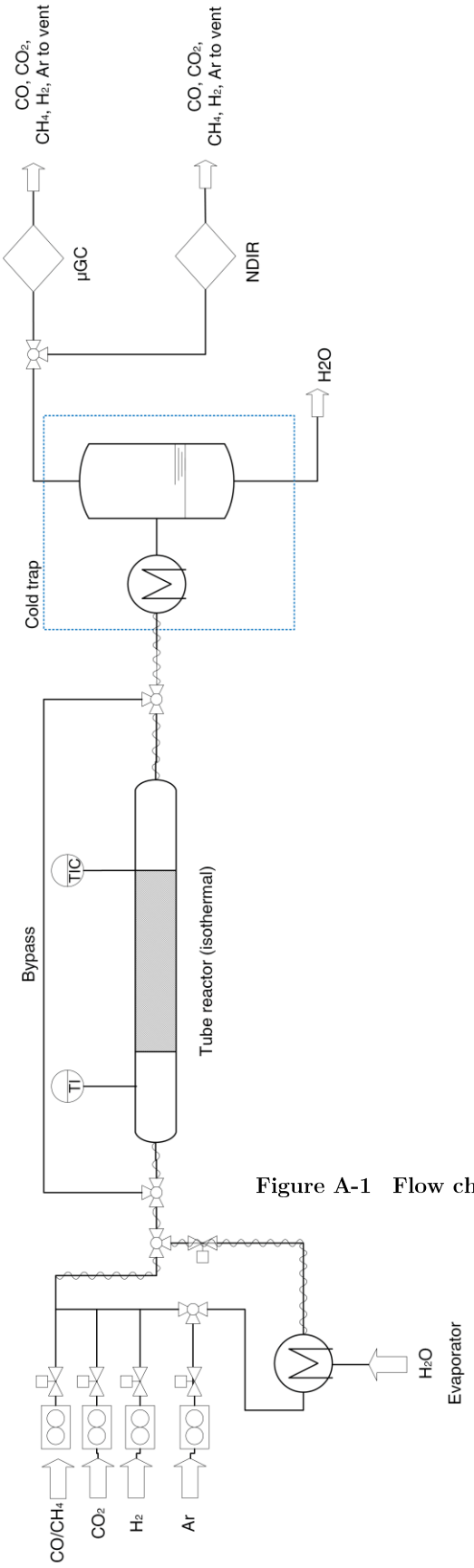

Figure A-1 Flow chart of the catalytic set-up

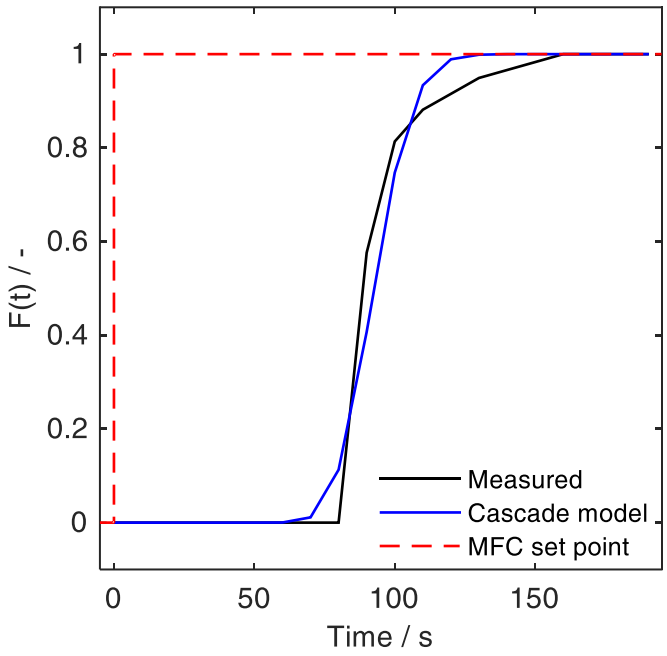

Figure A-2 **Residence time distribution of the catalytic set-up depicted as F-curve. At $t = 0$ s a new set point was send to the MFC.**

A.2 Standard Characterization Techniques

Powder XRD. The catalysts were characterized by XRD to identify and quantify the phases present as well as to calculate the average crystallite sizes. The samples were measured using a $\theta/2\theta$-Bragg-Brentano geometry on a X'Pert MPD powder diffractometer (Panalytical, Almelo, Netherlands). The instrument was equipped with a secondary Ni filter, Cu $K_{\alpha 1,2}$ radiation ($\lambda_1 = 154.05929(5)$ pm, $\lambda_2 = 154.4414(2)$ pm), and an X'Celerator multi-strip detector. Data were collected at ambient condition in the 2θ range from 15° to 90° with a step width of 0.0167°/step and a total collection time of 200 s/step. Selected catalysts were measured on a Stoe MP diffractometer (STOE & Cie GmbH, Darmstadt, Germany) equipped with a primary Ge(111) monochromator, Mo $K\alpha_1$ radiation ($\lambda_1 = 71.3607 \pm 0.0012$ pm), and a Mythen 1K detector. The diffractograms were collected at ambient conditions in the 2θ range from 5° to 45° with a step width of 0.015°/step and a total collection time of 180 s/step. X-ray powder data Rietveld refinements were carried out, using the "DiffracPlus Topas 4.2" software (Bruker AXS GmbH, Karlsruhe, Germany). To describe the X-ray diffraction profiles, the fundamental parameter approach was applied in the Rietveld refinements. For the diffractometer configuration, the corresponding fundamental parameters were fitted to powder data of standard LaB_6. During the refinements, general parameters, such as scale factors and background parameters (Chebychev polynomial), were optimized. Additionally, the lattice parameters, atomic coordinates, isotropic atomic displacement parameters, average crystallite size L_{vol}(IB) and micro-strain (ε_0) were refined.

N_2 physisorption. N_2 physisorption measurements were conducted in order to analyze the catalyst's porosity using a NOVA 4000e (Quantachrome Instruments, USA) gas sorption system. Prior to data collection, the samples were outgassed at 200 °C for at least 2 hours under vacuum. Adsorption/desorption isotherms were collected in the pressure range 0.01 - 0.99 p/p_0. The pore size distribution was calculated using the desorption branch on the basis of the Barret-Joyner-Halenda (BJH) model, whereas the pore volume was determined on the basis of the amount of adsorbed N_2 at $p/p_0 = 0.99$. The specific surface area was calculated based on five-point BET measurements in the pressure range 0.1 - 0.3 p/p_0. All measurements were conducted at -196 °C.

Transmission Electron Microscopy. TEM images were acquired using a Tecnai F20 S-TWIN (200 keV) microscope to gain insight into the catalyst microstructure and to determine the particle size. To this end, the catalysts were ground to a fine powder before being loaded onto a TEM grid (ultrathin carbon film, Quantifoil, Cu 200 mesh) by dragging the grid through the powder. The mean particle size was determined by analysing the micrographs with the software ImageJ (version 1.48). For each sample, at least 150 particles were measured.

B. Additional Experimental Details and Results – Chapter 4

B.1 Characterization

The procedural description of the standard characterizations (XRD, TEM and N_2 physisorption) are described in A.2.

Atomic Absorption Spectroscopy. To determine the Ru loading, AAS measurements were conducted using a flame atomic absorption spectrometer (Carl Zeiss Technology, AAS 5 FL). To this end, Ru was digested by a fusion method established by Taddia and Sternini[306], which was later confirmed to be the most efficient and reliable method to digest Ru^0 as well as RuO_x.[307] In short, 150 mg of the supported catalysts were mixed with 0.38 g KOH and 0.65 g KNO_3, subsequently heated within 60 min to 450°C in a muffle furnace and kept at this temperature for another 60 min. After cooling down, 50 mg of $K_2S_2O_8$ were added, before the melts were dissolved in Milli-Q water. Next, 10 mL of 1 M KOH were added and the resulting solution was further diluted with Milli-Q water to achieve a total volume of 50 mL. 10 mL of the solution were mixed with 5 mL of concentrated HCl and 10 mL Milli-Q water and then analyzed.

CO_2-Temperature Programmed Desorption. To probe the basicity of the various systems, i.e. the strength of the basic sites, CO_2-TPDs were recorded. About 100 mg of the powder catalysts were placed in a stainless-steel reactor and pretreated at 400 °C for 60 min (3 °C min^{-1}) in 20 vol.% H_2/Ar ($\dot{V}_{tot}$=50 mL_N min^{-1}), which corresponds to the activation of the catalysts in the catalytic experiments. After cooling down to 50 °C, the powders were saturated with CO_2 for 60 min, before flushing the set-up with pure Ar for 30 min to remove any remaining gaseous CO_2 from the system. Subsequently, the samples were heated to 950°C with a heating rate of 5 °C min^{-1} in Ar while desorbing CO_2 was detected using a mass spectrometer (HPR20, Hiden Analytical). To enable a quantitative comparison, the mass spectrometer was calibrated for CO_2 (44 amu), CO (28 amu) and Ar (40 amu), of which Ar was used as internal standard. The total amount of desorbing CO_2 was then determined by integrating the desorption peaks.

DRIFTS. Diffuse reflectance infrared Fourier-transformed spectroscopy (DRIFTS) measurements were conducted, on the one hand, to characterize CO_2 adsorption on the catalysts

and thus to complement the CO_2-TPD measurements. On the other hand, DRIFTS experiments under reaction conditions were carried out to gain mechanistic insights. All measurements were conducted using a Varian-670 FT-IR spectrometer equipped with a liquid nitrogen cooled MCT detector and an IR cell in praying mantis geometry (VC-DRM-5, Harrick). All spectra were recorded with a resolution of 4 cm^{-1} in absorbance mode and the average of 128 scans (acquisition time: 78 sec) is reported.

After placing the sample on the temperature-controlled sample holder in the IR cell, the sample compartment was flushed with He to remove any impurities prior to the spectra collection. Subsequently, the sample was heated to 400 °C in 20 vol.% H_2/He within 30 min. This temperature was then kept constant for another 60 min to activate the catalyst.

To determine the *CO_2 adsorption* modes, the same pre-treatment as used for the CO_2-TPD measurements was applied. After activation, the samples were cooled down to 50 °C in He and the background was recorded. Subsequently, the samples were saturated with CO_2 for 60 min. Next, the compartment was flushed with He (100 mL min^{-1}) for 30 min to remove any remaining gaseous CO_2 from the tubing and the sample stage. Afterwards, the spectra were collected.

For the *reaction studies*, the samples were cooled down to 100°C in He atmosphere after activation and after the background was recorded. Subsequently, the catalysts were exposed to 5 vol.% CO_2, 20 vol.% H_2 and 75 vol.% He at a total flow of 100 mL min^{-1}. The temperature was increased stepwise until 350 °C and a spectrum was recorded at each temperature after 5 min to ensure thermal equilibration.

In addition, *isothermal studies* were carried out. Again, the fresh catalysts were first activated and subsequently cooled down to 350 °C in He where the background was recorded. Next, 5 vol.% CO_2 were added to saturate the sample for 15 min while recording a spectrum every two minutes. Next, the CO_2 flow was stopped and the catalysts exposed to pure He (100 mL_N min^{-1}) for 30 min. A spectrum was recorded after 1, 3, 5, 7, 9, 11, 15, 20, 25 and 30 min. Afterwards, the sample was exposed to a H_2/He mixture (20 vol.% H_2) at a total flowrate of 100 mL_N min^{-1} for another 30 min during which spectra were collected in the same manner as before. Lastly, the samples were exposed to the reactant mixture (5 vol.% CO_2, 20 vol.% H_2 in He, total flowrate 100 mL_N min^{-1}) and one spectrum was acquired after 1 min of exposure.

For the Ru-TiO_2 catalyst, another procedure was chosen (for reasons explained later). A fresh catalyst was activated in H_2 at 400°C and then cooled down to 350 °C in He where a background spectrum was recorded. Subsequently, the sample was saturated with CO_2 for 15 min (5 vol.% CO_2 in He, total flowrate 100 mL_n min^{-1}), which corresponds to the saturation step of the other isothermal ad-/desorption experiments. In contrast to the other catalysts, however, the Ru-TiO_2 catalyst was then exposed to 5 vol.% CO_2 and 20 vol.% H_2 in

He at a total flow rate of 100 mL_N min^{-1}. During the entire experiment, the temporal evolution of the adsorbed species was followed by collecting spectra every two minutes.

RAMAN. Raman spectra were recorded on a LabRam ARAMIS (Horiba Jobin Yvon) Micro-Raman spectrometer equipped with a laser working at 785 nm and less than 20 mW. The use of a 50x long working distance objective (Olympus) with a numerical aperture of 0.55 provides a focus spot of about 5 µm diameter when closing the confocal hole to 1000 µm. The spectra were collected in the range 90 cm^{-1} to 800 cm^{-1} with a spectral resolution of approximately 1.2 cm^{-1} using a grating of 1800 grooves mm^{-1} and a thermoelectrically cooled CCD detector (Synapse, 1024 x 256 pixels). The spectral positions were calibrated against the Raman mode of Si before and after the sample measurements. In some cases, the optimized filtering was required to minimize the fluorescence and to reduce laser intensity to avoid sample damage. At least 15 spectra were collected with an acquisition time of 10 s /window for an adequate signal-to-noise ratio. The high-temperature spectra were performed using a Linkam heating stage (TS1500) connected to a continuous gas (5 vol.% H_2 + 95 vol.% Ar) supply to the stage. The powder samples were loaded and the compartment was flushed with the gas mixture for several minutes before heating at the sample 50 °C. Afterward, the temperature was ramped to 200 °C at 20 °C min^{-1} and kept for 45 min. In each case, the sample was then cooled down from the target temperature to 50 °C followed by collecting spectra to exclude the quasiharmonic (lattice thermal expansion effects) and anharmonic contributions in shifting the Raman bands. After a thermal equilibration period of 5 min spectra were collected, and the experiment was repeated between 50 °C and 400 °C with a 50 °C step (e.g., 50 °C -> 200 °C -> 50 °C -> 250 °C-> 50 °C -> 300 °C -> 50 °C -> 350 °C -> 50°C ->400 °C -> 50 °C). As much as three different locations were chosen at each temperature step, and an averaged spectrum was produced for better statistics. After background correction and normalization, the peaks were fitted with Gauss-Lorentzian model.

B.2 Catalytic Experiments

The reactor was filled with 50 mg (75 - 150 µm) catalyst which was diluted in the ratio 1:10 with quartz particles in the same size fraction. Prior to the catalytic experiments, all catalysts were reduced in-situ in flowing H_2 at 400°C for 1 h (heating ramp: 3 °C min^{-1}). After this activation step, the reactor was cooled down to the starting temperature of 200 °C in inert gas atmosphere. The activity and selectivity of the catalysts for the CO_2 methanation reaction were determined in the temperature range between 200 to 400 °C using a feed gas composition of 4/1/5 H_2/CO_2/Ar. The total flow rate was set to 50 mL_N min^{-1}, corresponding

to a weight hourly space velocity (WHSV) of 60 $L_N\ g_{cat}^{-1}\ h^{-1}$. Each temperature was kept constant for 42 min and conversion and selectivity were averaged over the last 24 mins.

In pre-experiments no C_{2+} hydrocarbons were detected. Based on the inlet and outlet molar flow rates, the formation and consumption rates (referred to mass of ruthenium) of the involved compounds were calculated according to Eq. (B-1),

$$r_x = \frac{\dot{n}_{x,in} - \dot{n}_{x,out}}{m_{Ru}}. \tag{B-1}$$

We furthermore define the methane selectivity according to Eq. (B-2),

$$S_{CH_4} = \frac{r_{CH_4}}{r_{CO_2}}. \tag{B-2}$$

B.3 Additional Characterizations

1. Raman spectra of Ru-TiO_2 and Ru-ZrO_2 (as-prepared)

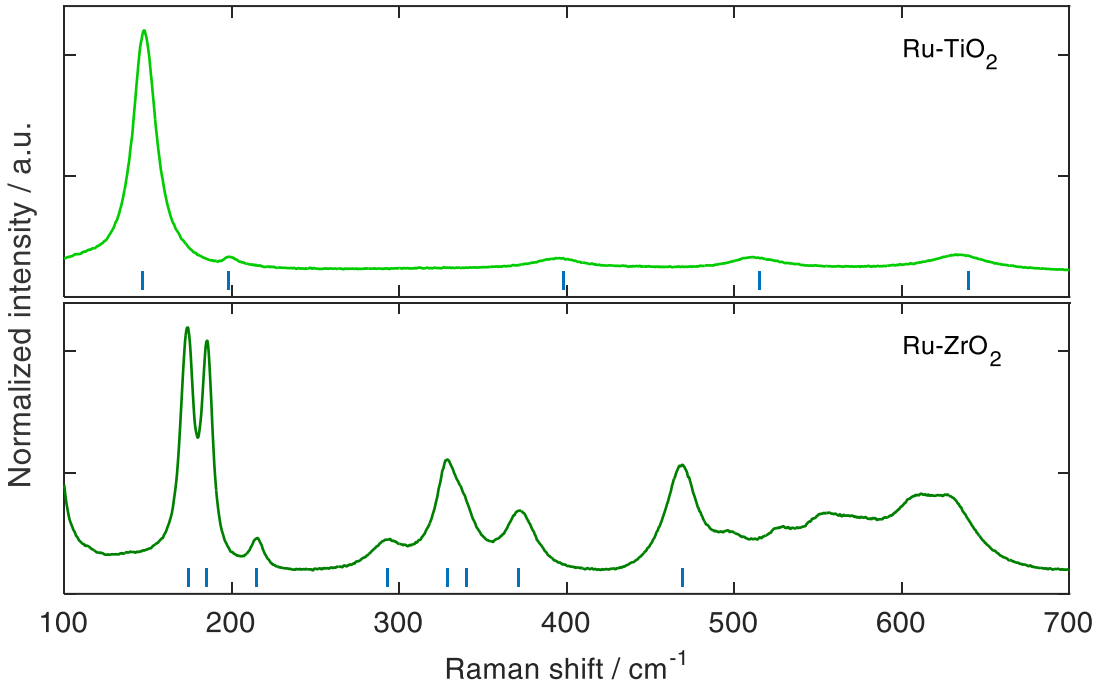

Figure B-1 Raman spectra of the as-prepared Ru-TiO_2 and Ru-ZrO_2 catalysts at ambient condition. The tick marks refer to observed band positions of anatase[308] and monoclinic ZrO_2[309].

B.4 Additional Catalytic Results

1. Weisz-Prater calculations

The criterion was calculated for all temperatures and catalysts according to the following equation

$$WP = \frac{r^{eff}\rho_{cat}d_{cat}^2}{4c_{CO_2}D_{CO_2}^{eff}} < 1. \quad \text{(B-3)}$$

Knudsen diffusion is taken into account for all catalysts except Ru-TiO_2 and Ru-ZrO_2 as these catalysts exhibit macropores. The following catalyst densities are assumed (as stated by the supplier, if available): $\rho_{Al2O3} = 2.3 \cdot 10^6$ g m^{-3}, $\rho_{MgO} = 3.6 \cdot 10^6$ g m^{-3}, $\rho_{TiO2} = 4.2 \cdot 10^6$ g m^{-3}, $\rho_{ZrO2} = 5.7 \cdot 10^6$ g m^{-3} and $\rho_{SiO2} = 2.7 \cdot 10^6$ g m^{-3}. For the REO catalysts, the densities were approximated as $\rho_{Sm2O3} = 6.9 \cdot 10^6$ g m^{-3}, $\rho_{Gd2O3} = 7.4 \cdot 10^6$ g m^{-3} and $\rho_{Y2O3} = 6.9 \cdot 10^6$ g m^{-3}. For the xerogel catalysts a tortuosity of 2 was assumed based on a previous study on rare earth metal oxide aerogels.[310] For all other catalysts, the tortuosity was presumed to be 3. The results are compiled below.

Table B-1 Results of Weisz-Prater criterion calculations.

	200 °C	230 °C	270 °C	290 °C	310 °C	350 °C	400 °C
Ru-Sm_2O_3	0	0.0092	0.0561	0.1185	0.2724	0.5420	0.6683
Ru-Gd_2O_3	0.0054	0.0217	0.0992	0.1854	0.3209	0.6174	0.6542
Ru-Y_2O_3	0	0.0039	0.0270	0.0593	0.1214	0.3709	0.4804
Ru-Al_2O_3	0.0028	0.0091	0.0347	0.0623	0.1037	0.2179	0.3294
Ru-MgO	0	0	0.0054	0.0150	0.0299	0.2034	0.4013
Ru-TiO_2	0.0229	0.0589	0.1564	0.2315	0.3184	0.4912	0.6123
Ru-ZrO_2	0.0030	0.0175	0.0998	0.1954	0.3173	0.5468	0.6554
Ru-SiO_2	0	0	0.0116	0.0292	0.0593	0.1661	0.3184

2. Arrhenius plots

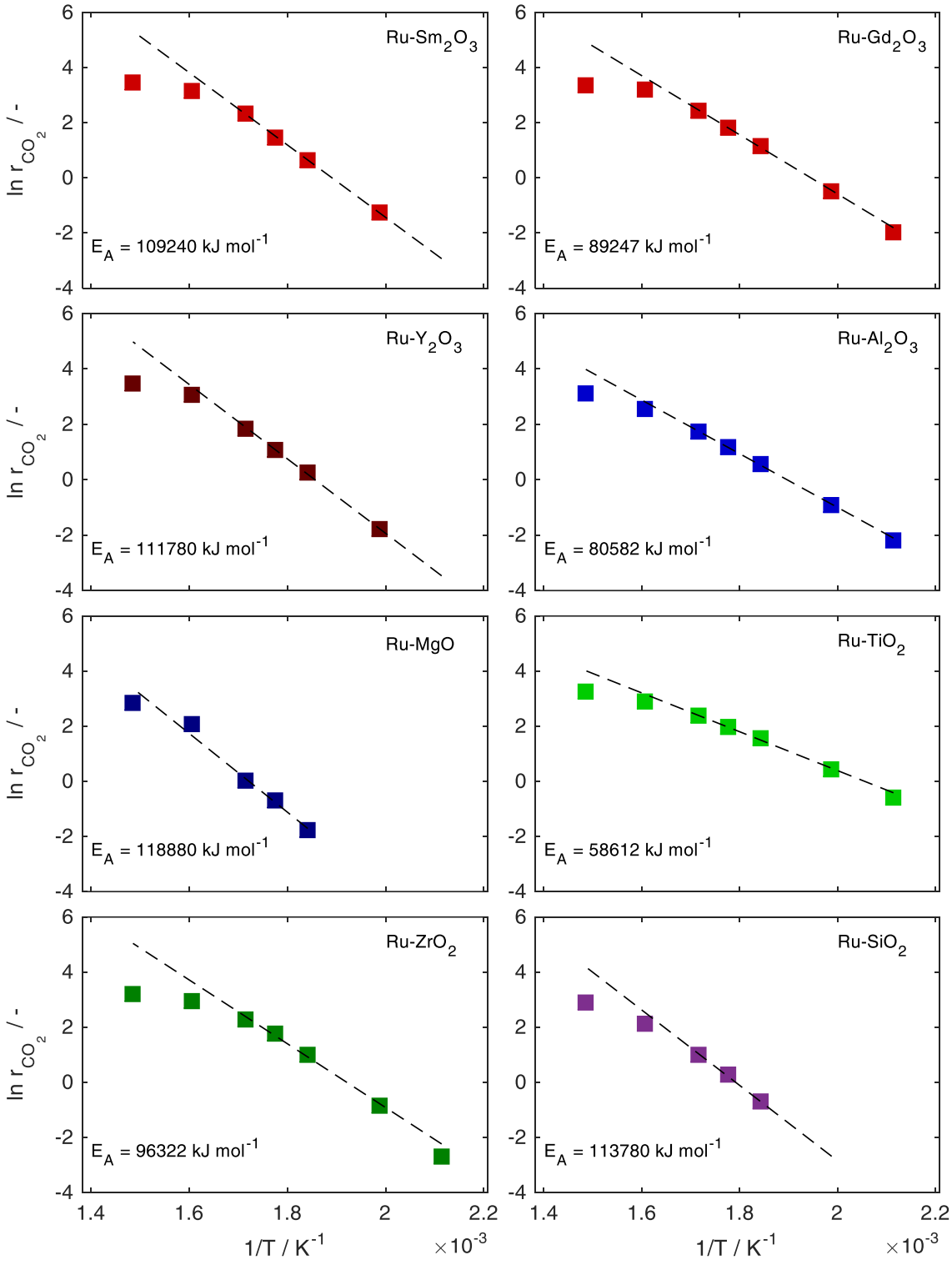

Figure B-2 Arrhenius presentation of all catalysts for the investigated temperatures. The dashed line refers to a linear fit in the temperature range 200-310 °C, showing the deviation at elevated temperatures.

3. Stability runs

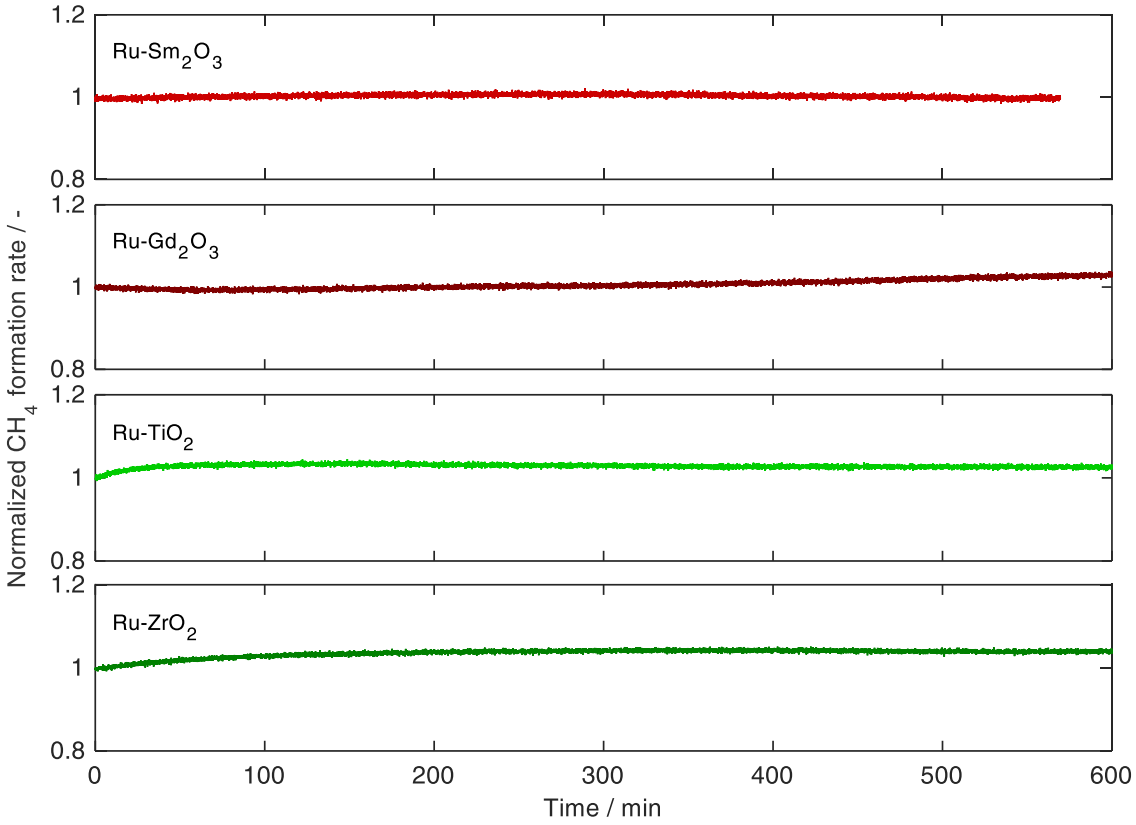

Figure B-3 Normalized methane formation rate vs. time at 400 °C for selected catalysts. The methane formation rate was chosen as a descriptor as it would reflect changes in the conversion rate as well as selectivity. The rates are normalized to the initial methane formation rate. Reaction conditions: pressure 1 bar, flow rate 50 mL min^{-1}, 4/1/5 $H_2/CO_2/Ar$, 50 mg catalyst.

4. *Reproducibility*

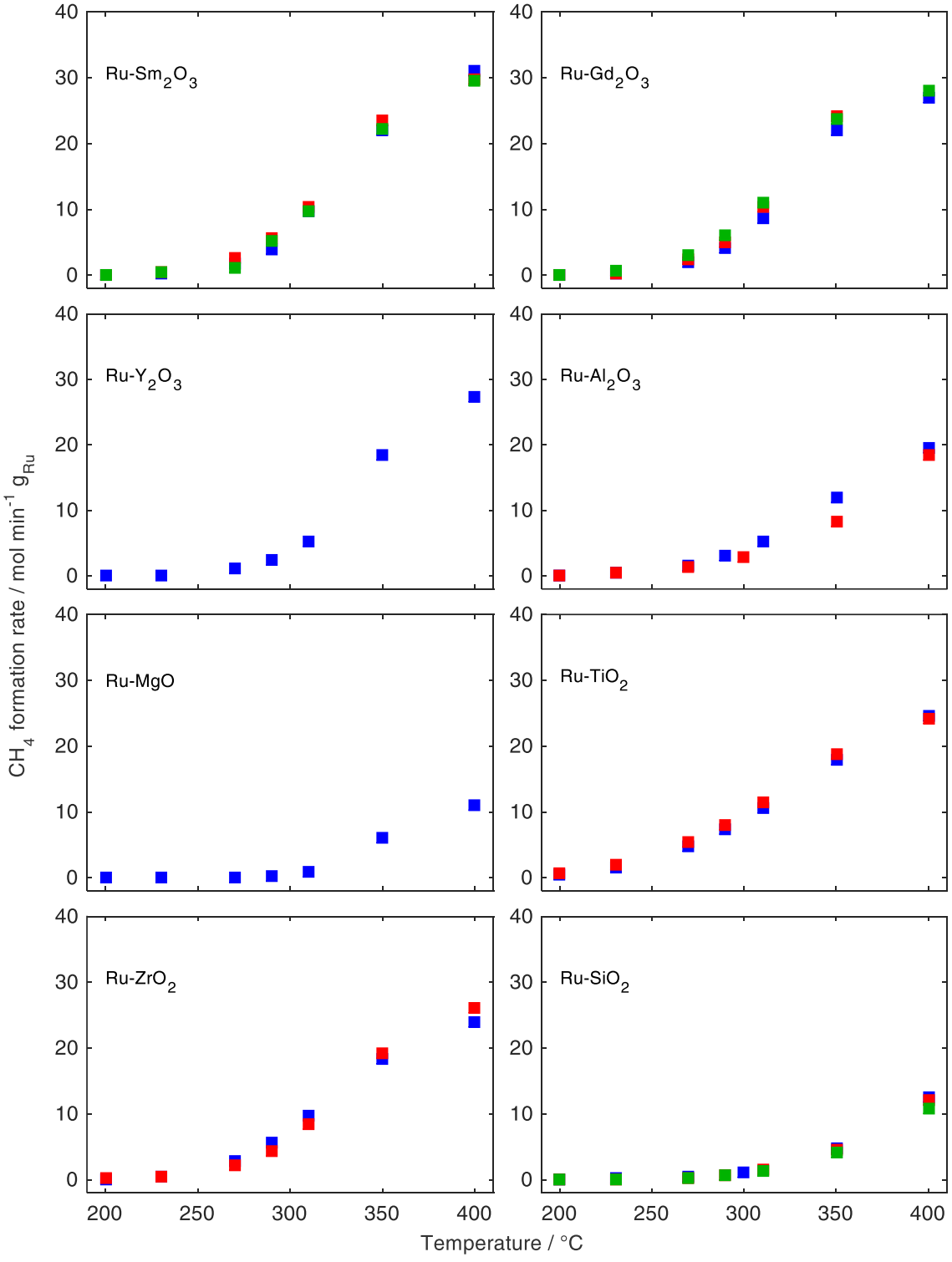

Figure B-4 Methane formation rates for the investigated catalysts and for various catalyst batches to ensure reproducibility of the synthesis route; blue symbols indicate catalyst batch 1, red symbols indicate batch 2, green symbols indicate batch 3. Another batch refers to newly synthesized Ru nanoparticles and support materials (if synthesized in-house). The methane formation rate was chosen as a descriptor as it would reflect changes in the conversion rate as well as selectivity. In the main text data corresponding to batch 1 is shown.

5. Additional DRIFTS data

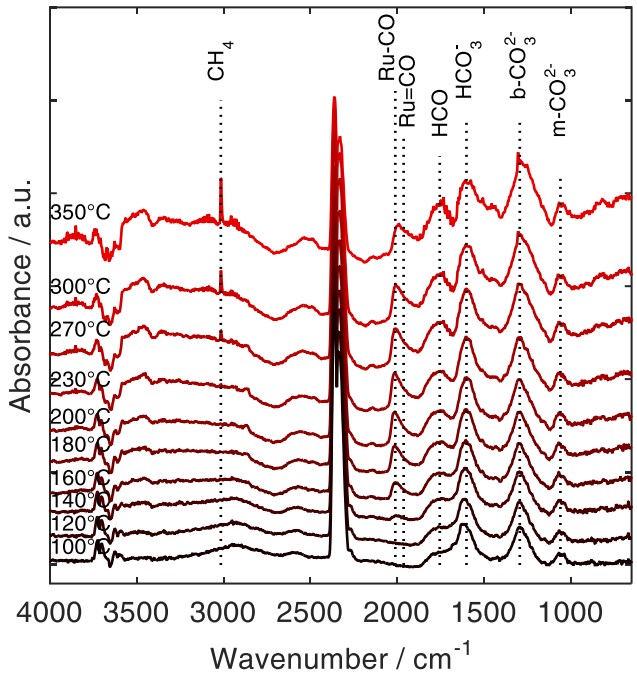

Figure B-5 Temperature-dependent DRIFTS – reaction study on **Ru-Sm_2O_3**; conditions: 5 vol.% CO_2, 20 vol.% H_2in He, $\dot{V}_{tot}$= 100 mL min^{-1} references: [44, 128, 154, 227, 242–244]

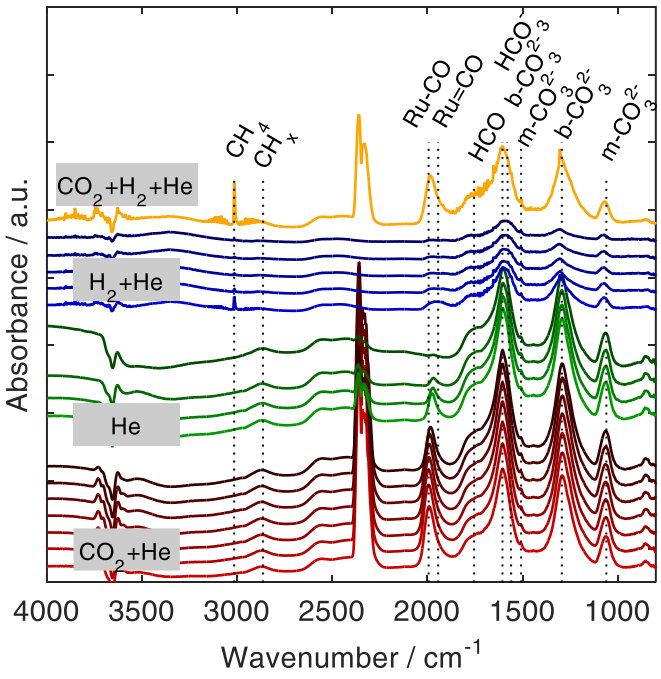

Figure B-6 Isothermal DRIFTS experiments carried out for Ru-Sm_2O_3 at 350 °C under different gas atmospheres. Red spectra: exposure to 5 vol.% CO_2 in He for 15 min; blue spectra: pure He for 20 min; green spectra: subsequent exposure to 20 vol.% H_2 in He; yellow trace: exposure to 5 vol.% CO_2 and 20 vol.% H_2 in He, $\dot{V}_{tot}$ = **100 mL min^{-1}**. Temporal evolution of the spectra from lighter to darker colors (bottom to top).

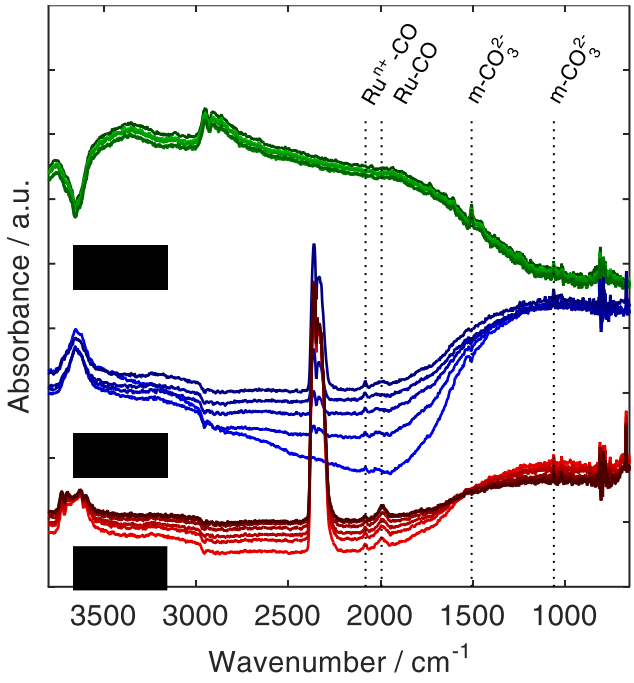

Figure B-7 Isothermal DRIFTS experiments carried out for Ru-TiO_2 at 350 °C under different gas atmospheres. Red spectra: exposure to 5 vol.% CO_2 in He for 15 min; blue spectra: pure He for 20 min; green traces: subsequent exposure to 20 vol.% H_2 in He, $\dot{V}_{tot}$ = **100 mL min^{-1}**. Temporal evolution of the spectra from lighter to darker colors (bottom to top).

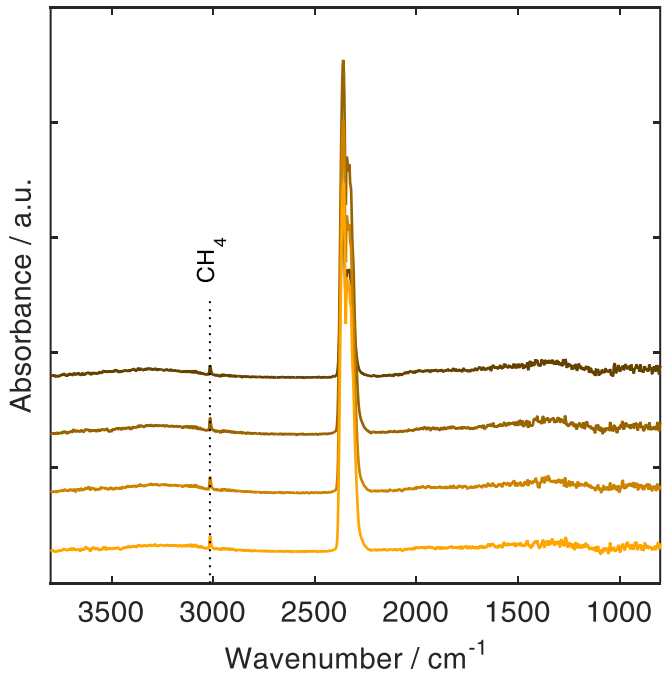

Figure B-8 Isothermal DRIFTS experiments carried out for Ru-SiO_2 at 350 °C under reactive atmosphere. As no surface adsorbates were visible, we refrained from exposing the catalyst to different gas atmospheres; conditions: 5 vol.% CO_2, 20 vol.% H_2 in He, $\dot{V}_{tot}$ = **100 mL min^{-1}**. Temporal evolution of the spectra from lighter to darker colors (bottom to top).

C ADDITIONAL EXPERIMENTAL DETAILS AND RESULTS – CHAPTER 5

C.1 Catalyst Synthesis

The following amounts of chemicals were used to prepare the catalysts.

Table C-1 Amounts of precursor to synthesize 1 g of catalyst.

	$Ni(NO_3)_2 \cdot 6H_2O$ / g	$Sm(NO_3)_3 \cdot xH_2O$ / g	Ethanol / mL	Propylene oxide / mL	Citric acid / g
Pure Sm_2O_3	-	2.20	9.9	3.8	0.95
4 wt.% Ni	0.20	2.06	10.6	4.1	1.02
11 wt.% Ni	0.55	1.95	12.5	4.8	1.20
33 wt.% Ni	1.63	1.49	17.9	6.8	1.72
39 wt.% Ni	1.93	1.34	19.3	7.4	1.86
63 wt.% Ni	3.12	0.81	25.1	9.7	2.41
89 wt.% Ni	4.41	0.24	30.8	11.9	2.96

C.2 Characterization Methods

The procedural description of the standard characterizations (XRD, TEM and N_2 physisorption) are described in A.2.

H_2 temperature-programmed reduction. To determine the optimal reduction temperature and to gain insights into the metal-support interaction, temperature-programmed reduction (TPR) profiles were recorded, using an Autosorb I (Quantachrome Instruments, USA) device equipped with a TCD detector. The samples (75 mg) were pre-treated at 400 °C for 10 h under flowing He to remove any adsorbed impurities. After cooling the samples down to 50 °C, the cell was purged with He until a steady TCD signal was observed and subsequently heated to 1000 °C with a linear heating ramp of 5 °C min^{-1} in 5% H_2/Ar.

Pulsed H_2 and CO_2 chemisorption. Hydrogen and carbon dioxide pulse titrations experiments were conducted on an Autosorb iQ (Quantachrome, USA) equipped with a thermal conductivity detector. For the measurements, 50 mg of the respective catalyst were fixated with quartz wool in a U-shaped quartz glass reactor. The catalysts were pre-treated in 5% H_2 in N_2 at 500 °C for 10 h to reduce NiO to metallic Ni, corresponding to the reduction temperature and duration during the catalytic experiments. Subsequently, the sample was cooled down and a pure H_2 pulse (volume per pulse: 272 µL) was injected into the N_2 carrier

gas stream monitoring the TCD signal with the provided TPRWin software. Once a stable base line was obtained, the next injection followed. In total, 16 injections were added. After that, the sample was heated to 200 °C in N_2 to remove any adsorbed H_2 before being cooled down to 30 °C again for the CO_2 pulse titration experiment. For that, pure CO_2 pulses (loop volume. 272 µL) were injected into a He carrier gas stream after the baseline was stabilized. This was repeated at least five times or until the deviations between the peak areas for the individual peaks was less than 3%.

Data processing was done manually by integrating the peak areas. For the H_2 pulse experiments that average of the last eight peak areas was used as calibration factor to calculate the H_2 uptake during the first eight injections, whereas for the CO_2 adsorption capacity the last three peak areas were averaged for the calibration factor.

Based on the H_2 adsorption capacity, the specific Ni surface area (S_{Ni}) was calculated by eq. (C-1) assuming dissociative H_2 adsorption on Ni:

$$S_{Ni} = \frac{N_{H2}\, N_A\, z}{m_{cat}\, \sigma_{Ni}} \tag{C-1}$$

in which S_{Ni} denotes the Ni surface area per gram catalyst, N_A the Avogadro constant, N_{H2} the amount of adsorbed H_2, z the stochiometric adsorption factor (here z = 2 for dissociative H_2 chemisorption on Ni), m_{cat} the catalyst mass prior to reduction and σ_{Ni} the number of Ni atoms per unit area (here: $1.54 \cdot 10^{19}$ m^{-2}). Additionally, the Ni dispersion (D_{Ni}) was determined under consideration of the molecular weight of Ni (M = 58.71 g mol^{-1}) and the Ni loading of the catalyst (u) according to eq. (C-2)

$$D_{Ni} = \frac{N_H\, z\, M_{Ni}}{m_{cat}\, w}. \tag{C-2}$$

C.3 Catalysis and Reference Kinetics

The general catalytic set-up is described in A.1. For the measurements in this chapter, the following specific condition apply:

For the catalytic experiments, 50 mg of the powder catalyst (75-200 µm) were used and diluted with 300 mg Al_2O_3 consisting of particles in the same size fraction.

Prior to the reaction, the catalysts were reduced in-situ in flowing H_2 at 500°C for 10 h (heating ramp 1 °C min^{-1}). After reduction, the reactor was cooled down to 200 °C in inert gas atmosphere.

During the catalytic experiments, the total flow rates remained fixed at 50 mL_N min^{-1} with the following feed composition: $H_2/CO_2/Ar$ = 4/1/5. The catalysts were tested between 200-400 °C in intervals of 50 °C. Each temperature was held for 42 min (corresponding to 7 runs on the µGC) during which the catalytic performance was monitored with an on-line compact gas chromatograph (Global Analyser Solution) and the CO_2 conversion and

selectivities were averaged over the last 24 min (= last 4 µGC runs). CO_2 conversion as well as CH_4 yield and selectivity were determined according to the following equations:

$$X_{CO_2} = 1 - \frac{c_{CO_2,out}}{c_{CO_2,out} + c_{CH_4,out} + c_{CO,out}}, \tag{C-3}$$

$$Y_{CH_4} = \frac{c_{CH_4,out}}{c_{CO_2,out} + c_{CH_4,out} + c_{CO,out}}, \tag{C-4}$$

$$S_{CH_4} = \frac{Y_{CH_4}}{X_{CO_2}}. \tag{C-5}$$

Pre-experiments confirmed the absence of any higher hydrocarbons.

As a reference, we used a micro kinetic model available in literature, which was implemented in an isothermal 1D pseudo-homogenous reactor model, assuming ideal conditions, e.g. no inter- or intraparticle diffusion limitations, such that only the mass balance (eq. C-4) had to be solved numerically in Matlab (R2015a).

$$\frac{\mathrm{d}\dot{n}_i}{\mathrm{d}m_{cat}} = \nu_i \, r \tag{C-6}$$

Choosing the reaction conditions according to our experimental conditions enabled a direct comparison of the catalytic performance under identical conditions. To this end, the rate expression of Koschany et al. [31] was employed without any alterations.

$$r = \frac{k \, p_{H_2}^{0.5} p_{CO_2}^{0.5} \left(1 - \frac{p_{CH_4} p_{H_2O}^2}{p_{CO_2} \, p_{H_2}^4 \, K_{eq}}\right)}{\left(1 + K_{OH} \frac{p_{H_2O}}{p_{H_2}^{0.5}} + K_{H_2} p_{H_2}^{0.5} + K_{mix} p_{CO_2}^{0.5}\right)^2} \tag{C-7}$$

Their kinetic parameters are given in Table C-2. It must be noted, though, that, prior to the kinetic measurements, Koschany et al.[31] aged their catalyst to avoid deactivation while collecting data for the kinetics, whereas, we did not subject our samples to such an aging procedure.

Table C-2 Applied kinetic parameters as determined by Koschany et al.[31].

Parameter		Parameter	
k_0	$3.46 * 10^{-4}$ mol bar^{-1}s^{-1}g$_{cat}^{-1}$	A_{H_2}	0.44 bar$^{-0.5}$
E_A	77.5 kJ mol^{-1}	ΔH_{H_2}	−6.2 kJ mol^{-1}
A_{OH}	0.5 bar$^{-0.5}$	A_{mix}	0.88 bar$^{-0.5}$
ΔH_{OH}	22.4 kJ mol^{-1}	ΔH_{mix}	−10 kJ mol^{-1}

C.4 Additional Characterization Results

1. X-ray diffractogram of 11 wt.%Ni-Sm_2O_3 after 5 hours of reduction

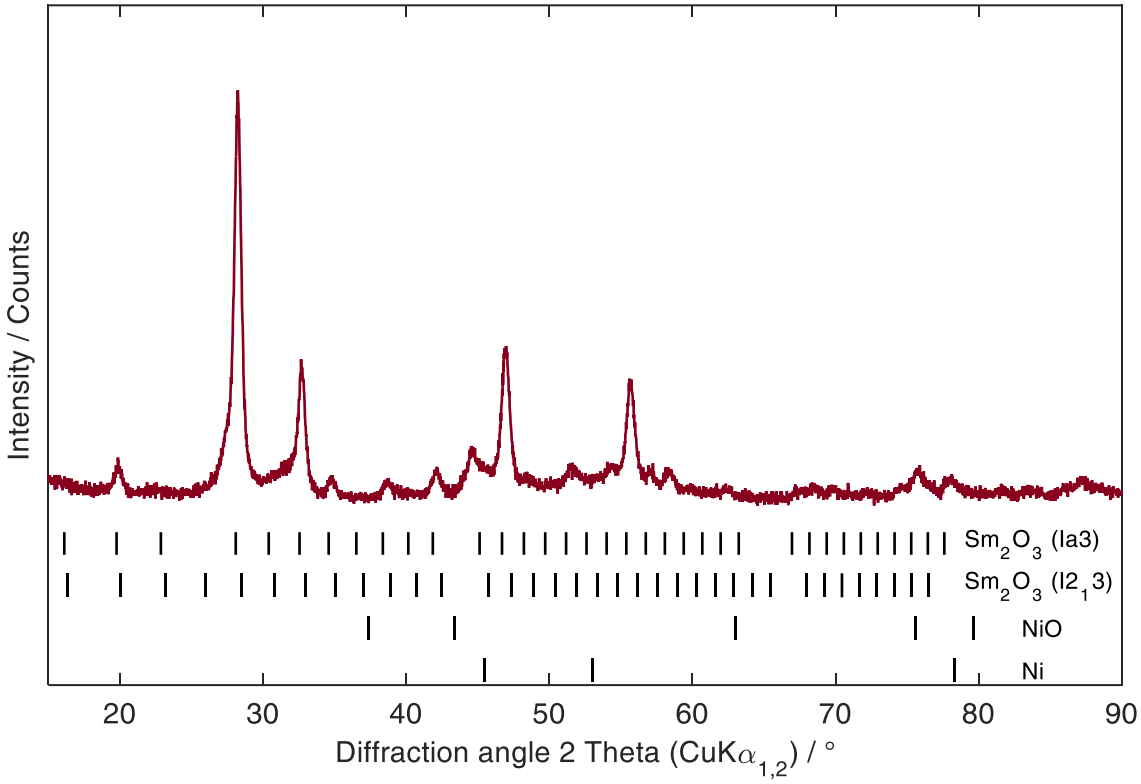

Figure C-1 Diffractogram after reduction of 11 wt.% Ni-Sm_2O_3; the possible reflection positions of Sm_2O_3 ($Ia\bar{3}$ and $I2_13$), Ni and NiO are given as tick marks below the pattern.

After five hours of reduction, the initially present peaks at 28.26°, 32.75° and 46.99° 2 Theta for the A-type samarium oxide (space group $I2_13$) are not present anymore.

2. Additional X-ray diffractograms of 4 wt.% Ni-Sm_2O_3-IWI after reduction and after reaction.

Figure C-2 shows the acquired X-ray diffraction pattern of 4 wt.% Ni-Sm_2O_3 catalyst after reduction and after the time-on-stream experiment discussed in Chapter D.3. The results from the Rietveld refinements are stated in Table C-3.

Note that the contributions of SmO(OH) probably stem from storing the catalyst at ambient conditions for several months before they were analyzed. During this period it is likely that Sm_2O_3 reacted with H_2O to form SmO(OH) (eq. (C-8)).

$$Sm_2O_3 + H_2O \rightarrow 2\ SmO(OH) \qquad \textbf{(C-8)}$$

It is not expected that this phase is present during the catalytic experiments. Furthermore, due to the low mass of H_2O the impact on the Rietveld results is small.

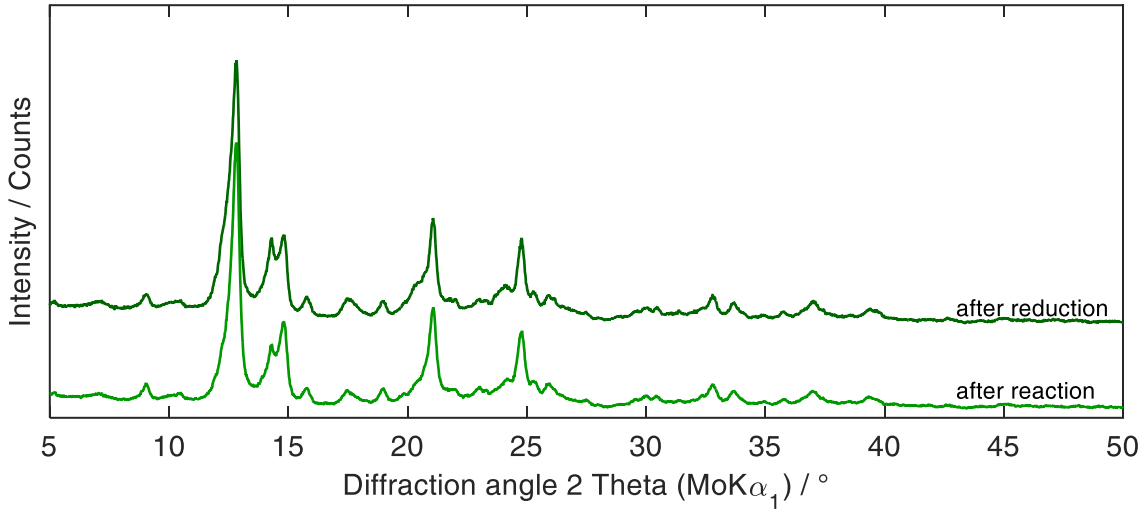

Figure C-2 **X-ray diffraction patterns for the 4 wt.% Ni-Sm_2O_3-IWI catalyst after reduction and after reaction. Note that unlike the diffractograms presented in Chapter 5 the patterns were recorded on a Stoe MP diffractometer equipped with Mo Kα_1 radiation.**

Table C-3 **Lattice parameters, crystallite size L_{Vol}(IB)and NiO loading as calculated by Rietveld refinement for the 4 wt.% Ni-Sm_2O_3-IWI catalyst after reduction and after reaction.**

Phase	Space group	Share / wt.%	Lattice parameters/ pm	L_{Vol}(IB) / nm
After reduction				
C-type Sm_2O_3	$Ia\bar{3}$	40±1	a = 1096±1	10±1
A-type Sm_2O_3	$I2_13$	38±1	a = 1128±1	6±1
SmO_2CO_3	P63/mmc	11±1	a = 394 ±1	18±1
			c = 1550 ±1	
SmO(OH)	P121/m1	8±1	a = 436	14±1
			b = 377	
			c = 615	
Ni	$Fm\bar{3}m$	3±1	a = 349±1	6±1
After reaction (10 h at 400 °C, see Chapter D.3)				
C-type Sm_2O_3	$Ia\bar{3}$	49±1	a = 1096±1	10±1
A-type Sm_2O_3	$I2_13$	30±1	a = 1123±1	6±1
SmO_2CO_3	P63/mmc	10±1	a = 394 ±1	18±1
			c = 1551 ±1	
SmO(OH)	P121/m1	8±1	a = 436	14±1
			b = 377	
			c = 615	
Ni	$Fm\bar{3}m$	3±1	a = 350±1	6±1

3. Mercury intrusion porosimetry

To confirm the absence of macropores Hg intrusion measurements were exemplarily conducted for the 64 wt.% Ni-Sm_2O_3 system. The pores in the micrometer range are the interparticle voids since a powder sample was used and can, therefore, not be attributed to the catalyst itself. The mercury intrusion measurements confirm the pore size distribution in the mesoporous range as determined by N_2 physisorption measurements.

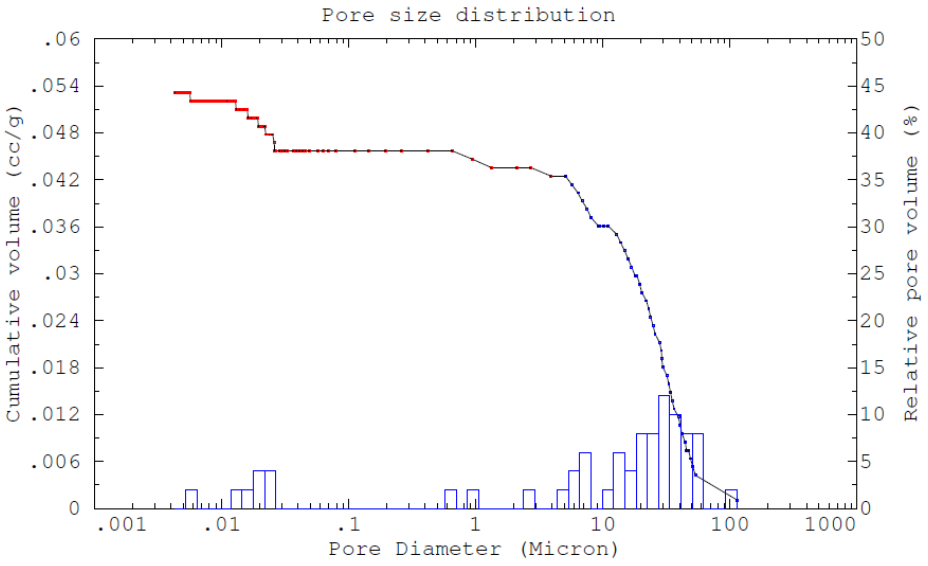

Figure C-3 Pore diameter distribution as determined by Hg intrusion porosimetry. Catalyst: 64 wt.% Ni-Sm_2O_3

C.5 Additional Catalytic Results

1. Determination of activation energies

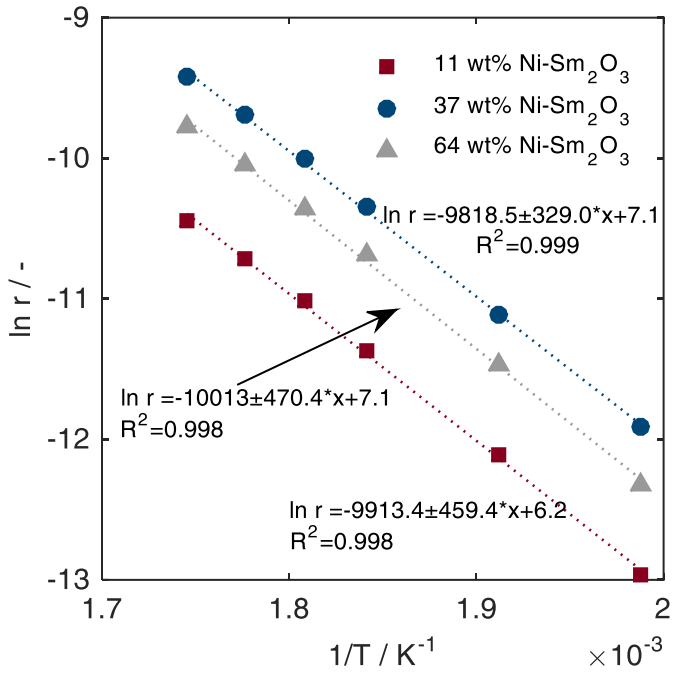

Figure C-4 **Arrhenius plot for the derivation of the activation energies of the 11 wt.%, 39 wt.% and 64 wt.% Ni-Sm_2O_3 catalysts. Conditions: T = 230-300 °C, p = 1 bar, $\dot{V}_{total}$ = 50 mL min^{-1}, 4/1/5 H_2/CO_2/Ar, m_{cat} = 10 mg.**

2. CO/CO_2 methanation

We, further, conducted simultaneous CO_2/CO methanation measurements to evaluate the influence of CO on the catalyst performance as well as to gain insights into the reaction mechanism. Therefore, we adjusted our measurement procedure. The reactor was loaded with 30 mg of 64 wt.% Ni-Sm_2O_3. The feed composition was set to 4/1/1.5 H_2/C/Ar at 50 mL min^{-1}. During the experiment CO_2 was replaced stepwise by CO such that a constant CO_x flow was maintained. The following CO_2/CO ratios were set: 1/0 > 0.88/0.12 > 0.65/0.35 > 0.44/0.56 > 0.12/0.88 > 0/1 and vice versa. The temperature remained fixed at 300 °C. The product gas composition was monitored using a quadrupole mass spectrometer (HPR-30, Hiden Analytical) and Ar as reference flow to quantify CO_2, CO and CH_4. The results are given in Figure C-5.

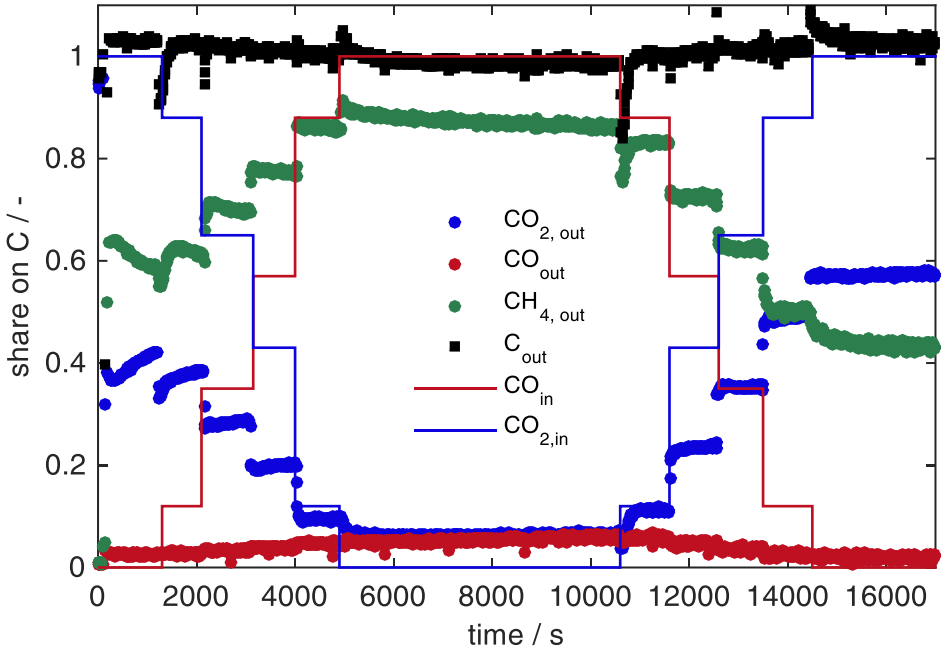

Figure C-5 Simultaneous CO_2/CO methanation at 300 °C, catalyst: 64 wt.% Ni-Sm_2O_3 (30 mg), feed: 4/1/1.5 H_2/CO_x/Ar at 50 mL min^{-1}. Solid lines indicate the carbon feed compositions.

The carbon balance is close to 1 at all times. Starting from pure CO_2 methanation, CO_2 was stepwise replaced in the feed with CO as indicated by the solid lines. Once the carbon feed consisted only of CO, CO_2 partial pressure was increased at the expense of CO. As can be easily seen, no deactivation or poisoning occurs after adding CO to the feed. In fact, the methane yield (= carbon conversion) increases with higher CO share proving the high activity not only for CO_2 but also for CO methanation. The methane yield is maximized under pure CO methanation conditions, whereas it is the lowest in pure CO_2 methanation conditions. The steep decline in CH_4 in the first 1000 s can be attributed to the rapid deactivation as has been discussed in Chapter 6. It is remarkable that CO conversion is under the present reaction conditions over 90%, while the reverse water-gas shift reaction (RWGS) contributes only little as indicated by the low CO_2 concentration in the product gas. Furthermore, judging from the conversion, CO is converted preferentially over CO_2 to methane. This indicates that the activation barrier for CO activation is lower compared to the activation of CO_2, which is in agreement with the literature. Kopyscinski et al.[311] found an activation energy for CO methanation of 74.1 kJ mol^{-1} which is within the 72-78 kJ mol^{-1} interval reported by Gardner and Bartholomew[168]. In opposition, we determined the activation energy for CO_2 methanation at the applied catalyst to be 83.5 kJ mol^{-1}, which is in the reported range of 80–106 kJ mol^{-1} for different Ni-Al_2O_3 systems.[31, 275, 276] Inui et al.[312] suggest that the preferential methanation of CO under co methanation conditions results from a stronger adsorption of CO on the surface. Tada and Kikuchi[202] performed a meta study to gain mechanistic

insights into the selective methanation of carbon monoxide and developed a mechanism based on numerous literature findings. They assume that CO_2 adsorption takes place on the support to form carbonates, whereas CO and H_2 adsorb on the Ni surface. After the dissociation of H_2, hydrogen either hydrogenates CO adsorbed on the metal or spills over to carbonates on the support to form formates. However, only the formates in close proximity to the metal are subsequently decomposed to CO and further hydrogenated to methane. Unfortunately, the authors do not elaborate further on the steps involved in the hydrogenation of CO, nor on the rate determining step (RDS). If the RDS is not the C-O bond cleavage of the CO intermediate/educt or the conversion of the carbonates proceeds by formaldehyd and methoxy species as suggested by Aldana et al., this mechanism can very well explain the observed lower reaction rate of CO_2, in line with the observations in Chapter 4.8.1 and 6.3.3. While several studies assume that CO_2 conversion takes place once CO has been removed from the feed,[312–314] our results point in the same direction, however, cannot fully confirm their findings, yet. We, thus, conclude, that the addition of CO to the feed at least significantly retards CO_2 methanation. The exceptional performance for the simultaneous as well as pure CO methanation proves the suitability of the investigated materials for other catalytical applications such as syngas conversion or efficient CO removal.

C.6 Characterization of the Industrial Ni-Al_2O_3 Catalyst

The following data were provided by the manufacturer and by Ronny Zimmermann (Max Planck Institute for Dynamics of Complex Systems):

- Ni loading: 9 wt.% determined by ICP-OES
- Mean pore diameter: 9.9 nm determined by mercury intrusion
- Porosity: 69% determined by mercury intrusion
- Specific surface area: 145 $m^2\ g^{-1}$ determined by N_2 physisorption
- Recommended reduction procedure: 400 °C for at least 8 h (temperature ramp: 20-40 °C min^{-1}) in 50% H_2 in N_2

Additionally, we carried out XRD and H_2-TPR measurements in-house following the procedures described in A.2 and C.2.

1. X-ray diffraction

The X-ray diffraction pattern of the industrial catalyst is shown in Figure C-6 and reveals the presence of small crystallites and a rather poor crystallinity as indicated by the broad and unresolved peaks as well as the low signal-to-noise ratio, respectively. The peak positions match well with cubic NiO as well as γ-Al_2O_3.

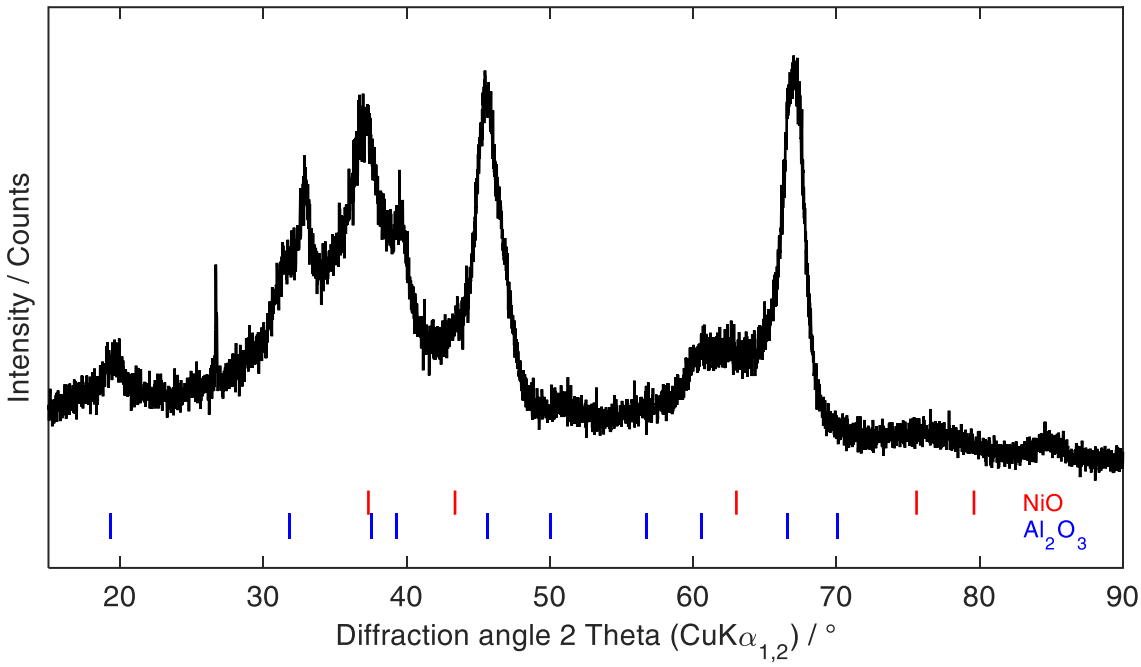

Figure C-6 X-ray diffraction pattern of the industrial Ni-Al_2O_3 catalyst.

2. H_2-temperature programmed reduction

H_2-TPR was measured analogous to the Ni-Sm_2O_3 catalyst, except for the pre-treatment duration and temperature, which was reduced to 2 h at 200 °C. The measured profile Figure C-7) exhibits two pronounced reduction peaks, a sharp low temperature peak at 270 °C as well as an additional broad peak between 380-800 °C. The former can be attributed to the reduction of NiO to metallic Ni, whereas the high temperature peak indicates the presence and reduction of an additional Ni oxide species. Although not clearly evidenced in the X-ray diffraction pattern, the peak most likely corresponds to the reduction of the thermally stable $NiAl_2O_4$.

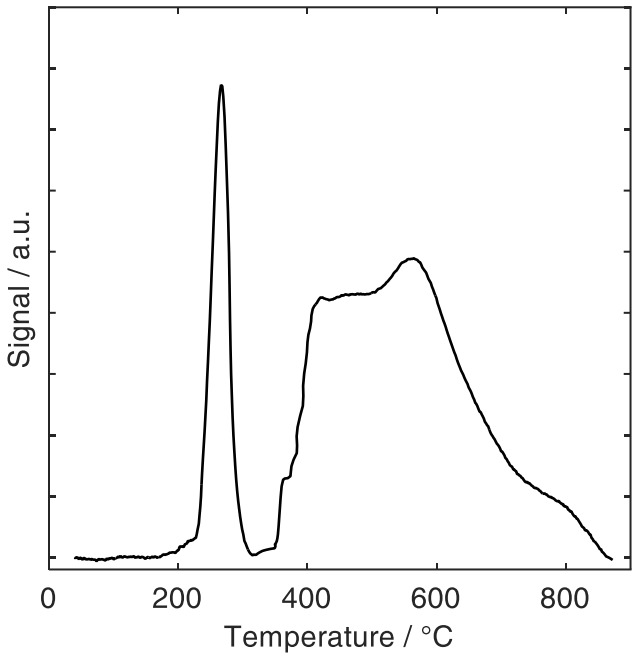

Figure C-7 **TPR profile of the industrial Ni-Al_2O_3 catalyst. Heating ramp 5 °C min^{-1}. The samples were pre-treated at 200 °C in He for 2 h prior to the reaction.**

D ADDITIONAL EXPERIMENTAL DETAILS AND RESULTS – CHAPTER 6

D.1 Experimental Description - DRIFTS

To verify the proposed deactivation mechanism, Diffusive Reflectance Infrared Fourier-Transformed Spectroscopy (DRIFTS) studies were conducted on a Varian-670 FT-IR spectrometer equipped with a liquid nitrogen cooled MCT detector and an IR cell in praying mantis geometry (VC-DRM-5, Harrick). All spectra were recorded with a resolution of 4 cm^{-1} in absorbance mode and the average of 128 scans (acquisition time: 78 sec) is reported.

As the cell could not achieve temperatures high enough for in-situ reduction, the samples were pre-reduced in the catalytic set-up and stored in inert gas atmosphere before being placed on the temperature-controlled sample holder in the IR cell. To remove any impurities and air, the chamber was purged with He for 15 min, followed by an additional mild reduction step at 400 °C in 20 vol.% H_2 in He at a total flowrate of 100 mL min^{-1} for 30 min. Subsequently, the catalyst was cooled down to the intended reaction temperature of 300 °C and the background was recorded in H_2-He atmosphere. Next, the sample was exposed to the reactant mixture composed of 5 vol.% CO_2, 20 vol.% H_2 in He (total flowrate: 100 mL min^{-1}) and a spectrum was recorded after 15 min. After which CO_2 was removed from the feed stream, and the temporal evolution of the surface coverage in 20 vol.% H_2 in He (total flowrate: 100 mL min^{-1}) was tracked by collecting spectra after 5, 10, 20, 60, 90 and 120 min. Finally, the catalyst was exposed to the initial reactant mixture again and a spectrum was recorded after 5 min.

D.2 Influence of Ni loading

The stability of selected Ni-Sm_2O_3 catalysts with Ni loadings of 4, 11, 37 and 64 wt.% Ni was tested at 300 °C. Figure D-1 illustrates the deactivation profile over time for the investigated Ni-Sm_2O_3 catalysts under the standard reaction conditions. All catalysts exhibit a significant drop in conversion at 300 °C over 600 min. However, after applying a subsequent re-reduction step in pure H_2 at 490 °C (hydrogen bracketing technique), the initial conversion level can be completely restored. The selectivity remains unchanged over the measurement period. Deactivation is independent of the catalyst used, as they all loose about 14% (rel.) of activity over the measurement period, thus, structural changes are unlikely due to the differing morphology of the catalysts. This point is further strengthened by the reversibility of the deactivation as sintering or structural changes are usually irreversible.

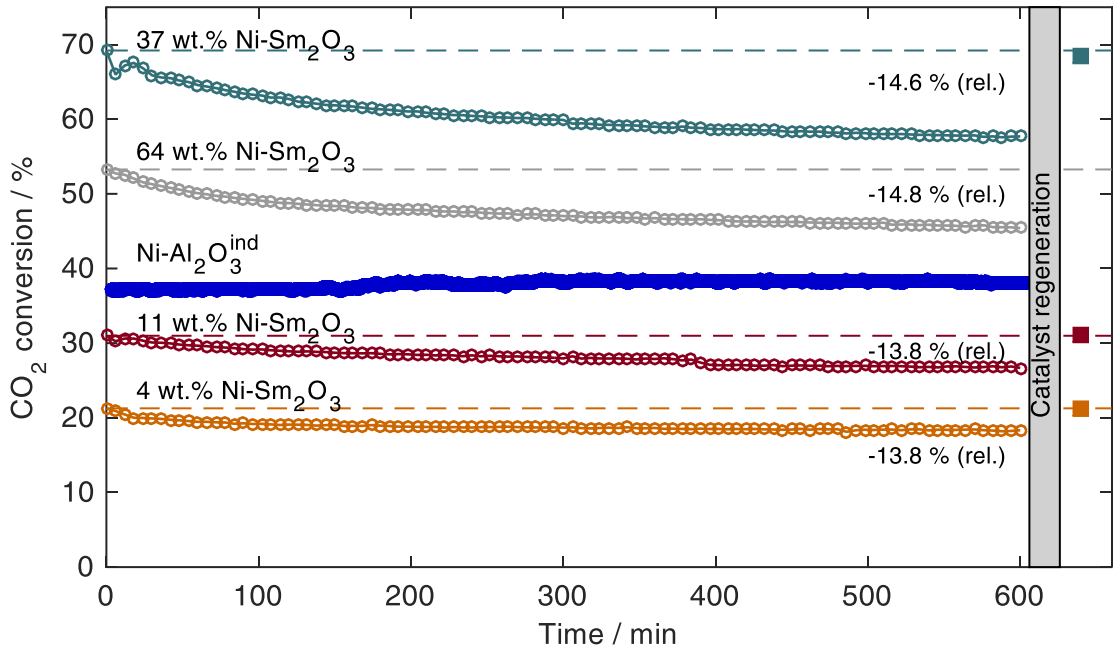

Figure D-1 **Time-on-stream experiments with various Ni-Sm_2O_3 catalysts and the Ni-Al_2O_3 reference catalyst. Conditions: $T = 300$ °C, $p = 1$ bar, $\dot{V}_{total} = 50$ mL min^{-1} composed of 4/1/5 $H_2/CO_2/Ar$, $m_{cat} = 50$ mg. Catalyst regeneration has been performed at 490 °C in pure H_2 for 4 h. The square denotes the CO_2 conversion after the regeneration procedure and under identical reaction conditions.**

D.3 Influence of Preparation Method

To understand how the preparation method influences the catalyst stability, we performed four successive runs at 400 °C over the 4 wt.% Ni-Sm_2O_3 xerogel and impregnated catalyst. After each run the catalyst was regenerated at 490 °C in pure H_2 for 10 h and subsequently exposed to the initial reaction conditions. The results are shown in Figure D-2. For a better comparison, we normalized the data to the initial activity measured in the first run. As becomes immediately obvious, the impregnated catalyst suffers from a more severe and progressive deactivation as the initial activity cannot be restored by the regeneration procedure, whereas even in the fourth run, the activity of the xerogel catalyst is still very similar to the first run. We characterized the catalyst after the extended experiments by XRD and N_2 physisorption to check for indications of sintering, however, found no significant crystallite growth or decrease in surface area for either catalyst (Table D-1). At the current state, the origin for the more pronounced deactivation is still unclear; however, poisoning due to carbonates is expected to be the governing deactivation phenomena.

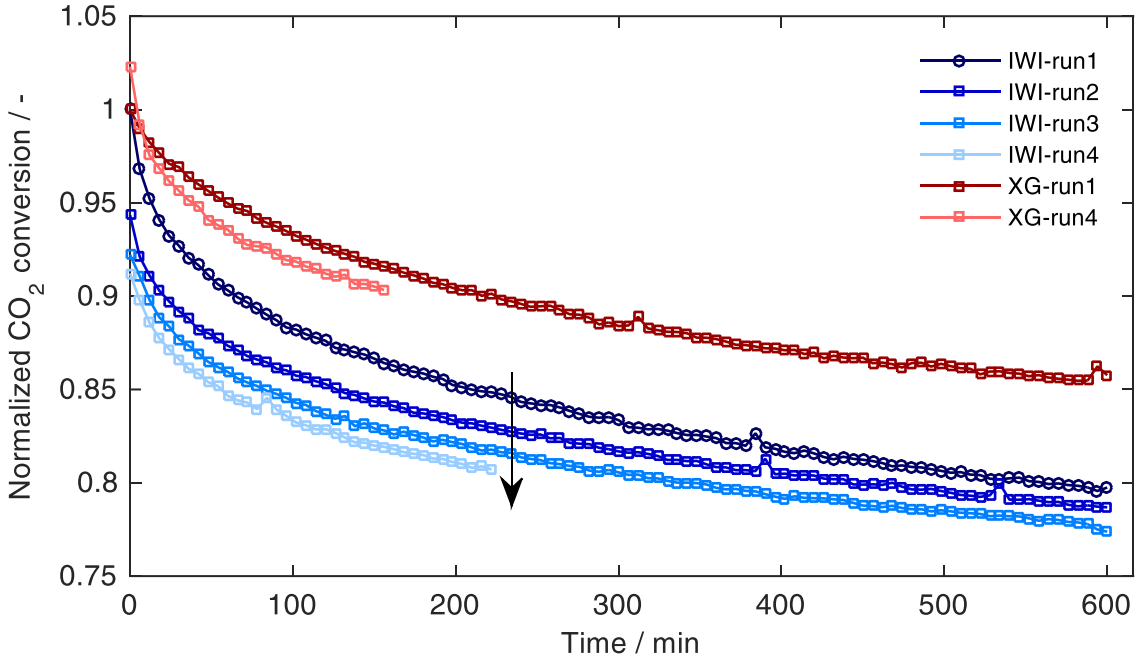

Figure D-2 **Repetitive time-on-stream experiments for the 4 wt.% Ni-Sm_2O_3 xerogel (XG) and 4 wt.% Ni-Sm_2O_3 impregnated catalyst (IWI). After each run the catalyst was regenerated at 490 C for 10 h in H_2. Conditions: T = 400 °C, p = 1 bar, $\dot{V}_{total}$= 50 mL min^{-1} composed of 4/1/5 H_2/CO_2/Ar, m_{cat} = 50 mg. For a better visibility only the first and the fourth run of the xerogel catalyst are shown. Run 2 and 3 do not deviate significantly.**

Table D-1 **Comparison of the structural properties - Ni crystallite size (determined by XRD) and specific surface area (determined by N_2 physisorption) - for the 4 wt.% Ni-Sm_2O_3 xerogel catalyst and the 4 wt.% Ni-Sm_2O_3 impregnated catalyst as-synthesized, after reduction and after reaction.**

	Xerogel catalyst	Impregnated catalyst
Crystallite sizes…		
as-synthesized (NiO) / nm	14 ±1	7 ±1
after reduction (Ni) / nm	9 ±1	6 ±1
after reaction (Ni) / nm	7 ±2	6 ±1
Specific surface area…		
as-synthesized / $m^2\ g^{-1}$	28	27
after reaction / $m^2\ g^{-1}$	25	28

The corresponding X-ray diffraction pattern of the impregnated catalyst are shown in Figure C-2.

D.4 Additional Characterizations by XRD

The X-ray diffraction pattern of the 33 wt.% Ni-Sm_2O_3 catalyst after reduction and after the time-on-stream experiment is shown in Figure D-3.

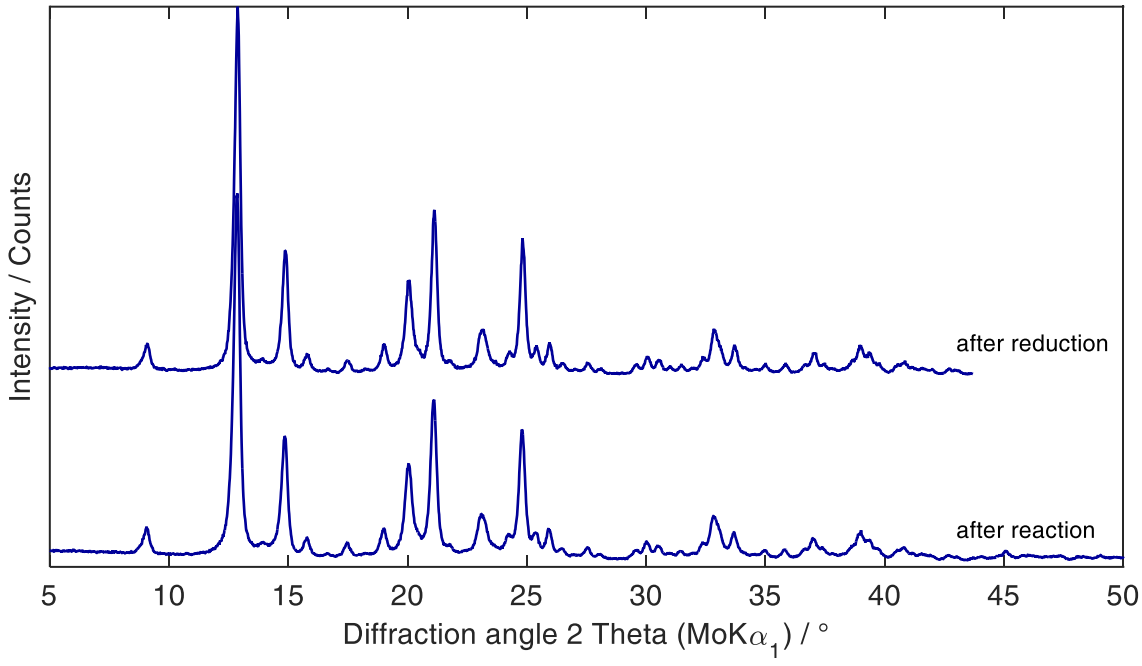

Figure D-3 **X-ray diffraction patterns for 33 wt.% Ni-Sm_2O_3 xerogel catalyst after reduction and after reaction. Note that unlike the diffractograms presented in Chapter 5 the patterns were recorded on a Stoe MP diffractometer equipped with Mo Kα_1 radiation.**

D.5 Additional Catalytic Results

An additional experiment was performed at 490 °C comprised of three subsequent time-on-stream experiments with varying H_2/CO_2 ratio (Figure D-4). We chose 490 °C as reaction temperature for two reasons. For one, it marked the harshest conditions to test the sinter stability of the catalyst. Secondly, as it is also the regeneration temperature, the idea was to prevent the formation of thermally stable carbonates and/or regenerate the catalyst *in-operando*. To this end, we exposed the catalyst to strongly over- as well as under-stochiometric H_2/CO_2 feed ratios, apart from the stochiometric 4/1 ratio.

After reduction, the catalyst was first exposed to a stochiometric H_2/CO_2 ratio for about 600 min (red trace). Subsequently, the catalyst was regenerated at 490 °C for 10 h. At the start of the second run, a stochiometric feed was supplied again for 30 min to check for irreversible effects, before the H_2/CO_2 ratio was decreased to 1.3/1 for about 500 min (yellow trace). At the end of the run, the feed gas was switched back to the stochiometric ratio for ~30 min again. Subsequently, the catalyst was regenerated, followed by run 3 which was conducted analogously but with an over-stochiometric H_2/CO_2 ratios (blue trace). To ensure

that no irreversible effects occurred, the catalyst was regenerated one last time and subsequently exposed to the stochiometric H_2/CO_2 ratio for 30 min again.

While the experiment confirms the high sinter stability of the catalyst, an *in-operando* regeneration by supplying additional H_2 to regenerate oxygen vacancies is not possible as the final activity is independent of the H_2 supply. This contrasts with the observations made in Figure 6-2 and points towards a temperature-dependent H_2 dependence of the deactivation rate.

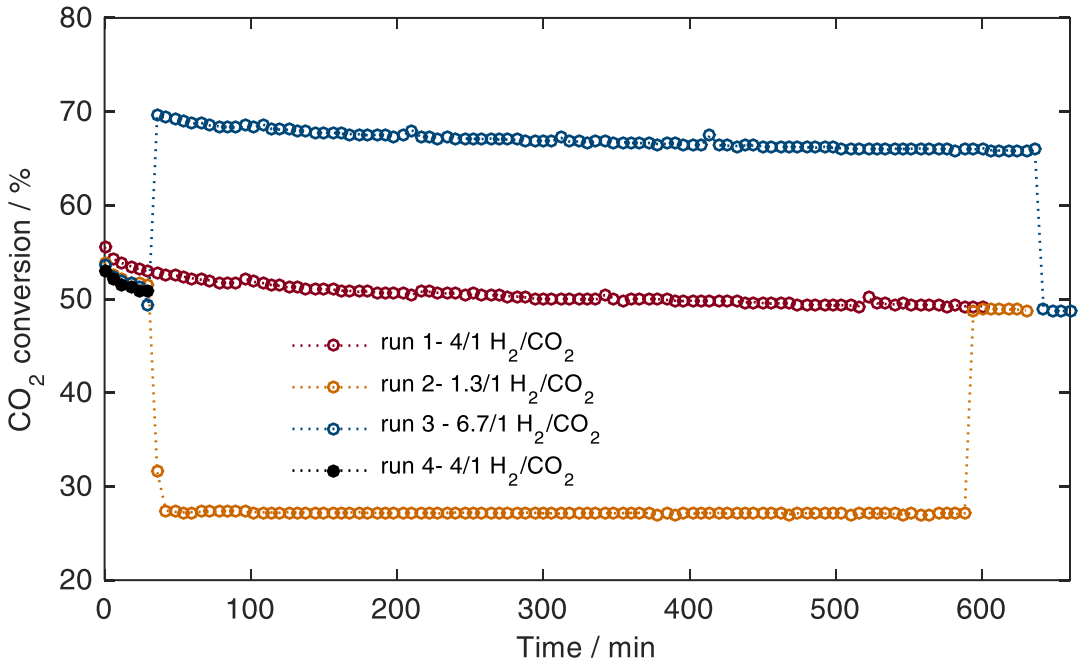

Figure D-4 **CO_2 conversion vs. time for repetitive time-on-stream experiments at 490 °C and different H_2/CO_2 ratios; Reaction conditions: pressure 1 bar, flow rate 50 mL min^{-1}, CO_2 flow rate 5 mL min^{-1}, Ar used as balance, 8 mg catalyst. Note that at the start and at the end, the H_2/CO_2 ratio was set to 4/1.**

E TIME-ON-STREAM BEHAVIOR UNDER TRANSIENT REACTION CONDITIONS

At this point, we do not aim to fully elucidate the effect of transient conditions on the catalyst, but rather aim at demonstrating the ability of the Ni-Sm_2O_3 catalyst to react flexibly to changing H_2/CO_2 ratios while transient reaction temperatures are problematic. Additionally, we investigated if the catalyst stability can be improved by frequent short-term regeneration steps.

E.1 Catalysts and Reaction Conditions

If transient reaction conditions are to be studied, they need to be carefully defined not only in regard to the reaction conditions but also to the time scale. Apart from the scope of the study, the latter depends on the characteristics of the experimental set-up, i.e. the residence time distribution (RTD). When the reaction conditions are changed stepwise, the RTD needs to be sufficiently short in relation to the step width. In pre-experiments the delay between mass flow controller and analytics was determined to be 160 s. (see appendix A.1).

For the following experiments, we focused on the influence of a step-wise change of the H_2/CO_2 ratio and the reaction temperature. As in Chapter 6, the xerogel catalyst with 33 wt.% Ni is applied for all experiments. The experimental conditions for the transient experiments were chosen to reflect realistic process conditions, and when averaged equal the conditions of the steady-state reference experiment. As inlet temperature 300 °C was chosen, while the hot-spot temperature was assumed to be 450 °C, which is a reasonable guess for a reactor with high thermal control.[315] Specifically, the reaction conditions were defined

for the transient H_2/CO_2 ratio experiments as:

- H_2/CO_2: 1.3/1 - 4/1 - 6.7/1 with Ar as balance gas such that a constant total flow rate of 50 mL min^{-1} was achieved,
- temperature: 400 °C, and
- step time: 18 min (= 3 runs on the µGC).

for the transient temperature experiments as:

- H_2/CO_2/Ar: 4/1/5 at a total flowrate of 50 mL min^{-1},
- temperature: (cycle 1) 300 °C – 375 °C – 450 °C – (cycle 2) 300 °C - …,
- step time: 30 min, with a
- ramp time between steps of 5 min.

E.2 Catalytic Results I - Stepwise H_2 Supply @400°C

The effect of a stepwise H_2 supply (4/1 -> 6.7/1 -> 1.3/1 -> 4/1 ->…) at 400 °C is shown in Figure E-1 (yellow). For reference purposes, an additional three runs under stationary feed compositions with the same H_2/CO_2 ratios as during the step experiment were conducted (blue traces: 6.7/1 H_2/CO_2; red traces: 4/1; green traces: 1.3/1). No significant effects of a stepwise changing H_2 supply is observed. In fact, the methane yield almost perfectly switches between the different yield levels measured in the stationary experiments. Note that the first measurement of the 6.7/1 H_2/CO_2 ratio during the step experiments is off, due to bad timing of the µGC run which injected when the set-up was still in the transient regime.

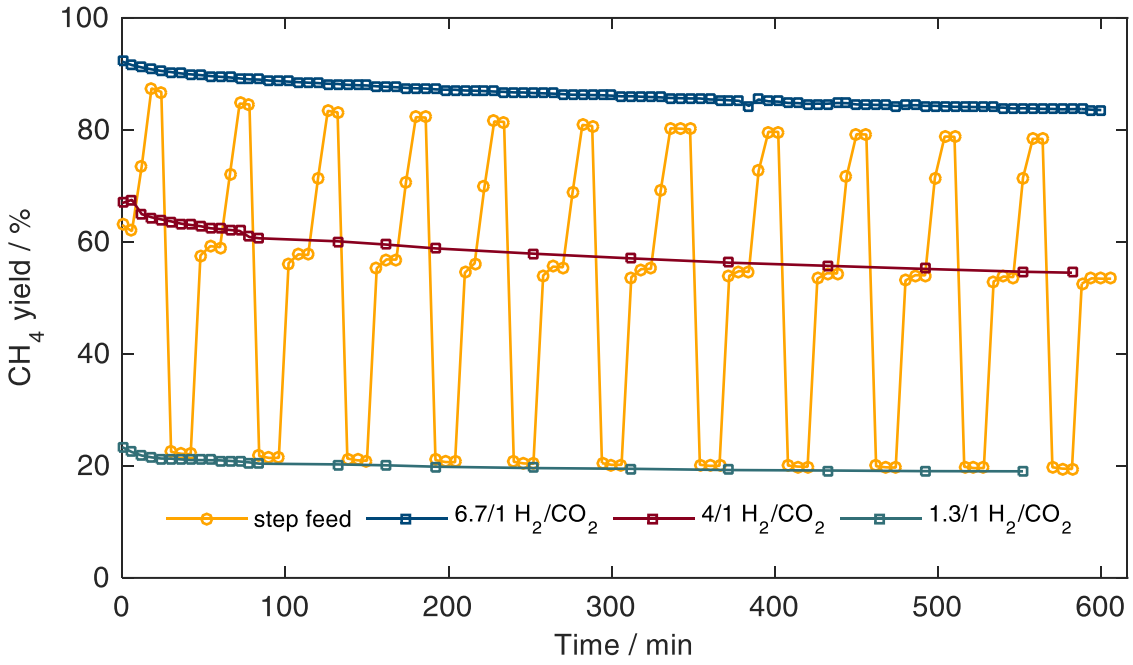

Figure E-1 **Influence of a stepwise changing H_2 supply on the methane yield over time and in comparison to steady-state experiments with different H_2/CO_2 ratios. Reaction conditions: $T = 400$ °C, $p = 1$ bar, $\dot{V}_{tot} = 50$ mL min^{-1} with 5 mL min^{-1} CO_2, Ar as balance, $m_{cat} = 40$ mg. Step feed in the order: 4/1 -> 6.7/1 -> 1.3/1 -> 4/1 ->… H_2/CO_2. Each step is held for 18 min.**

E.3 Catalytic Results II - Transient Temperatures

In two experiments the impact of a transient reaction temperature was investigated. Usually, such a situation is not encountered during most steady-state operations; yet, when the hydrogen supply suddenly changes in a polytropic reactor, it affects the conversion and temperature profile in the reactor as a result of the exothermicity of the reaction. This situation was mimicked by modulating the reaction temperature between three temperatures (300, 375 and 450 °C), while ramping up/cooling down quickly (5 min) in between the individual steps. In total, four such cycles were performed and compared with an additionally performed

steady-state experiment at the mean reaction temperature of the cyclic experiment (375 °C) over a fresh catalyst (Figure E-2). During steady-state operation, the catalyst looses about ~17% (rel.) of its initial activity, which is, in line with the observations in Chapter 6.3.2. In comparison, the deactivation is accelerated when the reaction temperature is not constant over time-on-stream. In fact, the difference in CO_2 conversion between the steady-state and the cyclic temperature modulating experiment increases with increasing cycle number, although the average reaction temperature is the same for the cyclic and steady-state operation, suggesting that transients lead to irreversible catalyst deactivation. This can be reasoned with the temperature dependence of catalyst poisoning by carbonate formation as shown in Figure 6-3, which is more severe at low temperatures. Consequently, conditions which lead to lower reaction temperatures should be avoided from a catalyst stability perspective.

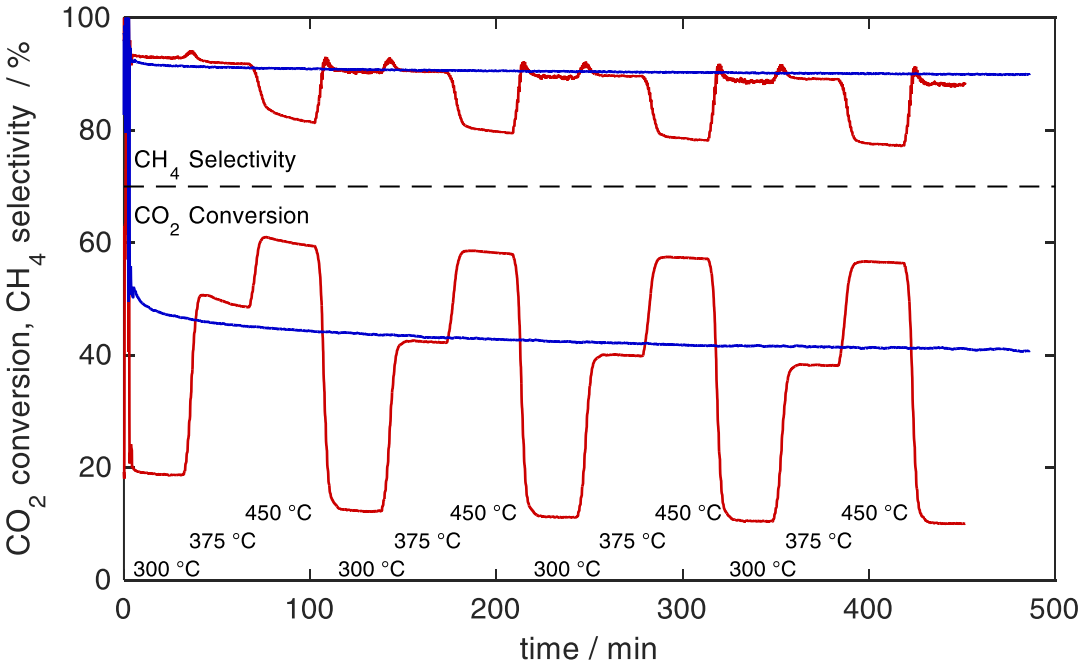

Figure E-2 (red traces) Temperature modulation experiment, (blue traces) steady-state experiment at 375 °C. Conditions: pressure 1 bar, $H_2/CO_2/Ar$ 4/1/5 at a total flow rate of 50 mL min^{-1}, 8 mg catalyst (33 wt.% Ni-Sm_2O_3) Note that instead of the µGC, the NDIR was used to detect CO_2, CO and CH_4.

E.4 Catalytic Results III - Periodic Regeneration Experiments – Intermittent CO_2 Supply

As the catalyst could be regenerated by applying a regeneration step after 600 min, we checked if periodic regeneration steps but for a short term only (12 min) can significantly improve the stability. To this end, we performed two additional experiments at 490 °C (Figure E-3). For the periodic regeneration experiment, CO_2 was removed from the feed every

30 min for a duration of 12 min. By applying such a periodic regeneration step, the activity can be maintained at a higher lever; however, 12 min are not sufficient to restore the initial activity level again. Ultimately, the decision on the regeneration period and frequency will be an economic one which will aim at maximizing the methane yield in a given time period.

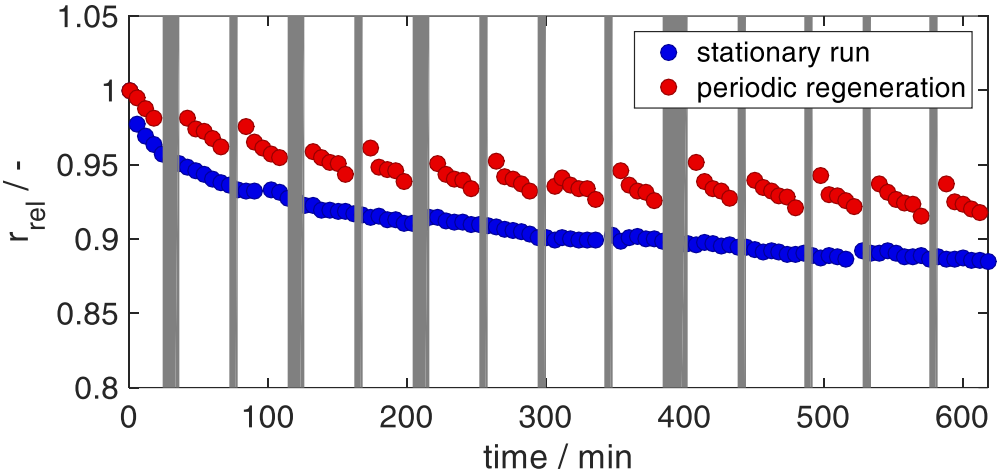

Figure E-3 Effect of an intermittent CO_2 supply on the catalyst stability. Conditions: $T = 490$ °C, $p = 1$ bar, $\dot{V}_{tot} = 50$ mL min^{-1} composed of 5 mL min^{-1} CO_2 and 20 mL min^{-1} H_2 in Ar, $m_{cat} = 4$ mg.

F ADDITIONAL EXPERIMENTAL DETAILS – CHAPTER 7

F.1 Synthesis procedures

For a typical batch of 0.5 g Sm_2O_3 the following amounts of precursor and additives were used:

- 1.27 g of $Sm(NO_3)_3 \cdot 6H_2O$ (99%, Chempur) were dissolved in 5.7 mL ethanol (p.a., Sigma Aldrich) in a glass vial.
- For the screening of different additives, 0.01 g of an additive, either:
    - PEG8000: polyethylene glycol, MW=8000 g mol^{-1},
    - PEO100K: polyethylene oxide, MW=100,000 g mol^{-1},
    - PEO600K: polyethylene oxide, MW=600,000 g mol^{-1},
    - PEO1M: polyethylene oxide, MW=1,000,000 g mol^{-1}, or
    - Pluronic P123, MW=5800 mol g^{-1}

  and 1 mL of deion. water were added and stirred until fully dissolved. For the concentration series with PEG8000, either 0.001, 0.005, 0.01, 0.05 or 0.1 g were added. The amount of deion. water remained fixed at 1 mL.
- 0.55 g citric acid (anhydrous, 99.5%, Roth) were added and dissolved under rapid stirring. (standard solution)

For the synthesis at ambient conditions the next steps were as follows:

- 2.21 mL of propylene oxide (99.5%, Sigma Aldrich) were added to the standard solution and the solution was stirred vigorously for a few seconds before the stir bar was removed.
- Gelation occurred within a few seconds and an opaque white-yellowish monolith formed. A few cracks formed.

For the synthesis in the ice bath:

- An ice bath was prepared by mixing ice and natrium chloride in the ratio 3 to 1 (-18 °C).
- The standard solution was allowed to cool down for about 5 min.
- 2.21 mL of propylene oxide were added to the cooled standard solution and the solution was stirred vigorously for a few seconds and the stir bar was removed.
- Gelation occurred within several hours and resulted in a crack-free monolithic gel with an opaque white-yellowish appearance.

Processing of the wet gel was performed in the identical manner.

- The wet gels were allowed to age undisturbed for 24 h.
- Three solvent exchanges in hexane (99%, ACROS Organics) were performed by decanting the old solvent and replacing it such that the gel surface was covered with a solvent layer of about 2-3 mm in thickness.
- The gels were dried at ambient conditions in the fume hood for at least 5 days before being transferred into crucibles for calcination.
- The dried gels were calcined in a muffle furnace at 600 °C for 4 hours in air. The temperature was ramped up 1 °C min^{-1}.

F.2 Structural Characterizations

Scanning Electron Microscopy. SEM images were acquired on a SUPRA 40 (Zeiss, Germany) operated at 10.0 kV acceleration voltage, 300 pA probe current and 4 mm working distance to gain insights into the catalyst microstructure. For the sample preparation, conductive double-sided carbon tape was placed on a microscope holder and dipped into the Sm_2O_3 powder. A gold layer was sputtered on the sample prior to acquiring the images in order to increase conduction.

NOTATION

Symbol	Description	Unit
Roman		
a_{rel}	relative activity	-
$c_{CH4,out}$	CH_4 concentration in the effluent gas stream	vol. %
$c_{CO,out}$	CO concentration in the effluent gas stream	vol. %
c_{CO2}	CO_2 concentration	mol m^{-3}
$c_{CO2,out}$	CO_2 concentration in the effluent gas stream	vol. %
d_{cat}	catalyst particle diameter	m, µm
D_{Ni}	Ni dispersion	-
$D_{CO_2}^{eff}$	effective binary diffusion coefficient of CO_2 in H_2	m^2 s^{-1}
E_A	Activation energy	kJ mol^{-1}
m_{cat}	catalyst mass	g
M_{Ni}	molar mass of Ni	g mol^{-1}
N	number of	
N_A	Avogadro constant	mol^{-1}
N_{H2}	amount of adsorbed H_2	mol
$\dot{n}_j$	molar flow rate of specie *j*	mol s^{-1}
p	pressure	Pa, bar
p_0	reference pressure	Pa
r^{eff}	measured reaction rate	mol s^{-1} g_{cat}^{-1}
r_j	reaction rate of specie *j*	mol min^{-1} g_{cat}^{-1}
S_{CH4}	CH_4 selectivity	%
$S_{CH4,0}$	CH_4 selectivity at t = 0 min	%
S_{Ni}	Ni surface area	m^2 g^{-1}
T	temperature	°C
t	time	s, min, h
$T_{Hüttig}$	Hüttig temperature	°C
T_{melt}	melting temperature	°C
T_{Tamman}	Tamman temperature	°C
$\dot{V}_{total}$	total volumetric flow rate	mL min^{-1}
w	Ni loading	wt.%
X_{CO2}	CO_2 conversion	%

continued on next page

continued from previous page

Symbol	Description	Unit
$X_{CO2,0}$	CO_2 conversion at t = 0 min	%
Y_{CH4}	CH_4 yield	%
z	stochiometric adsorption factor	-
Greek		
$\Delta_R G_{298K}$	Gibbs free energy at 298.15 K	kJ mol^{-1}
$\Delta_R H_{298K}$	reaction enthalpy at 298.15 K	kJ mol^{-1}
$\Delta\omega$	shift in Raman frequency	cm^{-1}
ν_j	stochiometric coefficient of specie j	-
ρ_{cat}	catalyst density	kg m^{-3}
σ_{Ni}	number of Ni atoms per unit area	m^{-2}
τ	residence time	s
Abbreviations		
µGC	compact gas chromatograph	
AAS	atomic absorption spectroscopy	
BET	Brunauer-Emmet-Teller method	
BJH	Barret-Joyner-Halenda method	
CA	citric acid	
DRIFTS	diffuse reflectance infrared fourier-transform spectroscopy	
EDX	energy dispersive X-ray spectroscopy	
EVD	equal-valence dopant	
HVD	high-valence dopant	
IWI	incipient wetness impregnation	
LVD	low-valence dopant	
MS	mass spectrometry	
NDIR	nondispersive infrared detector	
OCM	oxidative coupling of methane	
PEG	polyethylene glycol	
PEO	polyethylene oxide	
PO	propylene oxide	
REO	rare earth metal oxide	
SDA	structure-directing agent	
SEM	scanning electron spectroscopy	

continued on next page

continued from previous page

Symbol	Description	Unit
SSA	specific surface area	
SSITKA	Steady State Isotopic Transient Kinetic Analysis	
STEM	scanning transmission election microscopy	
TCD	thermal conductivity detector	
TEM	transmission electron microscopy	
TGA	thermal gravimetric analysis	
TOF	turnover frequency	
TPD	temperature-programmed desorption	
TPR	temperature-programmed reduction	
WHSV	weight hourly space velocity	
WP	Weisz-Prater modulus	
XG	xerogel	
XPS	X-ray photoelectron spectroscopy	
XRD	X-ray diffraction	

BIBLIOGRAPHY

1 Palzer, A. and H.-M. Henning, *Renew. Sustain. Energy Rev.*, 2014, **30**, 1019–1034.

2 Palzer, A. and H.-M. Henning, *Energy Technol.*, 2014, **2**, 13–28.

3 Schlögl, R., *Green*, 2012, **2**, 235–255.

4 Sterner, M. and I. Stadler, Berlin, Heidelberg: Springer Berlin Heidelberg, 2014.

5 Rönsch, S., J. Schneider, S. Matthischke, M. Schlüter, M. Götz, J. Lefebvre, P. Prabhakaran, and S. Bajohr, *Fuel*, 2016, **166**, 276–296.

6 Gao, J., Q. Liu, F. Gu, B. Liu, Z. Zhong, and F. Su, *RSC Adv.*, 2015, **5**, 22759–22776.

7 Riani, P., G. Garbarino, M.A. Lucchini, F. Canepa, and G. Busca, *J. Mol. Catal. A. Chem.*, 2014, **383–384**, 10–16.

8 Kattel, S., B. Yan, J.G. Chen, and P. Liu, *J. Catal.*, 2016, **343**, 115–126.

9 Goettmann, F. and C. Sanchez, *J. Mater. Chem.*, 2007, **17**, 24–30.

10 Gao, J., Y. Wang, Y. Ping, D. Hu, G. Xu, F. Gu, and F. Su, *RSC Adv.*, 2012, **2**, 2358–2368.

11 Ghaib, K., K. Nitz, and F. Ben-Fares, *ChemBioEng Rev.*, 2016, **3**, 266–275.

12 Osman, K., T. Götze, and A. Schönrock, *gwf-Gas+Energie*, 2014, **155**, 304–309.

13 Kiewidt, L., 2017.

14 Lee, G.D., M.J. Moon, J.H. Park, S.S. Park, and S.S. Hong, *Korean J. Chem. Eng.*, 2005, **22**, 541–546.

15 Lv, C., L. Xu, M. Chen, Y. Cui, X. Wen, Y. Li, C.E. Wu, B. Yang, Z. Miao, X. Hu, and Q. Shou, *Front. Chem.*, 2020, **8**, 1–32.

16 Aziz, M.A.A., A.A. Jalil, S. Triwahyono, and A. Ahmad, *Green Chem.*, 2015, **17**, 2647–2663.

17 Frontera, P., A. Macario, M. Ferraro, and P. Antonucci, *Catalysts*, 2017, **7**, 59.

18 Vannice, M.A., *Catal. Rev.*, 1976, **14**, 153–191.

19 Bligaard, T., J.K. Nørskov, S. Dahl, J. Matthiesen, C.H. Christensen, and J. Sehested, *J. Catal.*, 2004, **224**, 206–217.

20 Van der Laan, G.P. and A.A.C.M. Beenackers, *Catal. Rev.*, 1999, **41**, 255–318.

21 A. Y. Khodakov, W. Chu, P.F., *Chemical Revieu.* 1692–1744, 2007.

22 Ghaib, K. and F.-Z. Ben-Fares, *Renew. Sustain. Energy Rev.*, 2018, **81**, 433–446.

23 Munnik, P., M.E.Z. Velthoen, P.E. de Jongh, K.P. de Jong, and C.J. Gommes, *Angew. Chemie Int. Ed.*, 2014, **53**, 9493–9497.

24 Vogt, C., E. Groeneveld, G. Kamsma, M. Nachtegaal, L. Lu, C.J. Kiely, P.H. Berben, F. Meirer, and B.M. Weckhuysen, *Nat. Catal.*, 2018, **1**, 127–134.

25 Millet, M.-M., G. Algara-Siller, S. Wrabetz, A. Mazheika, F. Girgsdies, D. Teschner, F. Seitz, A. Tarasov, S. V. Levchenko, R. Schloegl, and E. Frei, *J. Am. Chem. Soc.*, 2019, jacs.8b11729.

26 Wu, H.C., Y.C. Chang, J.H. Wu, J.H. Lin, I.K. Lin, and C.S. Chen, *Catal. Sci. Technol.*, 2015, **5**, 4154–4163.

27 Chang, F.-W., M.-S. Kuo, M.-T. Tsay, and M.-C. Hsieh, *Appl. Catal. A Gen.*, 2003, **247**, 309–320.

28 Gao, J., C. Jia, J. Li, M. Zhang, F. Gu, G. Xu, Z. Zhong, and F. Su, *J. Energy Chem.*, 2013, **22**, 919–927.

29 Aljishi, A., G. Veilleux, J.A.H. Lalinde, and J. Kopyscinski, *Appl. Catal. A Gen.*, 2018, **549**, 263–272.

30 Abelló, S., C. Berrueco, and D. Montané, *Fuel*, 2013, **113**, 598–609.

31 Koschany, F., D. Schlereth, and O. Hinrichsen, *Appl. Catal. B Environ.*, 2016, **181**, 504–516.

32 Burger, T., F. Koschany, O. Thomys, K. Köhler, and O. Hinrichsen, *Appl. Catal. A Gen.*, 2018, **558**, 44–54.

33 Burger, T., F. Koschany, A. Wenng, O. Thomys, K. Köhler, and O. Hinrichsen, *Catal. Sci. Technol.*, 2018, **8**, 5920–5932.

34 Ewald, S., S. Standl, and O. Hinrichsen, *Appl. Catal. A Gen.*, 2018, **549**, 93–101.

35 Ewald, S., M. Kolbeck, T. Kratky, M. Wolf, and O. Hinrichsen, *Appl. Catal. A Gen.*, 2019, **570**, 376–386.

36 He, S., X. Zheng, L. Mo, W. Yu, H. Wang, and Y. Luo, *Mater. Res. Bull.*, 2014.

37 Zhang, Z., Y. Tian, L. Zhang, S. Hu, J. Xiang, Y. Wang, L. Xu, Q. Liu, S. Zhang, and X. Hu, *Int. J. Hydrogen Energy*, 2019, **44**, 9291–9306.

38 Hu, C.W., J. Yao, H.Q. Yang, Y. Chen, and A.M. Tian, *J. Catal.*, 1997, **166**, 1–7.

39 Lechkar, A., A. Barroso Bogeat, G. Blanco, J.M. Pintado, and M. Soussi el Begrani, *Fuel*, 2018, **234**, 1401–1413.

40 Qin, Z., J. Ren, M. Miao, Z. Li, J. Lin, and K. Xie, *Appl. Catal. B Environ.*, 2015, **164**, 18–30.

41 Kwak, J.H., L. Kovarik, and J. Szanyi, *ACS Catal.*, 2013, **3**, 2449–2455.

42 Kowalczyk, Z., K. Stołecki, W. Raróg-Pilecka, E. Miśkiewicz, E. Wilczkowska, and Z. Karpiński, *Appl. Catal. A Gen.*, 2008, **342**, 35–39.

43 Navarro-Jaén, S., J.C. Navarro, L.F. Bobadilla, M.A. Centeno, O.H. Laguna, and J.A. Odriozola, *Appl. Surf. Sci.*, 2019, **483**, 750–761.

44 Eckle, S., H.-G. Anfang, and R.J. Behm, *J. Phys. Chem. C*, 2011, **115**, 1361–1367.

45 Upham, D.C., A.R. Derk, S. Sharma, H. Metiu, and E.W. McFarland, *Catal. Sci. Technol.*, 2015, **5**, 1783–1791.

46 Sharma, S., Z. Hu, P. Zhang, E.W. Mcfarland, and H. Metiu, *J. Catal.*, 2011, **278**, 297–309.

47 Zhu, Y., S. Zhang, Y. Ye, X. Zhang, L. Wang, W. Zhu, F. Cheng, and F. Tao, *ACS Catal.*, 2012, **2**, 2403–2408.

48 Yan, Z., S. Chinta, A.A. Mohamed, J.P. Fackler, and D.W. Goodman, *J. Am. Chem. Soc.*, 2005, **127**, 1604–1605.

49 Mitsu, T., M.K. Rose, E. Fomin, D.F. Ogletree, and M. Salmeron, *Nature*, 2003, **422**, 705–707.

50 Romero-Sáez, M., A.B. Dongil, N. Benito, R. Espinoza-González, N. Escalona, and F. Gracia, *Appl. Catal. B Environ.*, 2018, **237**, 817–825.

51 Jiménez, V., P. Sánchez, P. Panagiotopoulou, J.L. Valverde, and A. Romero, *Appl. Catal. A Gen.*, 2010, **390**, 35–44.

52 Li, L., J. Zheng, Y. Liu, W. Wang, Q. Huang, and W. Chu, *ChemistrySelect*, 2017, **2**, 3750–3757.

53 Zhi, G., X. Guo, X. Guo, Y. Wang, and G. Jin, *Catal. Commun.*, 2011, **16**, 56–59.

54 Wang, Y., Y. Xu, Q. Liu, J. Sun, S. Ji, and Z. jun Wang, *J. Chem. Technol. Biotechnol.*, 2019, **94**, 3780–3786.

55 Gao, J., L.S. Jia, W.P. Fang, Q.B. Li, and H. Song, *Ranliao Huaxue Xuebao/Journal Fuel Chem. Technol.*, 2009, **37**, 573–577.

56 Gao, J., C. Jia, J. Li, F. Gu, G. Xu, Z. Zhong, and F. Su, *Ind. Eng. Chem. Res.*, 2012, **51**, 10345–10353.

57 Trueba, M. and S.P. Trasatti, *Eur. J. Inorg. Chem.*, 2005, 3393–3403.

58 Ivanova, A.S., *Kinet. Catal.*, 2012, **53**, 425–439.

59 Cui, H., M. Zayat, and D. Levy, *J. Non. Cryst. Solids*, 2005, **351**, 2102–2106.

60 Rahmani, S., M. Rezaei, and F. Meshkani, *J. Ind. Eng. Chem.*, 2014, **20**, 4176–4182.

61 Takehira, K., T. Shishido, P. Wang, T. Kosaka, and K. Takaki, *J. Catal.*, 2004, **221**, 43–54.

62 Hu, D., J. Gao, Y. Ping, L. Jia, P. Gunawan, Z. Zhong, G. Xu, F. Gu, and F. Su, *Ind. Eng. Chem. Res.*, 2012, **51**, 4875–4886.

63 Ilsemann, J., A. Straß-Eifert, J. Friedland, L. Kiewidt, J. Thöming, M. Bäumer, and R. Güttel, *ChemCatChem*, 2019, **11**, 4884–4893.

64 Chen, W., R. Pestman, B. Zijlstra, I.A.W. Filot, and E.J.M. Hensen, *ACS Catal.*, 2017, **7**, 8050–8060.

65 Chen, W., I.A.W. Filot, R. Pestman, and E.J.M. Hensen, *ACS Catal.*, 2017, **7**, 8061–8071.

66 Aziz, M.A.A., A.A. Jalil, S. Triwahyono, R.R. Mukti, Y.H. Taufiq-Yap, and M.R. Sazegar, *Appl. Catal. B Environ.*, 2014, **147**, 359–368.

67 Aziz, M.A.A., A.A. Jalil, S. Triwahyono, and M.W.A. Saad, *Chem. Eng. J.*, 2014, **260**, 757–764.

68 Aziz, M.A.A., A.A. Jalil, S. Triwahyono, and S.M. Sidik, *Appl. Catal. A Gen.*, 2014, **486**, 115–122.

69 Bagheri, S., N. Muhd Julkapli, and S. Bee Abd Hamid, *Sci. World J.*, 2014, **2014**, 1–21.

70 Bagheri, S., K. Shameli, and S.B. Abd Hamid, *J. Chem.*, 2013, **2013**.

71 Patra, S., C. Davoisne, H. Bouyanfif, D. Foix, and F. Sauvage, *Sci. Rep.*, 2015, **5**, 1–10.

72 Palcheva, R., L. Dimitrov, G. Tyuliev, A. Spojakina, and K. Jiratova, *Appl. Surf. Sci.*, 2013, **265**, 309–316.

73 Kim, A., D.P. Debecker, F. Devred, V. Dubois, C. Sanchez, and C. Sassoye, *Appl. Catal. B Environ.*, 2018, **220**, 615–625.

74 Lin, Q., X.Y. Liu, Y. Jiang, Y. Wang, Y. Huang, and T. Zhang, *Catal. Sci. Technol.*, 2014, **4**, 2058–2063.

75 Ekou, T., L. Ekou, A. Vicente, G. Lafaye, S. Pronier, C. Especel, and P. Marécot, *J. Mol. Catal. A Chem.*, 2011, **337**, 82–88.

76 Jabłońska, M., *Catal. Commun.*, 2015, **70**, 66–71.

77 Jabłońska, M., *Chem. Pap.*, 2015, **69**, 1141–1155.

78 Huygh, S., A. Bogaerts, and E.C. Neyts, 2016.

79 Varilla, L.A.A., N. Seriani, and J.A. Montoya, *J. Mol. Model.*, 2019, **25**, 1–8.

80 Panagiotopoulou, P., *Appl. Catal. A Gen.*, 2017, **542**, 63–70.

81 Panagiotopoulou, P., D.I. Kondarides, and X.E. Verykios, *J. Phys. Chem. C*, 2011, **115**, 1220–1230.

82 Panagiotopoulou, P., D.I. Kondarides, and X.E. Verykios, *Catal. Today*, 2012, **181**, 138–147.

83 Petala, A. and P. Panagiotopoulou, *Appl. Catal. B Environ.*, 2018, **224**, 919–927.

84 Panagiotopoulou, P., D.I. Kondarides, and X.E. Verykios, *Appl. Catal. B Environ.*, 2009, **88**, 470–478.

85 Yamaguchi, T., *Catal. Today*, 1994, **20**, 199–217.

86 Konstantin Pokrovski, and Kyeong Taek Jung, and A.T. Bell*, 2001.

87 Zhu, J., J.G. van Ommen, H.J.M. Bouwmeester, and L. Lefferts, *J. Catal.*, 2005, **233**, 434–441.

88 Kauppi, E.I., K. Honkala, A.O.I. Krause, J.M. Kanervo, and L. Lefferts, *Top. Catal.*, 2016, **59**, 823–832.

89 da Silva, D.C.D., S. Letichevsky, L.E.P. Borges, and L.G. Appel, *Int. J. Hydrogen Energy*, 2012, **37**, 8923–8928.

90 Muroyama, H., Y. Tsuda, T. Asakoshi, H. Masitah, T. Okanishi, T. Matsui, and K. Eguchi, *J. Catal.*, 2016, **343**, 178–184.

91 Li, W., X. Nie, X. Jiang, A. Zhang, F. Ding, M. Liu, Z. Liu, X. Guo, and C. Song, *Appl. Catal. B Environ.*, 2018, **220**.

92 Wang, H., J. Zhang, Y. Bai, W. Wang, Y. Tan, and Y. Han, *J. Fuel Chem. Technol.*, 2016, **44**, 548–556.

93 Da Silva, D.C.D., S. Letichevsky, E.P. Borges, and L.G. Appel, *Int. J. Hydrogen Energy*, 2012, **37**, 8923–8928.

94 Sato, S., R. Takahashi, M. Kobune, and H. Gotoh, *Appl. Catal. A Gen.*, 2009, **356**, 57–63.

95 Jhang, J.-H., A. Schaefer, W. Cartas, S. Epuri, M. Bäumer, and J.F. Weaver, *J. Phys. Chem. C*, 2013, **117**, 21396–21406.

96 Jhang, J.-H., .

97 Le, T.A., M.S. Kim, S.H. Lee, T.W. Kim, and E.D. Park, *Catal. Today*, 2017, **293294**,

89–96.
98 Ashok, J., M.L. Ang, and S. Kawi, *Catal. Today*, 2017, **281**, 304–311.
99 Atzori, L., M.G. Cutrufello, D. Meloni, C. Cannas, D. Gazzoli, R. Monaci, M.F. Sini, and E. Rombi, *Catal. Today*, 2018, **299**, 183–192.
100 Li, M., H. Amari, and A.C. van Veen, *Appl. Catal. B Environ.*, 2018.
101 Rahmani, S., M. Rezaei, and F. Meshkani, *J. Ind. Eng. Chem.*, 2014, **20**, 4176–4182.
102 Dreyer, J.A.H., P. Li, L. Zhang, G.K. Beh, R. Zhang, P.H.L. Sit, and W.Y. Teoh, *Appl. Catal. B Environ.*, 2017, **219**, 715–726.
103 Zhou, G., H. Liu, K. Cui, A. Jia, G. Hu, Z. Jiao, Y. Liu, and X. Zhang, *Appl. Surf. Sci.*, 2016, **383**, 248–252.
104 Pan, Q., J. Peng, T. Sun, S. Wang, and S. Wang, *Catal. Commun.*, 2014, **45**, 74–78.
105 Tada, S., T. Shimizu, H. Kameyama, T. Haneda, and R. Kikuchi, *Int. J. Hydrogen Energy*, 2012, **37**, 5527–5531.
106 Vrijburg, W.L., E. Moioli, W. Chen, M. Zhang, B.J.P. Terlingen, B. Zijlstra, I.A.W. Filot, A. Züttel, E.A. Pidko, and E.J.M. Hensen, *ACS Catal.*, 2019, 7823–7839.
107 Yamasaki, M., M. Komori, E. Akiyama, H. Habazaki, A. Kawashima, K. Asami, and K. Hashimoto, *Mater. Sci. Eng. A*, 1999, **267**, 220–226.
108 Morales, F. and B.M. Weckhuysen, *ChemInform*, 2007, **38**.
109 Fan, M.T., K.P. Miao, J.D. Lin, H. Bin Zhang, and D.W. Liao, *Appl. Surf. Sci.*, 2014, **307**, 682–688.
110 Le, Kim, Jeong, and Park, *Catalysts*, 2019, **9**, 599.
111 Zhao, A., W. Ying, H. Zhang, M. Hongfang, and D. Fang, *J. Nat. Gas Chem.*, 2012, **21**, 170–177.
112 Qin, H., C. Guo, Y. Wu, and J. Zhang, *Korean J. Chem. Eng*, 2014, **31**, 1168–1173.
113 Zhang, L., L. Bian, Z. Zhu, and Z. Li, *Int. J. Hydrogen Energy*, 2018, **43**, 2197–2206.
114 Wierzbicki, D., M. Motak, T. Grzybek, M.E. Gálvez, and P. Da Costa, *Catal. Today*, 2018, **307**, 205–211.
115 Han, Y., B. Wen, M. Zhu, and B. Dai, *J. Rare Earths*, 2018, **36**, 367–373.
116 Liu, H., X. Zou, X. Wang, X. Lu, and W. Ding, *J. Nat. Gas Chem.*, 2012, **21**, 703–707.
117 Schubert, M., S. Pokhrel, A. Thomé, V. Zielasek, T.M. Gesing, F. Roessner, L. Mädler, and M. Bäumer, *Catal. Sci. Technol.*, 2016, **6**, 7449–7460.
118 Beaumont, S.K., S. Alayoglu, C. Specht, W.D. Michalak, V. V Pushkarev, J. Guo, N. Kruse, and G.A. Somorjai, *J. Am. Chem. Soc.*, 2014, **136**, 9898–9901.
119 Liu, Q., F. Gu, J. Gao, H. Li, G. Xu, and F. Su, *J. Energy Chem.*, 2014, **23**, 761–770.
120 Lu, H., X. Yang, G. Gao, K. Wang, Q. Shi, J. Wang, C. Han, J. Liu, M. Tong, X. Liang, and C. Li, *Int. J. Hydrogen Energy*, 2014, **39**, 18894–18907.
121 Meng, F., Z. Li, F. Ji, and M. Li, *Int. J. Hydrogen Energy*, 2015, **40**, 8833–8843.
122 Liu, Q., F. Gu, Z. Zhong, G. Xu, and F. Su, *RSC Adv.*, 2016, **6**, 20979–20986.
123 Kowalczyk, Z., S. Jodzis, W. Raróg, J. Zieliński, and J. Pielaszek, *Appl. Catal. A Gen.*, 1998, **173**, 153–160.
124 Panagiotopoulou, P., *Appl. Catal. B Environ.*, 2018, **236**, 162–170.
125 Barrientos, J., N. Gonzalez, M. Boutonnet, and S. Järås, *Top. Catal.*, 2017, **60**, 1276–1284.

126 Schubert, M., L. Schubert, A. Thomé, L. Kiewidt, C. Rosebrock, J. Thöming, F. Roessner, and M. Bäumer, *J. Colloid Interface Sci.*, 2016, **477**, 64–73.

127 Minnermann, Neumann, Zielasek, and Baeumer, *Catal. Sci. Technol.*, 2013, **3**, 3256–3267.

128 Dreyer, J.A., P. Li, L. Zhang, G. Khai Beh, R. Zhang, P. H-L Sit, and W. Yang Teoh, *Appl. Catal. B Environ.*, 2017, **219**, 715–726.

129 Park, J.-N. and E.W. McFarland, *J. Catal.*, 2009, **266**, 92–97.

130 Borgschulte, A., N. Gallandat, B. Probst, R. Suter, E. Callini, D. Ferri, Y. Arroyo, R. Erni, H. Geerlings, and A. Züttel, *Phys. Chem. Chem. Phys.*, 2013, **15**, 9620–9625.

131 Zhao, A., W. Ying, H. Zhang, H. Ma, and D. Fang, *Catal. Commun.*, 2012, **17**, 34–38.

132 Guo, M. and G. Lu, *Catal. Commun.*, 2014, **54**, 55–60.

133 Zhen, W., B. Li, G. Lu, and J. Ma, *RSC Adv.*, 2014, **4**, 16472–16479.

134 Fratalocchi, L., L. Lietti, C.G. Visconti, N. Fischer, and M. Claeys, *Catal. Sci. Technol.*, 2019, **9**, 3177–3192.

135 Khassin, A.A., T.M. Yurieva, G.N. Kustova, I.S. Itenberg, M.P. Demeshkina, T.A. Krieger, L.M. Plyasova, G.K. Chermashentseva, and V.N. Parmon, *J. Mol. Catal. A Chem.*, 2001, **168**, 193–207.

136 Alzamora, L.E. and J.R.H. Ross, *J. Chrm. Soc*, 1980, **77**, 665–681.

137 Kruissink, E. and L.L. Van Reijen, *J. Chrm. Soc*, 1980, **77**, 649–663.

138 Hwang, S., U.G. Hong, J. Lee, J.G. Seo, J.H. Baik, D.J. Koh, H. Lim, and I.K. Song, *J. Ind. Eng. Chem.*, 2013, **19**, 2016–2021.

139 Liu, J., J. Yu, F. Su, and G. Xu, *Catal. Sci. Technol.*, 2014, **4**, 472–481.

140 Ocampo, F., B. Louis, A. Kiennemann, and A.C. Roger, *IOP Conf. Ser. Mater. Sci. Eng.*, 2011, **19**, 0–11.

141 Ocampo, F., B. Louis, L. Kiwi-Minsker, and A.C. Roger, *Appl. Catal. A Gen.*, 2011, **392**, 36–44.

142 Atzori, L., M.G. Cutrufello, D. Meloni, R. Monaci, C. Cannas, D. Gazzoli, M.F. Sini, P. Deiana, and E. Rombi, *Int. J. Hydrogen Energy*, 2017, **42**, 20689–20702.

143 Bang, Y., J.G. Seo, M.H. Youn, and I.K. Song, *Int. J. Hydrogen Energy*, 2012, **37**, 1436–1443.

144 Takahashi, R., S. Sato, S. Tomiyama, T. Ohashi, and N. Nakamura, *Microporous Mesoporous Mater.*, 2007, **98**, 107–114.

145 Hwang, S., U.G. Hong, J. Lee, J.H. Baik, D.J. Koh, H. Lim, and I.K. Song, *Catal. Letters*, 2012, **142**, 860–868.

146 Bao, J., J. He, Y. Zhang, Y. Yoneyama, and N. Tsubaki, *Angew. Chemie - Int. Ed.*, 2008, **47**, 353–356.

147 Arnal, P.M., M. Comotti, and F. Schüth, *Angew. Chemie Int. Ed.*, 2006, **45**, 8224–8227.

148 Prieto, G., H. Tüysüz, N. Duyckaerts, J. Knossalla, G.-H. Wang, and F. Schüth, *Chem. Rev.*, 2016, **116**, 14056–14119.

149 Güttel, R., M. Paul, and F. Schüth, *Chem. Commun.*, 2010, **46**, 895–897.

150 Zimmermann, R.T., J. Bremer, and K. Sundmacher, *Chem. Eng. J.*, 2019, 123704.

151 Han, Y., B. Wen, and M. Zhu, *Catalysts*, 2017, **7**, 21.

152 Miao, B., S.S.K. Ma, X. Wang, H. Su, and S.H. Chan, *Catal. Sci. Technol.*, 2016, **6**, 4048–4058.

153 Hernandez Lalinde, J.A., P. Roongruangsree, J. Ilsemann, M. Bäumer, and J. Kopyscinski, *Chem. Eng. J.*, 2020, **390**, 124629.

154 Aldana, P.A.U., F. Ocampo, K. Kobl, B. Louis, F. Thibault-Starzyk, M. Daturi, P. Bazin, S. Thomas, and A.C. Roger, *Catal. Today*, 2013, **215**, 201–207.

155 Wang, F., S. He, H. Chen, B. Wang, L. Zheng, M. Wei, D.G. Evans, and X. Duan, *J. Am. Chem. Soc.*, 2016, **138**, 6298–6305.

156 Cárdenas-Arenas, A., A. Quindimil, A. Davó-Quiñonero, E. Bailón-García, D. Lozano-Castelló, U. De-La-Torre, B. Pereda-Ayo, J.A. González-Marcos, J.R. González-Velasco, and A. Bueno-López, *Appl. Catal. B Environ.*, 2020, **265**, 118538.

157 Cornu, D., H. Guesmi, J.M. Krafft, and H. Lauron-Pernot, *J. Phys. Chem. C*, 2012, **116**, 6645–6654.

158 Lavalley, J.C., *Catal. Today*, 1996, **27**, 377–401.

159 Pan, Q., J. Peng, S. Wang, and S. Wang, *Catal. Sci. Technol.*, 2014, **4**, 502–509.

160 Vesselli, E., J. Schweicher, A. Bundhoo, A. Frennet, and N. Kruse, *J. Phys. Chem. C*, 2011, **115**, 1255–1260.

161 Forzatti, P. and L. Lietti, *Catal. Today*, 1999, **52**, 165–181.

162 Bartholomew, C.H., *Appl. Catal. A Gen.*, 2001, **212**, 17–60.

163 Sehested, J., J.A.P. Gelten, and S. Helveg, *Appl. Catal. A Gen.*, 2006, **309**, 237–246.

164 Behrens, M. and M. Armbrüster, in *Catalysis for Alternative Energy Generation*, New York, NY: Springer New York, 2012, 175–235.

165 Prieto, G., J. Zečević, H. Friedrich, K.P. De Jong, and P.E. De Jongh, *Nat. Mater.*, 2013, **12**, 34–39.

166 Fichtl, M.B., D. Schlereth, N. Jacobsen, I. Kasatkin, J. Schumann, M. Behrens, R. Schlögl, and O. Hinrichsen, *Appl. Catal. A Gen.*, 2015, **502**, 262–270.

167 Bartholomew, C.H., *Catal. Rev.*, 1982, **24**, 67–112.

168 Gardner, D.C. and C.H. Bartholomew, *Ind. Eng. Chem. Prod. Res. Dev.*, 1981, **20**, 80–87.

169 Wolf, M., C. Schüler, and O. Hinrichsen, *J. CO2 Util.*, 2019, **32**, 80–91.

170 Schubert, M., M. Wilhelm, S. Bragulla, C. Sun, S. Neumann, T.M. Gesing, P. Pfeifer, K. Rezwan, and M. Bäumer, *Catal. Letters*, 2017, **147**, 472–482.

171 Mutz, B., H.W.P. Carvalho, W. Kleist, and J.D. Grunwaldt, *J. Phys. Conf. Ser.*, 2016, **712**.

172 Mutz, B., H.W.P. Carvalho, S. Mangold, W. Kleist, and J.D. Grunwaldt, *J. Catal.*, 2015, **327**, 48–53.

173 Mutz, B., A. Gänzler, M. Nachtegaal, O. Müller, R. Frahm, W. Kleist, and J.-D. Grunwaldt, *Catalysts*, 2017, **7**, 279.

174 Hwan Kim, C. and L.T. Thompson, *J. Catal.*, 2005, **230**, 66–74.

175 Liu, J., F.R. Lucci, M. Yang, S. Lee, M.D. Marcinkowski, A.J. Therrien, C.T. Williams, E.C.H. Sykes, and M. Flytzani-Stephanopoulos, *J. Am. Chem. Soc.*, 2016, **138**, 6396–6399.

176 Gash, A.E., T.M. Tillotson, J.H. Satcher, J.F. Poco, L.W. Hrubesh, and R.L. Simpson, *Chem. Mater.*, 2001, **13**, 999–1007.

177 Brinker, C. and G. Scherer, 462, 1990.
178 Aegerter, M.A., N. Leventis, and M.M. Koebel, Eds., New York, NY: Springer New York, 2011.
179 Debecker, D.P. and P.H. Mutin, *Chem. Soc. Rev.*, 2012, **41**, 3624.
180 Baumann, T.F., A.E. Gash, S.C. Chinn, R.S. Maxwell, and J.H.S. Jr, 2004.
181 Cui, H., M. Zayat, and D. Levy, *Journal of Non-Crystalline Solids*, **352**. 3035–3040, 2006.
182 Neumann, B., T.W. Elkins, A.E. Gash, H. Hagelin-Weaver, and M. Bäumer, *Catal. Letters*, 2015, **145**, 1251–1261.
183 Mackenzie, J.D., *J. Non. Cryst. Solids*, 1988, **100**, 162–168.
184 Gash, A.E., J.H. Satcher, and R.L. Simpson, *J. Non. Cryst. Solids*, 2004, **350**, 145–151.
185 Clapsaddle, B.J., D.W. Sprehn, A.E. Gash, J.H. Satcher, and R.L. Simpson, *J. Non. Cryst. Solids*, 2004, **350**, 173–181.
186 Clapsaddle, B.J., B. Neumann, A. Wittstock, D.W. Sprehn, A.E. Gash, J.H. Satcher, R.L. Simpson, and M. Bäumer, *J. Sol-Gel Sci. Technol.*, 2012, **64**, 381–389.
187 Worsley, M.A., J. Ilsemann, T.M. Gesing, V. Zielasek, A.J. Nelson, R.A.S. Ferreira, L.D. Carlos, A.E. Gash, and M. Bäumer, *J. Sol-Gel Sci. Technol.*, 2019, **89**, 176–188.
188 Pecchini, M.P., 3,330,697, 1967.
189 Galadima, A. and O. Muraza, *J. Ind. Eng. Chem.*, 2016, **37**, 1–13.
190 Farrell, B.L., V.O. Igenegbai, and S. Linic, *ACS Catal.*, 2016, **6**, 4340–4346.
191 Alexiadis, V.I., M. Chaar, A. van Veen, M. Muhler, J.W. Thybaut, and G.B. Marin, *Appl. Catal. B Environ.*, 2016, **199**, 252–259.
192 Arndt, S., T. Otremba, U. Simon, M. Yildiz, H. Schubert, and R. Schomäcker, *Appl. Catal. A Gen.*, 2012, **425–426**, 53–61.
193 Choudhary, V.R., S.A.R. Mulla, and B.S. Uphade, *Fuel*, 1999, **78**, 427–437.
194 Othman, N.H., Z. Wu, and K. Li, *J. Memb. Sci.*, 2015, **488**, 182–193.
195 Cherrak, A., R. Hubaut, and Y. Barbaux, *J. Chem. Soc. Faraday Trans.*, 1992, **88**, 3241–3244.
196 Fu, B., T. Jiang, and Y. Zhu, *J. Nanosci. Nanotechnol.*, 2017, **18**, 3398–3404.
197 Özdemir, H., M.A.F. Öksüzömer, and M. Ali Gürkaynak, *Chem. Eng. Commun.*, 2019, **206**, 48–60.
198 McFarland, E.W. and H. Metiu, *Chem. Rev.*, 2013, **113**, 4391–4427.
199 Elkins, T.W., B. Neumann, M. Bäumer, and H.E. Hagelin-Weaver, *ACS Catal.*, 2014, **4**, 1972–1990.
200 Derk, A.R., B. Li, S. Sharma, G.M. Moore, E.W. McFarland, and H. Metiu, *Catal. Letters*, 2013, **143**, 406–410.
201 Choudhary, V.R., V.H. Rane, and S.T. Chaudhari, *Appl. Catal. A Gen.*, 1997, **158**, 121–136.
202 Tada, S. and R. Kikuchi, *Catal. Sci. Technol.*, 2015, **5**, 3061–3070.
203 Wang, Y., J. Ren, K. Deng, L. Gui, and Y. Tang, *Chem. Mater.*, 2000, **12**, 1622–1627.
204 Liotta, L.F., G.A. Martin, and G. Deganello, *J. Catal.*, 1996, **164**, 322–333.
205 Benitez, J.J., I. Carrizosa, and J.A. Odriozola, *Appl. Surf. Sci.*, 1993, **68**, 565–573.

206 Muroyama, H., Y. Tsuda, T. Asakoshi, H. Masitah, T. Okanishi, T. Matsui, and K. Eguchi, *J. Catal.*, 2016, **343**, 178–184.

207 Karim, W., C. Spreafico, A. Kleibert, J. Gobrecht, J. VandeVondele, Y. Ekinci, and J.A. van Bokhoven, *Nature*, 2017, **541**, 68–71.

208 Barzan, C., E. Groppo, S. Bordiga, and A. Zecchina, *ACS Catal.*, 2014, **4**, 986–989.

209 Liu, L., Y. Jiang, H. Zhao, J. Chen, J. Cheng, K. Yang, and Y. Li, *ACS Catal.*, 2016, **6**, 1097–1108.

210 Deleitenburg, C. and A. Trovarelli, *J. Catal.*, 1995, **156**, 171–174.

211 Trovarelli, A., C. Deleitenburg, G. Dolcetti, and J.L. Lorca, *J. Catal.*, 1995, **151**, 111–124.

212 Metiu, H., S. Chrétien, Z. Hu, B. Li, and X. Sun, *J. Phys. Chem. C*, 2012, **116**, 10439–10450.

213 Zhou, R., N. Rui, Z. Fan, and C. jun Liu, *Int. J. Hydrogen Energy*, 2016, **41**, 22017–22025.

214 Kogler, M., E.M. Köck, T. Bielz, K. Pfaller, B. Klötzer, D. Schmidmair, L. Perfler, and S. Penner, *J. Phys. Chem. C*, 2014, **118**, 8435–8444.

215 Verónica Ganduglia-Pirovano, M., A. Hofmann, and J. Sauer, *Surf. Sci. Rep.*, 2007, **62**, 219–270.

216 Pacchioni, G., *ChemPhysChem*, 2003, **4**, 1041–1047.

217 Scirè, S., C. Crisafulli, R. Maggiore, S. Minicò, and S. Galvagno, *Catal. Letters*, 1998, **51**, 41–45.

218 Chen, S., A.M. Abdel-Mageed, C. Gauckler, S.E. Olesen, I. Chorkendorff, and R.J. Behm, *J. Catal.*, 2019, **373**, 103–115.

219 Sato, S., R. Takahashi, M. Kobune, and H. Gotoh, *Appl. Catal. A Gen.*, 2009, **356**, 57–63.

220 Pacchioni, G., **58**. Cham: Springer International Publishing, 2015.

221 Pokrovski, K., K.T. Jung, and A.T. Bell, *Langmuir*, 2001, **17**, 4297–4303.

222 Smrčok, Ľ., V. Langer, and J. Křesťan, *Acta Crystallogr. Sect. C Cryst. Struct. Commun.*, 2006, **62**, 83–84.

223 Bernuy-Lopez, C., M. Allix, C.A. Bridges, J.B. Claridge, and M.J. Rosseinsky, *Chem. Mater.*, 2007, **19**, 1035–1043.

224 Baur, W.H., *Acta Crystallogr.*, 1956, **9**, 515–520.

225 Weirich, T.E., M. Winterer, S. Seifried, and J. Mayer, *Acta Crystallogr. Sect. A Found. Crystallogr.*, 2002, **58**, 308–315.

226 Whittle, K.R., G.R. Lumpkin, and S.E. Ashbrook, *J. Solid State Chem.*, 2006, **179**, 512–521.

227 Daturi, M., C. Binet, J.C. Lavalley, and G. Blanchard, *Surf. Interface Anal.*, 2000, **30**, 273–277.

228 Guo, M., J. Lu, Y. Wu, Y. Wang, and M. Luo, *Langmuir*, 2011, **27**, 3872–3877.

229 Liu, J., C. Liu, G. Zhou, S. Shen, and L. Rong, *Green Chem.*, 2012, **14**, 2499–2505.

230 Sato, K., K. Imamura, Y. Kawano, S. ichiro Miyahara, T. Yamamoto, S. Matsumura, and K. Nagaoka, *Chem. Sci.*, 2016, **8**, 674–679.

231 Mutch, G.A., S. Morandi, R. Walker, J.A. Anderson, D. Vega-Maza, L. Operti, and G. Cerrato, *J. Phys. Chem. C*, 2016, **120**, 17570–17578.

232 Busca, G. and V. Lorenzelli, *Mater. Chem.*, 1982, **7**, 89–126.
233 Compagnoni, M., A. Villa, E. Bahdori, D.J. Morgan, L. Prati, N. Dimitratos, I. Rossetti, and G. Ramis, *Catalysts*, 2018, **8**.
234 Liao, L.F., C.F. Lien, D.L. Shieh, M.T. Chen, and J.L. Lin, *J. Phys. Chem. B*, 2002, **106**, 11240–11245.
235 Kouva, S., J. Andersin, K. Honkala, J. Lehtonen, L. Lefferts, and J. Kanervo, *Phys. Chem. Chem. Phys.*, 2014, **16**, 20650–20664.
236 Akune, T., Y. Morita, S. Shirakawa, K. Katagiri, and K. Inumaru, *Langmuir*, 2018, **34**, 23–29.
237 Jung, K.T. and A.T. Bell, *J. Catal.*, 2001, **204**, 339–347.
238 Farfan-Arribas, E. and R.J. Madix, *J. Phys. Chem. B*, 2003, **107**, 3225–3233.
239 Tumuluri, U., J.D. Howe, W.P. Mounfield, M. Li, M. Chi, Z.D. Hood, K.S. Walton, D.S. Sholl, S. Dai, and Z. Wu, *ACS Sustain. Chem. Eng.*, 2017, **5**, 9295–9306.
240 Parker, J.C. and R.W. Siegel, *Appl. Phys. Lett.*, 1990, **57**, 943–945.
241 Ueno, A. and C.O. Bennett, *J. Catal.*, 1978, **54**, 31–41.
242 Wang, X., H. Shi, J.H. Kwak, and J. Szanyi, *ACS Catal.*, 2015, **5**, 6337–6349.
243 Baidya, T. and P. Bera, *Catal. Struct. React.*, 2015, **1**, 110–119.
244 Mitchell, W.J., Y. Wang, J. Xie, and W.H. Weinberg, *J. Am. Chem. Soc.*, 1993, **115**, 4381–4382.
245 Wambach, J., J. Zarfl, A. Wokaun, T.J. Schildhauer, and D. Ferri, *Appl. Catal. A Gen.*, 2015, **495**, 104–114.
246 Guo, J., Z. Hou, J. Gao, and X. Zheng, *Chinese J. Catal.*, 2007, **28**, 22–26.
247 Hertl, W., *Langmuir*, 1989, **5**, 96–100.
248 He, M.Y. and J.G. Ekerdt, *J. Catal.*, 1984, **87**, 381–388.
249 Wang, X., Y. Hong, H. Shi, and J. Szanyi, *J. Catal.*, 2016, **343**, 185–195.
250 Neumann, S., S. Grotheer, J. Tielke, I. Schrader, J. Quinson, A. Zana, M. Oezaslan, M. Arenz, and S. Kunz, *J. Mater. Chem. A*, 2017, **5**, 6140–6145.
251 Marwood, M., R. Doepper, and A. Renken, *Appl. Catal. A Gen.*, 1997, **151**, 223–246.
252 Morterra, C. and G. Magnacca, *Catal. Today*, 1996, **27**, 497–532.
253 Denkwitz, Y., A. Karpenko, V. Plzak, R. Leppelt, B. Schumacher, and R.J. Behm, *J. Catal.*, 2007, **246**, 74–90.
254 Solymosi, F. and M. Pásztor, *J. Phys. Chem.*, 1985, **89**, 4789–4793.
255 Kwon, H. and D.G. Park, *Bull. Korean Chem. Soc.*, 2009, **30**, 2567–2573.
256 Menezes, A.O., P.S. Silva, E.P. Hernández, L.E.P. Borges, and M.A. Fraga, *Langmuir*, 2010, **26**, 3382–3387.
257 Schweicher, J., A. Bundhoo, A. Frennet, N. Kruse, H. Daly, and F.C. Meunier, *J. Phys. Chem. C*, 2010, **114**, 2248–2255.
258 Wang, Z.H., T. Urisu, H. Watanabe, K. Ooi, G. Ranga Rao, S. Nanbu, J. Maki, and M. Aoyagi, *Surf. Sci.*, 2005, **575**, 330–342.
259 Kopani, M., M. Mikula, D. Kosnac, J. Gregus, and E. Pincik, *J. Electr. Eng.*, 2017, **68**, 53–57.
260 Oh, T. and C.K. Choi, *J. Korean Phys. Soc.*, 2010, **56**, 1150–1155.
261 Le, T.A., J.K. Kang, and E.D. Park, *Top. Catal.*, 2018, **0**.
262 Zhang, Y., *Synth. React. Inorganic, Met. Nano-Metal Chem.*, 2016, **46**, 1565–1570.

263 Yang, H., H. Wang, H.M. Luo, D.M. Feldmann, P.C. Dowden, R.F. DePaula, and Q.X. Jia, *Appl. Phys. Lett.*, 2008, **92**, 062905.
264 Lide, D.R., 79th ed. CRC, 2009.
265 Ruiz-Gómez, M.A., C. Gómez-Solís, M.E. Zarazúa-Morín, L.M. Torres-Martínez, I. Juárez-Ramírez, D. Sánchez-Martínez, and M.Z. Figueroa-Torres, *Ceram. Int.*, 2014, **40**, 1893–1899.
266 Queiroz, C.A. d. S., M.E. de Vasconcellos, S.M.R. da Rocha, J.A. Seneda, W.R. Pedreira, J. do R. Matos, and A. Abrão, *J. Alloys Compd.*, 2004, **374**, 401–404.
267 Zhang, W., B. Liu, and Y. Tian, *Catal. Commun.*, 2007, **8**, 661–667.
268 Gomez-Sainero, L.M., R.T. Baker, A.J. Vizcaı, S.M. Francis, A. Calles, I.S. Metcalfe, and J.J. Rodriguez, 2009, 8364–8372.
269 Janković, B., B. Adnadević, and S. Mentus, *Chem. Eng. Sci.*, 2008, **63**, 567–575.
270 Augusto, B.L., L.O.O. Costa, F.B. Noronha, R.C. Colman, and L. V. Mattos, *Int. J. Hydrogen Energy*, 2012, **37**, 12258–12270.
271 Stangeland, K., D.Y. Kalai, H. Li, and Z. Yu, *Appl. Energy*, 2018, **227**, 206–212.
272 Li, Y., G. Lu, and J. Ma, *RSC Adv.*, 2014, **4**, 17420–17428.
273 Weisz, P.B. and C.D. Prater, *Adv. Catal.*, 1954, **6**, 143–196.
274 Yang, J., J. Mcgregor, A.J. Sederman, and J.S. Dennis, *Chemical Engineering Science*, **141**. 28–45, 2016.
275 Van Herwijnen, T., H. Van Doesburg, and W.A. De Jong, *J. Catal.*, 1973, **28**, 391–402.
276 Maatman, R. and S. Hiemstra, *J. Catal.*, 1980, **62**, 349–356.
277 Lu, Z.L., E. Lindner, and H.A. Mayer, *Chem. Rev.*, 2002, **102**, 3543–3578.
278 Freidlin, L.K., A.A. Balandin, N. V. Borunova, and A.E. Agronomov, 1955, 935–942.
279 O'Connor, A.M., F.C. Meunier, and J.R.H. Ross, **119**. Elsevier Masson SAS, 1998.
280 Wu, H.-C., Y.C. Chang, J.H. Wu, J.H. Lin, I.K. Lin, and C.-S. Chen, *Catal. Sci. Technol.*, 2015, **5**, 4154–4163.
281 Loewert, M., J. Hoffmann, P. Piermartini, M. Selinsek, R. Dittmeyer, and P. Pfeifer, *Chem. Eng. Technol.*, 2019, **42**, 2202–2214.
282 Kalz, K.F., R. Kraehnert, M. Dvoyashkin, R. Dittmeyer, R. Gläser, U. Krewer, K. Reuter, and J.D. Grunwaldt, *ChemCatChem*, 2017, **9**, 17–29.
283 Takahashi, R., S. Sato, T. Sodesawa, K. Arai, and M. Yabuki, *J. Catal.*, 2005, **229**, 24–29.
284 Mahmoud, M.A., R. Narayanan, and M.A. El-Sayed, *Acc. Chem. Res.*, 2013, **46**, 1795–1805.
285 Polarz, S. and A. Kuschel, *Chem. - A Eur. J.*, 2008, **14**, 9816–9829.
286 Yang, F., D. Deng, X. Pan, Q. Fu, and X. Bao, *Natl. Sci. Rev.*, 2015, **2**, 183–201.
287 Sun, Q., X.-Q. Zhang, Y. Wang, and A.-H. Lu, *Chinese J. Catal.*, 2015, **36**, 683–691.
288 Xiao, J. and J. Wei, *Chem. Eng. Sci.*, 1992, **47**, 1123–1141.
289 Rytter, E., S. Eri, T.H. Skagseth, D. Schanke, E. Bergene, R. Myrstad, and A. Lindvåg, *Ind. Eng. Chem. Res.*, 2007, **46**, 9032–9036.
290 Li, H., J. Wang, C. Chen, L. Jia, B. Hou, and D. Li, *RSC Adv.*, 2017, **7**, 9436–9445.
291 Weatherbee, G. and C.H. Bartholomew, *J. Catal.*, 1982, **77**, 460–472.
292 Liu, Q., Y. Han, J. Cai, E.J. Crumlin, Y. Li, and Z. Liu, *Catal. Letters*, 2018, **148**,

1686–1691.
293 Le, T., A. Striolo, C.H. Turner, and D.R. Cole, *Sci. Rep.*, 2017, **7**, 9021.
294 Feinle, A., M.S. Elsaesser, and N. Hüsing, *Chem. Soc. Rev.*, 2016, **45**, 3377–3399.
295 Brinker, C.J., R. Sehgal, N.K. Raman, S.S. Prakash, and L. Delattre, *Mater. Res. Soc. Symp. - Proc.*, 1995, **368**, 329–343.
296 Brinker, C.J., G.C. Frye, A.J. Hurd, C.S. Ashley, S.N. Laboratories, and I. Introduction, *Thin Solid Films*, 1991, **201**, 97–108.
297 Fidalgo, A. and L.M. Ilharco, *J. Non. Cryst. Solids*, 2004, **347**, 128–137.
298 Ren, L., X. Li, and H. He, *ChemistrySelect*, 2016, **1**, 1072–1075.
299 Nakanishi, K., *Bull. Chem. Soc. Jpn.*, 2006, **79**, 673–691.
300 Tokudome, Y., K. Fujita, K. Nakanishi, K. Miura, and K. Hirao, *Chem. Mater.*, 2007, **19**, 3393–3398.
301 Tokudome, Y., K. Nakanishi, K. Kanamori, K. Fujita, H. Akamatsu, and T. Hanada, *J. Colloid Interface Sci.*, 2009, **338**, 506–513.
302 Takahashi, R., K. Nakanishi, and N. Soga, 2005.
303 Kido, Y., K. Nakanishi, A. Miyasaka, and K. Kanamori, *Chem. Mater.*, 2012, **24**, 2071–2077.
304 Hartmann, S., A. Sachse, and A. Galarneau, *Materials (Basel).*, 2012, **5**, 336–349.
305 Takahashi, R., S. Sato, T. Sodesawa, and M. Yabuki, *J. Catal.*, 2001, **200**, 197–202.
306 Taddia, M. and P. Sternini, *Ann. Chim.*, 2001, **91**, 239–244.
307 Suoranta, T., M. Niemelä, and P. Perämäki, *Talanta*, 2014, **119**, 425–429.
308 Wajid Shah, M., Y. Zhu, X. Fan, J. Zhao, Y. Li, S. Asim, and C. Wang, *Sci. Rep.*, 2015, **5**, 15804.
309 Eder, D. and R. Kramer, *Phys. Chem. Chem. Phys.*, 2002, **4**, 795–801.
310 Mueller, R., S. Zhang, M. Klink, M. Bäumer, and S. Vasenkov, *Phys. Chem. Chem. Phys.*, 2015, **17**, 27481–27487.
311 Kopyscinski, J., T.J. Schildhauer, F. Vogel, S.M.A. Biollaz, and A. Wokaun, *J. Catal.*, 2010, **271**, 262–279.
312 Inui, T., M. Funabiki, and Y. Takegami, *Ind. Eng. Chem. Prod. Res. Dev.*, 1980, **19**, 385–388.
313 Habazaki, H., M. Yamasaki, B.-P. Zhang, A. Kawashima, S. Kohno, T. Takai, and K. Hashimoto, *Appl. Catal. A Gen.*, 1998, **172**, 131–140.
314 Nematollahi, B., M. Rezaei, and E.N. Lay, *J. Rare Earths*, 2015, **33**, 619–628.
315 Kiewidt, L. and J. Thöming, *Chem. Eng. Sci.*, 2015, **132**, 59–71.
316 El-Moemen, A.A., G. Kučerová, and R.J. Behm, *Appl. Catal. B Environ.*, 2010, **95**, 57–70.
317 Abdel-Mageed, A.M., D. Widmann, S.E. Olesen, I. Chorkendorff, and R.J. Behm, *ACS Catal.*, 2018, **8**, 5399–5414.

Individual contributions to the papers relevant for this thesis

Paper I:

J. Ilsemann, A. Sonström, T.M. Gesing, R. Anwander, and M. Bäumer, "Highly Active Sm_2O_3-Ni Xerogel catalysts for CO_2 methanation", *ChemCatChem*, **2019**, 11, 6, 1732-1741.

TG performed the Rietveld refinements. AS developed the synthesis for pure Sm_2O_3. MB and RA supervised the project. JI carried out the experiments, analyzed the results and wrote the manuscript with input from all other authors.

Paper II:

J. Ilsemann, A. Straß-Eifert, J. Friedland, L. Kiewidt, J. Thöming, M. Bäumer, and R. Güttel, "Cobalt@Silica Core-Shell Catalysts for Hydrogenation of CO/CO_2 Mixtures to Methane", *ChemCatChem*, **2019**, 11, 19, 4884-4893.

ASE synthesized and characterized the catalysts. JI was responsible for the catalytic experiments. JF, LK, JT and MB contributed in interpreting the results. RG supervised the project. JI and ASE wrote the manuscript with input from all other authors.

Paper III:

J. Ilsemann, M.M. Murshed, T.M. Gesing, J. Kopyscinski, and M. Bäumer, "On the support dependency for the CO_2 methanation - Decoupling size and support effects", submitted to *Catalysis, Science & Technology*.

JI developed the concept and carried out all experiments. MMM oversaw the Raman experiments. TG assisted with the XRD measurements and performed the Rietveld refinements. JK and MB supervised the project. JI wrote the manuscript with input from all other authors.

Student's work in this thesis

In this dissertation the results from the supervision of the following students' works are included:

Petra Martinovic, "Modifying the Porosity of Pure Sm_2O_3 Aero- and Xerogels", 2019

Declaration

I hereby declare that I completed this dissertation without any unauthorized third-party assistance, used no other sources or aids than the ones specified, and properly marked content and text passages that have been included verbatim or by content from other sources as such.

Bremen, 22.06.2020

Erklärung

Ich erkläre hiermit, dass ich die vorliegende Arbeit ohne unerlaubte fremde Hilfe angefertigt, keine anderen als die von mir angegebenen Quellen und Hilfsmittel benutzt und Stellen, die den benutzen Werken wörtlich oder inhaltlich entnommen wurden, als solche kenntlich gemacht habe.

Bremen, 22.06.2020